# Thermoresponsive polymers under high pressure

Thermoresponsive Polymere unter Hochdruck

Dissertation of

*Bart-Jan Niebuur*

Technische Universität München
Physik-Department
Fachgebiet Physik weicher Materie

Supervised by
Prof. Christine M. Papadakis, Ph.D.

# TECHNISCHE UNIVERSITÄT MÜNCHEN

Physik-Department, Fachgebiet Physik weicher Materie

# Thermoresponsive polymers
# under high pressure

## Bart-Jan Niebuur

Vollständiger Abdruck der von der Fakultät für Physik der Technischen Universität München zur Erlangung des akademischen Grades eines

**Doktors der Naturwissenschaften (Dr. rer. nat.)**

genehmigten Dissertation.

|  |  |
|---|---|
| Vorsitzender: | Prof. Dr. Martin Zacharias |
| Prüfer der Dissertation: | 1. Prof. Christine M. Papadakis, Ph.D. |
|  | 2. Prof. Dr. Christoph P. Hugenschmidt |

Die Dissertation wurde am 31.07.2019 bei der Technischen Universität München eingereicht und durch die Fakultät für Physik am 01.10.2019 angenommen.

# Preface

The conducted research presented in this thesis was performed under supervision of Prof. Dr. Christine M. Papadakis in the Soft Matter Physics Group at the Physics Department of the Technical University of Munich. The research was performed in close collaboration with Prof. Dr. Alfons Schulte, University of Central Florida. In this framework, a part of the experimental work, Raman spectroscopy measurements and optical microscopy, was performed in the lab of Prof. Dr. Alfons Schulte.

The main results of this thesis are based on neutron scattering beamtimes. Very small angle neutron scattering experiments were performed in cooperation with Dr. Vitaliy Pipich, conducted at the instrument KWS-3 at the Heinz Maier-Leibnitz Zentrum (MLZ) in Garching, Germany. Quasi-elastic neutron scattering experiments were performed at the instrument TOFTOF at the MLZ, in cooperation with Dr. Wiebke Lohstroh. In both cases, the use of the high-pressure systems was facilitated by Dr. Marie-Sousai Appavou. Small-angle neutron scattering experiments were performed at the instrument D11 at the Institute Laue-Langevin, Grenoble, France, with help of Dr. Leornardo Chiappisi and Dr. Ralf Schweins. Technical support for the high-pressure equipment was provided by C. Payre and J. Maurice, Institute Laue-Langevin.

# Abstract

This thesis investigates the phase behavior in aqueous poly($N$-isopropylacrylamide) (PNIPAM) solutions under pressure using neutron and light scattering techniques. The influence of pressure on the hydration state of PNIPAM and on the formation of the mesoglobules were studied in detail. Time-resolved investigations after rapid pressure jumps allowed the characterization of the growth kinetics of the mesoglobules. The effect of pressure on the co-nonsolvency behavior was investigated as well.

# Zusammenfassung

In dieser Arbeit wird das Phasenverhalten in wässrigen Poly($N$-isopropylacrylamid) (PNIPAM) Lösungen unter Hochdruck mit Neutronen- und Lichtstreumethoden untersucht. Der Einfluss von Druck auf den Hydratationszustand von PNIPAM und auf die Bildung der Aggregate wurden im Detail untersucht. Zeitaufgelöste Untersuchungen nach schnellen Drucksprüngen erlauben die Charakterisierung der Wachstumskinetik der Aggregate. Der Einfluss von Druck auf das Co-nonsolvency-Verhalten wurde ebenfalls untersucht.

# List of abbreviations

| | |
|---|---|
| DHO | damped harmonic oscillator |
| DLA | diffusion-limited aggregation |
| DLC | diffusion-limited coalescence |
| DLS | dynamic light scattering |
| DSC | differential scanning calorimetry |
| FT-IR | Fourier-transform infrared spectroscopy |
| GP | Guinier-Porod |
| HP | high pressure |
| IR | infrared |
| LCST | lower critical solution temperature |
| LP | low pressure |
| MCR | monochromating counter rotation |
| MLZ | Heinz Maier-Leibnitz Zentrum |
| OZ | Ornstein-Zernike |
| PCR | pulsing counter rotation |
| PNIPAM | poly($N$-isopropylacrylamide) |
| QENS | quasi-elastic neutron scattering |
| SANS | small-angle neutron scattering |
| SDD | sample-detector distance |
| UCST | upper critical solution temperature |
| VSANS | very small angle neutron scattering |

# List of symbols

| | |
|---|---|
| $A$ | local entropic contribution to $\chi_{eff}$ |
| $a$ | monomer length |
| $B$ | enthalpic contribution to $\chi_{eff}$ |
| $b$ | scattering length |
| $C$ | scaling constant in the Beaucage model |
| $C_{el}(q)$ | elastic line strength |
| $C_{p,i}$ | isobaric heat capacity of system $i$ |
| $c$ | concentration |
| $c^*$ | overlap concentration |
| $c_m$ | concentration in molality |
| $D$ | diffusion coefficient |
| $d_i$ | density of system $i$ |
| $d$ | diffusion process of bulk water |
| $E$ | energy |
| $E(t)$ | electric field |
| $el$ | elastic contribution |
| $f(\lambda, \theta, t)$ | scattering strength |
| $G(\vec{R}, t)$ | self-correlation function |
| $G_{collapsed}$ | Gibbs free energy of collapsed chains |
| $G_{swollen}$ | Gibbs free energy of swollen chains |
| $g(\vec{r})$ | pair correlation function |
| $h$ | relaxation process of hydration water |
| $I(q)$ | scattered intensity in dependence on momentum transfer |
| $I_G$ | Guinier intensity |
| $K_P$ | Porod amplitude |
| $k$ | magnitude of the wave vector |
| $\vec{k}$ | wave vector |
| $\vec{k}_i$ | wave vector of incident particles |

| | |
|---|---|
| $\vec{k}_s$ | wave vector of scattered particles |
| $l$ | effective local process of bulk water |
| $l_j$ | apparent jump amplitude of process $j$ |
| $M_n$ | number-average molar mass |
| $M_w$ | weight-average molar mass |
| $m$ | Porod exponent |
| $m_n$ | neutron mass |
| $n_B(\omega)$ | Bose occupation number |
| NA | numerical aperture |
| $p$ | pressure |
| $p(t)$ | dipole moment |
| $Q^*$ | invariant scattering |
| $\vec{q}$ | momentum transfer |
| $q^*$ | transition $q$ value |
| $R(q, q')$ | SANS resolution function |
| $\vec{R}$ | position on sample |
| $\vec{r}$ | position on detector |
| $R_0$ | particle size at time $t = 0$ |
| $R_g$ | radius of gyration |
| $S(\vec{q}, \omega)$ | dynamic structure factor |
| $S_{coh}(\vec{q}, \omega)$ | coherent dynamic structure factor |
| $S_{inc}(\vec{q}, \omega)$ | incoherent dynamic structure factor |
| $S_v$ | specific surface of mesoglobules |
| $T$ | temperature |
| $T_c$ | critical temperature |
| $T_{cp}$ | cloud point temperature |
| $S$ | entropy |
| $t$ | time |
| $u_i$ | speed of sound of system $i$ |
| $\langle u_{\text{eff}}^2 \rangle$ | effective mean-square displacement |

| | |
|---|---|
| $V$ | volume |
| $V^{\varphi}$ | apparent molar volume |
| $v$ | vibrational process |
| $x$ | vibrational displacement coordinate |
| | |
| $\alpha$ | polarizability |
| $\alpha_{V,i}$ | thermal expansion coefficient of system $i$ |
| $\beta$ | growth exponent |
| $\beta_{T,i}$ | isothermal compressibility factor of system $i$ |
| $\epsilon$ | energy barrier for coalescence in units of $k_B T$ |
| $\epsilon_{pp}$ | polymer-polymer interaction energy |
| $\epsilon_{ps}$ | polymer-solvent interaction energy |
| $\epsilon_{ss}$ | solvent-solvent interaction energy |
| $\Gamma_q$ | damping factor in the DHO model |
| $\gamma_I$ | critical exponent of the susceptibility |
| $\gamma$ | Lorentzian line width |
| $\Delta E$ | energy transfer |
| $\Delta F_{mix}$ | Helmholtz free energy of mixing |
| $\Delta G_{mix}$ | Gibbs free energy of mixing |
| $\Delta p$ | pressure change of a pressure jump |
| $\Delta S_{conf}$ | change in configurational entropy upon mixing |
| $\Delta S_{water}$ | change in entropy upon mixing due to water structures |
| $\Delta U$ | change in enthalpy upon mixing |
| $\Delta \rho$ | difference in scattering length density between two phases |
| $2\theta$ | scattering angle |
| $\kappa_T$ | isothermal compressibility |
| $\kappa_T^{\varphi}$ | apparent molar isothermal compressibility |
| $\lambda$ | wavelength |
| $\mu$ | reduced mass |
| $\nu_{\xi}$ | critical exponent of the correlation length |
| $\nu$ | frequency |

| | |
|---|---|
| $\xi$ | correlation length of concentration fluctuations |
| $\rho(\vec{R}, t)$ | scattering length density |
| $\sigma$ | Gaussian line width (standard deviation) |
| $\sigma_q^2$ | variance in $q$ |
| $\sigma_{coh}$ | coherent scattering cross section |
| $\sigma_{inc}$ | incoherent scattering cross section |
| $\sigma_{tot}$ | total scattering cross section |
| $\tau$ | characteristic time scale |
| $\tau_c$ | collision time |
| $\tau_{cls}$ | encounter and coalescence time in the DLC model |
| $\tau_d$ | relaxation time of the diffusion process of bulk water |
| $\tau_e$ | entanglement time |
| $\tau_h$ | relaxation time of hydration water |
| $\tau_l$ | relaxation time of the effective local process of bulk water |
| $\tau_{log}$ | time between collisions in the hindered growth model |
| $\tau_{0,j}$ | residence time of process $j$ |
| $\Phi$ | flux of incident neutron beam |
| $\phi$ | volume fraction |
| $\chi$ | Flory-Huggins interaction parameter |
| $\chi_{eff}$ | effective Flory-Huggins interaction parameter |
| $\chi''(q,\nu)$ | imaginary part of the dynamic susceptibility |
| $\chi_j''(q,\nu)$ | contribution of $j$ to the imaginary part of the dynamic susceptibility |
| $\psi_i$ | wave function of incident wave |
| $\psi_s$ | wave function of scattered wave |
| $\Omega$ | solid angle |
| $\omega$ | (angular) frequency |
| $\omega_0$ | peak (angular) frequency |
| $\omega_i$ | (angular) frequency of incident particles |
| $\omega_m$ | frequency of vibrational mode in a molecule |
| $\omega_s$ | (angular) frequency of scattered particles |

# Contents

# Chapter 1. Introduction

Phase transitions are critically important in a wide range of fields, ranging from biology to material science. For example, the functionality of a system due to the change in the properties upon a phase transition regulates life functions in human organisms [1, 2] or is responsible for the storage of data in hard-disks [3]. The physical processes involved in phase transitions depend strongly on the interactions, and therefore on the type of the systems. In addition to interactions, also the structure of the components play an important role. In contrast to small molecules, macromolecules can be involved in complex or very specific functions, enabled by their complex structure. In this respect, the field of soft matter is particularly interesting, due to the wide variety of potential and existing applications [4]. Soft matter can be described as matter that can easily be deformed or altered in another way by relatively small external forces, since interactions and thermal fluctuations have similar energetic strengths [5]. As the basic structural units of soft matter are often large, they can be classified as macromolecules. Due to their large size, the formation of well-ordered structures at large length scales is hindered, making the material soft and sensitive for its environment [4, 5].

In nature, transitions of macromolecules in aqueous environments are vital for biological functions [1]. The functionality of these macromolecules, e.g. proteins or nucleic acids, is mediated by their interaction with water [6]. A change in this interaction, induced by a change in the conditions such as temperature of pH, may affect the conformation of the macromolecules or initiates the formation of complexes. Besides, protein misfolding and their subsequent aggregation may lead to various diseases [7, 8, 9]. A deep understanding of the mechanisms involved in protein aggregation is therefore key in the development of treatment methods.

An important class of synthetic macromolecules is that of polymers. Due to their tunable structure and potential responsiveness to external stimuli such as temperature, polymers are

often used as building blocks for structures on mesoscopic length scales, that find applications ranging from drug-delivery [10, 11] to actuators [12, 13]. Polymers consist of covalently bound repeating units, called monomers [14]. In their simplest form, polymers are long linear sequences of identical repeating units, called monomers. However, a wide variation of chain architecture is possible. For example, the properties of polymers can be altered by branching, i.e., deviations from a linear chain topology, or by the use of several monomers in different arrangements [4, 15]. Also the functionality of polymers is mediated by the interaction with water. Their hydration state mediates, for example, the chain conformation or their association. Polymers may phase separate, leading to structures on mesoscopic length scales, called aggregates. They may serve in a wide range of applications, such as nano-electronics, drug transport, bioengineering, solar cells, catalysis and cosmetics [16, 17, 18]. Understanding the process of self-assembly is therefore key to control their formation, and thereby their size, structure and functional properties.

Due to the technical challenges, pressure is a largely unexplored stimulus to initiate phase transitions. Besides temperature, it is a fundamental thermodynamic parameter that influences the hydration state of macromolecules. Knowledge of the dependence of a system on both parameters is therefore needed to fully describe it. Application of hydrostatic pressure changes the equilibrium state of a system to the one with the lowest overall volume [19]. Most research on its implications focused on biological macromolecules. It was shown that, whereas covalent bonds nearly incompressible [19], the interaction between macromolecules and water is strongly influenced by pressure. Compared to bulk water, the compressibility of the hydration layer is strongly reduced around charged groups, increased around apolar groups and not significantly changed around polar groups [20]. Thus, a change in pressure leads to the redistribution of water around macromolecules. In addition, it was shown that pressure promotes intermolecular hydrogen bonds in biological macromolecules, strongly influencing their conformation [21, 22].

Despite its importance, studies on the influence of pressure on phase transitions and aggregation behavior in polymer solutions are less numerous than that of protein solutions. Due to their simple chemical structure and the absence of secondary structure formation, polymers can be used as simple model systems to study complex macromolecules. In addition, numerous potential applications exist, especially in sensors [23, 24]. At atmospheric pressure, poly($N$-isopropylacrylamide) (PNIPAM) is one of the most widely studied stimuli-responsive polymers [25]. It serves as a simple model system to study fundamental interactions that

play a role in systems composed of more complex macromolecules. Upon heating of aqueous PNIPAM solutions temperatures above its cloud point of ~31 °C at atmospheric pressure, it changes from a dissolved state, where the chains are hydrated, to a two-phase state composed of a polymer-rich and a water-rich phase. Instead of macroscopic phase separation, as typically occurs in the two-phase state of polymer solutions, aqueous PNIPAM solutions form long-lived aggregates termed mesoglobules, shown in Figure 1.1. Their sizes range from ~10 to ~1000 nm, depending on the conditions [26, 27, 28, 29, 30]. Among other mechanisms, the visco-elastic effect was suggested to be responsible for their apparent stability [26, 28]. Due to the strong dehydration of the chains in the two-phase state, their mobility is very low, hindering the coalescence of mesoglobules. However, conclusive experimental evidence is lacking.
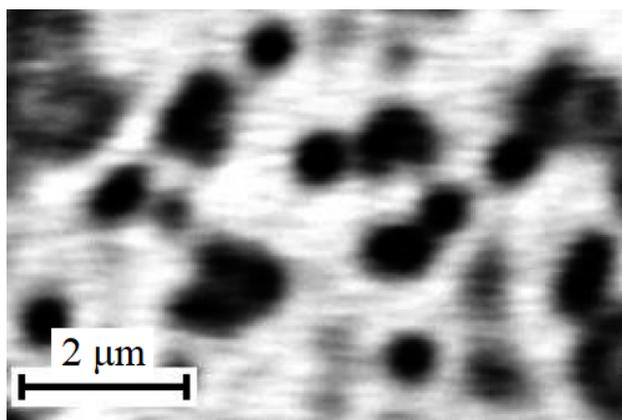


Figure 1.1: Optical microscopy image of mesoglobules formed in the two-phase state of a 1 wt% PNIPAM solution in $D_2O$. Reprinted with permission from [31]. Copyright (2019) American Chemical Society.

Phase separation in aqueous PNIPAM solutions also takes place at high pressure. As is the case for aqueous solutions of proteins, the coexistence line of the one-phase and two-phase state in the temperature-pressure frame adopts an elliptical shape: The cloud point temperature increases at first with pressure up to a maximum of ~60 MPa, and decreases at higher pressures. It has been shown previously, that pressure strongly changes the hydration state of PNIPAM [32]. Since the mobility of the chains depends on their hydration state, it can be expected that the structure of aqueous PNIPAM solutions is also strongly influenced by pressure, both in the one-phase and in the two-phase state.

The aim of this work is to systematically investigate the effect of pressure on phase separation in aqueous PNIPAM solutions, with a focus on structural properties and the role of hydration water. The results allow to elucidate the physical mechanism involved in the phase

separation at different pressures. In addition, the properties of the two-phase state at high pressure are explored, and the driving force of the apparent stability of the mesoglobules at atmospheric pressure may be found. At this, mainly light and neutron scattering methods are applied to focus on the different aspects of the phase transition.

In more detail, the phase diagram in the temperature-pressure frame of the aqueous PNIPAM solutions under study is established using turbidimetry. To quantify the solubility of PNIPAM at different positions in the phase diagram, calculations of the Gibbs free energy of mixing are performed. This investigation on the macroscopic properties is followed by a structural study at equilibrium conditions in the two-phase state, where mesoglobules are formed. Their size, shape and water content is determined in dependence on pressure using very small angle neutron scattering. In addition, Raman spectroscopy is applied to focus on the hydrophobic hydration of the chains. Subsequently, the interaction between PNIPAM and water is studied in detail, since it is key to understand the structural properties of the solution in dependence on temperature and pressure. At this, the dynamics of water in the solution is investigated using quasi-elastic neutron scattering. It allows to distinguish between bulk water and hydration water, i.e., water that is bound to some degree to the chains, to determine their dynamic properties separately. Furthermore, pressure offers the possibility to rapidly switch between different states, since changes in pressure can be applied much faster than changes in temperature. Using a combination of pressure jumps and small-angle neutron scattering, the structure of intermediate states involved in a phase transition can be followed with excellent time resolution, which allows to distinguish between thermodynamic driving forces for the phase transition and the kinetic effects that may hinder it.

The study on purely aqueous PNIPAM solutions is extended to systems with more complex solvent interactions. In the second part of this thesis, the solvent type is varied. Earlier work at atmospheric pressure showed that, although both water and methanol are good solvents for PNIPAM, its solubility is strongly reduced in mixtures of both solvents [33]. This effect, termed the co-nonsolvency effect in the literature, is in this thesis investigated at high pressure. Earlier work showed that the co-nonsolvency effect is destroyed at high pressure [34, 35, 36], i.e., at high pressure, the solubility of PNIPAM in mixtures of water and an organic solvent is enhanced compared to purely aqueous PNIPAM solutions. Pressure therefore strongly affects the complex interactions that are present in the system. Several theories describing this phenomenon were proposed [35, 37, 38, 39], and can roughly be divided into theories based on polymer-solvent and solvent-solvent interactions. Very few attempted an

experimental study on this effect [36], support for either of these theories is therefore lacking.

In this work, experimental methods are applied to investigate the molecular interactions in PNIPAM solutions in mixtures of water and methanol. To investigate the interaction between PNIPAM and the solvent, the chain conformation in the one-phase state of a semi-dilute PNIPAM solution in water and methanol is determined in dependence on temperature and pressure using small-angle neutron scattering. In a more direct approach, the dynamics of water in this system is determined using quasi-elastic neutron scattering. Its dynamic properties can expected to be influenced significantly by the presence of methanol, and allows therefore to study the polymer-solvent and solvent-solvent interactions directly. The combination of both approaches gives new insights in the dependence of the co-nonsolvency effect on pressure.

This thesis is organized as follows: After a discussion on the physical properties of thermoresponsive polymers in solution, background information about the investigated polymer PNIPAM is given. Following this, the theoretical and practical aspects of the used experimental aspects are discussed. In the main part, the results from the employed experimental techniques are given and discussed. In Chapters 5 to 9, the effect of pressure on the properties of PNIPAM solutions during the phase transitions in purely aqueous PNIPAM solutions are discussed. Following this, the results on aqueous PNIPAM solutions containing small amounts of methanol are given in Chapters 10 and 11, where the effect of pressure on the co-nonsolvency effect is investigated. In the final part, the main findings presented in this thesis are summarized.

# Chapter 2. Background information

In this chapter, the physical properties of thermoresponsive polymers is described. After the background information on their phase behavior, kinetic processes occurring during their phase separation are described. In the last section of this chapter, the influence of pressure on solutions of thermoresponsive polymers is discussed.

## 2.1 Thermoresponsive polymers in solution

Thermoresponsive polymers are polymers that react sharply to a change in temperature, which can, for example, be detected as a sharp change in their molecular conformation. In the following, the properties of solutions of soluble polymers, where the solution forms a one-phase state, are described at first. Subsequently, the different aspects of the transition upon a change in temperature to a state where the polymers are insoluble are discussed. The incompatibility of the chains with the solvent leads to phase separation into polymer-rich and solvent-rich phases, termed the two-phase state.

### 2.1.1 Concentration regimes

Polymers dissolved in a good solvent adopt a swollen conformation to maximize the number of polymer-solvent contacts, since there exists a favorable interaction between the polymer and the solvent [4]. In this case, the solutions can be classified according to the concentration of the polymer in the solution. Figure 2.1 displays a schematic representation of a polymer solution at different concentration regimes. At low concentrations, the chains form coils that are well-separated from each other, and is therefore called the dilute concentration regime. The structure of the system is characterized by the radius of gyration $R_g$ of the coils, which depends on the conformation of the chains, and therefore on the solvent quality (Figure 2.1a).

With increasing concentration, the coils come closer to each other until they start to overlap at the overlap concentration $c^*$. From geometrical considerations, $c^*$ can be estimated
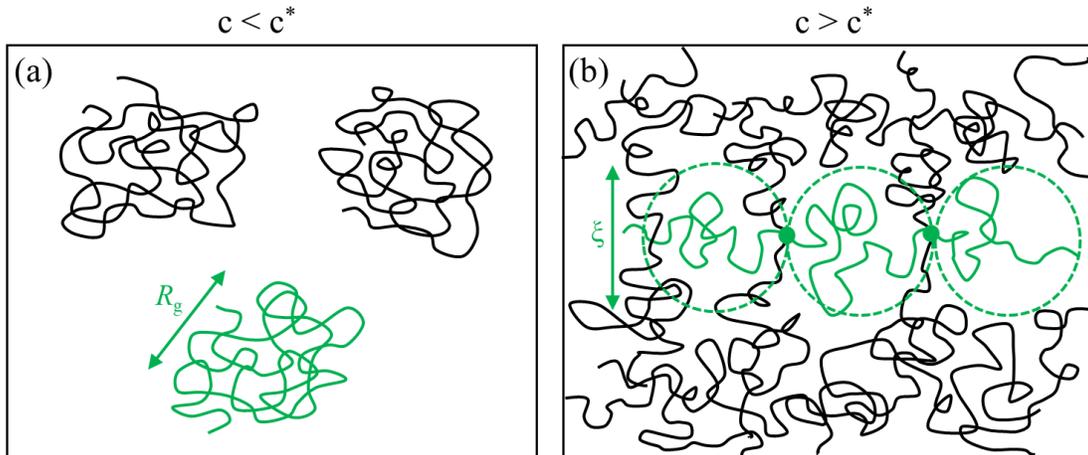
Figure 2.1: Solutions with a polymer concentration below (a) and above the overlap concentration (b). The green chain is highlighted to visualize the difference in chain conformation for both cases. The green dots in (b) indicates the overlap points.

from $R_g$ in the dilute regime as [40]

$$\frac{3M_w}{4\pi N_A R_g^3} < c^* < \frac{M_w}{N_A(\sqrt{2}R_g)^3} \tag{2.1}$$

where $M_w$ is the weight-average molar mass of the chains and $N_A$ the Avogadro constant. Above $c^*$, but still at relatively low polymer concentrations, the system is in the semi-dilute concentration regime. In this case, overlap points between chains exist, and the structure of the system can be characterized by the distance between these overlap points $\xi$, visualized in Figure 2.1b. The regions between the overlap points are called 'blobs'. The chain segments inside one blob do not interact with chain segments in other blobs. Therefore, the conformation of the chain segments inside these blobs is identical with the conformation of an entire chain in the dilute regime. With increasing concentration, also the number of overlap points increases. It was shown that, in the semi-dilute concentration regime, $\xi$ follows a $c^{-3/4}$ dependence [41]. The spatial correlation between monomers can be described by the Ornstein-Zernike pair correlation function,

$$g(r) = A\frac{\xi}{r}\exp(-\frac{r}{\xi}) \tag{2.2}$$

with $A$ a constant [41].

At high polymer concentrations, the concentrated concentration regime is reached. In this case, monomer-monomer interactions dominate, since the segments do not have suffi-

cient space to move freely. As this influences the local chain conformation, deviations from equation 2.2 are expected [41, 42].

## 2.1.2   Segregation behavior

Different types of thermoresponsive polymers are distinguished: thermoresponsive polymers with an upper critical solution temperature (UCST) and with a lower critical solution temperature (LCST). UCST polymers are soluble at high temperatures, and undergo phase separation upon cooling. Apart from temperature, the solubility of these polymers depend significantly on the polymer concentration. Figure 2.2a shows the Gibbs free energy of mixing of a UCST-type polymer in dependence on concentration at a certain temperature $T_1$. At this temperature, the free energy displays two minima. At concentrations between the binodal points b and b', defined as the contact points of a double tangent line close to the minima, two new phases with different composition can form to reduce the total free energy, resulting in phase separation. At lower or higher compositions, this is not possible, and the system is therefore stable. At compositions between b and b', two different scenarios may take place. Firstly, at compositions at which the free energy has a positive curvature, i.e., between b and s, and between b' and s', small variations in composition lead to an increase in the free energy and are therefore unfavorable. Consequently, phase separation can only take place with large variations in composition, i.e., where one of the new phases has a composition located at the other side of the maximum in the free energy. An energy barrier for phase separation is present, and the system is in a metastable state. Secondly, at compositions where the free energy has a negative curvature, i.e., between the spinodal points s and s', the system is unstable against every fluctuation in composition. An energy barrier hindering phase separation is therefore not present, and the system is completely unstable.

From the Gibbs free energy of mixing at different temperatures, the phase diagram of polymer solutions in the temperature-composition frame can be constructed, shown in Figure 2.2b for a UCST-type polymer. Different regions can be distinguished. The binodal line is constructed from the points b and b' in the free energy curve at different temperatures. It separates the stable region from the region where phase separation occurs. The spinodal line is constructed from points s and s' in the free energy curve at different temperatures. Between the binodal and spinodal line, the metastable region is located. Below the spinodal line, the system is unstable. After deep quenches, i.e., to states below the spinodal line in Figure 2.2b, the system is unstable to every composition fluctuations and phase sepa-
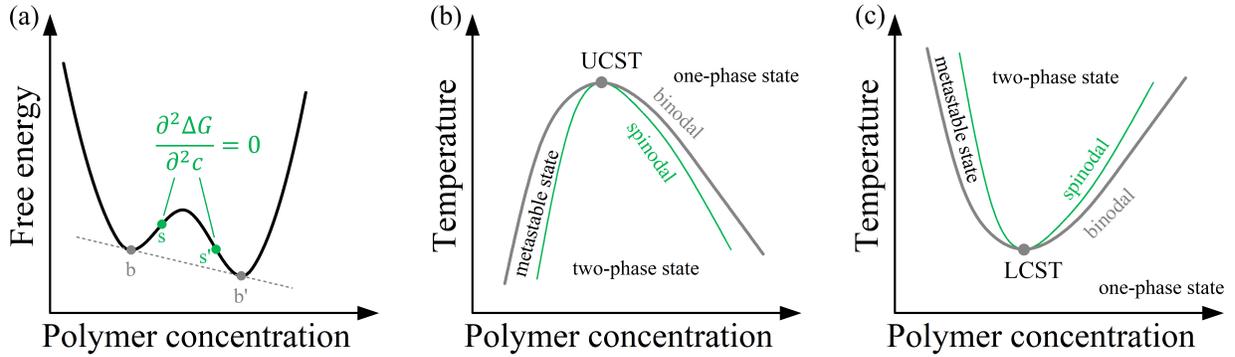
Figure 2.2: (a) Gibbs free energy of mixing in dependence on composition at temperature $T_1$. Points b and b' are the binodal points, points s and s' are the spinodal points. (b) Phase diagram in the temperature-composition frame of thermoresponsive polymers with UCST and (c) with LCST behavior.

ration follows the spinodal decomposition mechanism [43]. In the early stages of spinodal decomposition, all composition fluctuations persist and phase separation is initiated at every position in the system. Due to the surface tension between the formed interfaces, a periodic variation in composition is formed throughout the system that increases in amplitude with time but maintains its inter-domain distance, as follows from Cahn's linear theory for spinodal decomposition [43, 44]. At later times, coarsening of the domains becomes evident. After the formation of sharp surfaces between the domains in the early stages of spinodal decomposition, the interfacial free energy can be reduced by the coalescence of domains [45]. During these stages, the time dependence of the domain size is expected to follow $R \propto t^{-\beta}$ with an exponent $\beta$ depending on the coarsening mechanism [44, 46].

After shallow quenches, i.e., to states between the binodal and spinodal line, the metastable phase is reached. In this case, phase separation is not spontaneous, as for deep quenches, but follows a nucleation and growth mechanism. In this scenario, small fluctuations in composition are unstable and again vanish. Large composition fluctuations, however, persist, and clusters of chains form in the system at random positions. The gain in free energy for cluster formation is governed by a competition between a volume term, favoring the formation of clusters, and a surface term, opposing the formation of clusters. Thus, an energy barrier $E^*$ needs to be overcome, which corresponds to a minimum size of the clusters that persist after their formation [47, 48]. The formed clusters grow by a mechanism that depends on the system. In many cases, clusters grow by coalescence, which may be a diffusion-controlled process. In this case, the growth is expected to follow $R \propto t^{1/3}$ [47, 49]. Other mechanisms of growth, such as reaction-limited coalescence [50], can lead to other growth laws.

Also for LCST-type polymers, both types of segregation were observed [4]. In this case, the phase diagram in the temperature-composition frame has a convex-downward shape (Figure 2.2c) with the LCST located at the minimum. Segregation by spinodal decomposition and nucleation and growth therefore occurs upon quenches to higher temperatures.

### 2.1.3 Dynamic asymmetry

As described in Section 2.1.2, phase separation can proceed via nucleation and growth or spinodal decomposition, depending on the location in the temperature-concentration phase diagram. Furthermore, phase separation in polymer solutions is influenced by dynamic asymmetry. The differences in the mobility of the different species in the system, i.e., slow chains and fast solvent molecules due to the large differences in size, may lead to visco-elastic effects. In addition to the limitations due to the diffusional processes, included in conventional theories for phase separation, visco-elastic effects hinder the phase separation even further.

Different scenarios of phase separation that is influenced by the visco-elastic effect are possible, and depend on the polymer concentration. In case of dilute polymer solutions, the chains dehydrate and therefore collapse into small globules upon a quench into the two-phase state. These move through the solution due to Brownian motion. On might expect that phase separation in the system occurs due to the coalescence of these globules. It is, however, hindered by the visco-elastic effect. In order to coalesce, the chains from both globules need to penetrate into each other, which is only possible by a reptation mechanism. As is illustrated in Figure 2.3, this can be achieved if the time needed to form these entanglements $\tau_e$, is smaller than the collision time $\tau_c$ (which is roughly the time needed to diffuse over the length of the diameter of the globules) [51]. In most cases, $\tau_e \gg \tau_c$. This means that the probability of coalescence upon each collision is very small, and the globular phase is kinetically stable [49, 52].

The phase separation of semi-dilute and concentrated solutions proceeds via 'visco-elastic spinodal decomposition' [53]. Due to the higher concentration, entanglements are present in the system that hinder the chains to collapse immediately after the quench. The initial stages of phase separation are therefore characterized by the formation of a temporal network of chains. With time, defects in the network develop and solvent-rich domains appear. During this stage, the network of chains disrupts completely, and the system undergoes a change from solvent-rich domains in a polymer-rich matrix to polymer-rich domains in the solvent matrix, i.e., a phase inversion. At the final stage, the system contains spherical polymer-rich
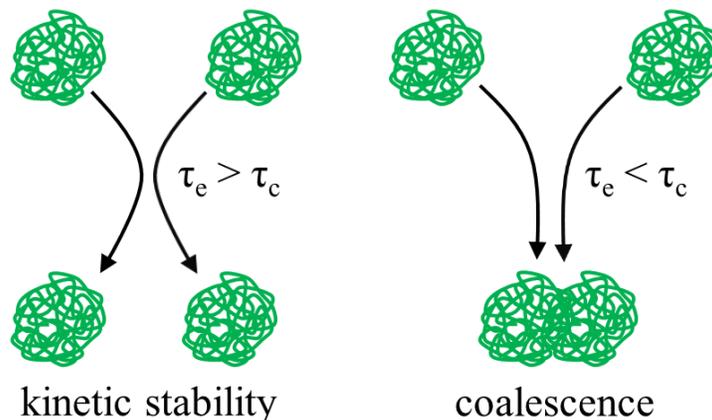
Figure 2.3: Visco-elastic effect in globules of polymers in solution. Kinetic stability of the solution is reach if the entanglement time $\tau_e$ is longer than the collision time $\tau_c$. Globules coalesce if $\tau_e$ is smaller than $\tau_c$.

droplets consisting of numerous chains that resemble the kinetically stable globular phase present after the phase transition in dilute polymer solutions [49].

### 2.1.4    Critical behavior in polymer solutions

In the one-phase state, the chains are soluble. Upon changing the temperature, the critical temperature is reached and the system undergoes a phase transition. To quantify the properties during the phase transition, an order parameter describing the system af different positions can be defined, which, for polymer solutions, may be the composition relative to the average composition in the system [54]. The free energy of a system can be written in terms of the order parameter. Higher-order phase transitions are characterized by singularities in the second derivatives of the free energy with respect to the order parameter at the critical temperature. Macroscopic physical properties proportional to the second derivatives, such as the susceptibility or the correlation length of concentration fluctuations, can therefore be described by power laws that diverge at the critical temperature, characterized by critical exponents. Whereas the critical temperature depends sensitively on the type and range of interactions playing a role in the system, the critical exponents depend mainly on the dimensionality of the system as well as on the symmetry of the order parameter, i.e., its invariance under certain symmetry transformations. The critical exponents are therefore said to be universal, they adopt similar values in a wide variety of phase transitions, for example the spontaneous magnetization below the Curie-temperature of a ferromagnetic material [55] and the demixing transition in binary mixtures of liquids [56, 57] or polymer melts [58, 59, 60, 61]. Depending on the dimensionality or symmetry of their order parameter, phase transitions can be classified according to the universality classes they belong to,

which are based on physical models that predict the critical exponents. Prominent examples of such physical models are the 3D Ising lattice model and mean-field theory [55].

The divergence of the macroscopic properties follows from the behavior of the system at microscopic length scales. For example, the correlation length of concentration fluctuations $\xi$, a measure of the order of a system, diverges at the critical temperature, meaning that order exists at all length scales in the system. Below as well as above the critical temperature, $\xi$ follows a power law of the form

$$\xi = \xi_0 \left| \frac{T - T_c}{T_c} \right|^{\nu_\xi} \tag{2.3}$$

with $T_c$ the critical temperature, $\nu_\xi$ the critical exponent describing the correlation length and $\xi_0$ a constant. Various experimental methods can be used to measure $\xi$ of a system, which therefore offers a possibility to determine to which universality class the system belongs. Also semi-dilute solutions of thermoresponsive polymers were shown to display critical behavior [62, 63, 64, 65, 66]. With a change in temperature, the local chain conformation changes, leading to an increases or decreases of the distance between overlap points, and therefore of $\xi$ [40].

## 2.2 Kinetics of aggregation

Upon a quench from the one-phase state to the two-phase state, phase separation is induced. As described in Section 2.1.2, the initial stages of phase separation may follow spinodal decomposition or nucleation and growth. The growth of domains after their formation can follow several mechanisms, depending on the system. In the following, examples that are important in polymeric systems are given.

**Diffusion-limited aggregation.** The aggregation of homopolymers was subject of numerous papers in the last decades. An obvious starting point for describing aggregation behavior is the standard diffusion-limited aggregation (DLA) model. In this model, it is assumed that the system consists of hard particles that stick to each other upon collision. The growth of the clusters formed by these particles is therefore limited by the time the particles need to pass by each other due to Brownian motion through the solution. In this model, the predicted growth of the clusters takes the form [67, 68]

$$R(t) \sim t^{0.57} \tag{2.4}$$

with $R(t)$ the size of the clusters at time $t$. Since DLA treats the case of hard particles that do not deform during their aggregation, the resulting aggregates have a fractal shape. However, aggregates from several types of homopolymers are shown not to be fractal, but compact clusters [31, 69]. Furthermore, the observed growth rates are usually much lower than those predicted by DLA [51].

**Diffusion-limited coalescence.**   As polymers are flexible molecules, clusters of polymers are able to deform to the thermodynamically most favorable state. To avoid contact with water, aggregates from hydrophobic polymers strive for minimization of the surface, leading to a spherical shape. In case the aggregation of soft particles is limited by diffusion, i.e., each encounter of two particles leads to their coalescence, it can theoretically be described by the diffusion-limited coalescence (DLC) model, which predicts a growth law of the form [70]

$$R(t) \sim \left(1 + \frac{t}{\tau_{cls}}\right)^{1/3} \tag{2.5}$$

where $\tau_{cls}$ is the coalescence time of two particles. As the growth exponent equals 1/3, the predicted growth is slower than the one predicted by the DLA model.

**Hindered growth model.**   In most cases, however, the situation is more complex. Since the observed growth rates of polymeric aggregates were found to be too small to be described by DLC, the presence of an energy barrier $E_a$ that needs to be overcome for the coalescence of two particles, was predicted [71]. As a result, coalescence occurs with a probability exp(-$E_a/k_B T$) after each encounter between two particles, resulting in lower growth rates than predicted by the DLC model. Various mechanisms and interactions can be responsible for this energy barrier. For example, in case of amphiphilic polymers, the polar units on the polymer screen the hydrophobic units from the water, making the surface of the aggregates more hydrophilic [30].

The hindered growth model predicts the dependence of the radius of merging particles on time. By extending the DLC model with a factor that specifies the probability of coalescence when two particles collide, it results that the growth of the particles follows a logarithmic trend, given by [71]

$$R(t) = \frac{R_0}{\epsilon} \ln\left(\frac{\epsilon}{3} \frac{t}{\tau_{log}}\right) \tag{2.6}$$

Here, $R_0$ is the size of the particles before coalescence starts, $\tau_{log}$ the average time interval

between collisions and $\epsilon$ the energy barrier hindering coalescence in units of $k_B T$.

## 2.3   Pressure effects on thermoresponsive polymers in solution

Because of experimental challenges, pressure as a thermodynamic variable to alter the state of thermoresponsive polymers, or biomolecules such as proteins, is not as widely used as temperature. However, also a change in pressure allows changing the hydration state of molecules, which may influence the formed structure greatly. Most research focused on the pressure-temperature phase diagrams of proteins [72, 73]. At atmospheric pressure, the unfolded, denatured state of a protein can be reached by heating above the transition temperature. It was shown that pressures up to 100 MPa stabilize the native state of certain proteins, which increases the transition temperature to the denatured state. At significantly higher pressures ($\sim$500 MPa) denaturing can be induced by a change in pressure with, as a result, the unfolding of the protein [74].

Also thermoresponsive polymers respond strongly to variations in pressure. For several LCST-type polymers, it was shown that the stability of the one-phase state is increased up to pressures of around 100 MPa [75, 76, 77, 78]. At even higher pressures, an opposite effect sets in, which decreases the stability and thus reduces the cloud point. For UCST-type polymers the behavior is opposite, the cloud point temperature, i.e., the temperature at which phase separation takes place, decreases until it reaches a minimum at moderate pressures. At higher pressures, it shifts to higher temperatures again [79, 80, 81, 82, 34].

### 2.3.1   Hawley theory for pressure-temperature phase diagrams of protein solutions

Using a purely thermodynamic approach, Hawley [74] showed that the coexistence line of the native and denatured state in the pressure-temperature phase diagram of proteins can be described by an ellipse, determined from the Gibbs free energy. If one assumes that no intermediate state is present during the phase transition, the change in Gibbs free energy $\Delta G$ between both states is formulated as

$$\Delta G = G_{denatured} - G_{native} \qquad (2.7)$$

with $\Delta G$ a function of pressure $p$ and temperature $T$. Thus, $\Delta G$ can be approximated by a two-dimensional Taylor series around a reference point $(p_0, T_0)$ [77]. Up to the second order, it is given by

$$\Delta G(p,T) = \Delta G(p_0, T_0) + (p - p_0)\left(\frac{\partial \Delta G}{\partial p}\right)_{p_0, T_0} + (T - T_0)\left(\frac{\partial \Delta G}{\partial T}\right)_{p_0, T_0} + \frac{1}{2}(p - p_0)^2\left(\frac{\partial^2 \Delta G}{\partial p^2}\right)_{p_0, T_0}$$
$$+ (p - p_0)(T - T_0)\left(\frac{\partial^2 \Delta G}{\partial p \partial T}\right)_{p_0, T_0} + \frac{1}{2}(T - T_0)^2\left(\frac{\partial^2 \Delta G}{\partial T^2}\right)_{p_0, T_0}$$

$$(2.8)$$

The first and second derivatives of $\Delta G$ with respect to temperature and pressure are related to the volume $V$, entropy $S$, thermal expansion coefficient $\alpha_V$, isothermal compressibility $\kappa_T$ and the isobaric heat capacity $C_p$ as [83]

$$\frac{\partial G}{\partial p} = V, \quad \frac{\partial G}{\partial T} = -S, \quad \frac{\partial^2 G}{\partial p^2} = -V\kappa_T, \quad \frac{\partial^2 G}{\partial p \partial T} = V\alpha_V, \quad \frac{\partial^2 G}{\partial T^2} = -\frac{V}{T}C_p \quad (2.9)$$

Inserting the relations from equation 2.9 into equation 2.8 yields [77]

$$\Delta G(p,T) = \Delta G(p_0, T_0) + (p - p_0)\Delta V_0 - (T - T_0)\Delta S_0 - (p - p_0)^2\frac{V_0 \Delta \kappa_T}{2}$$
$$+ (p - p_0)(T - T_0)V_0 \Delta \alpha_V - (T - T_0)^2\frac{V_0 \Delta C_p}{2T_0} \quad (2.10)$$

The transition line between the native and denatured state is by definition the line in the temperature-pressure frame where $\Delta G = 0$. As at this line, both states are present in equal fractions, it is also named the coexistence line. By assuming that the phase change does not cause a change in volume and entropy, this equation reduces to the equation of an ellipse in the pressure-temperature frame around a center defined by $(p_0, T_0)$, given by [74, 77]

$$\frac{V_0 \Delta \kappa_T}{2 \Delta G_0}(p - p_0)^2 + \frac{V_0 \Delta C_p}{2T_0 \Delta G_0}(T - T_0)^2 = 1 \quad (2.11)$$

The Hawley theory was confirmed experimentally for numerous proteins, for example for staphylococcal nuclease [84], ribonuclease [85, 86] and $\beta$-lactoglobulin [87]. The predicted shape of the phase diagram displays interesting features. At low pressures, the slope of the ellipse is positive. Because the change in volume upon thermal unfolding is positive for most proteins, an increased pressure stabilizes the folded state, marked by the increased unfolding

temperature. At higher pressures, other effects come into play. According to the Clausius-Clapeyron equation, the volume change upon unfolding changes it sign and the slope of the coexistence line changes to negative. Increasing pressure from this point on therefore destabilizes the folded state. The negative change in volume upon unfolding makes it possible to induce unfolding by increasing the pressure even further [73, 88]. In some cases, however, the Hawley theory does not satisfactorily describe the temperature-pressure phase diagram of protein solutions [89, 90], and higher-order derivatives have to be taken into account. These lead to a slight distortion of the elliptical shape. As these may be too small to be detected, the Hawley theory agrees with cloud point data in most cases [91].

### 2.3.2    Effects of pressure on molecular interactions

Despite the success of the Hawley theory, it does not unravel the mechanism of denaturing of proteins or the phase separation of polymer solutions at different pressures. For a deeper understanding of the underlying processes, one needs to consider the effect of pressure on the structure of water. The hydrophobic interaction is the main driving force for stabilizing the collapsed state of macromolecules. An ordered clathrate-like structure of water is formed around the hydrophobic groups in the extended state, reducing the entropy of the system greatly. A more favorable state is the collapsed state, in which most of the hydrophobic groups are protected from water by the hydrophilic groups. The effect of the hydrophobic interaction is lowered when the pressure is increased. Because water changes from an open tetrahedral structure to a more ordered hexagonal one with increasing pressure, the entropic penalty of the clathrate-like structure of water around the hydrophobic groups decreases, lowering the relative importance of the hydrophobic interaction. The collapsed state is in this case not favorable anymore, and the macromolecule extends [92].

As a state with a minimized volume becomes favorable with increasing the pressure, phase transitions are, besides a weakened hydrophobic effect, governed by a negative $\Delta V$ at the transition. For protein solutions it was found that, due to packing effects, the compressibility of the hydration layer around the surface of proteins in their native state is higher than the one of bulk water. The net compressibility increase is due to the combination of the different compressibilities of hydration water around the charged, polar and apolar groups at the surface of proteins in the native state. Compared to bulk water, the compressibility of the hydration layer is strongly reduced around charged groups, enhanced around apolar groups and not significantly changed around polar groups [20]. Because a relatively large fraction of

the to water exposed surface of proteins in their native state is of apolar nature, the overall effect results in an increased compressibility of the hydration layer with respect to bulk water [20]. An increase in pressure leads at first to the compression of voids, roughing the surface of the proteins. Therefore, water can penetrate the inside of the protein. Exposing the hydrophobic, apolar, core of the proteins leads to the possibility to further compress the water in the newly formed hydration layers, leading to the unfolding of the protein [93, 94]. Furthermore, it was found that the change in compressibility of the hydration layer of different groups is only present in case of additive contributions from similar groups next to each other and seems therefore to be a macromolecule-specific effect. Studies on charged, polar and apolar groups attached to small molecules did not show a change in compressibility of the respective hydration layers [20].

# Chapter 3.  System under investigation

In this chapter, the physical properties of poly($N$-isopropylacrylamide), the thermoresponsive polymer under study in the present thesis, is described. After an overview of its phase behavior in aqueous solutions at atmospheric pressure, findings from previous studies on the influence of pressure on aqueous PNIPAM solution are summarized. Subsequently, the co-nonsolvency effect in PNIPAM solutions is described, both at atmospheric and at high pressure. In the final section, a detailed overview of the present study is given.

## 3.1   Poly($N$-isopropylacrylamide)

In the present thesis, the thermoresponsive polymer poly($N$-isopropylacrylamide) (PNIPAM) is investigated. Because of its versatility in a wide range of application, it is one of the most widely studied thermoresponsive polymers in the last decades [25, 95]. Most promising is the use of PNIPAM in biomedical applications, due to its LCST of $\sim$31 °C, which is close to the human body temperature. Its response to temperature can, for example, be employed in carriers for the site-specific delivery of drugs or tissue engineering [96, 97]. Furthermore, the sharp and tunable temperature-dependent switching properties of PNIPAM gels can be used in sensors [98, 99], or separation processes due to selective absorption of certain components by the gels [95]. The numerous previous studies on the thermoresponsive properties of PNIPAM, mostly performed at atmospheric pressure conditions, will provide a good basis of understanding for comparison with the results obtained at high pressure conditions, which is in the focus of this thesis.

Figure 3.1 presents the chemical structure of PNIPAM. To the vinyl backbone, side groups consisting of a hydrophilic amide group and a hydrophobic isopropyl group are attached. The delicate balance between hydrophobicity and hydrophilicity is responsible for the LCST behavior of PNIPAM, illustrated in Figure 3.1: At temperatures below the cloud point temperature $T_{cp}$, PNIPAM is soluble and an aqueous PNIPAM solutions has a transpar-

ent appearance. At temperatures above, the chains become insoluble, leading to a two-phase state and, therefore, a turbid appearance.
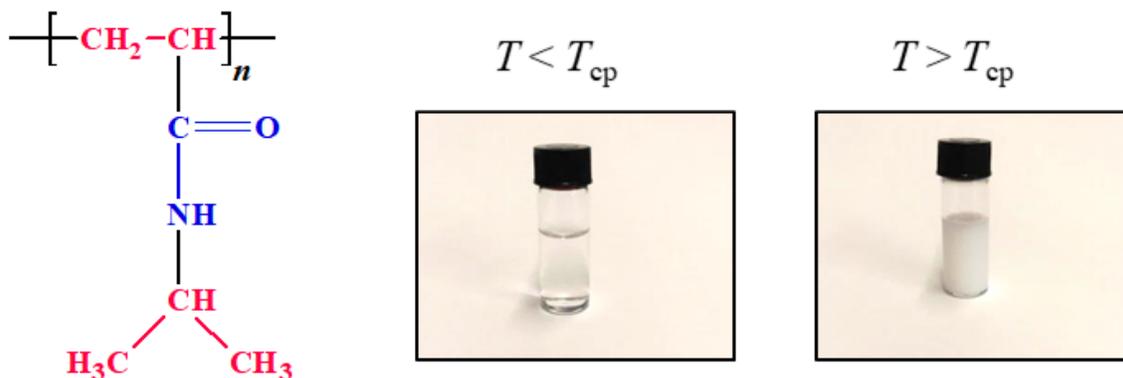


Figure 3.1: Left: Chemical structure of Poly($N$-isopropylacrylamide). The colors represent the hydrophobic (red) and the hydrophilic groups (blue). Middle: aqueous 3 wt% PNIPAM solution at a temperature below $T_{cp}$. Right: aqueous 3 wt% PNIPAM solution at a temperature above $T_{cp}$.

### 3.1.1 Phase transition mechanism

To successfully design smart structures for use in aqueous environments based on PNIPAM, its phase transition mechanism must be understood in detail at various conditions. The solubility of PNIPAM is governed by the interplay between the hydrophobic and hydrophilic groups on the chain, as shown in Figure 3.1. In the Flory-Huggins theory, the Helmholtz free energy of mixing $\Delta F_{mix}$ is used to determine the solubility of polymers in a solution, and is given by [14]

$$\Delta F_{mix} = \Delta U - T\Delta S_{conf} \tag{3.1}$$

with $\Delta U$ the change in enthalpy and $\Delta S_{conf}$ the change in configurational entropy upon mixing. In this theory, $\Delta U$ is determined from the Flory-Huggins interaction parameter $\chi$, which quantifies the interaction strength between the polymer and the solvent molecules. $\Delta U$ and $\chi$ are related as

$$\Delta U = k_B T \chi \phi (1 - \phi) \tag{3.2}$$

with $\phi$ the volume fraction of the polymer. The sign and magnitude of $\Delta U$ therefore depends on the type of polymer and solvent in the system. $\Delta S_{conf}$ always favors mixing of the system, since a two-phase state is entropically unfavorable, and is therefore positive.

In case of PNIPAM in aqueous solutions, hydrogen bonding between the polymer and water always favors mixing, thus, $\Delta U$ is negative. In addition, the presence of hydrophobic groups on the chains leads to an ordered structure of water around them. In addition to the configurational entropy, the decrease in entropy due to these water structures needs to be taken into account as well. Equation 3.1 can therefore be rewritten as [100, 101]

$$\Delta F_{mix} = \Delta U - T\Delta S_{conf} - T\Delta S_{water} \tag{3.3}$$

with $\Delta S_{water}$ the change in entropy due to the formation of ordered water structures upon mixing. $\Delta S_{water}$ is always negative, since it always favors de-mixing of the system. At low temperatures, $\Delta U$ dominates and the system is miscible. With increasing temperature, thermal motion increases, and the hydrogen bonds between water and the hydrophilic groups of PNIPAM become weaker, lowering the absolute value of $\Delta U$. At the same time, both the $T\Delta S_{conf}$ and the $T\Delta S_{water}$ terms increase in magnitude. At the LCST, the $T\Delta S_{water}$ term dominates, and the system demixes [100, 101].

In addition to these purely thermodynamic considerations, various methods were used to gain a deeper understanding in the mechanisms involved in phase separating PNIPAM solutions in more detail.

**Coil-to-globule transition.** Below the LCST, the PNIPAM chains are hydrated, resulting in their coil-like conformation. After heating through the phase transitions temperature, the chains dehydrate and therefore undergo a coil-to-globule transition [102, 103]. Contrary to many other thermoresponsive polymers, the coil-to-globule transition in aqueous PNIPAM solutions occurs in a very narrow temperature range around $T_{cp}$ [104], which is due to cooperative hydration of the chains [105]. After the formation of a hydrogen bond between a water molecule and an amide group at the chains, additional space at the amide group on adjacent monomers is created for the formation of a bond with a second water molecule. Due to this cooperative interaction, a sequence of hydrated monomers is formed along the chains. Between these sequences, the chain is dehydrated and forms a globule-like structure, which leads to a pearl-necklace structure of the chains, as shown in Figure 3.2. At $T_{cp}$, the dehydration of a certain monomer induces the dehydration of the adjacent ones. The sequences of hydrated monomers thus dehydrate entirely, leading to a narrow transition range [106].
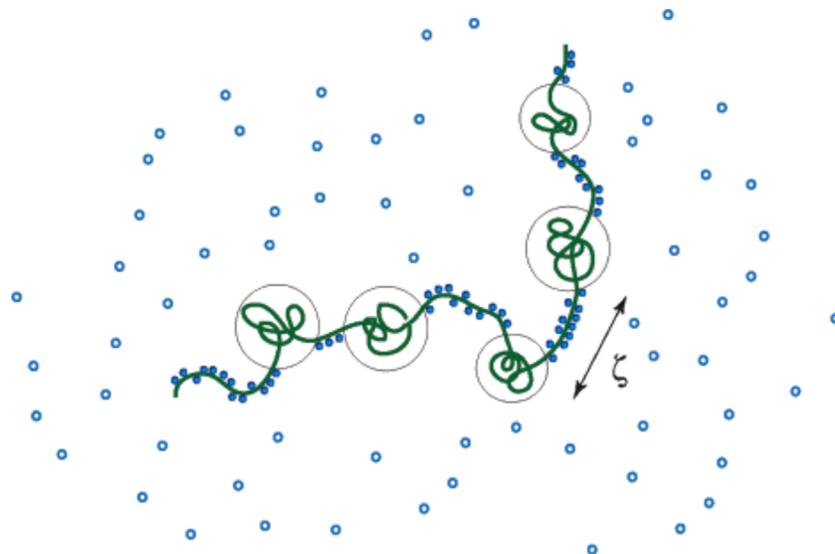
Figure 3.2:  Pearl-necklace structure of a polymer due to sequential hydrogen bonds, predicted by the cooperative hydration model. Reprinted with permission from [105]. Copyright (2019) American Chemical Society

The kinetics of this transition was the focus of numerous theoretical and experimental studies during the last decades. From theoretical considerations, it was shown that the coil-to-globule transition of a single chain is a two-step process [107, 108, 109]. Firstly, a fast local collapse of chain segments takes place, leading to the crumpling of the coil. At longer times, the crumpled coil collapses further into a globule.

Also from experimental work, it follows that the coil-to-globule transition of PNIPAM chains is a two-stage process. Using fluorescence measurements after a temperature jump induced by laser-heating [110, 111] and after the rapid mixing of PNIPAM solutions with a co-solvent to induce the phase transition [112], two relaxation processes with relaxation times of ~0.1 ms and ~1 ms were found and attributed to the ones described above. In a study of semi-dilute PNIPAM solutions, a slower third stage related to the disentanglement of overlapping chains was found [113].

**PNIPAM-water interactions.**   Spectroscopic methods such as infrared spectroscopy or Raman spectroscopy were proven to be exceptionally useful to measure the changes in interactions in the system, leading to the phase transition of PNIPAM. Terada et al. [114] were among the first to investigate aqueous PNIPAM solutions using Raman spectroscopy, focusing on the behavior of water during the phase transition. Their work showed that, whereas

below $T_{cp}$ water participates in intermolecular coupling to a similar extent as in bulk water, a significant fraction of very weakly bound water is found above. This was attributed to the trapping of water molecules inside PNIPAM globules; water molecules are isolated from each other, which reduces the number of hydrogen bonds that can be formed.

Other work focused on the hydrophilic groups of PNIPAM. The amide I and amide II band, which are accessible with both Fourier-transform infrared (FT-IR) and Raman spectroscopy, were shown to be sensitive to hydrogen bond formation by the hydrophilic groups. In PNIPAM, the amide I band, which is mainly due to C=O stretching, may form hydrogen bonds with water as well as with N-H groups, accessible via the amide II band [115, 116]. As the vibrational modes are sensitive to the formation of hydrogen bonds, changes in the vibrational frequency of both amide bands in aqueous PNIPAM solutions at the phase transition give insight into its driving forces. An FT-IR study by Lin et al. [117] showed that both the amide I and the amide II band can be decomposed into three subbands, assigned to unbound, intramolecular hydrogen bound and intermolecular bound amide groups with water molecules. From their relative presence, it was deduced that, below $T_{cp}$, intermolecular hydrogen bonded C=O and N-H groups with water account for more than half of the measured intensity from the amide bands. Above $T_{cp}$, however, the C=O and N-H groups significantly dehydrate and intramolecular hydrogen bonded hydrophilic groups become responsible for more than half of the measured intensity of the amide bands. Independently, Maeda et al. [116] interpreted similar data differently. By decomposing the amide I band into contributions from C=O hydrogen bonded with N-H and C=O hydrogen bonded with water, the authors concluded that, below $T_{cp}$, all the C=O groups are hydrated. Above $T_{cp}$, the C=O groups only slightly dehydrate; 87 % of the C=O groups stay hydrated, and only 13 % form hydrogen bonds with N-H groups.

A more detailed study performed by Ramon et al. [118] described in detail the mechanism of the phase transition of PNIPAM from the intensities of the amide I and II bands. It was found that, below $T_{cp}$, the number of free amide groups increases with temperature at the expense of hydrated amide groups, making the chains more flexible. At $T_{cp}$, they are sufficiently flexible to allow hydrophobic interactions between the hydrophobic moieties in the side groups and/or the backbone of the polymer. Simultaneously, free C=O and N-H groups start to form intramolecular hydrogen bonds. Further indications of this mechanism were found in the temperature dependence of the water-related contributions to the spectra: Water and PNIPAM are separated from each other at $T_{cp}$. At higher temperatures, a small

increase in the amount of hydrogen bonds between water and hydrophilic groups of PNIPAM was found and attributed to water trapped inside polymeric aggregates reconnecting to the free amide groups.

A completely different mechanism of the collapse was proposed by Ahmed et al. [119]. In UV resonance Raman spectroscopy, the different contributions of the amide I band were assigned to C=O stretching bands hydrogen bonded to a varying number of water molecules. Together with the $C_aH_b$ bending mode, of which the intensity depends strongly on the chain conformation, the authors explained the behavior of aqueous PNIPAM solutions with the presence of large water clusters attached to the chains in the one-phase state. A trans-amide conformation allows the hydrophilic groups to act as nucleation sites for large water clusters. Because the hydrogen bond energy of the large water clusters is significantly larger than in bulk water, the expanded coil-like structure of PNIPAM is stabilized. Above $T_{cp}$, the hydrophobic groups collapse, thereby forcing the amide groups to face away from the clusters of water molecules, and the water clusters disintegrate. The amide groups remain, however, hydrated.

### 3.1.2   Structural properties of semi-dilute PNIPAM solutions

The structure of the one-phase state of semi-dilute PNIPAM solutions was investigated previously using SANS [120, 121]. It was shown that the scattering from concentration fluctuations follows critical behavior, described in Section 2.1.4. Both the scattered intensity, a measure of the susceptibility, and the correlation length of concentration fluctuations diverge at the critical temperature. The resulting critical exponents of the correlation length and susceptibility were $\nu_\xi \sim 0.45$ and $\gamma_I \sim 0.8$, respectively. This is below the value that is expected from mean-field theories such as the Flory-Huggins theory, where the values are $\nu_\xi = 0.5$ and $\gamma_I = 1$ [122]. This deviation is presumably due to the presence of long-range interactions, which is not accounted for in Flory-Huggins theory. Furthermore, DLS measurements on semi-dilute PNIPAM solutions revealed, besides a relaxation mode related to the cooperative diffusion of chain segments, the presence of correlation at longer time-scales, which also points to long-range interactions [40, 123].

In the two-phase state, the aggregation of PNIPAM chains leads to the formation of apparently stable aggregates with sizes in the order of ~100 nm, termed mesoglobules in the literature [28, 29, 30]. Their size depends on, for example, polymer concentration

[26, 27, 28], polymer molar mass [28], quenching temperature [31], heating rate [26, 124] and ionic strength of the solvent [27]. Several mechanisms that contribute to the stability were proposed. It was recognized that the visco-elastic effect, discussed in Section 2.1.3, plays a major role in the stability of mesoglobules formed by PNIPAM [26, 28]. Furthermore, due to the amphiphilic nature of PNIPAM, hydrophilic groups may accumulate at the surface, thereby reducing the surface tension of the mesoglobules and enhancing their stability [28, 30, 125, 126]. The third mechanism proposed regards the accumulation of charges at the surface of the mesoglobules, which would result in a repulsive force, hindering aggregation [31]. This is consistent with the finding that macro-phase separation occurs in PNIPAM solution upon addition of salt [27, 31]. The relative importance of each of these mechanisms remains, however, unclear.

## 3.2 Pressure studies on PNIPAM

Several high-pressure studies on PNIPAM were conducted during the last decades [35, 76, 77, 127, 128, 129]. The phase behavior of aqueous PNIPAM solutions was extensively studied using turbidimetry at several concentrations. It was shown that, similar to the phase behavior of protein solutions, the coexistence line in the temperature-pressure of PNIPAM solutions has an elliptical shape that can be modeled with the Hawley theory for the phase behavior of proteins (Section 2.3). Figure 3.3 shows the results of Otake et al. [76], Kunugi et al. [127], Kunugi et al. [128], Shibayama et al. [77], Osaka et al. [129], and Ebeling et al. [35], together with the results from measurements performed during the present research, which are extensively discussed in Chapter 6. Except for the curve measured by Kunugi et al. [127], the results are consistent with each other, despite their differences in concentration and solvent, listed in Table 3.1. As a wide range of polymer concentration was measured, it can be concluded that concentration only has a minor influence on the phase behavior. In a study on the influence of PNIPAM molar mass on its phase behavior in a narrow pressure range, it was suggested that the maximum of $T_{cp}$ shifts weakly to higher pressures with decreasing molar mass [130]. This may also partly explain the different results obtained by Kunugi et al. [127] with respect to the other presented phase diagrams in Figure 3.3: The PNIPAM molar mass in this study was very low.

Different methods were applied to investigate the pressure-dependent interaction between water and PNIPAM. Specific volume measurements on PNIPAM solutions indicated that the
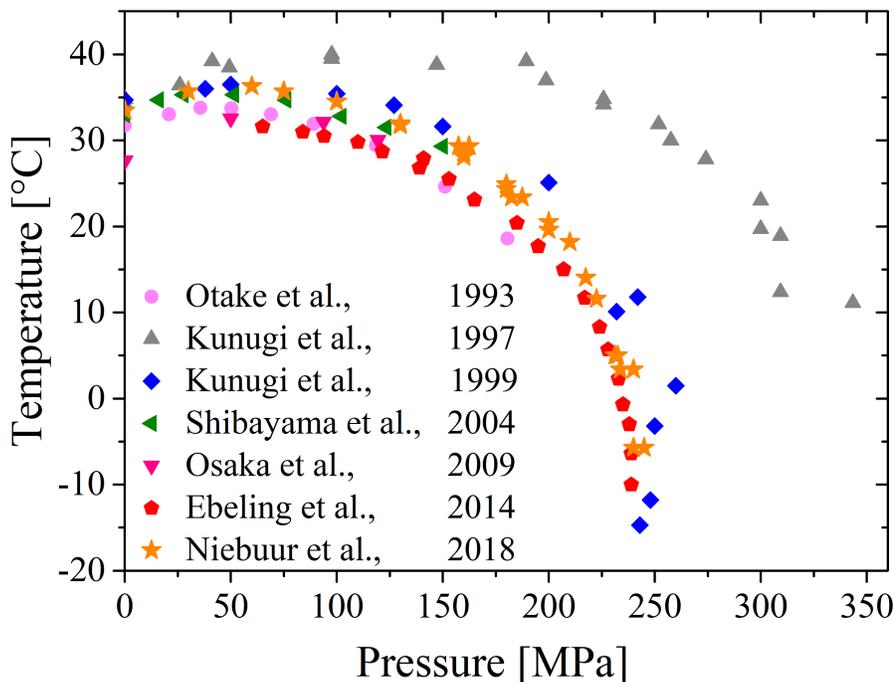
Figure 3.3:  Phase diagram of PNIPAM solutions in the temperature-pressure frame measured bin several studies in the past decades [35, 76, 77, 127, 128, 129, 131].  The used concentrations, molar masses and solvents are listed in table 3.1.

mechanism of phase separation is fundamentally different at high pressure.  It was shown that the increase in volume upon temperature-induced phase separation becomes weaker with increasing pressure [133].  It was concluded that, at low pressures, pressure stabilizes the one-phase state, which is indeed observed from the positive slope of the coexistence line in the pressure-temperature frame at low pressures (Figure 3.3).  When the phase separation is induced by pressure, no change in the specific volume is observed [76].  Molecular dynamics simulations showed that pressure-induced phase separation is caused by a decrease of the excess volume due to the tightness of the solvation shell [134].  Therefore, at high pressures, pressure favors the phase separation of PNIPAM solutions, which is consistent with the negative slope of the coexistence line in the pressure-temperature frame at high pressures (Figure 3.3).

A more detailed study of the pressure-dependent hydration behavior was performed with FT-IR.  It was shown that, upon temperature-induced phase separation, both hydrophilic and hydrophobic groups strongly dehydrate [32].  In case of pressure-induced phase separation, however, both hydrophilic and hydrophobic groups remain hydrated, suggesting that

| Research | Concentration [wt%] | Molar mass [g mol$^{-1}$] | Solvent |
|---|---|---|---|
| Otake et al. 1993 [76] | 3 | $M_w = 2.4 \times 10^5$ | $H_2O$ |
| Kunugi et al. 1997 [127] | 0.5 | $M_n = 1.4 \times 10^4$ | $H_2O$ |
| Kunugi et al. 1999 [128] | 0.5 | $M_n = 4.9 \times 10^4$ | $H_2O$ |
| Shibayama et al. 2004 [77] | 7.8 | unknown | $D_2O$ |
| Osaka et al. 2009 [129] | 24.9 | $M_n = 3.9 \times 10^4$ | $D_2O$ |
| Ebeling et al. 2014 [35] | 0.5 | $M_n = 2.7 \times 10^4$ | $H_2O$ |
| Niebuur et al. 2018 [132] | 3 | $M_n = 3.6 \times 10^4$ | $D_2O$ |

Table 3.1: Sample characteristics of the data shown in Figure 3.3.

the chains remain in a coil-like conformation in the two-phase state [32, 135]. Therefore, also this study suggests that fundamentally different mechanisms are responsible for phase separation in both pressure regimes.

Other studies focused on the role of water during the phase transition. Using NMR, it was shown that the mobility of water in aqueous PNIPAM solutions gradually increases with temperature, but displays a sudden drop at the phase transition temperature at atmospheric pressure. During temperature-induced phase transition at high pressures, the mobility of water decreases gradually at $T_{cp}$, i.e., the phase transition occurs over a broader temperature range than at atmospheric pressure [133]. Also differential scanning calorimetry measurements showed a broadening of the temperature-induced phase transition with increasing pressure [136]. Furthermore, this study revealed that the transition enthalpy decreases with pressure, which is in accordance with the reduced dehydration found with FT-IR measurements [32]. Quasi-elastic neutron scattering was used to probe the diffusion of water in a PNIPAM solution [129]. Also in this case, a gradual increase of its diffusion coefficient was found with increasing temperature. At the phase transition temperature, an additional increase in the diffusion coefficient was observed, which shows that hydration water is released from the chains, and thus joins the bulk water phase. Also in the two-phase state, the diffusion coefficient is below the one of pure water, which was explained by the confinement of water inside the polymer-rich domains. With increasing pressure, the increase of the diffusion coefficient at the phase transition temperature becomes weaker due to the reduced dehydration [129].

Moreover, structural methods were used to study the effect of pressure on the phase transition mechanism. Using dynamic light scattering (DLS) [129, 137], it was shown that the relaxation time related to the cooperative diffusion of chain segments strongly increases when approaching the transition point, both with increasing temperature and with increasing pressure. This is also observed using small-angle neutron scattering measurements on semi-dilute PNIPAM solutions in dependence on temperature [121] and pressure [77]. The correlation length of concentration fluctuations diverges at the cloud point, suggesting the presence of critical phenomena in the system. The relaxation time of the observed slower relaxation mode with DLS , which is related to the long-range concentration fluctuations of correlated chains [40, 123], is different in both cases. When reaching the cloud point with increasing temperature, the relaxation mode becomes faster, whereas with increasing pressure, it becomes slower [129, 137]. Therefore, long-range interactions become more pronounced in the one-phase state at high pressure.

Besides solutions of PNIPAM homopolymers, the influence of pressure on microgels composed of PNIPAM was in the focus of many studies [77, 138, 139, 140, 141, 142, 143, 144, 145, 146]. Their volume phase transition line also features an elliptical shape in the temperature-pressure frame. It was shown, however, that the maximum of the ellipse is shifted to a higher temperature and pressure compared to homopolymer solutions [77, 141, 143], which may be due to the enhanced local concentration in comparison with the homopolymer solutions and the effect of the crosslinks. If the shrunken state is reached at low pressures, the decrease in volume is strong and the dehydration of the chains is significant. The volume phase transition is therefore driven by dehydration. If the shrunken state is, however, reached at high pressures, only a weak volume decrease is observed which is not accompanied by any dehydration of PNIPAM. Therefore, in this case, other effects must play a role [145].

## 3.3   Co-nonsolvency effect in PNIPAM solutions

The co-nonsolvency effect is the reduction of the solubility of a solute in a mixture of two solvents that are both good solvents to the solute in their pure form. For example, PNIPAM is soluble in water up to 31 °C and in methanol at all temperatures. In a mixture of water and methanol in a 70:30 volume ratio, however, its cloud point is decreased to below 0 °C [147]. Not only mixtures of water and methanol show co-nonsolvency behavior. For a wide variety of combinations of water and organic solvents, it was observed that adding small

amounts of the co-solvent results in a decrease in the LCST of PNIPAM [33].

The properties of the re-entrance transition at higher fractions of the organic solvents depends strongly on the solvent used, exemplified in Figure 3.4. It was observed that, in mixtures of water and methanol, acetone, tetrahydrofuran and dioxane, PNIPAM shows LCST behavior at the re-entrance transition, whereas mixtures of water and heavier alcohols than methanol (e.g. ethanol and propanol) as well as other solvents such as DMSO and DMF lead to UCST behavior [34, 147, 148]. Generally, adding water to an organic solvent worsens the solvent quality: Independent of the critical solution behavior (LCST or UCST), the addition of a certain fraction of water leads to the phase separation of PNIPAM and the solvent [148].
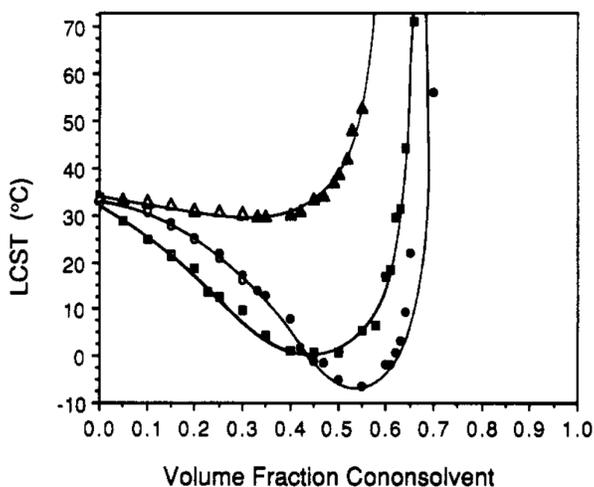


Figure 3.4: LCST of PNIPAM in mixtures of water and methanol (circles), water and tetrahydrofuran (squares) and water and dioxane (triangles) in dependence of the volume fraction of the co-solvent. Reprinted with permission from [147]. Copyright (2019) American Chemical Society.

Several theories attempted to explain the co-nonsolvency effect, and can be divided into theories based on solvent-polymer or solvent-solvent interactions. The earliest attempts to explain this effect were made by considering the interaction between water and the co-solvent. In case the methanol content in the mixture is low, water and methanol form complexes which mainly consist of 5 water molecules and one methanol molecule [149]. At the methanol concentration at which the largest amount of these water/methanol complexes can be formed, a strong decrease in the radius of gyration of PNIPAM chains was observed [150], suggesting that the interaction between water and methanol is much stronger than the interaction between PNIPAM and the solvent molecules. From this observation, it was concluded that the complexes form a poorer solvent for the polymer than the individual components [150]. A similar explanation was suggested for the coil-to-globule transition of

PNIPAM in mixtures of water and tetrahydrofuran. Here, it was suggested that, because of the formation of complexes between water and tetrahydrofuran, not enough water molecules are available to form hydrogen bonds with PNIPAM [151].

Several theories in which the co-nonsolvency effect is explained by polymer-solvent interactions were proposed, and were heavily debated in the literature. As described in Section 3.1.1, the hydration of PNIPAM chains is a cooperative effect, i.e., there is attractive interaction between water molecules on adjacent monomers. It was argued by Tanaka et al. [152] that the same effect may be responsible for the co-nonsolvency of PNIPAM in water/methanol mixtures. If PNIPAM is dissolved in a mixture of water and methanol, the binding of both species with the chains is cooperative as well as competitive: Although sequences of hydrated monomers and sequences of monomers solvated with methanol are formed, the interaction between hydrated monomers and monomers solvated by methanol is repulsive. This results in a lower overall solvation of the chain and therefore its contraction. This effect is enhanced by the preferential adsorption of methanol, which increases the competition between solvents on the chain for small amounts of added methanol. The solubility of PNIPAM is therefore strongly affected by methanol, resulting in the asymmetric shape of the phase diagram (Figure 3.4).

Mukherji et al. [153, 154, 155] proposed a theory based on segmental loop formation due to bridging by methanol molecules. Using MD simulations on NIPAM monomers, the authors suggested that the energetic interactions between PNIPAM and methanol are stronger than the one between PNIPAM and water, leading to the preferential adsorption of methanol on the chains. Using subsequent simulations on a bead-spring polymer model that interacts with with particles with two different interaction strengths (which represent water and methanol molecules), it was suggested that the chains indeed collapse due to the formation of bridges by the particle with stronger interaction strength.

Rodríguez-Ropero et al. [156] proposed that the preferential binding of methanol to PNIPAM leads to an increase in the configurational entropy of the globular state, inducing chain collapse. In their work, the excess chemical potential for frozen chain conformations was calculated from the interaction energies of PNIPAM with the solvent molecules, the reversible work to create cavities and from the variance of the polymer-solvent potential energy. The conformational entropy, which was not considered in the calculation of the excess chemical potential, was argued to be increased in the globular state in comparison with the coil-state.

Thus, this increase, which is due to the preferential interactions of methanol with the isopropyl side groups of PNIPAM, leads to the co-nonsolvency effect in PNIPAM solutions in mixtures of water and methanol.

Pica et al. [157] determined the Gibbs free energy difference between a swollen and a collapsed conformational state of PNIPAM at atmospheric pressure in dependence on the methanol content in the solution. It was shown that, upon a slight increase in methanol content, the interaction energy between the polymer and the solvent molecules decreases strongly, driving the collapse of the chains. Because methanol mainly interacts with the hydrophobic isopropyl groups and water mainly with the hydrophilic amide groups, competition between the two types of solvent molecules leads to geometric frustration and therefore the collapse of the chains. Overall, solvation of the chains by methanol is preferred, since the isopropyl groups have a larger solvent-accessible surface area than the amide groups.

## 3.4   Effect of pressure on co-nonsolveny

As discussed above, pressure has a significant effect on the interaction between water and PNIPAM. It can therefore be expected that also the co-nonsolvency effect is strongly influenced by hydrostatic pressure. In experiments, it was shown that high pressure breaks down the co-nonsolvency effect [34, 35, 36]. This means that, whereas the cloud point of PNIPAM is decreased in aqueous solutions that include a small fraction of an organic solvent, it is increased at high pressures. As is the case for purely aqueous PNIPAM solutions, the coexistence line in the temperature-pressure frame adopts a convex-upward shape. The position of its maximum is, however, shifted to significantly higher pressures as well as to higher temperatures, even for systems containing only small fractions of an organic solvent [34, 35].

Anologous to the co-nonsolvency effect at atmospheric pressure, theories based on solvent-solvent and polymer-solvent interactions were proposed to explain the findings at high pressures. As discussed in Section 3.3, it was proposed that the structures formed by water and the organic solvent form a poorer solvent than the individual components, leading to the decreased cloud point at atmospheric pressures. Application of high pressure was suggested to destroy these structures, setting the organic solvent molecules free to interact with PNIPAM. Because organic solvents are generally better solvents for PNIPAM than water, this results

in an increase of the cloud point temperature [35]. However, no experimental or theoretical studies support this theory so far.

Other theories are based on polymer-solvent interactions. The competitive binding of water and organic solvent molecules with the chain leads to a decrease in the cloud point temperature at atmospheric pressure, as described above. At high pressure, mechanisms that reduce the total volume of the system dominate. It was argued that this results in the loss of the preferential adsorption of the organic solvent on the chains, as observed at atmospheric pressure, which may be due to two effects: Firstly, the simultaneous binding between water and the organic solvent with the chains requires more volume than pure hydration [35], and secondly, a hydrated monomer has a smaller volume than a monomer solvated with organic solvents, because of the more efficient packing of the small water molecules at the chain [37, 38]. Due to the lack of competitive binding, the overall solvation of the chains increases, which stabilizes the one-phase state of the chains. Furthermore, the solvent phase is enriched with the organic solvent and thus becomes more hydrophobic. The hydrophobic effect therefore weakens, which further stabilizes the one-phase state [36, 37]. This scenario is supported by a Fourier-transform infrared spectroscopy study of PNIPAM in mixtures of water and methanol [36]. In this study, it was shown that the carbonyl groups of PNIPAM can form hydrogen bonds with methanol as well as with water. With increasing pressure, the fraction of methanol molecules attached to the carbonyl groups decreased, thereby increasing the hydration of these groups.

More detailed descriptions of this mechanism in PNIPAM solutions in water/methanol mixtures were provided using simulations and theoretical work. Oliveira et al. [37] used large-scale molecular dynamics simulations to describe the effect of pressure on co-nonsolvency. Their interpretation of the results is based on the theory of the co-nonsolvency at atmospheric pressure of Mukherji et al. [153, 154, 155], described in Section 3.3. Whereas chains are in a globular state at atmospheric pressure due to the presence of loops formed by bridging methanol molecules that bind distant monomers along the backbone, an expanded chain conformation is observed at high pressure. This was shown to be due to the partial replacement of methanol by water in the solvation shell of PNIPAM, leading to the disruption of the bridges.

Pica et al. [38] determined the Gibbs free energy of mixing from the water-accessible surface area in dependence on pressure to describe the breakdown of the co-nonsolvency at

high pressure microscopically. From their calculations, it follows that, at atmospheric pressure, chain collapse is favored because of geometric frustrations caused by the competition between water and methanol to interact with the polymer, since water interacts preferentially with the amide groups whereas methanol favors the interaction with the isopropyl groups [157]. Therefore, the chains cannot realize all attractive interactions that would be possible in pure water, reducing the solvation of the chains. At high pressure, two effects influence the solvation of the chains. Firstly, a more compact chain conformation decreases the water-accessible surface area, leading to a decreased Gibbs free energy of mixing which makes collapse less favorable. Secondly, the replacement of methanol by water on the chains due to volume effects enhances the possibility to form energetic interactions. Thus, geometric frustrations, responsible for the co-nonsolvency effect at atmospheric pressure, are reduced because the competition between water and methanol to bind with PNIPAM is weakened.

Budkov et al. [39] showed that the breakdown of the co-nonsolvency at high pressure can also be explained without the effect of hydrogen bonding between solvent molecules and PNIPAM. By calculating the Gibbs free energy of mixing, taking only van der Waals and excluded volume interactions into account, the authors related the radius of gyration of the chains to both the overall mole fraction of the co-solvent and the applied pressure. Whereas at low pressure, an increasing mole fraction of the co-solvent results in a lowered radius of gyration, the radius of gyration does not depend on the mole fraction of the co-solvent at high pressure. From this, it was deduced that excluded volume effects dominate over attractive interactions due to the high density of the system. Furthermore, also this model suggest that the preferential adsorption of methanol at the chains at atmospheric pressure is lost at high pressure.

Only very few experimental studies focused on molecular interactions in solutions of PNIPAM in mixtures of water and organic solvents exist, especially at high pressure. Therefore, proof of either of the described theories, both for the co-nonsolvency effect at atmospheric and at high pressure, is lacking. A part of the present study is devoted to the investigation of co-nonsolvency effect at high pressure, where molecular interactions are deduced from experimental data to support or disprove the proposed theories.

# 3.5   Overview of the present study

Although the pressure effects on aqueous PNIPAM solutions were investigated in the past, as discussed in Section 3.2, the findings are far from conclusive. As most of these studies focused on molecular interactions and/or macroscopic properties, the dependence of pressure on structural properties is mainly unknown. The aim of the present study is to fill this gap in knowledge. A deepened understanding of the structural properties of aqueous PNIPAM solutions during the phase transition at high pressure contributes to the overall understanding of the phase behavior of PNIPAM, also at atmospheric pressure. Insights in the behavior of this relatively simple model system may furthermore help to understand interactions and aggregation processes in more complex systems, such as complex polymers composed of several blocks, or biological macromolecules. In addition, it allows the use of pressure to control the size and structure of mesoglobules composed of PNIPAM or other polymers for existing applications, and may open up the possibility for new ones. To achieve this, mainly light and neutron scattering techniques are applied, as they give insights in the microscopic and mesoscopic length scales, i.e., between $\sim 1$ nm and $\sim 1$ $\mu$m, which are the relevant length scales for polymer solutions. Complementary, spectroscopic methods are used to relate the structural findings to molecular interactions in the system under the same conditions.

In more detail, Chapter 5 is devoted to the phase behavior of the PNIPAM solution under study. Using turbidimetry measurements, the solubility of PNIPAM in dependence on temperature and pressure is determined to identify the relevant ranges for pressure- and temperature-dependent studies. Furthermore, it is attempted to quantify the solubility of PNIPAM at different temperatures and pressures using Gibbs free energy of mixing calculations, which gives an estimate for the thermodynamic driving force of phase separation or mixing at different locations in the temperature-pressure phase diagram.

In Chapter 6, the relationship between chain hydration and mesoglobule size is elucidated. Using optical microscopy and very small angle neutron scattering (VSANS), the aggregate size and structure are determined after heating a purely aqueous PNIPAM solution through the cloud point temperature at both atmospheric and high pressures. Raman spectroscopy allows the determination of the hydrophobic hydration under the same conditions. Chapter 7 is devoted to the investigation of the role of hydration water during phase separation of aqueous PNIPAM solutions. At this, the diffusive properties of water in PNIPAM solutions in dependence on pressure and temperature are investigated using quasi-elastic neutron

scattering (QENS) experiments. With these, it is possible to relate the interaction strength between water and PNIPAM to the relative hydration of hydrophobic and hydrophilic groups.

Following these studies at equilibrium conditions, the formation and disintegration of mesoglobules is investigated using time-resolved small-angle neutron scattering (SANS) to follow the processes involved at time-scales from 0.05 s up to the point that a stable state is reached, discussed in Chapter 8 and 9. Here, it is attempted to reveal the influence of kinetic and thermodynamic effectson the formation pathway and final size and inner structure of the mesoglobules, and on their disintegration mechanism. By addressing different locations in the temperature-pressure phase diagram, it is attempted to establish a systematic approach to manipulate the size and structure of the mesoglobules.

Using the acquired knowledge about the pressure effects on purely aqueous PNIPAM solutions, this work is continued with the study of the effect of pressure on PNIPAM solutions in mixtures of water and methanol, where the effect of pressure on the co-nonsolvency effect, described in Sections 3.3 and 3.4, is investigated. This part starts with a structural study at equilibrium conditions using SANS, with a focus on the one-phase state, as well as VSANS to probe the two-phase state (Chapter 10). Using SANS, the effects of pressure on the chain conformation, influenced by the pressure-dependent interactions between the two types of solvent molecules and the chains, is determined. Similarly, VSANS elucidates the influence of methanol on the size and structure of the mesoglobules, which may also be strongly influenced by the pressure-dependent interactions between the solvent and the chains. In Chapter 11, QENS is applied to investigate the interactions between both the solvent molecules with the chains and the different solvent molecules with each other. The results are discussed in view of the existing theories, described in Section 3.4.

# Chapter 4. Experimental techniques

In the present thesis, mainly scattering techniques are employed to gain insights in the structure, dynamics and interactions of the investigated systems. The accessible length scales and energy ranges depend strongly on the type of radiation used for the experiments. Two important classes of scattering techniques are light scattering and neutron scattering, both with their own restrictions and advantages, as described in the following.

## 4.1 Theory of neutron scattering

This section is based on refs. [158] and [159].

Scattering of neutrons by a sample is due to the interaction between neutrons and the atoms in the sample, and can be explained by the intrinsic properties of neutrons. Unlike light or X-rays, neutrons interact with the nuclei of the atoms, mediated by the strong nuclear force. Due to the small size of the nuclei, the neutrons have a large penetration depth, which allows for the investigation of bulk properties of the investigated sample. Although neutrons have no charge, they possess a magnetic moment due to the charge distribution of valance quarks inside the neutrons. Therefore, dipole-dipole interactions between the neutrons and atoms in the investigated system allow the study of the magnetic properties of the system. In the present thesis, non-magnetic materials are investigated, and thus, this contribution to the total scattering is negligible [159].

Neutrons exhibit both particle-like and wave-like properties. In the non-relativistic limit, i.e., for slow neutrons, their kinetic energy $E$ can be expressed in terms of the wave vector $\vec{k}$ as

$$E = \frac{\hbar^2 k^2}{2m_n} \tag{4.1}$$

with $\hbar$ the reduced Planck constant, $k$ the magnitude of the wave vector and $m_n$ the neutron mass. Neutron scattering experiments are typically performed using neutrons with a

wavelength, $\lambda = 2\pi/k$, of several Ångstroms and probe therefore structures with sizes in the nanometer range, which is relevant for polymer solutions. Furthermore, their kinetic energy, a few tens of meV, lies in the relevant range to investigate dynamic processes in polymer solutions [160].

### 4.1.1   Scattering geometry

During a scattering event of a neutron, the incoming neutron with incident frequency $\omega_i$ and wave vector $\vec{k}_i$ interacts with the sample. After the scattering event, the frequency $\omega_s$ and wave vector $\vec{k}_s$ of the scattered neutron may have changed. The energy transfer,

$$\Delta E = \hbar\omega_i - \hbar\omega_s \tag{4.2}$$

and the momentum transfer,

$$\vec{q} = \vec{k}_i - \vec{k}_s \tag{4.3}$$

characterize the interaction of the neutrons with the sample and are therefore suitable quantities to describe these scattering events. Upon scattering with a particle, the neutron can gain or loose energy. A special case is elastic scattering, $\omega_i - \omega_s = 0$, where the magnitude of the wave vector stays unchanged, and only its direction changes. A schematic overview of the possible scattering events is given in Figure 4.1. From this, a more general equation
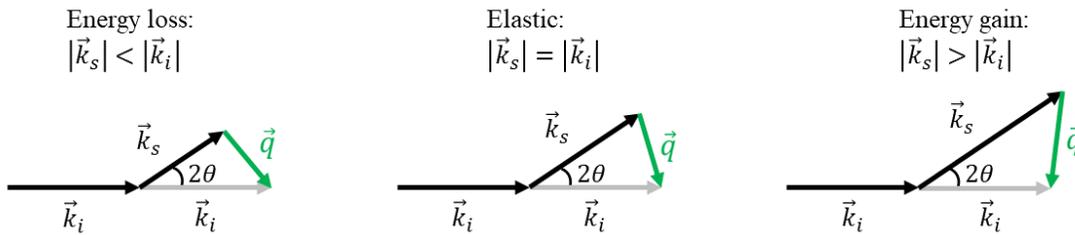


Figure 4.1:  wave vector diagram for a scattering event of neutrons with incident wave vector $\vec{k}_i$ to scattered wave vector $\vec{k}_s$. $2\theta$ denotes the scattering angle and $\vec{q}$ the momentum transfer.

relating the momentum transfer to the moduli of the wave vectors can be deduced, given by

$$q^2 = k_i^2 + k_s^2 - 2k_ik_s\cos 2\theta \tag{4.4}$$

where $2\theta$ denotes the scattering angle.

### 4.1.2 Scattering cross sections

The wave-like properties of neutrons allow a description of the neutrons during a scattering experiment in terms of wave functions. In a typical neutron scattering experiment, a monochromatic parallel incident neutron beam is used. It can be described as a plane wave with a wave vector with modulus $k_i$ and frequency $\omega_i$ moving in the $x$-direction,

$$\psi_i = \psi_0 e^{i(k_i x - \omega_i t)} \tag{4.5}$$

where $\Phi = |\psi_0|^2$ is the flux of the incident neutron beam. In case of a single point in space located at the origin, the wave function of the scattered neutrons at position $\vec{r}$ adopts the form of a spherical wave, given by

$$\psi_s = \psi_0 e^{-\omega_i t} f(\lambda, \theta, t) \frac{e^{i(\vec{k}_s \cdot \vec{r} - \omega_s t)}}{|\vec{r}|} \tag{4.6}$$

Here, $f(\lambda, \theta, t)$ denotes the probability that the neutron of wavelength $\lambda$ is deflected in direction $\theta$, and therefore describes the scattering strength. As mentioned above, the neutrons are scattered by the nuclei of atoms in the sample. Due to the relatively long wavelength of neutrons in comparison with the interaction range of the nuclei, the scattering is isotropic, i.e., $f(\lambda, \theta, t)$ is independent of $\theta$. Furthermore, $f(\lambda, \theta, t)$ is almost independent of $\lambda$ for neutrons with wavelengths in the Ångstrom range. In case of a stationary nucleus, $f(\lambda, \theta, t)$ is time-independent and depends on the type of nucleus. This value, termed 'scattering length' $b$, is defined as the negative value of $f(\lambda, \theta, t)$. For neutron scattering, $b$ is not only element-specific, but different isotopes of a certain element may have significantly different scattering lengths. Furthermore, the neutron-nucleus spin state during a scattering event influences the scattering length, as discussed below in more detail. These properties give scattering with neutrons an advantage above scattering with X-rays, where the scattering length depends on scattering angle, but is isotope-independent.

A real sample consists of many scattering centers that furthermore may move. To describe the scattering from these complex systems, the scattering probability can be quantified in terms of the scattering length density $\rho(\vec{R}, t)$, which is related to the scattering probability function as

$$f(\lambda, \theta, t) = \rho(\vec{R}, t) d\vec{R} dt \tag{4.7}$$

and therefore describes the scattering strength at a point $\vec{R}$ in space in dependence on time.

The contribution of a volume element $\mathrm{d}\vec{R}$ at position $\vec{R}$ and time between $t$ and $t + \mathrm{d}t$ to the scattered wave measured at position $\vec{r}$ is therefore given by

$$\mathrm{d}\psi_s = \psi_0 \mathrm{e}^{\mathrm{i}(\vec{k}_i \cdot \vec{R} - \omega_i t)} \left[ \rho(\vec{R}, t) \mathrm{d}\vec{R} \mathrm{d}t \right] \frac{\mathrm{e}^{\mathrm{i}(\vec{k}_s \cdot (\vec{r} - \vec{R}) - \omega_s t)}}{|\vec{r} - \vec{R}|} \tag{4.8}$$

In most cases, the distance between sample and detector is much larger than the size of the sample. Therefore, the Fraunhofer limit applies, and one can simplify the above equation by assuming $|\vec{r} - \vec{R}| \approx |\vec{r}| = r$. The wavefunction at position $\vec{r}$ describing the total scattering of neutrons by the sample with change in frequency $\omega = \omega_i - \omega_s$ and momentum transfer $\vec{q}$ is obtained by integration of equation 4.8, which gives

$$\psi_s = \frac{\psi_0 \mathrm{e}^{\mathrm{i}(\vec{k}_s \cdot \vec{r})}}{r} \int_\tau \iiint_V \rho(\vec{R}, t) \mathrm{e}^{\mathrm{i}(\vec{q} \cdot \vec{R} - \omega t)} \mathrm{d}\vec{R} \mathrm{d}t \tag{4.9}$$

Here, $V$ is the volume of the sample and $\tau$ a characteristic time scale of the observed process.

To relate $\psi_s$ to the measured intensity at different positions on the detector, the scattering cross section $\sigma_{tot}$ is introduced. It is defined as the number of scattered neutrons per second divided by the incoming neutron flux $\Phi$. In a neutron scattering experiment, one is, however, interested in the scattering probability in dependence on scattering direction and energy transfer. The scattering direction is expressed by the solid angle $\Omega$, which is the area of a spherical shell fragment around the location of the scattering event divided by the squared radius of the shell, $\mathrm{d}\Omega = \mathrm{d}A / r^2$. The scattering probability can be expressed in terms of the partial differential cross section,

$$\frac{\partial^2 \sigma}{\partial \Omega \partial E'} = \frac{R(2\theta, \phi, E')}{N \Phi d\Omega dE'} \tag{4.10}$$

where $R(2\theta, \phi, E')$ is the scattering rate and $N$ the number of scattering centers in the sample. It follows that the total scattering cross section is derived by integration over the entire solid angle and energy range as

$$\sigma_{tot} = \iint \frac{\partial^2 \sigma}{\partial \Omega \partial E'} d\Omega dE' \tag{4.11}$$

The scattering rate $R(2\theta, \phi, E')$ per area $\mathrm{d}A$ at the detector at a distance $r$ is proportional to $|\psi_s|^2$. Thus, the partial differential scattering cross section can be rewritten by combining

equation 4.9 and 4.10 as

$$\frac{\partial^2 \sigma}{\partial\Omega\partial E'} \propto \frac{c_s}{c_i} S(\vec{q}, \omega) \tag{4.12}$$

where $c_i$ and $c_s$ are the velocities of the incident and scattered neutrons, respectively. $S(\vec{q}, \omega)$ is called the dynamic structure factor, and is determined as

$$S(\vec{q}, \omega) = \left| \int_\tau \iiint_V \rho(\vec{R}, t) e^{i(\vec{q}\cdot\vec{R} - \omega t)} d\vec{R} dt \right|^2 \tag{4.13}$$

Therefore, in a neutron scattering experiment, one measures the squared modulus of the space-time Fourier transform of the time-dependent scattering length density function of the sample, given by $S(\vec{q}, \omega)$.

### 4.1.3 Coherent and incoherent scattering

As mentioned above, the scattering length of a certain isotope is not identical for every scattering event. For nuclei with non-zero spin, different neutron-nucleus spin states during a scattering event lead to different interaction strengths, which influences the scattering length of the nucleus. The scattering length density function can be written as the sum of the scattering length density related to the mean value and to the standard deviation of the scattering length, which give the coherent and incoherent part of the scattering length density, respectively, written as

$$\rho(\vec{R}, t) = \langle \rho(\vec{R}, t) \rangle + \Delta\rho(\vec{R}, t) \tag{4.14}$$

As a result, also the dynamic structure factor can be written as the linear combination of both contributions. Inserting equation 4.14 into equation 4.13 yields

$$S(\vec{q}, \omega) = S_{coh}(\vec{q}, \omega) + S_{inc}(\vec{q}, \omega) \tag{4.15}$$

because the cross term resulting from the squared modulus in equation 4.13 equals zero. For coherent scattering, the scattered waves from different nuclei can interfere with each other and therefore provide information on the structure or collective dynamics in the sample. For incoherent scattering, no interference of waves from different nuclei occurs, since the scattered neutrons have random phases with respect to the phases of the incident neutrons. Incoherent scattering therefore provides information on the dynamics of single atoms.

### 4.1.4  Elastic scattering

A special case of scattering is elastic scattering. Here, the neutrons are scattered by the sample without a change in frequency, i.e., $\omega = \omega_i - \omega_s = 0$, or $|\vec{k}_s| = |\vec{k}_i| = k$, which reduces equation 4.4 to

$$q = 2k \cdot \sin\theta \tag{4.16}$$

The corresponding time-independent structure factor is obtained by substituting $\omega = 0$ into equation 4.13, which yields

$$S(\vec{q}, \omega = 0) = \left| \iiint_V \langle \rho(\vec{R}, t) \rangle_\tau e^{i(\vec{q} \cdot \vec{R})} d\vec{R} \right|^2 \tag{4.17}$$

with

$$\langle \rho(\vec{R}, t) \rangle_\tau = \frac{1}{\tau} \int_0^\tau \rho(\vec{R}, t) dt \tag{4.18}$$

Here, $\langle \rho(\vec{R}, t) \rangle_\tau$ denotes the time-averaged scattering length density function of the sample over the duration of the experiment, which equals $\rho(\vec{R})$ in case of static samples. Thus, the time-independent structure factor, obtained in an elastic scattering experiment, equals the squared modulus of the Fourier transform of the scattering length density function of the sample. In a real scattering experiment, the sample is not completely static, also inelastic scattering events occur. However, this contribution is usually very weak, it results in a small nuisance that is ignored in most elastic scattering experiments without energy discrimination of the scattered neutrons.

Also in case of elastic scattering, the measured signal is a linear combination of the coherent and incoherent contribution to the time-independent structure factor. Because the incoherent part does not contain structural information of the sample, it is measured as white noise that overlaps with the coherent contribution. For a successful experiment, incoherent scattering therefore needs to be minimized.

### 4.1.5  Quasi-elastic scattering

Another special case of inelastic scattering is quasi-elastic scattering, where only small energy transfers are considered. Its signal comes from stochastic motions in the sample, which gives rise to a broad peak of $S(q, \omega)$ centered at $\omega = 0$. Because the stochastic motions follow an energy distribution, the scattering signal is observed as the broadening of the elastic scattering peak. This differs from inelastic scattering in a general sense, where maxima of

$S(\vec{q}, \omega)$, resulting from processes with quantized energies, may be located at $\omega \neq 0$.

For quasi-elastic scattering, it is convenient to write the dynamic structure factor, given by equation 4.13, in terms of the self-correlation function of the scattering length density distribution $G(\vec{R}, t)$, since it may serve as a starting point to describe dynamic processes. $G(\vec{R}, t)$, also called the van Hove function, is related to $\rho(\vec{R}, t)$ as

$$G(\vec{R}, t) = \int_\tau \iiint_V \rho(\vec{r}, t')^* \rho(\vec{r} + \vec{R}, t + t') \mathrm{d}\vec{r}\mathrm{d}t' \tag{4.19}$$

It follows that the dynamic structure factor equals the space and time Fourier transforms of $G(\vec{r}, t)$,

$$S(\vec{q}, \omega) = \int_\tau \iiint_V G(\vec{R}, t) \mathrm{e}^{\mathrm{i}(\vec{q}\cdot\vec{R} - \omega t)} \mathrm{d}\vec{R}\mathrm{d}t \tag{4.20}$$

## 4.1.6 Imaginary part of the dynamic susceptibility

In many cases, the analysis of $S(\vec{q},\omega)$ is complicated by the overlap of different dynamic processes. An alternative method is the analysis of the dynamic part of the dynamic susceptibility $\chi''(\vec{q},\omega)$, which is related to $S(\vec{q},\omega)$ via the fluctuation-dissipation theorem, originally proposed by Nyquist [161] to describe thermal noise in electrical conductors. It states that a relation exists between the response of a system to an external disturbance and internal fluctuations in the system in absence of the disturbance. It was shown that the fluctuation-dissipation theorem is generally valid for systems that follow the detailed-balance equation [162], given by

$$S(\vec{q}, -\omega) = \exp\left(-\frac{\hbar\omega}{k_B T}\right) S(\vec{q}, \omega) \tag{4.21}$$

which describes the balance between occupied and unoccupied excited states in dependence on temperature. At zero temperature, only the ground states are populated and therefore, only energy-gain processes can exist. At higher temperatures, other states are populated as well due to thermal excitation, quantified by the Boltzmann factor, $\exp(-\hbar\omega/k_B T)$, and also energy-loss processes may occur. From equation 4.21 it follows that $S(\vec{q}, \omega)$ and $\chi''(\vec{q},\omega)$ are related as [163]

$$\chi''(\vec{q}, \omega) \propto \frac{S(\vec{q}, \omega)}{[1 + n_B(\omega)]} \tag{4.22}$$

Here, $n_B(\omega)$ is the Bose occupation factor, given by

$$n_B(\omega) = \left[\exp\left(\frac{\hbar\omega}{k_B T}\right) - 1\right]^{-1} \tag{4.23}$$

with $k_B$ being Boltzmann's constant and $T$ the absolute temperature. $S(\vec{q},\omega)$ serves as a correlation function to describe fluctuations at equilibrium. In case of a periodic perturbation with frequency $\omega$, relaxation of the system occurs due to energy dissipation caused by friction which originates from the same physical process that caused the fluctuations at equilibrium. The relaxation of the system is in this case described by the response function $\chi''(\vec{q},\omega)$. As a consequence, analyzing $\chi''(\vec{q},\omega)$ instead of $S(\vec{q},\omega)$ has the advantage that different processes are separated from each other in frequency.

## 4.2    Small-angle neutron scattering

In a small-angle neutron scattering (SANS) experiment, the structure of the investigated system is probed on length scales ranging from $\sim 1$ to $\sim 100$ nm, which can be extended to length scales up so several $\mu$m with very small angle neutron scattering (VSANS). With these methods, the scattered intensity of a monochromatic neutron beam in dependence on momentum transfer $q$ (related to the scattering angle $\theta$ according to equation 4.16) is measured at small $q$ values, without discrimination of the energy transfer of the scattered neutrons. The scattering pattern of coherently scattered neutrons reveals the structure of the investigated sample, while incoherently scattered neutrons contribute as a $q$-independent background signal.

### 4.2.1    Experimental setup

In the following, the setups used for SANS and VSANS experiments presented in this work are described.

**D11 SANS instrument, ILL.**   All SANS experiments presented in this thesis were performed at the SANS instrument D11 at the Institute Laue-Langevin (ILL) in Grenoble, France [164]. A schematic sketch of this instrument is given in Figure 4.2. The incident neutron beam passes a velocity selector, where neutrons with the desired wavelength are selected. The nearly monochromatic beam subsequently passes a series of neutron guides to reduce its divergence. The size and shape of the beam can be tuned further using diaphragms, that block the neutron beam except at the aperture which can be varied in size and shape. The chosen aperture is a trade-off between beam divergence and neutron flux at the sample, determined by the requirement of the measurement. For example, a small beam allows measurements with a high resolution, but only a low neutron flux reaches the sample. The scattered neutrons are measured with a 2D $^3$He gas detector, located in an evacuation

tube. The distance between the detector and the sample can be varied between 1.2 and 39 m to cover a wide range of momentum transfers.
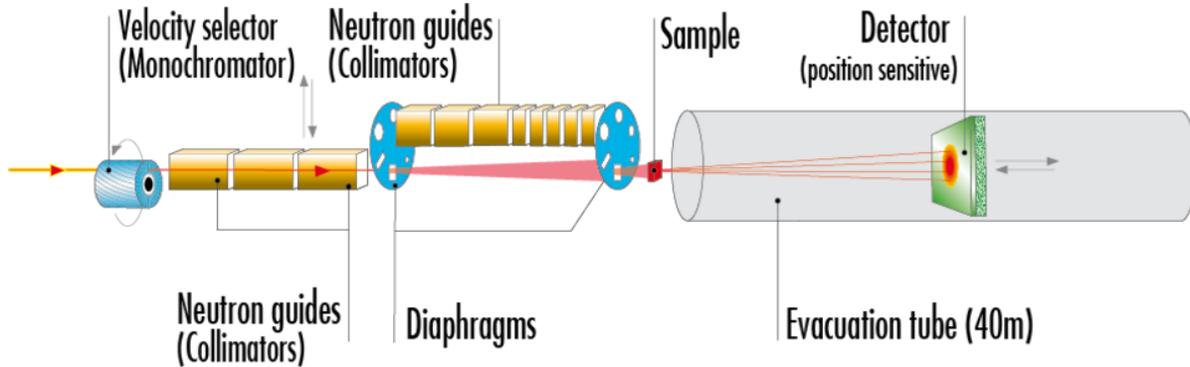


Figure 4.2: Schematic sketch of the SANS instrument D11 located at the ILL, Grenoble, France [164].

**KWS-3 VSANS instrument, MLZ.** All VSANS experiments presented in this thesis were performed at the VSANS instrument KWS-3 at the Heinz Maier-Leibnitz Zentrum (MLZ) in Garching, Germany [165], schematically shown in Figure 4.3. After the selection of the neutron wavelength at the velocity selector, the beam passes through the entrance aperture, which can be varied in size and shape to tune the shape of the beam, depending on the required resolution of the measurement. Contrary to pinhole-type SANS instruments such as the D11 instrument, a toroidal mirror reduces the divergence of the incident neutron beam. This allows a relatively narrow direct neutron beam at the detector and therefore the detection of scattered neutrons at very small scattering angles, but restricts the position of the detector. Different ranges in momentum transfer can be probed by placing the sample at ∼1 or ∼10 m from the detector.

## 4.2.2 SANS and VSANS data analysis

The data obtained from SANS and VSANS experiments can be analyzed by fitting structural models. At this, corrections to the data using reference measurements need to be performed to account for scattering from sources other than the sample.

To isolate the scattering from the sample, the contribution from the sample holder to the scattered intensity needs to be removed. At this, the empty sample cell is measured as well. Prior to subtraction, the scattered intensities from the sample holder including the sample and from the empty sample holder are corrected for their respective neutron trans-
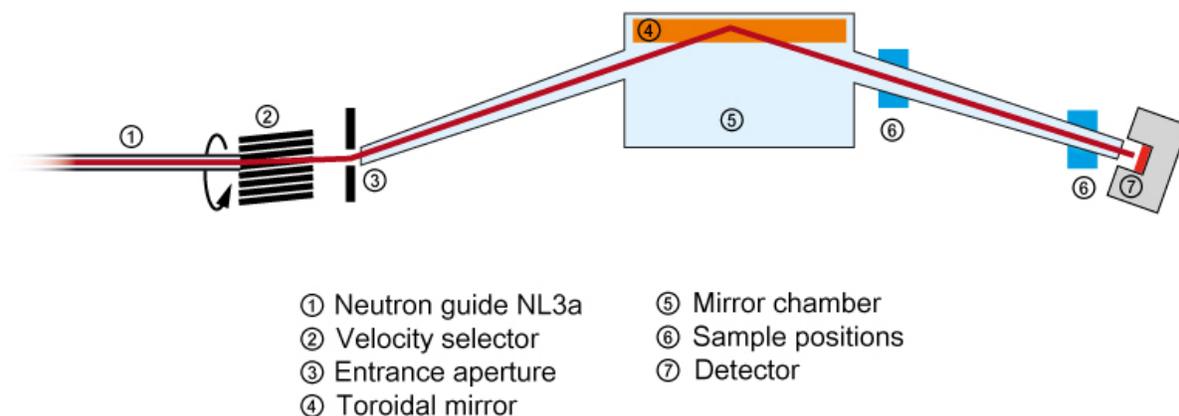
Figure 4.3:  Schematic sketch of the VSANS instrument KWS-3 located at the MLZ, Garching, Germany. Adapted from [165].

missions and the dark current, measured with boron carbide at the sample position, which is a strong neutron absorber [166]. Further corrections are performed using a measurement of an isotropic scatterer with known scattering strength to correct for the varying sensitivity of the individual pixels on the 2D detector, and to bring the data to absolute scale to be able to compare the scattering strength of different samples or a sample measured at different conditions. The 2D scattering pattern from isotropic samples is usually azimuthally integrated to obtain the time-independent structure factor in dependence on the absolute value of the momentum transfer $q$, which will be called the scattered intensity $I(q)$ from this point on.

Several models describing isotropic structures are used in this thesis and are described in the following.

**Guinier approximation.**    In the Guinier approximation, the scattering pattern from particles is approximated in the low-$q$ limit, i.e., $qR_g \ll 1$ with $R_g$ their radius of gyration. For spherical particles, the Guinier approximation is given by

$$I(q) = I_G \cdot \exp\left( -\frac{q^2 R_g^2}{3} \right) \tag{4.24}$$

with $I_G$ the scattered intensity at $q = 0$. In a plot of $\log[I(q)]$ versus $q^2$, the model predicts a straight line with a slope equal to $R_g^2/3$ [167]. Figure 4.4 displays a few examples of the Guinier approximation of spherical particles with different sizes.
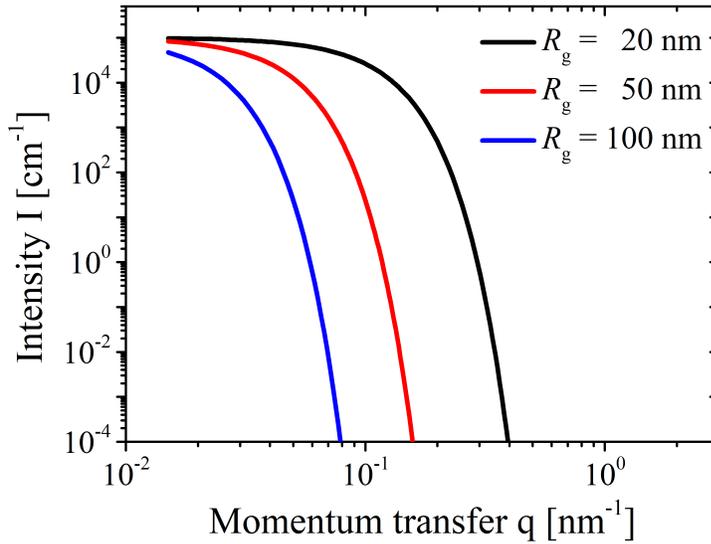
Figure 4.4: Examples of the Guinier approximation with different values of $R_g$, as indicated in the graph.

**Porod approximation.** The Porod approximation allows a description of the surface structure of particles. Their scattering in the high-$q$ limit, i.e., $qR_g \gg 1$, is approximated by a power law,

$$I(q) = \frac{K_P}{q^m} \tag{4.25}$$

with $m$ the Porod exponent and $K_P$ the Porod amplitude [168]. In a plot of $\log I$ versus $\log q$, the Porod approximation predicts a straight line with a slope equal to -$m$. In case of particles with a smooth surface, $m = 4$. A value of $m$ below 4 points to a rough surface structure, whereas values above 4 are expected for particles with a composition gradient perpendicular to the particles surface [169, 170]. Figure 4.5 displays a few examples of the Porod approximation for different values of $m$.

**Guinier-Porod model.** In the Guinier-Porod model, the contributions from the Guinier approximation at low $q$ values and the Porod approximation at high $q$ values are mathematically combined to form an expression that describes the total scattering pattern of particles [171]. To ensure a smooth transition between both limits, the magnitude and first derivative of both functions are assumed to be equal at the $q$ value of their transition, $q^*$. The $q$
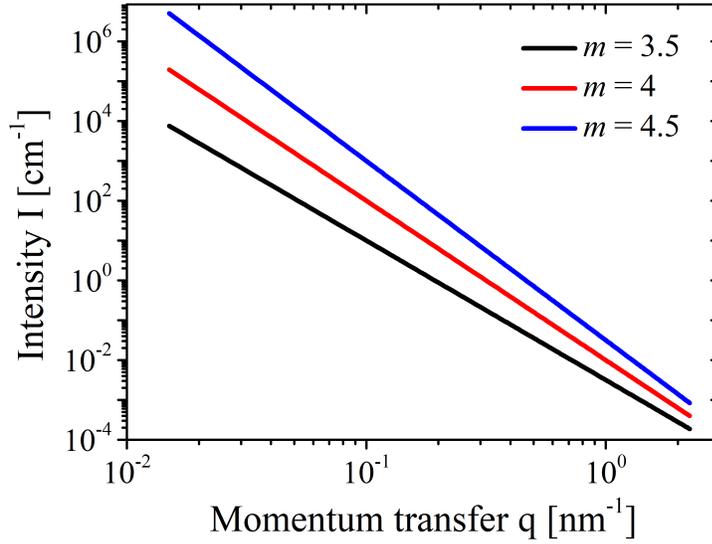
Figure 4.5: Examples of the Guinier approximation with different values of $m$, as indicated in the graph.

dependence of the scattered intensity is therefore given by

$$I(q) = I_G \cdot \exp\left(-\frac{q^2 R_g^2}{3}\right) \text{ for } q \leq q^*$$

$$I(q) = \frac{K_P}{q^m} \text{ for } q \geq q^*$$

(4.26)

with the values of $q^*$ and $K_P$ determined from the continuity requirement, and depend only on $I_G$, $R_g$ and $m$ as

$$q^* = \frac{1}{R_g}\sqrt{\frac{3m}{2}}$$

(4.27)

and

$$K_P = \frac{G}{R_g^m}\exp\left(-\frac{m}{2}\right)\left(\frac{3m}{2}\right)^{m/2}$$

(4.28)

Figure 4.6 displays a few examples of the Guinier-Porod model for different values of $R_g$ and $m$. Furthermore, the positions of $q^*$ on each curve are marked with a star.

**Beaucage model.** Similar to the Guinier-Porod model, the Beaucage model combines the Guinier approximation and the Porod approximation to describe the scattering pattern of particles [172, 173]. In this case, a smooth transition between both limits is provided by the error function, which strongly reduces the intensity of the Porod approximation at low
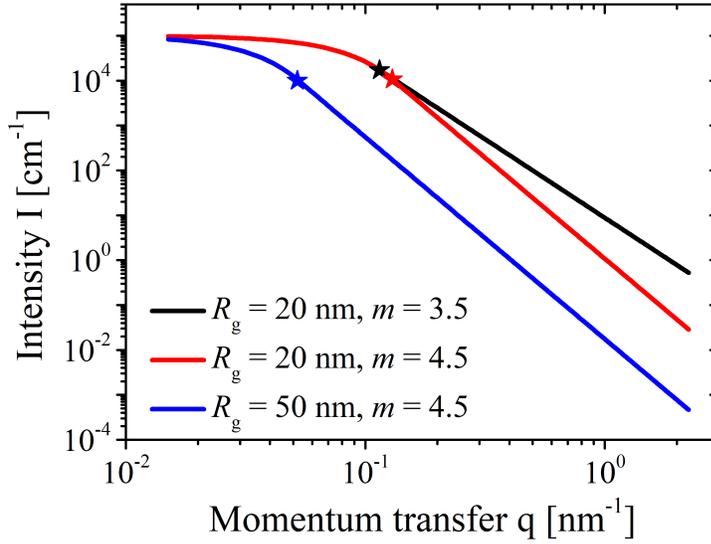
Figure 4.6: Examples of the Guinier-Porod approximation with different values of $R_g$ and $m$, as indicated in the graph. The stars mark the position of $q^*$ for each curve.

$q$ values. The combination of both limits can therefore be expressed as their sum, given by

$$I(q) = I_G \cdot \exp\left(-\frac{q^2 R_g^2}{3}\right) + \frac{C}{q^m}\left[\text{erf}\left(\frac{q R_g}{6^{1/2}}\right)\right]^{3m} \tag{4.29}$$

with $C$ a scaling constant and $\text{erf}(x)$ the error function. $C$ is related to $I_G$, $R_g$ and $m$ by

$$C = \frac{Gm}{R_g^m}\left[\frac{6m^2}{(2+m)(2+2m)}\right]^{m/2} \Gamma\left(\frac{m}{2}\right) \tag{4.30}$$

with $\Gamma(x)$ the gamma function. $C$ is, however, often used as an additional fitting parameter to allow more freedom during the fit. Figure 4.7 displays an example of the Beaucage model. Furthermore, the contributions from the Guinier approximation and the Porod approximation are given.

**Ornstein-Zernike structure factor.** The Ornstein-Zernike structure factor may be used to describe structures on a local scale having a pair-correlation function, given by equation 2.2. Its Fourier transform leads to an expression describing the corresponding scattering pattern, given by

$$I(q) = \frac{I_{OZ}}{1 + (q\xi)^2} \tag{4.31}$$

where $I_{OZ}$ is a scaling factor. It was shown that scattering from polymer solutions in the semi-dilute regime can be described by equation 4.31 [41]. In this case, $\xi$ is assigned to the average
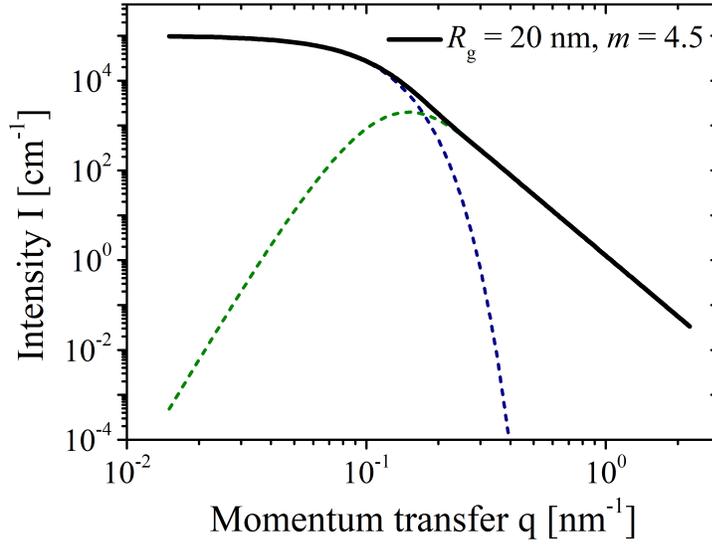
Figure 4.7:   Example of the Beaucage model with $R_g = 20$ nm and $m = 4.5$. The contribution from the Guinier approximation is given by the dark blue dotted line, and the contribution from the Porod approximation multiplied with the error function is shown with the green dotted line.

distance between overlap points of the chains, which is related to the chain conformation. Furthermore, the Ornstein-Zernike structure factor may be used to describe scattering from concentration fluctuations in concentrated solutions or other dense polymeric systems and provides a measure of the size of the concentration fluctuations [121, 174]. However, an unambiguous assignment of $\xi$ is in this case not possible. In Figure 4.8, a few examples of the Ornstein-Zernike structure factor with varying values of $I_{OZ}$ and $\xi$ are shown.

## 4.2.3   Effects of instrumental resolution

Instrumental resolution effects in a SANS experiment leads to a smearing of the scattering pattern and is mainly caused by a distribution of the neutron wavelength of the incident beam and its divergence. The resolution function $R(q, q')$ describes the probability that a scattered neutron with momentum transfer $q'$ is measured as a scattered neutron with momentum transfer $q$. The measured scattered intensity $I_M(q)$ is related to the real scattered intensity $I(q)$ via the convolution product with $R(q, q')$, given by

$$I_M(q) = \int R(q, q')I(q')\mathrm{d}q' \tag{4.32}$$

In good approximation, $R(q, q')$ can be described as a Gaussian function with a $q$-dependent variance $\sigma_q^2$ determined from the wavelength spread, beam divergence and the detector res-
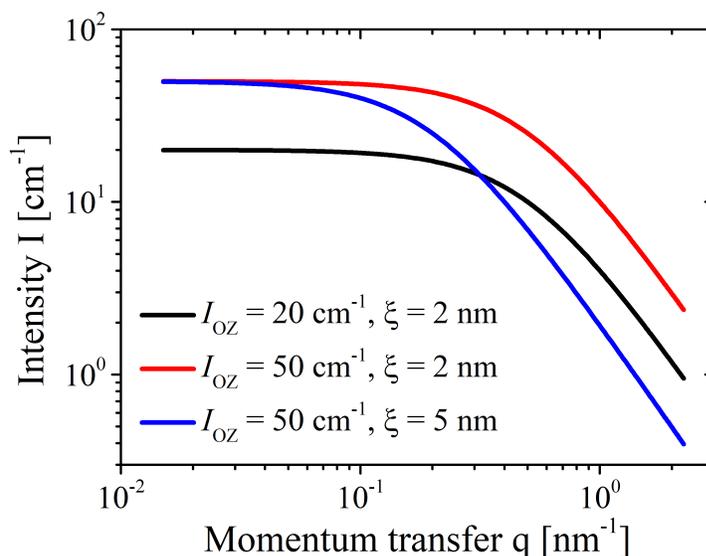
Figure 4.8: Examples of the Ornstein-Zernike structure factor with different values of $I_{OZ}$ and $\xi$, as indicated in the graph.

olution, and is given by [166, 175]

$$R(q, q') = \frac{1}{\sqrt{2\pi\sigma_q^2}} \exp\left(-\frac{(q-q')^2}{2\sigma_q^2}\right) \tag{4.33}$$

To fit a structural model to the measured scattered intensity, the model needs to be convoluted with the resolution function.

## 4.3 Quasi-elastic neutron scattering

A quasi-elastic neutron scattering (QENS) experiment focuses on the detection of inelastic scattering events with small energy transfers. In this way, the stochastic motions of particles in the system are probed to investigate their dynamic properties. Using neutrons with wavelengths comparable to inter-atomic distances in the investigated system, both temporal and geometrical information on relevant time and length scales are probed. By measuring the time-of-flight of scattered neutrons between the sample and the detector in dependence on the scattering angle, the dynamic structure factor of the sample is obtained.

### 4.3.1 Experimental setup

**TOFTOF time-of-flight spectrometer, MLZ.** All QENS experiments presented in this thesis were performed at the TOFTOF time-of-flight spectrometer at the Heinz Maier-

Leibnitz Zentrum (MLZ) in Garching, Germany [176]. A series of 7 disc choppers transforms

① Neutron guide NL2a-u
② PCR chopper-pair
③ 1st higher order removal chopper
④ 2nd higher order removal and
    frame overlap chopper
⑤ MCR chopper-pair

⑥ Sample position
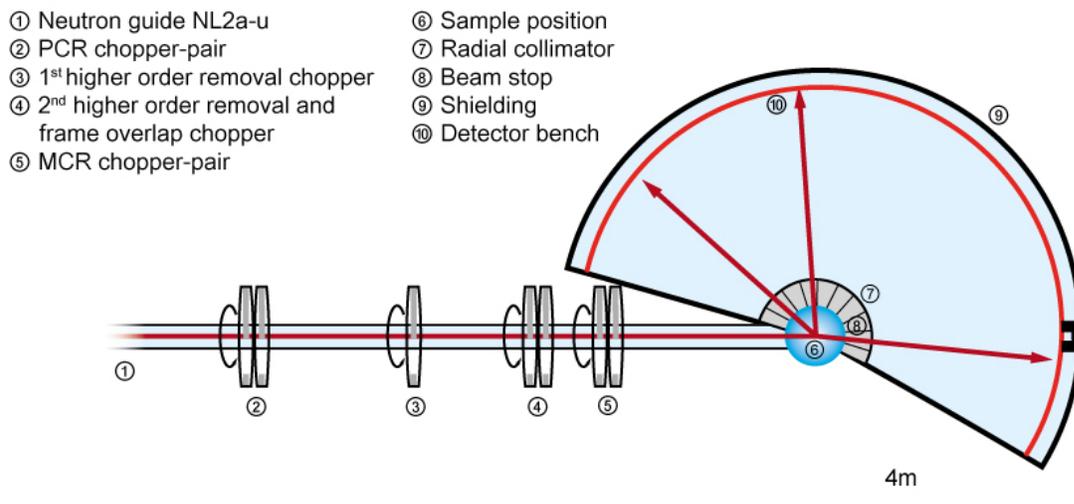⑦ Radial collimator
⑧ Beam stop
⑨ Shielding
⑩ Detector bench

4m

Figure 4.9:  Schematic sketch of the TOFTOF time-of-flight spectrometer at the MLZ, Garching, Germany. Adapted from [176].

the continuous polychromatic incident neutron beam into a pulsed monochromatic one [177]. The first pair of choppers, the pulsing counter rotating (PCR) chopper-pair, produces pulses of polychromatic neutrons. The last pair of choppers, the monochromating counter rotating (MCR) chopper-pair, is used to select neutrons in a narrow wavelength range. The remaining three choppers (labeled (3) and (4) in Figure 4.9) remove neutrons with higher order wavelength and can furthermore be used to decrease the pulse frequency in order to avoid the overlap of scattered neutrons from successive pulses.

After interaction with the sample, the time-of-flight of the scattered neutrons is measured with approximately 1000 $^3$He detectors, covering a wide range of scattering angles with a sample-detector distance of 4 m. A radial collimator is placed between the sample and the detectors to prevent the detection of neutrons scattered by other objects.

### 4.3.2   QENS data analysis

Before the obtained data from QENS experiments can be fitted by structural models, corrections to the data need to be performed. To eliminate the signal from other sources than the sample, reference measurements are performed.

Most significantly, elastic scattering from the sample holder contributes to the measured signal. Therefore, a measurement of the empty sample holder must be subtracted from the

data. Prior to subtraction, the scattered intensity from the sample holder including the sample, and from the empty sample holder are normalized to the incident flux to determine the absolute scattered intensity. Secondly, self-shielding of the sample holder needs to be considered: Due to the scattering of neutrons by the sample, the sample holder is shielded from the incident neutron flux, i.e., the scattering of neutrons by an empty sample holder is stronger than the one of a sample holder in which the sample is mounted [178]. Therefore, the measurement of the empty cell needs to be multiplied with a self-shielding factor prior to subtraction.

The measured time-of-flight of the neutrons are converted to energy transfer using a measurement of a thin vanadium slab. As vanadium mainly scatters incoherently and elastically, the arrival time of the neutrons at each detector corresponds to an energy transfer $\hbar\omega = 0$. Furthermore, the measurement on vanadium allows the determination of the individual detector sensitivities, as its scattering strength in dependence on momentum transfer is known. Finally, the signals from all detectors are binned in groups according to their absolute value of the momentum transfer $q$ to obtain $S(q,\omega)$.

Several physical models describing the obtained QENS spectra were used in this thesis and are described in the following.

**Translational diffusion processes.** The Brownian motion of a particle in a liquid can be described by its diffusion coefficient $D$. According to Fick's second law, the diffusion of particles occurs to minimize a concentration gradient in the liquid, mathematically described by a differential equation of the self-correlation function $G(\vec{R}, t)$ [178],

$$D\nabla^2 G(\vec{R}, t) = \frac{\partial}{\partial t} G(\vec{R}, t) \tag{4.34}$$

As it serves as a proportionality constant in this equation, $D$ is a measure of the mobility of the particle. The solution of equation 4.34 gives an expression for $G(\vec{R}, t)$,

$$G(\vec{R}, t) = (4\pi Dt)^{-3/2} \exp\left(\frac{-R^2}{4Dt}\right) \tag{4.35}$$

Inserting equation 4.35 into equation 4.20 yields the scattering law that describes the incoherent scattering from diffusing particles, which is given by a Lorentzian function,

$$S(q,\omega) = \frac{1}{\pi}\frac{\Gamma(q)}{\omega^2 + \Gamma^2(q)} \tag{4.36}$$

with $\Gamma(q)$ the half width at half maximum of the Lorentzian, and $\Gamma(q) = Dq^2$. In Figure 4.10, an example of equation 4.36 for different $q$ values is shown.
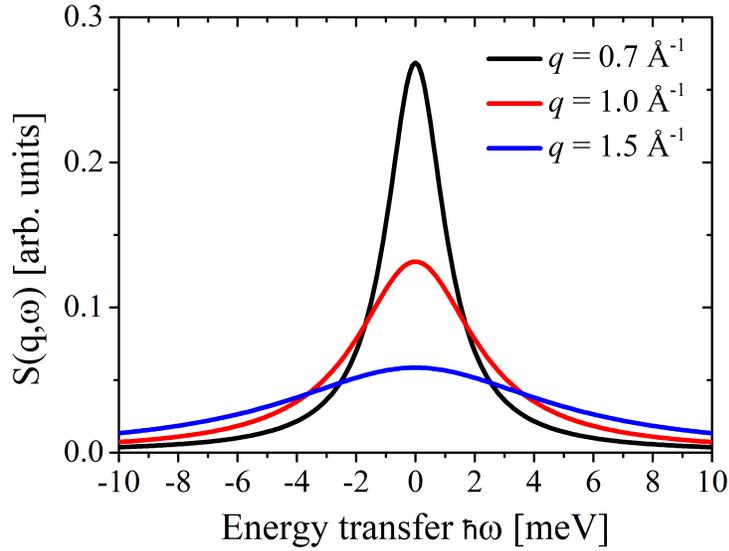


Figure 4.10:   Example of a Lorentzian describing a diffusion process with diffusion coefficient $D = 10^{-11}$ $\text{Å}^2\text{s}^{-1}$ at different $q$ values, as indicated in the graph.

**Vibrational processes.**   In a QENS experiment, inelastic scattering of neutrons by phonons may contribute to the spectrum. In liquids, phonons are influenced by anharmonic effects, and their vibration can be described by a damped harmonic oscillator (DHO). For scattering by single phonons, the dynamic structure factor is given by [179, 180]

$$S(q,\omega) = \frac{Z(q)}{\pi}[n(\omega) + 1]\frac{4\omega\Gamma_q}{[(\omega - \omega_q)^2 + \Gamma_q^2][(\omega + \omega_q)^2 + \Gamma_q^2]} \tag{4.37}$$

with $\omega_q$ the harmonic phonon frequency, $\Gamma_q$ the damping factor taking into account anharmonic effects, and $Z(q)$ a $q$-dependent prefactor. The two terms in brackets in the denominator describe the energy loss and gain of the scattered neutron due to the creation or annihilation of a phonon, respectively. $n_B(\omega)$ is the Bose occupation number, given by $n_B(\omega) = [\exp(\hbar\omega/k_BT) - 1]^{-1}$, which describes the ratio between the number of phonon-

creation and phonon-annihilation events.

Two regimes of damping can be distinguished [181]. In case of under-damping, $\Gamma_q < \omega_q$, the spectrum consists of two single peaks centered at $\pm\omega_q$ with their broadening determined by $\Gamma_q$. Over-damping occurs when $\Gamma_q > \omega_q$, and results in a spectrum consisting of one broad peak centered at $\omega = 0$. An example of each case is given in Figure 4.11.
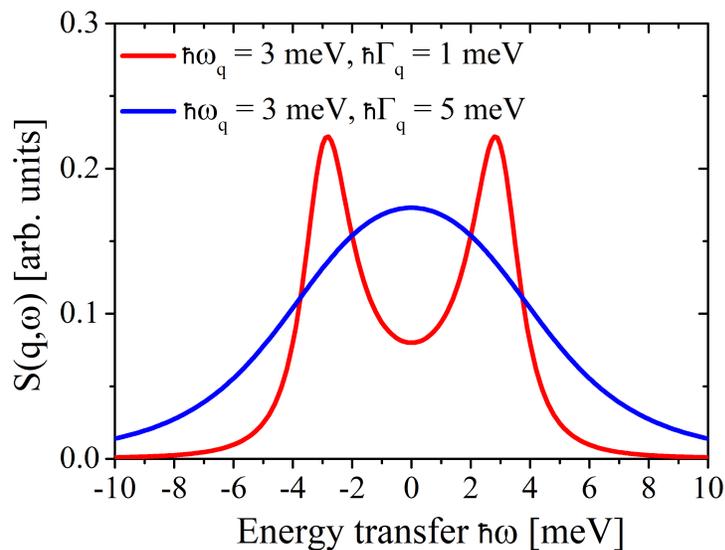


Figure 4.11: Example of a damped harmonic oscillator at an arbitrary $q$ value in the under-damped ($\Gamma_q < \omega_q$, red curve) and the over-damped ($\Gamma_q > \omega_q$, blue curve) regime.

**Intrumental resolution.** As is the case for almost all neutron scattering experiment, also a QENS experiment is affected by the experimental resolution, which is determined by, among other effects, the wavelength distribution, the duration and size of each pulse, and the sample geometry. The resolution function $R(\omega, \omega')$ describes the probability that a scattering event with energy transfer $\hbar\omega'$ is measured as a scattering event with energy transfer $\hbar\omega$. The measured dynamic structure factor $S_M(q, \omega)$ is related to the real dynamic structure factor $S(q, \omega)$ via a convolution product with $R(\omega, \omega')$, given by [182]

$$S_M(q, \omega) = \int R(\omega, \omega')S(q, \omega')\mathrm{d}\omega' \tag{4.38}$$

$R(\omega, \omega')$ can experimentally be determined using a purely elastically and incoherently scattering sample. In most cases, vanadium is used for this purpose, since it has a negligible coherent scattering cross section [183]. To fit a physical model to $S_M(q, \omega)$, the model needs

to be convoluted with $R(\omega, \omega')$. Alternatively, the resolution effects of $S_M(q, \omega)$ can be discarded by a Fourier deconvolution. However, this procedure is numerically unstable and usually leads to noisy data.

## 4.4    Turbidimetry

A commmon method to determine the cloud point of thermoresponsive polymers is the measurement of light transmission, turbidimetry. For this method, a laser is focused on the sample, and the transmission is measured with a photodiode. The fraction of transmitted light is reduced if particles are present, that are large enough to scatter the incident light. This may, for example, be the case if thermoresponsive polymers form aggregates.

## 4.5    Optical microscopy

Optical microscopy is a method to take magnified real-space images of small objects. Typical optical microscopes contain few key components, depicted in Figure 4.12. For a sufficient brightness of the magnified image, the sample is illuminated by a light source from below. The light from the sample is captured by the objective, which is located directly above the sample. It subsequently magnifies and focuses the captured light to produce a magnified real-space image of the sample [184]. Besides by their magnification factor, objectives can also be characterized by their numerical aperture, NA. It describes the ability of the objective to capture light, i.e., the range of incident angles of the light over which the objective can focus the light. The magnified image produced by the objective is projected by the projection lens on a CCD camera, which can be read out using a computer.

The resolution is limited by the diffraction of light in the objective. If the range of incident angles is increased, more closely located points can be distinguished from each other and are therefore resolvable [186]. Quantitatively, the minimum resolution that can be achieved with a certain objective is given by the Rayleigh criterion,

$$r = \lambda/2\mathrm{NA}, \tag{4.39}$$

where $\lambda$ is the wavelength of the light probing the sample and NA the numerical aperture.
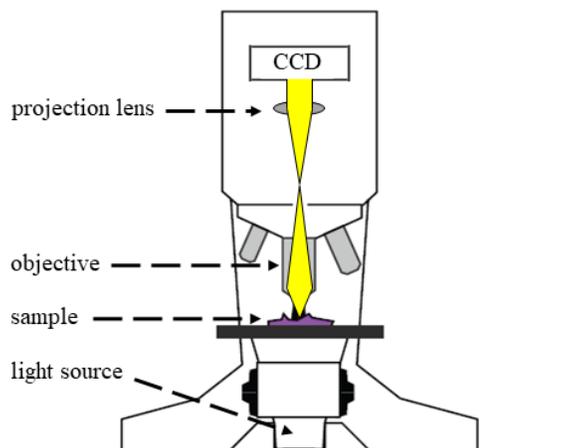
Figure 4.12: Schematic representation of an optical microscopy setup with the key components indicated in the figure. Adapted from ref. [185].

## 4.6 Raman scattering

Although methods suitable for structural investigation are very useful to describe polymeric systems, they are not capable of probing the interactions in the system directly. For a deeper understanding, spectroscopic methods can be applied to investigate interactions on a molecular scale.

### 4.6.1 Molecular vibrations

Molecular vibration is the periodic motion of atoms in a molecule due to the covalent bonds between them, which act as springs. For diatomic molecules of atoms with masses $m_1$ and $m_2$, the stretching vibration can be approximated as a harmonic oscillation with a vibrational frequency $\nu$ given by [187]

$$\nu = \frac{1}{2\pi} \sqrt{\frac{K}{\mu}} \quad (4.40)$$

with $K$ the spring constant describing the strength of the covalent bond, and $\mu$ the reduced mass of the two atoms, given by

$$\mu = \frac{m_1 m_2}{m_1 + m_2} \quad (4.41)$$

The stretching frequency of the molecular vibration in a diatomic molecules therefore identifies the moiety because of the differences in mass and binding of different atoms. Furthermore, because the strength of the covalent bond between atoms depends on the local

environment around the molecule, the frequency contains information on the interactions in the sample. For molecules containing $N$ atoms, the number of possible vibrational modes equals 3$N$-6, which, for large molecules, can lead to a very complex vibrational signature. For polymers, however, vibrational modes in the repeating units are similar to each other, therefore restricting the total number of vibrational modes.

## 4.6.2   Spectroscopic methods

A wide range of spectroscopy methods exist. For example, infrared (IR) absorption spectroscopy and Raman spectroscopy allow to investigate the molecular vibrations or other excitations of atoms and molecules in the sample using their interaction with light. In Figure 4.13, a schematic overview of the working principle of both methods is illustrated. For IR absorption spectroscopy, an incident beam with polychromatic light interacts with the sample. Due to the absorption of the light at wavelengths corresponding to vibrational modes in the system, the spectrum of the transmitted light contains information on the composition of the sample as well as on interactions between its components. Raman scattering is a fundamentally different process. An incident photon interacts with a phonon, thereby losing or gaining the vibrational energy of the phonon, and is therefore an inelastic scattering process. Thus, the differences in energy between the incident and scattered photons contain information on the vibrational modes in the investigated system.
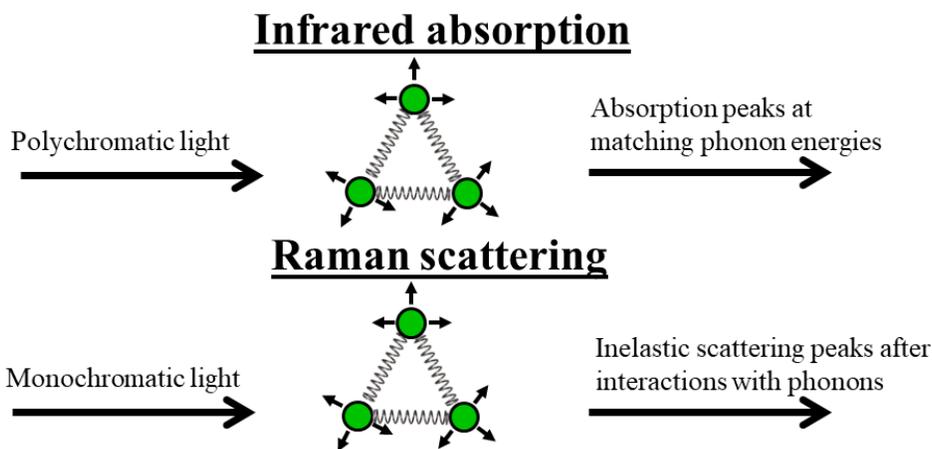


Figure 4.13:   Overview of the resemblances and differences between IR spectroscopy and Raman spectroscopy [188].

Although in both methods the same vibrational modes are probed, their difference in physical nature results in different coupling strengths between the incident light and the vibrational modes. The experimental method of choice therefore depends strongly on the

vibrational modes of interest. For example, Raman scattering on water is weak in comparison with its IR absorption, and is therefore more suitable for the study of aqueous polymer solutions. However, both methods are often used complementary to each other. For the work presented in this thesis, Raman spectroscopy sufficed. The following discussion therefore focuses on the theoretical background of Raman spectroscopy only.

### 4.6.3 Raman scattering theory

This section is based on refs. [189] and [190].

Scattering of photons by a particle is due to the polarizability of the particle: An incident photon induces an oscillating dipole moment due to the oscillating electric field $E(t)$ of the photon, given by

$$p(t) = \alpha E(t) \tag{4.42}$$

with the time dependence of the electric field of the incident photon with frequency $\omega$ given by

$$E(t) = E_0 \cdot \cos(\omega t) \tag{4.43}$$

As oscillating dipoles emit electromagnetic radiation, the incident photon is scattered by the particle. In case of a constant value of $\alpha$, the frequency of the scattered photon equals that of the incident photon. The scattering is therefore elastic and corresponds to the well-known Rayleigh scattering. For Raman-active molecular vibrations, the polarizability is not constant, but depends on the vibrational displacement coordinate $x$. In a classical derivation of the Raman scattering intensity, the polarizability is expressed as a Taylor series around the point $x = 0$. Up to first order, it is given by

$$\alpha(x) = \alpha_0 + \left(\frac{\partial \alpha}{\partial x}\right)_0 x \tag{4.44}$$

The vibrational displacement of a vibrational mode inside a molecule with frequency $\omega_m$ can be approximated as

$$x(t) = x_0 \cdot \cos(\omega_m t) \tag{4.45}$$

Combining eqs. 4.42 to 4.45 yields an expression for the time dependence of the induced dipole moment, given by

$$p(t) = \alpha_0 E_0 \cdot \cos(\omega t) + \left(\frac{\partial \alpha}{\partial x}\right)_0 E_0 x_0 \cos(\omega t)\cos(\omega_m t) \tag{4.46}$$

which, after rearrangements, gives

$$p(t) = \alpha_0 E_0 \cdot \cos(\omega t) + \frac{1}{2}\alpha_1 E_0 \cos[(\omega + \omega_m)t] + \frac{1}{2}\alpha_1 E_0 \cos[(\omega - \omega_m)t] \tag{4.47}$$

with

$$\alpha_1 = \left(\frac{\partial \alpha}{\partial x}\right)_0 x_0 \tag{4.48}$$

This result shows that the incident light may be scattered with three different frequencies. The first term of equation 4.47 represents Rayleigh scattering, i.e., the scattering of light at the same frequency as the incident light. The second and third term of equation 4.47 correspond to anti-Stokes Raman and Stokes Raman scattering, respectively, where the frequency of the scattering photon is increased or decreased with the frequency of the vibrational mode of the molecule $\omega_m$. Thus, both terms only appear if the molecular vibration involves a change in polarizability.

Generally, $\alpha_0 \gg \alpha_1$, which means that Raman scattering is very weak in comparison with Rayleigh scattering. The main technical challenge for a Raman spectroscopy experiment is therefore the separation of the weak Raman signal from Rayleigh scattering. Furthermore, differences in scattered intensities exist between Stokes and anti-Stokes scattering. For anti-Stokes scattering, vibrational modes can be populated by thermal energy before the scattering event. The ratio in intensity of anti-Stokes to Stokes scattering equals the Boltzmann factor, given by $\exp(-\hbar\omega/k_B T)$. For a better signal-to-noise ratio, Raman spectroscopy measurements are usually performed on the Stokes side of the spectrum.

### 4.6.4   Raman spectroscopy setup

In Figure 4.14, a schematic sketch of a typical Raman spectroscopy setup is presented. The sample is irradiated by a laser. The light is focused onto the sample via a microscope objective, which allows the illumination of a very small area on the sample, in the order of a few $\mu m^2$. The scattered light follows the same path back into the setup, where the Raman signal is separated from the Rayleigh signal by a filter. In a typical Raman spectroscopy setup, a band-stop filter is used to strongly weaken the intensity at the wavelength of the used light source, i.e., the Rayleigh scattering.

After the Raman scattered light has passed the filter, it passes through a grating, where it is diffracted at angles that depend on the wavelength. A CCD camera positioned behind
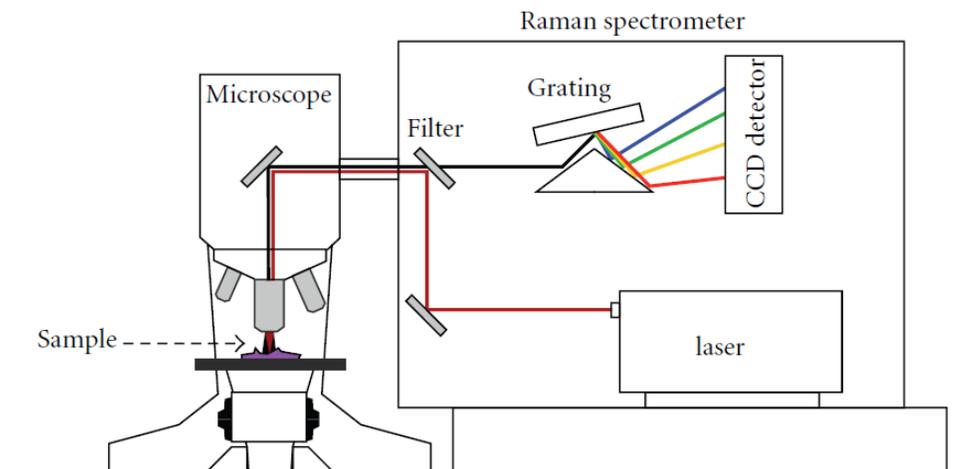
Figure 4.14: Schematic sketch of a Raman spectroscopy setup [185]. Adapted from ref. [185].

the grating records photons of different wavelengths at different positions, which allows to distinguish the presence of vibrational modes in the sample.

## 4.6.5 Raman spectroscopy analysis

In a Raman spectrum, intensity peaks are observed at frequencies corresponding to the energy of vibrational modes in the system. Every type of molecule exhibits a unique combination of vibrational modes, and its Raman spectrum can be used to identify the species in the investigated sample. Furthermore, the composition of a sample can be determined, since the intensity of the peaks in the system is linearly proportional to the number of a certain molecule in the sample. Besides the composition of the sample, other factors may influence the appearance of the Raman spectrum. The frequency, shape and width of a peak arising from a certain vibrational mode in a molecule depends strongly on its local environment, e.g. its hydration, which is described in detail in the following.

**Frequency of a Raman peak.** Vibrational modes are influenced by surrounding atoms that may induce changes in the local charge density distribution. For example, an increase in the electron density between two atoms increases the strength of the covalent bond between the atoms. As is evident from equation 4.40, this would lead to an increase in the frequency of the vibrational mode, which can be detected in a Raman scattering experiment. The effect of the interaction depends strongly on the type of interaction and the involved atoms,

and varies from case to case.

**Width of a Raman peak.**   Instead of a signal with a discrete energy corresponding to the energy of the observed vibrational mode, the measured photons always feature a distribution of energies, which is due to natural broadening [191]. This is an intrinsic feature of Raman scattering, and results from the fact that the excitation energy $E$ cannot be determined exactly. Its uncertainty is related to the lifetime $\tau$ of the vibrational state according to the Heisenberg uncertainty principle,

$$\Delta E \cdot \tau \geq \frac{\hbar}{2} \tag{4.49}$$

It follows that the Raman signal of an ensemble of identical vibrational states can be described by a Lorentzian function,

$$L(\omega) = \frac{1}{\pi\gamma} \frac{\gamma^2}{(\omega - \omega_0)^2 + \gamma^2} \tag{4.50}$$

with $\omega_0$ the mean frequency and $\gamma$ the Lorentzian width. An example of a Lorentzian function is shown in Figure 4.15.

Additional sources of signal broadening are collisions between particles or network formation. Collisions between molecules hosting the vibrational modes as well as strong interactions between them allow a reduction of the lifetime. According to equation 4.49, this increases the uncertainty in energy and therefore the width of the measured signal. Also in this case, the measured spectral line follows a Lorentzian function. The effect of collisional broadening depends on the density of the system, and therefore also on pressure. In most cases, its effect is much more pronounced than the one of natural broadening [191].

Thermal motion of molecules contributes to the broadening of spectral lines as well. The Doppler effect, resulting from the velocities of the molecules, causes a variation of the observed excitation energy, and therefore a broadening of the spectral line. It was shown that a spectral line broadened by thermal effects follows a Gaussian function [191], given by

$$G(\omega) = \frac{1}{\sqrt{2\pi\sigma^2}} \exp\left( - \frac{(\omega - \omega_0)^2}{2\sigma^2} \right) \tag{4.51}$$

with $\sigma$ the Gaussian width. An example of a Gaussian function is shown in Figure 4.15.

In a real measurement, a combination of all broadening mechanisms may be observed. The measured spectral line is in this case a convolution of a Lorentzian and a Gaussian function, which is a Voigtian function,

$$V(\omega) = \int L(\omega') \cdot G(\omega - \omega') d\omega' \qquad (4.52)$$

also shown in Figure 4.15. A Gaussian function decays more rapidly than a Lorentzian function, and their differences are most evident in the wings. In principle, it is possible to distinguish collisional broadening and thermal broadening using a Voigtian function to model the signal from Raman scattering.
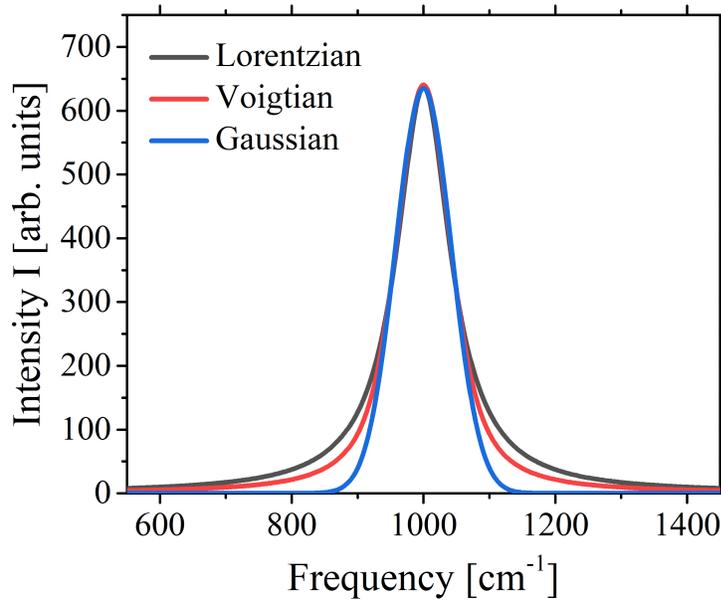


Figure 4.15: Example of a Lorentzian (black line), Voigtian (red line) and a Gaussian (blue line) profile with similar widths and a peak frequency of 1000 cm$^{-1}$.

# Chapter 5. Phase behavior of purely aqueous PNIPAM solutions

In this chapter, an initial characterization of the phase behavior of PNIPAM is provided. The phase diagram in the temperature-pressure frame is constructed using turbidimetry. Additionally, it is attempted to calculate the Gibbs free energy of mixing of a PNIPAM solution in dependence on both temperature and pressure. A part of this chapter was previously published in B.-J. Niebuur et al., *ACS Macro Lett.*, 6:1180-1185, 2017 [131].

## 5.1 Introduction

As an initial characterization, the phase behavior of a 3 wt% PNIPAM solution in $D_2O$ is investigated using macroscopic experimental methods. At first, the phase diagram in the temperature-pressure frame is constructed using turbidimetry to determine the ranges in temperature and pressure where PNIPAM is soluble. Although the phase diagram of aqueous PNIPAM solutions was already measured previously, as summarized in Section 3.2, the investigated solutions differed in concentration, molar mass and solvent. As this may lead to small changes, the phase diagram of the PNIPAM solution used for the measurements presented in this thesis needs to be known.

A further description of the solubility of PNIPAM at different locations in the temperature-pressure phase diagram is given using a calculation of the Gibbs free energy of mixing of the PNIPAM solution in dependence on temperature and pressure. The results from density, sound velocity and differential scanning calorimetry measurements at atmospheric pressure are related to the Gibbs free energy of mixing using thermodynamic relations, and it is extrapolated to higher pressures by means of a second-order Taylor expansion. This description of the stability and instability of the solution in the one-phase and two-phase state, respectively, provides a basic understanding of the phase behavior of PNIPAM solutions, and may

help to understand results from structural studies, presented in the subsequent chapters.

## 5.2 Experimental details

**Materials.** Poly($N$-isopropylacrylamide) (PNIPAM) with a molar mass $M_n = 36\ 000$ g mol$^{-1}$ and a dispersity of 1.26 (end groups carboxylic acid and a hydrogen atom, respectively) was purchased from Sigma-Aldrich. It was dissolved at a concentration of 3 wt% in $D_2O$ and stirred for at least 24 h to ensure complete dissolution.

**Turbidimetry.** Turbidimetry measurements were performed using a 10 mW HeNe laser ($\lambda$ = 632.8 nm) in combination with a photodiode detector. A custom-made copper-beryllium pressure cell with sapphire windows, capable of withstanding pressures up to 400 MPa, was placed in between the laser and the detector. A Viton O-ring separated the sample from the pressure medium (water) with a sample thickness of 1 mm. A pressure generator from SITEC (Maur, Switzerland) was connected to the pressure cell. The temperature in the pressure cell was controlled by a Julabo F12 circulating bath thermostat. A Pt100 resistance thermometer, attached to the pressure cell, was used to precisely determine its temperature.

The measured transmitted intensity was normalized to the maximum intensity that was reached during the measurement. During transitions from the one-phase to the two-phase state, the cloud point was defined as the temperature and pressure at which the transmitted intensity starts to decrease. The clearing point during scans from the two-phase to the one-phase state was defined as the temperature and pressure at which the maximum intensity is again reached. Temperature scans were performed with a gradual temperature increase or decrease with a rate of 0.06 K min$^{-1}$, whereas pressure scans were performed in discrete steps of 2.5 MPa in the vicinity of the cloud/clearing point.

**Free energy of mixing determination.** In order to quantify the free energy of mixing in dependence on temperature and pressure, the molar volumes and isothermal compressibilities of both the 3 wt% PNIPAM solution in $D_2O$ and pure $D_2O$ in dependence on temperature at atmospheric pressure were determined from density and sound velocity measurements, using a DSA 5000 M setup (Anton Paar, Graz, Austria), and differential scanning calorimetry (DSC) measurements, using a DSC III setup (Setaram, Caluire, France). The density measurements were performed using the pulsed excitation method [192], resulting in an accuracy of 0,000007 g cm$^{-3}$. Both the density and sound velocity measurements were performed dur-

ing heating scans in steps of 2.5 K with an equilibration time of ∼20 min after each change in temperature.

The DSC measurements were performed during heating scans from ∼10 to ∼70 °C with a heating rate of 0.02 K s$^{-1}$. The empty cell measurement was subtracted from the data and the curves were corrected for the weight of the sample as well as for the heating rate to obtain the isobaric heat capacity of both substances in dependence on temperature.

## 5.3   Cloud point determination

The measurements presented in this section were performed by Simon Pinzek [193].

It is well known that semi-dilute aqueous PNIPAM solutions phase-separate upon heating at ∼31 °C at atmospheric pressure, with a weak dependence on concentration and molar mass [25]. It was previously shown that, also at higher pressures, aqueous PNIPAM solutions phase-separate at a certain cloud point temperature $T_{cp}$, following an elliptical trend in the temperature-pressure frame, presented in Figure 3.3 for all previously published results. To investigate the phase behavior of the PNIPAM solution at the concentration and molar mass under study, turbidimetry measurements are performed in wide ranges of temperature and pressure range.

In Figure 5.1a, transmission curves obtained during heating scans at different pressures are presented. At atmospheric pressure, a sharp decrease in the normalized transmission from 1 to 0 is observed at ∼34 °C. At this temperature, a transition from a transparent homogeneous state to an inhomogeneous state, where the light is scattered by large-scale inhomogeneities, takes place and aggregates are formed. The intensity measurements at this pressure are performed with large temperature steps, thus, statements about the width of the temperature range at which separation takes place are not possible. With increasing pressure, the transition temperature shifts at first to higher temperatures and, starting at $p$ = 100 MPa, to lower temperatures, which shows that the effect of pressure on $T_{cp}$ is non-linear. In addition, the temperature range over which the transmission decreases, broadens at high pressures. Thus, the phase transition at high pressure occurs more gradually, and other physical processes may play a role. From these measurements, it is, however, not possible to determine the physical nature of these processes.
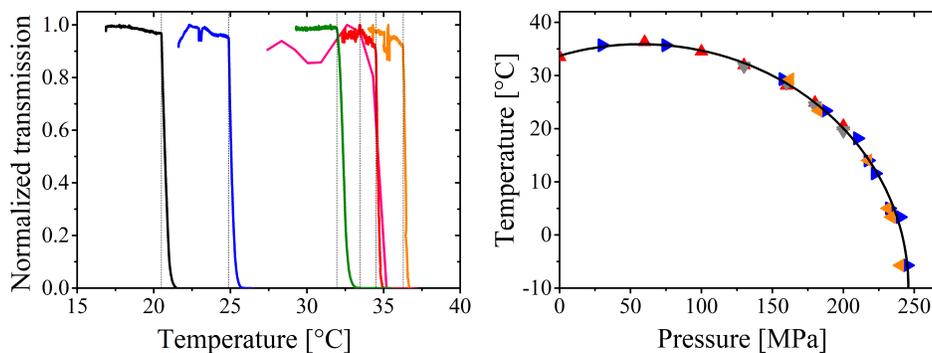
Figure 5.1: (a) Transmission curves in dependence on temperature at 0.1 MPA (pink line), 60 MPa (orange line), 100 MPa (red line), 130 MPa (olive line), 180 MPa (blue line), and 200 MPa (black line). The dotted lines mark the respective cloud points at each pressure. (b) Cloud points of the 3 wt% PNIPAM solution in $D_2O$. The symbols represent the direction of the scan: heating: red ▲, cooling: grey ▼, increasing pressure: blue ▶, decreasing pressure: orange ◀. The line is a fit of equation 2.11.

From the cloud and clearing points obtained in all performed pressure and temperature scans, the phase diagram of the 3 wt% PNIPAM solution in $D_2O$ is constructed, shown in Figure 5.1b. A convex-upward shape is observed, where the one-phase state is located below the data, and the two-phase state above. Only slight deviations from the general trend are present, i.e., cloud and clearing points at the same temperature or pressure are very close to each other. From this observation, it follows that hysteresis effects in the switching between the two states is insignificant.

In accordance with previous studies [77, 128], the phase diagram of the 3 wt% PNIPAM solution in $D_2O$ can be modeled with the Hawley theory for pressure-temperature phase diagrams of protein solutions (equation 2.11). As shown in Figure 5.1b, the obtained fit is excellent, and therefore represents the coexistence line of both states in the temperature-pressure frame. The resulting fit parameters, given in table 5.1, are similar to the ones found in earlier studies on PNIPAM solutions [77, 128].

Table 5.1: Results from fitting the cloud point data from Figure 5.1 with the Hawley theory (equation 2.11).

|  | $p_0$ [MPa] | $T_0$ [K] | $\frac{V_0\Delta\beta}{\Delta G_0}$ [MPa$^{-2}$] | $\frac{V_0\Delta C_p}{\Delta G_0}$ [K$^{-1}$] |
|---|---|---|---|---|
| 3 wt% PNIPAM in $D_2O$ | $59.5 \pm 5.9$ | $263.3 \pm 1.9$ | $(5.89 \pm 0.36)\times10^{-5}$ | $(2.50 \pm 0.23)\times10^{-1}$ |

## 5.4  Free energy calculation

The measurements presented in this section were performed by Leonardo Chiappisi, ILL.

It can be expected that the solvent quality strongly depends on the location in the temperature-pressure phase diagram. For example, the polymers are soluble in the one-phase state. Here, the solvent quality is therefore better than in the two-phase state, where a poor solvent quality is expected. Furthermore, it may vary with distance to the coexistence line in both states. In order to quantify the solvent quality, it is attempted to determine the Gibbs free energy of mixing in dependence on temperature and pressure for a 3 wt % PNIPAM solution in $D_2O$. As the Hawley theory is based on a second-order Taylor expansion of the Gibbs free energy of mixing, the good agreement between the data and the fit suggests that the third derivatives of the free energy with respect to $p$ and $T$ are zero. As shown below, this allows for a calculation of the Gibbs free energy of mixing in dependence on pressure from measurements of thermodynamic parameters at atmospheric pressure.

The molar Gibbs free energy of mixing is defined as the difference in Gibbs free energy between the two-phase state $G_{collapsed}$, where the chains are collapsed, and the one-phase state $G_{swollen}$, where the chains are swollen:

$$\Delta G_{mix} = G_{collapsed} - G_{swollen} \tag{5.1}$$

To derive the pressure dependence of $\Delta G_{mix}$, it can be approximated by a Taylor expansion up to the second order in $p$ around a reference point $p_0$, given by [73, 77, 194]

$$\Delta G_{mix} \approx \Delta G_{mix,0} + \left(\frac{\partial \Delta G_{mix}}{\partial p}\right)_0 (p - p_0) + \frac{1}{2}\left(\frac{\partial^2 \Delta G_{mix}}{\partial p^2}\right)_0 (p - p_0)^2$$
$$= \Delta G_{mix,0} + \Delta V_0 (p - p_0) - \frac{1}{2}\Delta(\beta_T V)_0 (p - p_0)^2 \tag{5.2}$$

with $\Delta G_{mix,0}$ the change in molar Gibbs free energy of mixing at $p_0$, $\Delta V_0$ the difference in volume between the swollen and collapsed state at $p_0$, and $\Delta(\beta_T V)_0$ the difference in the product of isothermal compressibility coefficient and volume between the swollen and collapsed state at $p_0$.

To isolate the changes due to the varying interaction between PNIPAM and water, i.e., the non-ideal contributions to the system, $\Delta G_{mix}$ is determined from the apparent molar volume $V^\varphi$ and the apparent molar isothermal compressibility $\kappa_T^\varphi$ of PNIPAM in the solution. It follows that the second-order Taylor expansion of equation 5.2 can be rewritten as

$$\Delta G_{mix} \approx \Delta G_{mix,0} + \Delta V_0^\varphi (p - p_0) - \frac{1}{2}\Delta \kappa_{T,0}^\varphi (p - p_0)^2 \tag{5.3}$$

with $\Delta V_0^{\varphi}$ the difference in apparent molar volume between the swollen and collapsed state at $p_0$, and $\Delta \kappa_{T,0}^{\varphi}$ its difference in the apparent molar isothermal compressibility. $V^{\varphi}$ is determined from the densities of the solution and the solvent as [195, 196]

$$V^{\varphi} = \frac{M_w}{d_{sol}} - \frac{d_{sol} - d_{D_2O}}{c_m d_{sol} d_{D_2O}} \tag{5.4}$$

with $M_w$ the weight-average molar mass of the polymer, $c_m$ its concentration in molality, and $d_{sol}$ and $d_{D_2O}$ the densities of the polymer solution and of the solvent, respectively. $\kappa_T^{\varphi}$ can be derived from $V^{\varphi}$ as [197]

$$\kappa_T^{\varphi} = \beta_{T,sol} V^{\varphi} + \frac{\beta_{T,sol} - \beta_{T,D_2O}}{c_m d_{D_2O}} \tag{5.5}$$

with $\beta_{T,sol}$ and $\beta_{T,D_2O}$ the isothermal compressibility coefficients of the solution and the solvent, respectively. These are determined from $d_i$, the speed of sound $u_i$ in the sample, the thermal expansion coefficient $\alpha_{V,i}$ and the isobaric heat capacity $C_{p,i}$ as [198]

$$\beta_{T,i} = \frac{1}{d_i u_i^2} + \frac{T \alpha_{V,i}^2}{d_i C_{p,i}} \tag{5.6}$$

where the index $i$ stands for 'sol' or 'D$_2$O', i.e., for the polymer solution or the pure solvent, respectively. $\alpha_{V,i}$ is determined from the temperature depedence of the density as

$$\alpha_{V,i} = d_i \frac{\partial (\frac{1}{d_i})}{\partial T} \tag{5.7}$$

To obtain the values needed to determine $\Delta G_{mix}$ according to equation 5.3, the density, sound velocity and isobaric heat capacity of both the 3 wt% PNIPAM solution in D$_2$O and in pure D$_2$O were measured at atmospheric pressure (Figure 5.2). The density, Figure 5.2a, decreases with temperature for both samples. Below $T_{cp}$, the density of the polymer solution is slightly higher than the one of pure D$_2$O, whereas above $T_{cp}$, both curves overlap. Thus, in the one-phase state, the interaction between PNIPAM and D$_2$O allows for a denser packing than in the two-phase state, where both substances are mainly separated from each other. This result is in agreement with previous specific volume measurements of PNIPAM solutions, where it was shown that the specific volume of the PNIPAM solution increases above $T_{cp}$ [76, 133].

In Figure 5.2b, the sound velocity $u_i$ of both the pure D$_2$O and the 3 wt% PNIPAM solution in D$_2$O is shown. The value of D$_2$O increases with temperature, and the values are
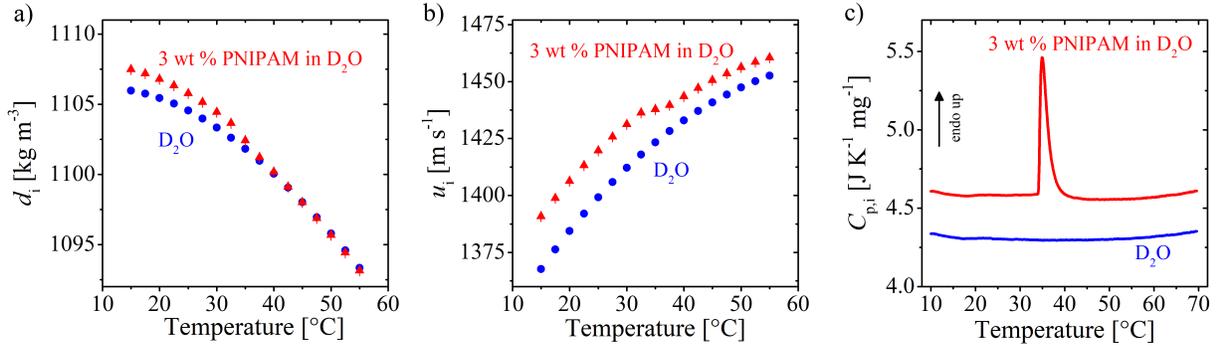
Figure 5.2: Densities (a), sound velocities (b) and isobaric heat capacities (c) of the 3 wt% PNIPAM solution in $D_2O$ (red data) and of pure $D_2O$ (blue data), all measured at atmospheric pressure. The index $i$ stands for 'sol' and '$D_2O$'

similar to previously reported ones [199, 200]. Also the sound velocity in the PNIPAM solution shows an overall increasing trend with increasing temperature; the values are, however, generally larger than the ones of $D_2O$, which may be due to the higher elasticity of PNIPAM compared to pure water. As was already reported earlier [201], the sound velocity shows a weak drop at the phase transition temperature, resulting from the structural rearrangements in the sample.

The isobaric heat capacity, shown in Figure 5.2c, strongly differs between pure water and the PNIPAM solution. Whereas for $D_2O$ it stays constant at $\sim$4.3 J K$^{-1}$ mg$^{-1}$ with temperature, a pronounced endothermic peak around $T_{cp}$ is observed for the isobaric heat capacity of the PNIPAM solution. At the phase transition, this strong absorption of heat is due to the release of water molecules from the chains [202, 203, 204].

Figure 5.3a displays $V^\varphi$ of PNIPAM in the solution at a concentration of 3 wt % in $D_2O$, determined according to equation 5.4. In the entire temperature range, the molar volume increases with a sharp increase at $T_{cp}$ ($\sim$34 °C), in consistency with previous research [76]. This increase can be attributed to the changes in packing due to the strong dehydration of the chains. $\kappa_T^\varphi$ (Figure 5.3b), determined according to equation 5.5, behaves similarly: An increasing trend is seen in the entire measured temperature range, with an additional sharp increase at $T_{cp}$. The notably higher value in the two-phase state is mainly due to the differences in the compressibility between hydration water, associated with the polymer, and bulk water.

The differences in $V^\varphi$ and $\kappa_T^\varphi$ between the collapsed and the swollen region of PNIPAM in
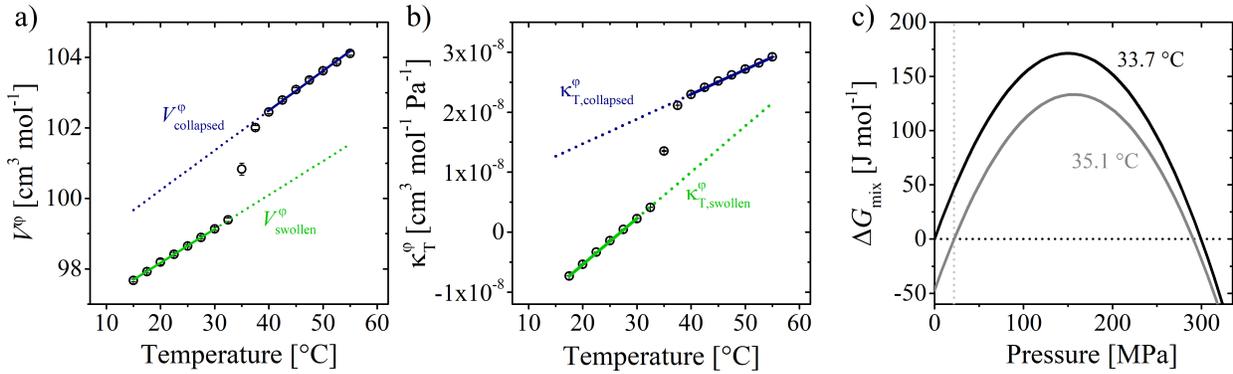
Figure 5.3: Apparent molar volume (a) and apparent molar isothermal compressibility (b) of the 3 wt% PNIPAM solution in $D_2O$ in dependence on temperature, measured at atmospheric pressure. The green and blue solid lines are linear fits in the one-phase state and in the two-phase state, respectively. The dotted lines represent their extrapolations. (c) Gibbs free energy of mixing in dependence on pressure, determined according to equation 5.3 for $T = 33.7$ °C (black line) and 35.1 °C (grey line). The black dotted line indicates the $\Delta G_{mix} = 0$ line, the grey dotted line the cloud point pressure at 35.1 °C (22 MPa).

dependence on temperature, $\Delta V_0$ and $\Delta \kappa_{T,0}$, are obtained from extrapolations of linear fits of both quantities in the two-phase state and the one-phase state, respectively (also shown in Figure 5.3a and b). From the values of $\Delta V_0$ and $\Delta \kappa_{T,0}$, $\Delta G_{mix}$ is determined in dependence on pressure according to equation 5.3 at two different temperatures. In Figure 5.3c, $\Delta G_{mix}$ is shown for $T = 33.7$ °C, i.e., at $T_{cp}$ at atmospheric pressure, as well as at $T = 35.1$ °C. In both cases, $\Delta G_{mix,0}$ is chosen such that $\Delta G_{mix} = 0$ at $T_{cp}$ at 0.1 MPa and 22 MPa, respectively, as follows from turbidimetry.

At 33.7 °C, $\Delta G_{mix}$ increases up to 150 MPa, where it reaches a value of $\sim$171 J mol$^{-1}$. At higher pressures, $\Delta G_{mix}$ decreases and reaches negative values at $\sim$300 MPa. At pressures up to 300 MPa, $\Delta G_{mix}$ is positive, which means that polymer-water interactions are favorable and the chains are expected to be soluble. At the maximum of $\Delta G_{mix}$, the polymer-water interaction is the strongest, and the solution is at its most stable point. At $\sim$300 MPa, where $\Delta G_{mix}$ becomes negative, a transition to a two-phase state is expected, since polymer-water interactions become unfavorable. As this pressure is much higher than the cloud point pressure at the right side of the maximum, as measured with turbidimetry ($\sim$120 MPa, Figure 5.1b), $\Delta G_{mix}$ is strongly overestimated at high pressures.

At 35.1 °C, $\Delta G_{mix}$ is negative below 22 MPa. Thus, the solution is expected to be phase-separated, which is in accordance with the measured phase diagram (Figure 5.1). The increasing trend up to 22 MPa shows that the solution becomes less unstable close to the cloud point, i.e., the thermodynamic driving force for phase separation is weaker. Above 22

MPa, $\Delta G_{mix}$ is positive, and thus, the chains are soluble. At 35.1 °C, $\Delta G_{mix}$ increases up to ∼150 MPa and reaches again negative values at ∼290 MPa. It can be concluded that, also in this case, $\Delta G_{mix}$ is strongly overestimated at high pressure.

Several reasons for the observed deviation from the experimentally determined cloud points in the HP regime may exist. Firstly, the calculation of $\Delta G_{mix}$ is based on the assumption that only two conformational states of the chains exist in the entire pressure-temperature frame: the collapsed and the swollen state. In previous work [77, 142], it was shown, however, that the structure of aqueous PNIPAM solutions in both, the one-phase and in the two-phase state, differ strongly from each other in both pressure regimes. Furthermore, the broader temperature range at which phase separation takes place at high pressure, observed with turbidimetry (Figure 5.1a), suggests the presence of intermediate states, which is not accounted for in the calculation of $\Delta G_{mix}$ [136]. Secondly, by truncating the Taylor series of $\Delta G_{mix}$ after the second order, it is assumed that the isothermal compressibility factor is constant in the entire investigated pressure range. However, for protein solutions, the compressibility changes with a factor up to ∼5 at pressures between 0.1 and 100 MPa [198]. Although the interactions of polymers and proteins with water are not identical, it suggests that this assumption is not valid. From these considerations, it is therefore surprising that the pressure-temperature phase diagram of PNIPAM solutions can be adequately described with the Hawley theory for pressure-temperature phase diagrams of proteins [74], which is also based on a Taylor series of $\Delta G_{mix}$ up to the second order, as discussed in Section 3.2.

## 5.5   Conclusion

Using turbidimetry and the determination of the Gibbs free energy of mixing, first insights in the phase behavior of aqueous PNIPAM solutions at different pressures are obtained. Turbidimetry revealed that, at high pressures, the phase transition spans over a broader range than at low pressures. This indicates the presence of different interactions, which may also influence structural properties. In accordance with previous studies, an elliptical shape of the coexistence line in the temperature-pressure frame is observed, which can be modeled with the Hawley theory for pressure-temperature phase diagrams of proteins [74].

The Gibbs free energy of mixing in dependence on pressure was determined using a second-order Taylor expansion from density, sound velocity, and differential scanning calorimetry measurements at atmospheric pressure, and quantifies the stability of the solution at

different positions in the temperature-pressure phase diagram. In agreement with the results from turbidimetry, phase transitions at both low and high pressures are found. The phase transition pressures at high pressure are, however, strongly overestimated. As both the Gibbs free energy and the Hawley theory for temperature-pressure phase diagrams follow similar calculations, it was argued that both may not be valid in the present case. Firstly, more than two different states may be present at different pressures, i.e., the structure in both, the one-phase state and two-phase state, may depend on pressure. Secondly, third-order derivatives of the free energy may be pressure-dependent, which implies differences in molecular interactions.

Following this thermodynamic approach, scattering methods are employed to further investigate these pressure-dependent structures and molecular interactions in aqueous PNIPAM solutions, presented in the subsequent chapters.

# Chapter 6. Equilibrium-state structure characterization of purely aqueous PNIPAM solutions

In this chapter, the equilibrium-state structure of an aqueous PNIPAM solution in the two-phase state, determined with a combination of optical microscopy and very small angle neutron scattering, is related to the hydration properties of the chains, measured with Raman spectroscopy. A part of this chapter was previously published in B.-J. Niebuur et al., *ACS Macro Lett.*, 6:1180-1185, 2017 [131].

## 6.1  Introduction

This chapter focuses on the characterization of the two-phase state under equilibrium conditions. It is aimed to identify the varying molecular interactions with pressure, as followed from the thermodynamic approach (Chapter 5), and its effect on the structural properties of aqueous PNIPAM solutions. While the structure of the two-phase state of PNIPAM homopolymers was already investigated extensively at atmospheric pressure [26, 27, 28, 29, 30], knowledge about the structure in the two-phase state at high pressure is lacking.

As described in Chapter 3, it was shown that, at atmospheric pressure, stable mesoglobules with sizes in the order of ∼100 nm are formed in the two-phase state. Their stability may be due to the visco-elastic effect, resulting from the strong dehydration of the chains. High pressure enhances hydrophobic hydration, as previously determined using FT-IR spectroscopy [32]. It can be expected that pressure also strongly influences the structure of the solution in the two-phase state. The aim of this work is to elucidate the relation between the hydration state of the chains in the two-phase state and the size and structure of the mesoglobules in a semi-dilute PNIPAM solution. At this, a combination of experimental

methods is used. Optical microscopy allows for an initial characterization of the two-phase state. Subsequently, very small angle neutron scattering (VSANS) is applied to determine the structure of the investigated PNIPAM solution in the two-phase state, which allows the investigation of length scales between ~100 nm and ~5 $\mu$m. As shown below, this range is suitable to characterize the structure of the system at both atmospheric pressure and at high pressure. Complementary, Raman spectroscopy is used to investigate the PNIPAM-water interaction. Combining these methods, the hydration state of PNIPAM can be related to the structure of the two-phase state.

After an initial characterization of the structure using optical microscopy, both Raman spectroscopy and VSANS measurements are performed during heating scans at 0.1, 80 and 113 MPa, which allows for a comparison of phase separation induced by temperature at different pressures.

## 6.2    Experimental details

**Materials.**    Poly($N$-isopropylacrylamide) (PNIPAM) with a molar mass $M_n = 36\ 000$ g mol$^{-1}$ and a dispersity of 1.26 (end groups carboxylic acid and a hydrogen atom, respectively) was purchased from Sigma-Aldrich. It was dissolved at a concentration of 3 wt% in D$_2$O, which is above the overlap concentration. D$_2$O was used to ensure a maximum contrast between water-rich and polymer-rich phases in VSANS measurements and to avoid overlap of the contributions from the stretching vibrations of the C$\cdots$H groups and those of water in Raman spectroscopy measurements.

**Optical microscopy.**    For optical microscopy, an Olympus X41 microscope in combination with a CCD camera was used. The used sample environment is based on previously reported systems [205]: The sample was mounted in a fused silica micro capillary with a squared cross section with inner and outer side lengths of 75 and 350 $\mu$m, respectively. One side of the micro capillary was connected to a pressure generator from High Pressure Equipment Company (Erie, Pennsylvania, U.S.A.). The other side of the capillary was sealed by melting the fused silica, and was capable of withstanding pressures up to 300 MPa. The sample and the pressure medium (ethanol) were not separated. However, the length of the micro capillary (~30 cm) prevented mixing of both liquids at the probed spot for at least the duration of the experiment. The micro capillary was placed between two copper blocks to ensure good thermal contact. The temperature of the setup was controlled using a circulating

bath thermostat. A Pt100 resistance thermometer attached close to the micro capillary at the probed spot was used to determine the temperature. The temperature was calibrated afterwards to determine its value at the position of the sample.

**Very small angle neutron scattering.** Very small angle neutron scattering (VSANS) measurement were performed at the instrument KWS-3 at the Heinz Maier-Leibnitz Zentrum, Garching, Germany [165]. Using a neutron wavelength $\lambda = 1.28$ nm with a spread $\Delta\lambda/\lambda = 0.18$ and a sample-detector distance of 9.4 m, a $q$ range of $2.1\times10^{-3}$ - $2.3\times10^{-2}$ nm$^{-1}$ is covered. The sample was mounted in a temperature-controlled custom-made pressure cell based on the one described in ref. [206], which is capable of withstanding pressures up to 500 MPa. The sample was placed between sapphire windows and had a thickness of 2 mm, independent of pressure. After each change in temperature or pressure, the sample was equilibrated for 5 min, followed by at least 3 measurements of 5 min. The data reduction was performed as described in Section 4.2.2, with a measurement of plexiglass to determine the detector sensitivity.

**Raman spectropscopy.** Raman spectroscopy was performed using the same pressure system as for optical microscopy. A LabRam Hr 800 system from JY Horiba (Kyoto, Japan) in combination with a frequency-doubled Nd:YAG laser with a wavelength of 532 nm was used, resulting in a spectral resolution of 2 cm$^{-1}$. The laser beam was focused on the sample with a spot size of $\sim$1.5 $\mu$m with a power of less than 3 mW. Raman spectra were acquired with an integration time of 5 min, following an equilibration time of 10 min after each change of temperature or pressure. A dark current measurement was subtracted from the data.

## 6.3 First structural insights by optical microscopy

Optical microscopy was applied to observe the domains in real space. According to equation 4.39, the minimum distance between two resolvable points for the used experimental set-up is around 400 nm, sufficiently small to obtain detailed images of the structure. Figure 6.1 displays optical images of the solution below $T_{cp}$ at 0.1 MPa, i.e., in the one-phase state, and of the structures formed at 0.1 MPa and 114 MPa just after heating to approximately 2 K above $T_{cp}(p)$. At atmospheric pressure below $T_{cp}$ (Figure 6.1a), the chains are soluble, thus, the solution has a transparent appearance. Above $T_{cp}$ (Figure 6.1b and c), however, the images provide clear evidence of the presence of mesoglobules. Although the shape of the mesoglobules cannot be resolved in detail at atmospheric pressure, it is obvious

that a binary structure is formed at atmospheric pressure as well as at higher pressures with typical length scales of around 1 $\mu$m at 0.1 MPa and around 5 $\mu$m at 114 MPa. Thus, high pressure leads to larger sizes of the mesoglobules. As their shape and composition cannot be determined with optical microscopy, Raman spectroscopy and VSANS are applied to determine their composition and structure.
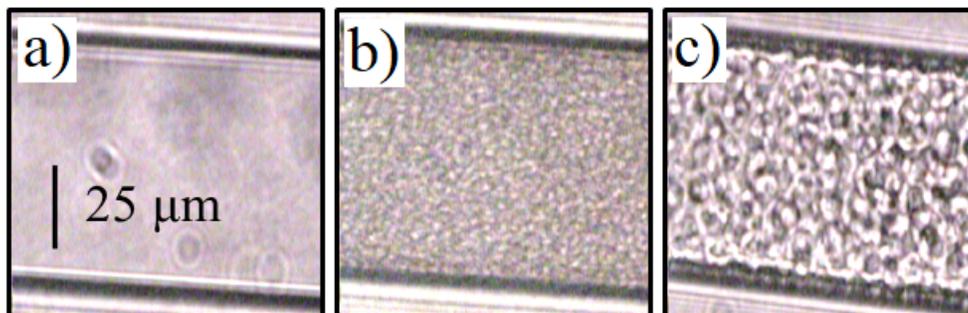


Figure 6.1: Optical images in the two-phase state of PNIPAM at 0.1 MPa below $T_{cp}(p)$ (a), and at 0.1 MPa (b) and 114 MPa (c) at approximately 2 K above $T_{cp}(p)$. Reprinted with permission from [131]. Copyright (2019) American Chemical Society.

## 6.4   Investigation on hydrophobic hydration

The interactions on a molecular level are investigated using Raman spectroscopy. In this work, the CH-stretching region is in focus, which gives insights into the hydrophobic hydration of the backbone and of the side groups of PNIPAM. In Figure 6.2, the Raman spectra at the CH-stretching region in dependence on temperature at 0.1 MPa (a), 79 MPa (b) and 114 MPa (c) are presented. Four pronounced peaks are present in this region, which can be assigned to symmetric CH$_3$ stretching in the side groups ($\nu_s(\text{CH}_3)$), CH stretching ($\nu(\text{CH})$), antisymmetric CH$_2$ stretching at the backbone ($\nu_{as}(\text{CH}_2)$), and antisymmetric CH$_3$ stretching in the side groups ($\nu_{as}(\text{CH}_3)$) at around 2884, 2923, 2947 and 2990 cm$^{-1}$, respectively [116, 207, 208].

The spectra taken at atmospheric pressure change visibly with increasing temperature. Above $T_{cp}$ (between 36.4 and 38.4 °C), a sharp decrease in the peak frequencies of the $\nu_s(\text{CH}_3)$ and $\nu_{as}(\text{CH}_3)$ modes is visible, pointing to a change in the hydration of the side groups. Furthermore, the contribution from the $\nu_{as}(\text{CH}_2)$ band decreases in intensity. At both 79 and 114 MPa, the changes in the spectra at $T_{cp}$ are less pronounced, but also in this case, a decrease in the peak frequency of the $\nu_s(\text{CH}_3)$ and $\nu_{as}(\text{CH}_3)$ modes is discernible.
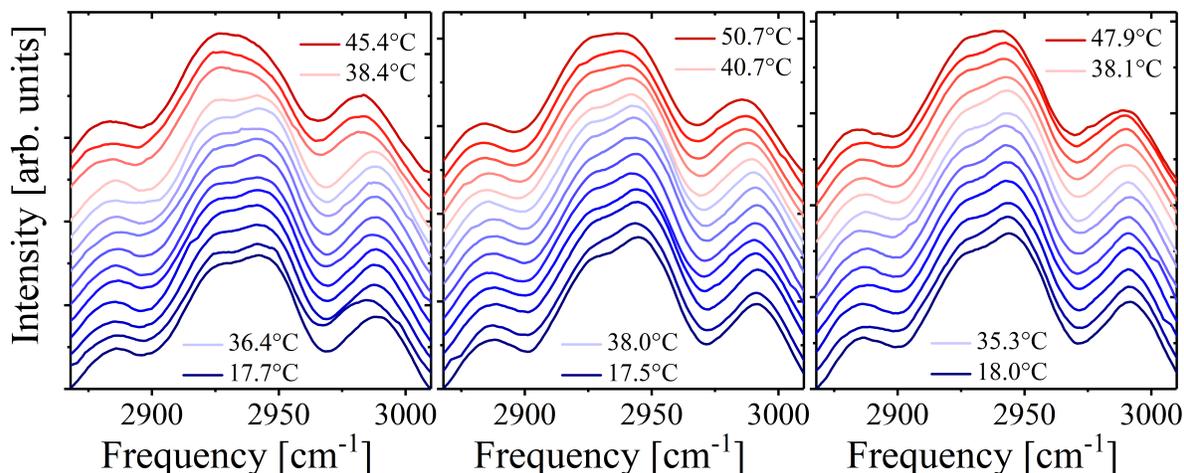
Figure 6.2: Raman spectra in the CH stretching region in dependence on temperature at 0.1 MPa (left panel), 79 MPa (middle panel) and 114 MPa (right panel). Spectra taken in the one-phase state are given in blue, spectra taken in the two-phase state in red. The measured start- and end-temperatures of both states are given in each graph. For clarity, the curves are shifted in intensity and smoothed using the Savitzky-Golay algorithm.

These are, however, much weaker than at atmospheric pressure.

Curve fitting can be applied for a precise determination of the peak frequencies. At this, the spectra are fitted by a series of four Lorentzian functions (equation 4.50) and a constant background, i.e., it is assumed that only natural broadening plays a role. Figure 6.3 displays examples of the deconvolution of the Raman spectra at the highest temperatures measured at 0.1 MPa and 114 MPa. In all cases, excellent fits are obtained.
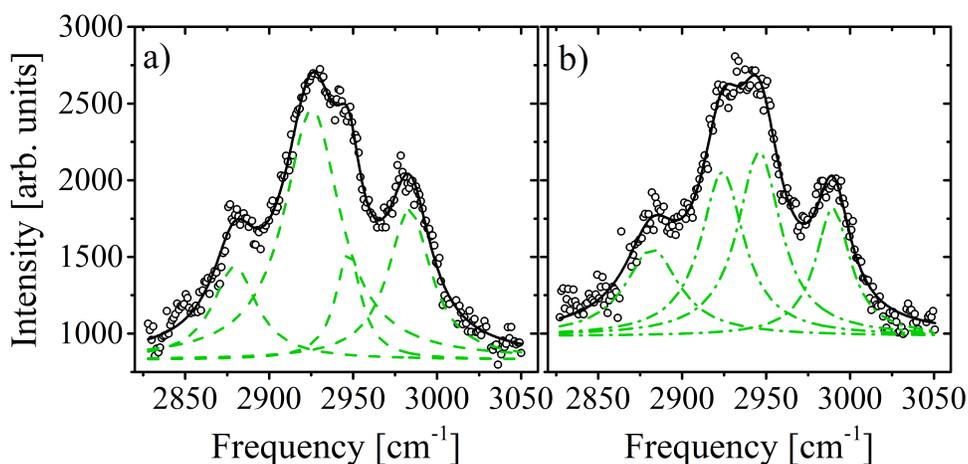


Figure 6.3: Deconvolution of Raman spectra at 0.1 MPa and 45.4 °C (a), and at 114 MPa and 47.9 °C (b). Open circles: reduced data, black lines: cumulative fits, and green dashed lines: individual contributions (for details, see text).

Figure 6.4 displays the stretching frequencies of the $\nu_{as}(CH_3)$ and $\nu_{as}(CH_2)$ modes, which provide information about the interaction of the side groups and backbone with water, respectively. As CH groups are present at the backbone as well as in the side groups of PNIPAM, the $\nu(CH)$ cannot be used to obtain unambiguous information about either of both, and is therefore not discussed further. The peak frequencies of the $\nu_{as}(CH_3)$ mode at atmospheric pressure (Figure 6.4a) confirm the first observations from the spectra. Below the cloud point, determined by in-situ optical microscopy measurements, $\nu_{as}(CH_3)$ stays constant at $\sim2989$ cm$^{-1}$. At $T_{cp}$, a sharp red-shift in $\nu_{as}(CH_3)$ to $\sim2984$ cm$^{-1}$ is observed, after which it remains constant.
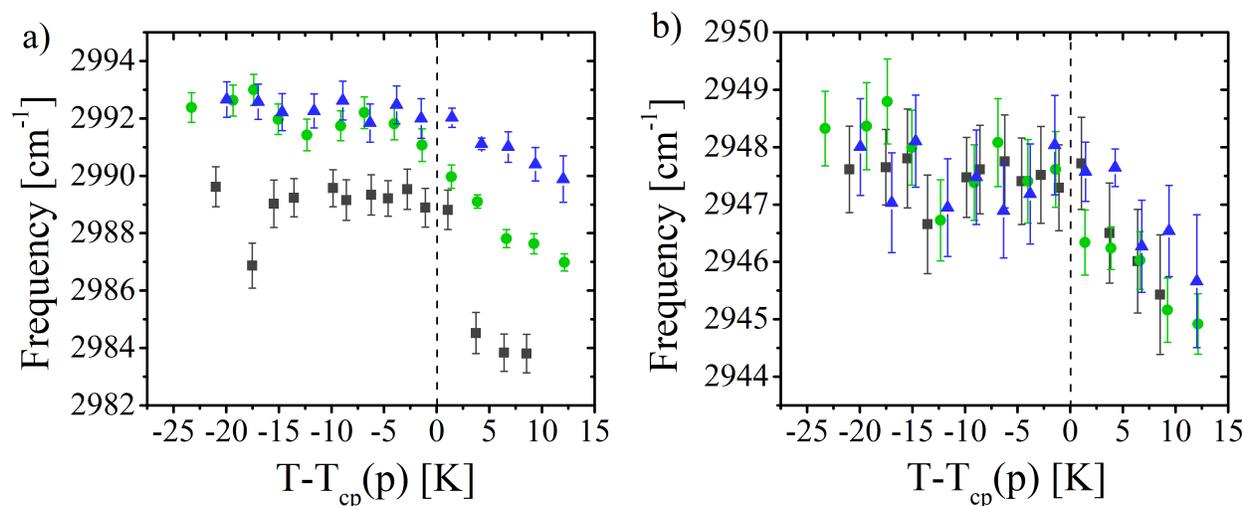


Figure 6.4: Peak frequencies $\nu_{as}(CH_3)$ (a) and $\nu_{as}(CH_2)$ (b) of the 3 wt% PNIPAM solution in D$_2$O at 0.1 MPa (black squares), 79 MPa (green circles) and 114 MPa (blue triangles), in dependence on the temperature distance from the cloud point.

This shift in frequency is due to the changes in the interaction of the methyl group with water by means of hydrogen bonds. The frequency at which a certain chemical bond vibrates is mainly determined by its length. The effect of a hydrogen bond on the length of a chemical bond in the system $X — H \cdots Y$ is well investigated for a wide variety of molecules, in particular for the hydrogen bond formation of a molecule with water [209, 210]. In general, the literature distinguishes two kinds of hydrogen bonds between H and Y. Firstly, proper hydrogen bonds lead to an elongation of the X—H bond, and secondly, improper hydrogen bonds lead to a contraction of the X—H bond [209, 211]. This distinction is caused by two effects: lengthening of the $X — H$ due to attractive interaction between H and Y, and shortening of the $X — H$ bond by the net electron density gain between X and H. The relative importance of both effects determines the properness of the formed hydrogen bond [211].

Hydrogen bonds formed between C-H and water are usually improper [209, 212, 213]. The red-shift of the $\nu_{as}(CH_3)$ mode observed is therefore a result of the dehydration of the $CH_3$ groups, as observed earlier [116, 214]. At 79 and 114 MPa below $T_{cp}$, the frequency is significantly larger than at 0.1 MPa, pointing to a stronger hydration of $CH_3$ groups in the one-phase state. Also at $T_{cp}$ at both 79 and 114 MPa, a red-shift of the $\nu_{as}(CH_3)$ mode is observed. However, the magnitude of the decrease is smaller than at 0.1 MPa and the changes occur gradually. Although dehydration of the $CH_3$ takes place at high pressure, it is significantly weaker than at atmospheric pressure, i.e., the hydrophobic moieties in the side groups remain partially hydrated in the two-phase state. Furthermore, the dehydration is weaker at 114 MPa than at 79 MPa. In previous work, Meersman et al. [32] found similar results by comparing the hydration properties of PNIPAM during a temperature scan at atmospheric pressure and a pressure scan. Whereas a strong dehydration of the $CH_3$ groups was found upon heating through the cloud point at atmospheric pressure, the degree of hydration increases with pressure at constant temperature, both in the one-phase and in the two-phase state.

The frequency of the $\nu_{as}(CH_2)$ mode, shown in Figure 6.4b, does not depend on pressure. At all measured pressures, a constant value of $\sim 2947\,cm^{-1}$ is observed below $T_{cp}$. Above, the frequency decreases slightly for all pressures. Therefore, dehydration of the backbone occurs at all investigated pressures above $T_{cp}$. Contrary to the findings of the dehydration of the side groups, no significant differences between the three investigated pressures are observed, but the uncertainties are large.

## 6.5   Characterization of mesoglobule structure

To investigate the structural properties in more detail, VSANS is chosen because it allows the characterization of the size and shape of particles in the $\mu$m size range. Using a $q$ range of $2\times10^{-4}$ - $2\times10^{-3}$Å$^{-1}$, length scales of sub $\mu$m to several $\mu$m are probed. The scattering intensity $I(q)$ is presented in Figure 6.5 for 0.1 (a), 80 (b) and 113 MPa (c) in dependence on temperature. The appearance of the scattering curves confirm the first insights from optical microscopy. Whereas below $T_{cp}(p)$ at atmospheric pressure, the scattering is very weak, a clear shoulder is present above, which shows the presence of finite-sized clusters in the two-phase state. With temperature, the intensity of the shoulder increases, but does not change

notably in position. At high pressure, shown in Figure 6.5b and c for 80 MPa and 113 MPa, respectively, a shoulder is present as well, but it is shifted to lower $q$ values with respect to the shoulder present in the scattering curves at atmospheric pressure. This result shows that the typical lengths are significantly larger at high pressure than at atmospheric pressure.
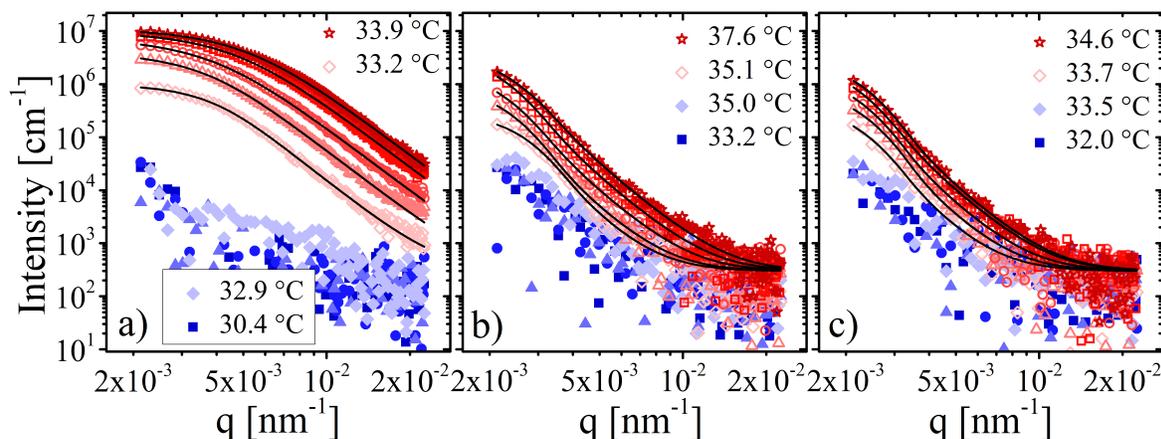


Figure 6.5: Scattering curves from VSANS measurements at 0.1 (a), 80 (b) and 113 MPa (c) in dependence on temperature. Blue curves: below $T_{cp}(p)$, red curves: above $T_{cp}(p)$. Black lines: fits of equation 6.1. See the text for details.

To extract quantitative information, the scattering curves were modeled by

$$I(q) = I_{Beaucage}(q) + I_{bkg} \tag{6.1}$$

where $I_{Beaucage}(q)$ is the Beaucage model, given by equation 4.29. $I_{bkg}$ is an incoherent background, which was fixed at a value of 300 cm$^{-1}$ in all cases. The Beaucage model gives the radius of gyration $R_g$ of the mesoglobules as well as their Porod exponent $m$. From optical images, weak correlation is expected at high pressure (Figure 6.1), but the used $q$ range for these VSANS measurements does not allow its characterization. In addition, a contribution from chain scattering may be present in the one-phase state [121]. However, it is too weak to be detected due to the strong background scattering and the noisy data. In the two-phase state, the Beaucage model is able to reconstruct the obtained data excellently (Figure 6.5).

Figure 6.6 displays the resulting fit parameters. As was already apparent from the scattering curves, $R_g$ of the mesoglobules, shown in Figure 6.6a, increases with pressure. At atmospheric pressure, the maximum value is ~0.5 $\mu$m, whereas at 80 and 113 MPA, it is ~1.5 $\mu$m. Furthermore, a temperature dependence is observed for both pressure regimes. At 0.1 MPa as well as at 80 MPa, $R_g$ increases directly after the phase separation starts and

reaches a maximum at around $T_{cp}(p)$ + 0.5 K. At higher temperatures, $R_g$ again decreases and reaches a stable value at $T_{cp}(p)$ + 2 K at 0.1 MPa and $T_{cp}(p)$ + 1 K at 80 MPa. Also at 113 MPa, a shallow maximum in $R_g$ may be present, but the covered temperature range is too small for conclusive statements. The multiple values of $R_g$ given for each temperature and pressure result from fits to the different VSANS measurements after each increase in temperature. The observed differences may be due to non-equilibrium effects in the sample. At all measured pressures, $R_g$ remains constant at later times, and kinetic stability of the mesoglobules is therefore reached in all cases.
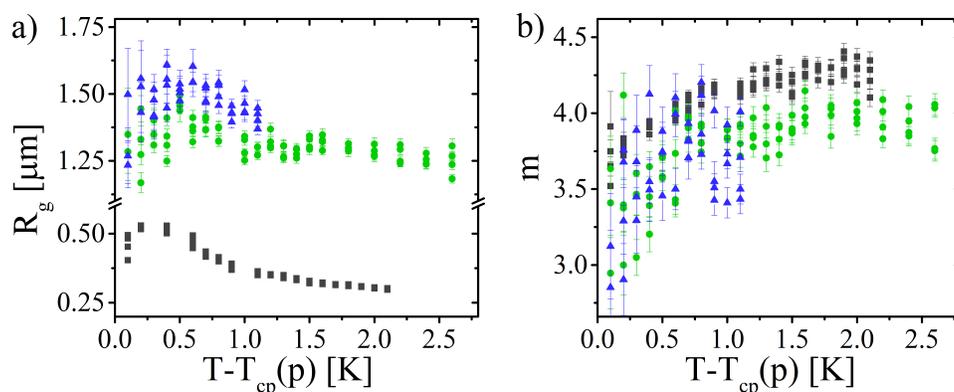


Figure 6.6: Radius of gyration $R_g$, (a) and Porod exponent $m$, (b) in dependence on temperature at 0.1 MPa (grey squares), 80 MPa (green circles) and 113 MPa (blue triangles).

The Porod exponent (Figure 6.6b) gives insights into the surface structure of the mesoglobules. At atmospheric pressure, a weak increase of $m$ from ∼3.7 to ∼4.2 is observed. As discussed in Section 4.2, a value of $m$ below 4 points to a certain surface roughness of the mesoglobules, whereas values above 4 indicate the presence of a concentration gradient perpendicular to the surface. Therefore, the surface of the mesoglobules changes from rough directly after their formation, to smooth with a concentration gradient at higher temperatures. From this analysis, it is not possible to determine the direction of the concentration gradient. However, it is physically unlikely that the water content increases towards the surfaces of the mesoglobules, since, in this case, the chains at the surface would be in a swollen conformation. Thus, the mesoglobules presumably consist of a polymer-rich outer layer consisting of dehydrated chains that capture the water molecules inside. The dense polymeric shell may be the origin of the stability of the mesoglobules. Merging of two mesoglobules is prevented by the visco-elastic effect, described in Section 2.1.3, which is a result of the low mobility of the strongly dehydrated chains at the mesoglobule surface.

At high pressure, a different behavior is observed. At 80 MPa, $m$ increases with temperature only slightly from ~3.5 to ~3.9, whereas at 113 MPa, it is approximately constant at ~3.7. I can be concluded that the mesoglobules are initially rough at high pressure, but become smoother with increasing temperature. As shown using Raman spectroscopy, the chains remain more hydrated at high pressure than at atmospheric pressure. Therefore, a dense polymeric shell is presumably not formed, which leads to a homogeneous structure of the mesoglobules and possibly the large mesoglobule size. The mechanism preventing further aggregation after the mesoglobule formation at high pressure remains, however, unclear.

The overall composition of the mesoglobules can be characterized by considering the invariant scattering $Q^*$ [215]. It relates the total scattering by the sample to the scattering contrast, and thus to the composition of different phases in the system. $Q^*$ can be determined from the scattering curve by integrating the intensity over the entire $q$ range as

$$Q^* = \int_0^\infty I(q)q^2 \mathrm{d}q \tag{6.2}$$

Since the $q$ range of the performed experiment is limited, the Beaucage model with the obtained fit parameters is integrated according to equation 6.2. This is, however, only an approximation. From previous studies, it is expected that the scattering from smaller structures present in the sample also contributes to the total scattering, however, this contribution is relatively small [77, 121].

Figure 6.7 displays $Q^*$ for the three measured pressures in dependence on temperature above the cloud point. For all pressures, $Q^*$ increases significantly with temperature up to $T_{cp} + 1$ K. Furthermore, at atmospheric pressure, $Q^*$ is a factor of ~100 larger than at high pressure. The invariant scattering is not related to the structure itself, but only to the volume fraction of the different phases and their differences in scattering length density, and is given by

$$Q^* = 2\pi\phi(1 - \phi)(\Delta\rho)^2 \tag{6.3}$$

with $\phi$ the volume fraction of the polymer-rich phase and $\Delta\rho$ the difference in scattering length densities between the two phases. From the optical microscopy images at 0.1 MPa and at 114 MPa (Figure 6.1), it is observed that both the water-rich and the polymer-rich phases are present in significant volume at both pressures, i.e., $\phi$ changes only slightly with pressure. Thus, the difference in scattering length densities of both phases is mainly responsible for the dependence of $Q^*$ on pressure, and therefore their composition. Since $Q^*$

adopts much lower values at high pressure, phase separation is weaker at high pressure than at low pressure, which implies water-rich mesoglobules or a polymer-rich solvent. In case of water-rich mesoglobules, the mesoglobules are less dense and occupy therefore a larger volume fraction in the sample. This is consistent with the observed differences in domain size in dependence on pressure. Because no significant differences in volume fraction of the two phases are seen in the optical images, it follows that the solvent-rich phase also contains a significant amount of polymer.
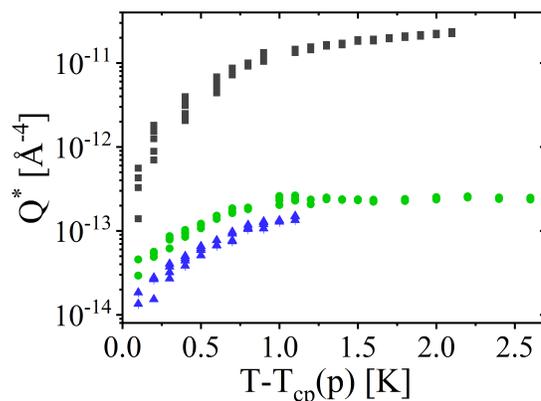


Figure 6.7: Invariant scattering $Q^*$, determined according to equation 6.3, in dependence on temperature at 0.1 MPa (grey squares), 80 MPa (green circles) and 113 MPa (blue triangles).

The increasing trend of $Q^*$ up to temperatures of $T_{cp}(p) + 1$ K at all measured pressures shows that phase separation continues at these temperatures. The maximum in $R_g$ during this stage at atmospheric pressure (Figure 6.6a) can therefore be explained as follows: The initial increase in mesoglobule size is due to their formation. Mesoglobule stability is reached at $T_{cp}(p) + 0.5$ K, where $R_g$ shows a maximum value. The increase in $Q^*$ in this temperature range suggests, however, that phase separation continues. It can be concluded that water leaves the mesoglobules, resulting in a decrease in $R_g$ until a stable value is reached. Due to the dense polymeric shell of the mesoglobules, as followed from the behavior of $m$, this process is presumably due to the slow diffusion of water molecules through the shell. At high pressure, a similar process occurs, but is much less pronounced than at atmospheric pressure.

The profound differences between the structure of the two-phase state at atmospheric and at high pressure, and the similarities between the measurements at 80 and 113 MPa, raises the question if the transition between the both structures follows a continuous trend with changing pressure or is a sharp one. To investigate this, VSANS is applied during pressure scans at different temperatures in the two-phase state, extensively described in

Appendix 13.1. In summary, a sharp transition from a state containing small mesoglobules at low pressure to a state with large clusters of mesoglobules at high pressure is present. At 38 °C, the transition pressure is located at ∼35 MPa, and shifts to higher pressures with temperature. Thus, with these measurements, an additional branch in the phase diagram of aqueous PNIPAM solutions in the temperature-pressure frame is constructed.

## 6.6    Conclusions

In this chapter, the relationship between chain hydration and the structure of a 3 wt % PNIPAM solution is investigated in dependence on pressure during heating scans at atmospheric pressure and high pressures of ∼80 and ∼114 MPa. Using Raman spectroscopy, it was found that pressure strongly influences the hydration state of PNIPAM. At atmospheric pressure, the PNIPAM side groups sharply dehydrate upon heating through the cloud point. At high pressure, however, the chains also dehydrate, but the dehydration was found to be significantly weaker and more gradual. Also the backbone of PNIPAM dehydrates in the two-phase state. Its hydration properties were found to be pressure-independent: At all measured pressures, the backbone in the two-phase state dehydrates to a similar degree.
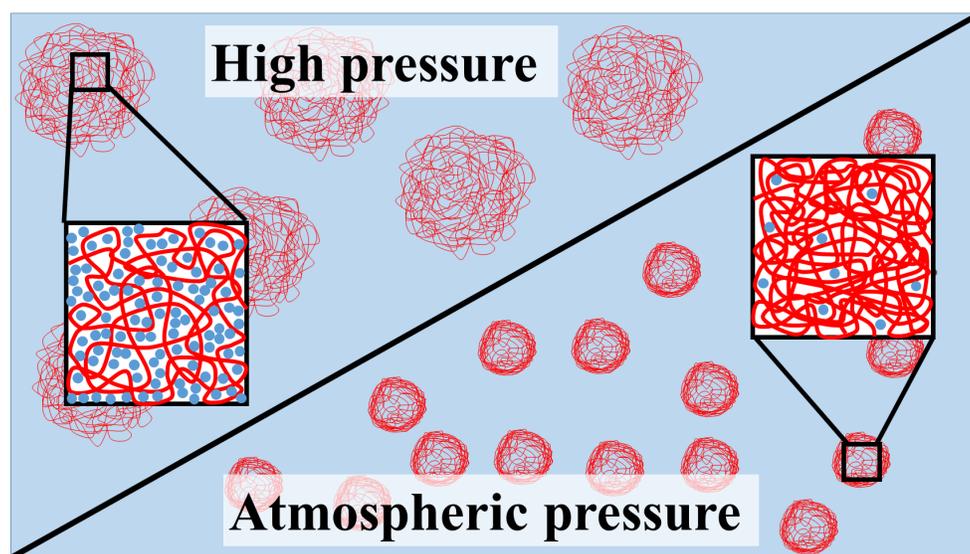


Figure 6.8:   Sketch of the structure in the two-phase state at atmospheric and at high pressure.

In Figure 6.8, the results from the structural investigations using optical microscopy and very small angle neutron scattering are summarized. At both low and high pressures, heating through the cloud point leads to phase separation in the system. Whereas the solution

is optically transparent below $T_{cp}$, particles consisting of both PNIPAM and water, termed mesoglobules, are formed above. The size, composition and structure depend strongly on pressure. At atmospheric pressure, the mesoglobules are small and consist of a polymer-rich outer shell, which traps water molecules inside the mesoglobules. It was argued that the low mobility of the strongly dehydrated chains at the outer shell are mainly responsible for the stability and the small size of the mesoglobules. At high pressure, the mesoglobules are large and contain a large amount of water. Because the chains only weakly dehydrate in this case, no dense outer shell is formed, which may be the reason for the larger size of the mesoglobules at high pressure.

The results state the importance of the hydration properties of PNIPAM for its structure in aqueous solutions. In the next chapter, quasi-elastic neutron scattering is applied for an in-depth study of hydration water at different pressures. In addition, the strong differences between the mesoglobules at low and high pressure point to a fundamentally different growth process. To investigate this further, time-resolved small-angle neutron scattering was applied, presented Chapter 8.

# Chapter 7. Water dynamics in purely aqueous PNIPAM solutions

In this chapter, the role of water during temperature-induced phase separation of a concentrated aqueous PNIPAM solution is investigated. At this, quasi-elastic neutron scattering experiments are performed during heating scans at low and high pressure. The work presented in this chapter was previously published in B.-J. Niebuur et al., *Macromolecules*, 52:1942-1954, 2019 [216].

## 7.1  Introduction

The significant differences in size and water content between mesoglobules formed at low and high pressure, as shown in Chapter 6, suggest that the interaction between PNIPAM and water during phase separation depends strongly on pressure. In addition to the structural study presented in the previous chapter, the dynamics of water during the phase transition is investigated in dependence on pressure to obtain a comprehensive picture of the phase separation mechanism at different pressures.

Information about both the temporal and spatial variations during the diffusion of water molecules is required to determine its dynamic behavior. Therefore, quasi-elastic neutron scattering (QENS) is the method of choice to investigate water during the phase transition of PNIPAM solutions. In previous work, QENS was employed to investigate the phase transition at atmospheric pressure [217]. By separating the contributions from bulk water and hydration water, i.e., water that is bound to the chains to some degree, it was shown that hydration water diffuses ∼2 times slower than bulk water. Similar to bulk water, it follows the jump-diffusion mechanism, which means that the diffusion of the water molecules on the chains is not continuous but occurs via discrete jumps. Starting at the phase transition temperature, hydration water is released over a temperature range of ∼6 K. However, a

significant fraction of slow water molecules persists, even deep in the two-phase state. A high-pressure study using QENS on an aqueous PNIPAM solution revealed that pressure weakens the hydrogen bonding between PNIPAM and water in the one-phase state [129]. Furthermore, the temperature range in which phase separation takes place was found to be broadened at high pressure, but the restricted ranges in both energy and momentum transfer in this study made it impossible to differentiate hydration water and bulk water, i.e., the dynamic properties of hydration water could not be determined.

In this chapter, QENS is applied in wide ranges of energy and momentum transfer, which allows an unambiguous description of the dynamic properties of hydration water. The results provide new insights in the interaction between water and PNIPAM, and therefore in the role of water during the phase transition at different pressures. A concentrated aqueous PNIPAM solution is measured during heating scans at 0.1 and 130 MPa to investigate the water dynamics around the phase transition at low and high pressures. For an unambiguous description of the data, pure water is measured at both pressures at selected temperatures.

## 7.2    Experimental details

**Materials.**    Poly($N$-isopropylacrylamide) (PNIPAM) with a molar mass $M_n = 36\,000$ g mol$^{-1}$ and a dispersity of 1.26 (end groups carboxylic acid and a hydrogen atom, respectively) was purchased from Sigma-Aldrich. It was dissolved at a concentration of 25 wt% in H$_2$O. H$_2$O was used as the solvent to maximize the incoherent scattering from water in the system to probe the motion of single water molecules. The cloud points of this sample at 0.1 and 130 MPa are 31.4 $\pm$ 0.1 and 34.1 $\pm$ 0.1 °C, respectively, measured with turbidimetry (see Appendix 13.2 for more details). From the composition of the sample and the scattering cross sections of the present elements [183], it follows that 74 % of the measured neutrons are incoherently scattered by water molecules (see Appendix 13.3).

**Quasi-elastic neutron scattering.**    Quasi-elastic neutron scattering (QENS) measurements were performed at the instrument TOFTOF at the FRM II, Garching, Germany. An incident neutron beam with a wavelength $\lambda = 6$ Å$^{-1}$ was used with a chopper rotation speed of 14 000 rpm, resulting in an energy resolution of $\sim$0.03 meV.

The sample was mounted in a flat aluminum (EN AW-7075) pressure cell with a thickness

of 5 mm [218]. Inside the cell, the sample is located in 10 parallel channels with a diameter of 1.6 mm which a maximum pressure of 200 MPa can be applied to. A membrane, placed between the pressure cell and the pressure generator, prevents mixing of the sample and the pressure transmitting medium ($D_2O$). The temperature of the pressure cell was controlled using a circulating bath thermostat, which heats the pressure cell at one side. The temperature of the pressure cell was measured using a Pt100 resistance thermometer attached close to the sample location. As the geometry of the pressure cell did not allow a proper insulation, the temperature was calibrated afterwards to determine the temperature at the position of the sample. The pressure cell was positioned at an angle of 135° with respect to the incident neutron beam, resulting in an accessible $q$ range of 0.1-1.7 Å$^{-1}$. The sample was measured during heating scans at 0.1 and 130 MPa with an integration time of 120 min at each temperature, following an equilibration time of 30 min after each temperature change. In addition, pure water was measured at both pressures at selected temperatures. The empty cell and a thin vanadium slab were measured as a reference.

The data reduction is performed as described in Section 4.3.2. The self-shielding factor due to the pressure cell geometry is estimated using the measurement of pure water. Since elastic scattering is not expected in pure water, the entire elastic signal that is measured originates from scattering of neutrons at the pressure cell, which allows for an estimation of the self-shielding factor.

## 7.3 Dynamic properties of pure water

For an unambiguous description of the dynamic properties of PNIPAM solutions, the dynamics of pure $H_2O$ at atmospheric and high pressure was measured. Figure 7.1 displays the dynamic structure factor $S(q, \Delta E)$ of water at 27.2 and 55.2 °C at both 0.1 and 130 MPa, together with $S(q, \Delta E)$ of vanadium. At all conditions, $S(q, \Delta E)$ of water is much broader than that of vanadium, i.e., a quasi-elastic signal centered at $\Delta E = 0$ is observed. Thus, with the settings chosen, the dynamic processes in pure water can be resolved. At 0.1 MPa (Figure 7.1a), broadening of the signal is observed at 55.2 °C, therefore, the motion of the water molecules is faster. Also at 130 MPa (Figure 7.1b), a broadening is observed, but appears weaker than at 0.1 MPa.
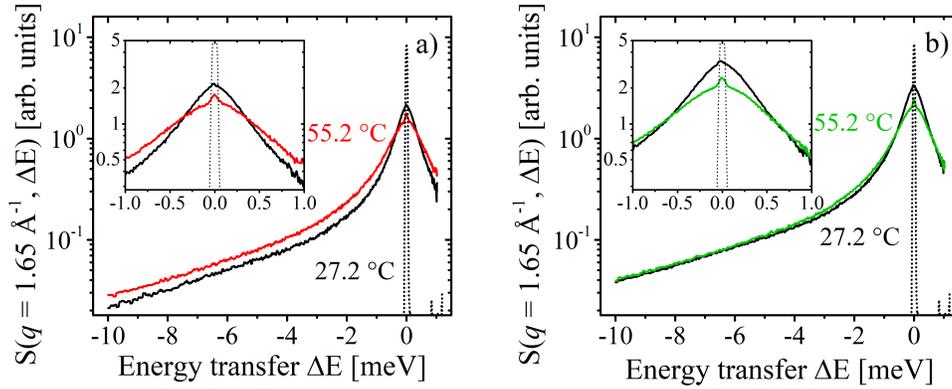
Figure 7.1:  Dynamic structure factors $S(q, \Delta E)$ of pure $H_2O$ at $q = 1.65$ Å$^{-1}$ and 0.1 MPa (a) and 130 MPa (b) at several temperatures, as depicted in the graphs. Black dashed lines: elastic line from the measurement on vanadium. The insets show $S(q, \Delta E)$ at small values of $\Delta E$.

## 7.3.1   Data analysis

For a better discrimination between different dynamic processes, $S(q, \Delta E)$ is transformed into the imaginary part of the dynamic susceptibility $\chi''(q, \nu)$. In this representation, the dynamic process of hydration water can be more easily distinguished from each other. Furthermore, the elastic contribution is suppressed, i.e., the quasi-elastic and inelastic regions are emphasized. As described in Section 4.1.6, $\chi''(q, \nu)$ is determined from $S(q, \Delta E)$ via the fluctuation-dissipation theorem. The present measurements were performed on the energy-loss side of the spectrum. In this case, equation 4.22 can be transformed to

$$\chi''(q, \nu) \propto \frac{S(q, -\nu)}{n_B(\nu)} \tag{7.1}$$

with $n_B(\nu)$ the Bose occupation factor, given by equation 4.23, and $\nu$ the frequency, which relates to the energy transfer as $\Delta E = h\nu$.

In Figure 7.2, $\chi''(q, \nu)$ is exemplarily presented at 27.2 and 55.2 °C at both 0.1 and 130 MPa. Consistent with recent work by Arbe et al. [219] at ambient pressure, three relaxation processes in pure water are observable with neutron scattering in the frequency range from 1 to $\sim$5 GHz: a diffusional process $(d)$ at low frequencies, an effective local process $(l)$ at intermediate frequencies, and a vibrational process $(v)$ at high frequencies. The susceptibility spectra of pure water are therefore modeled by

$$\chi''(q, \nu) = \chi''_d(q, \nu) + \chi''_l(q, \nu) + \chi''_v(q, \nu) \tag{7.2}$$

Both the diffusional process and the effective local process are modeled with Debye functions, given by [220]

$$\chi_j''(q,\nu) = -\text{Im}\left[ C_j(q) \frac{1}{1 + 2\pi i \tau_j(q)\nu} \right] \tag{7.3}$$

with $C_j(q)$ a $q$-dependent scaling factor, $\tau_j(q)$ a $q$-dependent relaxation time, and the index $j$ standing for $d$ or $l$. The Debye function corresponds to a Lorentzian function in the $S(q, \Delta E)$ representation (equation 4.36) and implies dynamic homogeneity. For the vibrational process, a damped harmonic oscillator (DHO) is used (equation 4.37), which is in the $\chi''(q,\nu)$ representation given by [180, 221]

$$\chi_v''(q,\nu) = -\text{Im}\left[ C_v(q)\nu_0^2 \frac{1}{\nu^2 - \nu_0^2 - (i\nu\Gamma/2\pi)} \right] \tag{7.4}$$

with $C_v(q)$ a $q$-dependent scaling factor, $\nu_0$ the peak frequency and $\Gamma$ the FWHM of the peak. This process was previously assigned to intermolecular O–O–O bending in the hydrogen bond network, and therefore reflects its stiffness [222, 223, 224, 225]. As this mode is a localized process, both $\nu_0$ and $\Gamma$ are assumed to be independent of $q$. Average values from the measurements at 1.45 Å$^{-1}$, 1.55 Å$^{-1}$ and 1.65 Å$^{-1}$ are kept fixed during the fits at the other $q$ values.
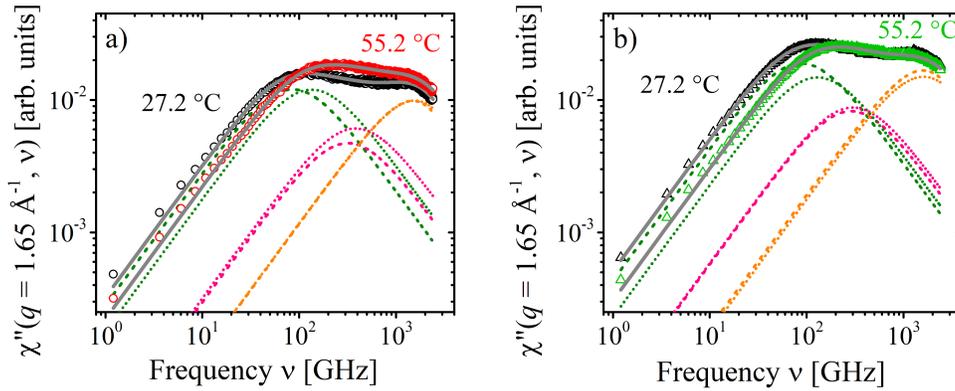


Figure 7.2: Imaginary part of the dynamic susceptibility $\chi''(q,\nu)$ of pure H$_2$O, determined according to equation 7.1, at 0.1 MPa (a) and 130 MPa (b). The temperatures are given in the graphs. Also shown are fits of equation 7.2 (grey lines) and their individual contributions: diffusion process $d$ (olive lines), local process $l$ (pink lines) and the vibrational process $v$ (orange lines) at 27.2 °C (dashed lines) and 55.2 °C (dotted lines).

## 7.3.2   Results

Fits of the spectra using equation 7.2 are also given in Figure 7.2. Whereas the effective local process and the vibrational process change position only slightly with temperature, a

significant increase in the peak frequency with increasing temperature is observed for the dif-
fusion process at both pressures. Thus, the diffusion of water molecules becomes faster with
increasing temperature, as expected. No significant differences in the susceptibility spectra
are observed between the measurements at both pressures, which shows that pressures up
to 130 MPa do not have a significant influence on the dynamics of water molecules.

The physical nature of the diffusive and the effective local process can be further charac-
terized by the $q$ dependence of the respective relaxation times. In Figure 7.3, the suscepti-
bility spectra of water, measured at 0.1 MPa, are shown at different $q$ values along with their
fits. At both 27.2 and 55.2 °C, the contribution from the diffusion process shifts to higher
frequencies with increasing $q$. Thus, if smaller length scales are probed, the relaxation time
$\tau_d$ of the diffusion process decreases. In Figure 7.4, $\tau_d$ in dependence on $q$ is presented. At
27.2 and 55.2 °C at both 0.1 and 130 MPa, $\tau_d$ approaches a slope of $q^{-2}$ at low $q$ values,
confirming that the peak at low frequencies indeed arises from a diffusive relaxation process.
At higher $q$ values, the dependence becomes weaker, pointing to a more localized process at
high $q$ values. Several theories addressed the molecular dynamics in liquid water. Chen et al.
described the dynamics in supercooled water with the relaxing cage model [226, 227, 228]. In
this theory, which is based on the mode-coupling theory [229], dynamics on two time scales
are predicted. On short time scales, water molecules are trapped in cages made by other
molecules, and vibrate at their equilibrium position. As the migration of water molecules
can only occur due to the rearrangement of many other molecules, their is a strong coupling
between single molecule translation and density fluctuations on larger length scales, therefore
leading to a relatively slow diffusion process with a broad distribution of relaxation times.
Laage et al. interpreted QENS data from liquid water in a different way [230, 231]. In their
work, the diffusion of water molecules is explained by large angular jumps that are coupled
to translational motion. The duration of the jump is similar to the time between successive
jumps, and it is therefore not possible to distinguish between continuous diffusion and jump
diffusion.

In agreement with previous studies on water at various temperatures [232, 233] and
pressures [234, 235], the $q$ dependence of the relaxation time can also be modeled with
the isotropic jump model. This model, which predicts a local motion of water molecules
for a certain residence time before they rapidly jump to a new position, is chosen for the
present work, since it is also capable of describing the relaxation process of hydration water of
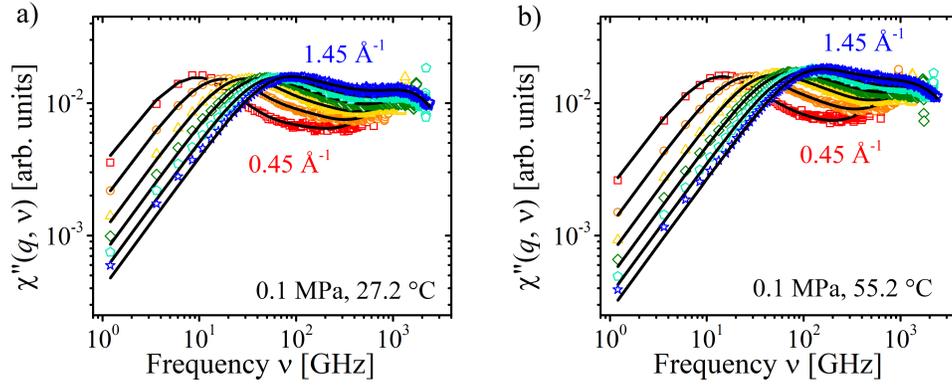PNIPAM, as shown below. It reconciles the continuous diffusion of water molecules observed

Figure 7.3: Imaginary part of the dynamic susceptibility $\chi''(q,\nu)$ of pure $H_2O$ at 0.1 MPa at 27.2 °C (a) and 55.2 °C (b) at 1.45 Å$^{-1}$ (blue stars), 1.25 Å$^{-1}$ (light green pentagons), 1.05 Å$^{-1}$ (olive diamonds), 0.85 Å$^{-1}$ (yellow triangles), 0.65 Å$^{-1}$ (orange circles) and 0.45 Å$^{-1}$ (red squares). Black lines: fits of equation 7.2 to the data.

at small $q$ values and with the localized motion at large $q$ values, and predicts

$$\tau_j = \tau_{0,j}\left[1 + \frac{6}{q^2 l_j^2}\right] \tag{7.5}$$

with $\tau_{0,j}$ the residence time between jumps and $l_j$ the apparent amplitude of the jump. From these values, the diffusion coefficient $D_j$ is determined as $D_j = l_j^2/(6\tau_{0,j})$. In Figure 7.4 the fits of equation 7.5 to $\tau_d$ are given. They describe the data excellently in the entire measured $q$ range.
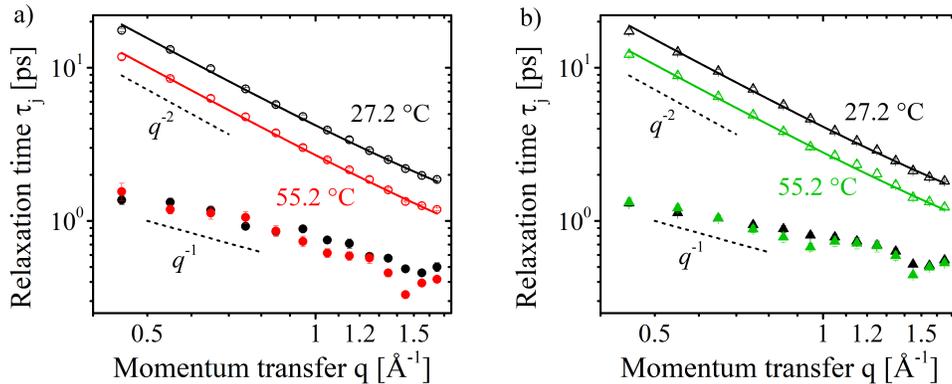


Figure 7.4: Relaxation times $\tau_d$ (open symbols) and $\tau_l$ (closed symbols) in dependence on $q$ at 0.1 MPa (a) and 130 MPa (b). The temperatures are given in the graphs. Solid lines: fits of equation 7.5 to $\tau_d$.

The resulting residence time and apparent jump length of pure water, $\tau_{0,d}$ and $l_d$, are shown in Figure 7.5a and b, respectively. At both 0.1 and 130 MPa, $\tau_{0,d}$ decreases from

$\sim$0.4 to $\sim$0.2 ps with increasing temperature, whereas $l_d$ remains constant at $\sim$0.75 Å. Since the intermolecular distance of water molecules does not change in the temperature range considered, the faster motion of water molecules at high temperatures is mainly due to a faster jump rate. The diffusion coefficients $D_d$, determined from $\tau_{0,d}$ and $l_d$, are given in Figure 7.4c. An increasing trend of $D_d$ is indeed observed. At 0.1 MPa, it is $(2.6 \pm 0.4) \times 10^{11}$ Å$^2$s$^{-1}$ at 27.2 °C and $(4.0 \pm 1.1) \times 10^{11}$ Å$^2$s$^{-1}$ at 55.2 °C, which is in excellent agreement with literature values [236, 237, 238]. Furthermore, pressure does not influence the diffusion coefficient of water in the measured pressure range, also in accordance with previous work [239].
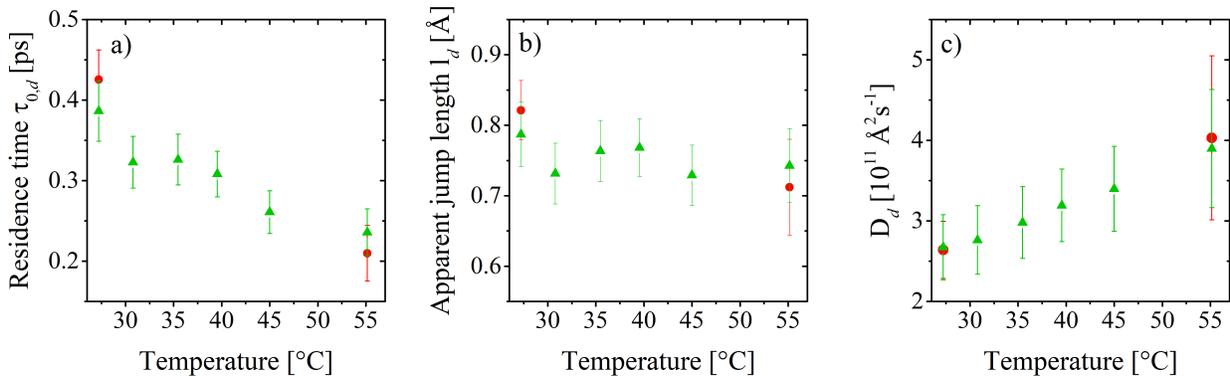


Figure 7.5: Residence time $\tau_{0,d}$ (a), apparent jump length $l_d$ (b) and the diffusion coefficient $D_d$ (c) of the diffusion process of pure water, obtained from fits of the isotropic jump model (equation 7.5) to $\tau_d(q)$.

The relaxation time of the effective local process $\tau_l$, also shown in Figure 7.4 depends only weakly on $q$ with a slope of approximately $q^{-1}$. Several theories on the physical nature of this process were discussed in the literature. Firstly, it was assigned to the motion of weakly bound molecules [240, 241], i.e., only water molecules that are weakly connected to the hydrogen bond network in water contribute. Secondly, it was proposed that this process is due to rotational relaxation between quasi-equilibrium orientations of water molecules in the hydrogen bond network [241, 242], i.e., almost all water molecules contribute. With these experiments, however, it is not possible to distinguish between both processes.

## 7.4   Water dynamics in the PNIPAM solution

In Figure 7.6, $S(q, \Delta E)$ of the 25 wt% PNIPAM solution in H$_2$O is given at different temperatures at both 0.1 and 130 MPa. As for pure water, a broad quasi-elastic contribution is observed that changes slightly with temperature at both pressures. At 0.1 MPa (Figure 7.6a),

the signal broadens at intermediate energy transfers ($\sim$ -3 meV). At small energy transfers ($\sim$0.2 meV, see inset), it narrows abruptly, following the trend of $S(q, \Delta E)$ of vanadium, i.e., elastic scattering is observed. It follows that the relaxation of water in the system becomes faster at high temperatures in a non-linear fashion. Also at 130 MPa (Figure 7.6b), a similar effect is observed. However, in this case the narrowing of the quasi-elastic signal at small energy transfers is gradual.
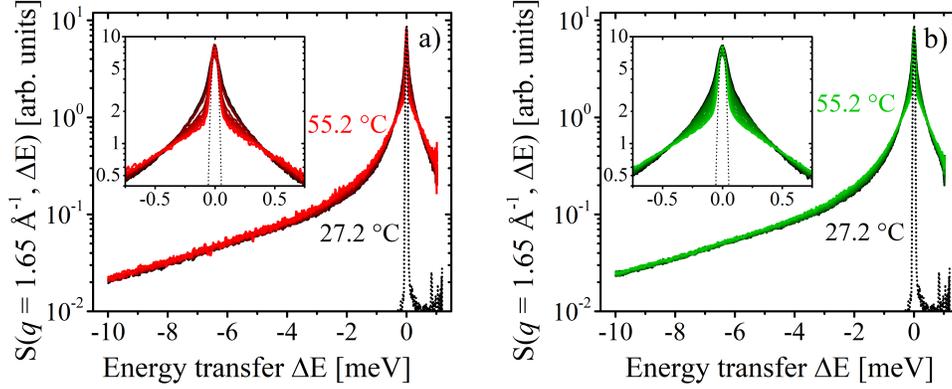


Figure 7.6: Dynamic structure factors $S(q, \Delta E)$ of 25 wt% PNIPAM in $H_2O$ at $q = 1.65$ Å$^{-1}$ and 0.1 MPa (a) and 130 MPa (b) at several temperatures, as depicted in the graphs. Black dashed lines: elastic line from the measurement on vanadium. The insets show $S(q, \Delta E)$ at small values of $\Delta E$.

## 7.4.1    Data analysis

For a better analysis of the data, the spectra are again transformed into the imaginary part of the dynamic susceptibility using equation 7.1, and are shown in Figure 7.7. In comparison with the data of pure $H_2O$, an additional strong contribution at low frequencies (below $\sim$10 GHz) is observed at 0.1 MPa and low temperatures, which is assigned to the relaxation of water that interacts strongly with the polymers. At 37 °C, this contribution decreases sharply in intensity, showing that the chains dehydrate abruptly. This temperature is, however, higher than the cloud point temperature measured with turbidimetry (31.4 °C). At the phase transition temperature, water is released from the chains due to the hydrophobic effect, as previously observed with FT-IR spectroscopy [116, 208], and therefore leads to the aggregation of the chains. At high temperatures, however, a weak contribution at frequencies below 10 GHz remains, which shows that very slowly moving moieties that cannot be resolved with the resolution of the experiment remain present in the system. This contribution is assigned to scattering from chains as well as very strongly bound water molecules.
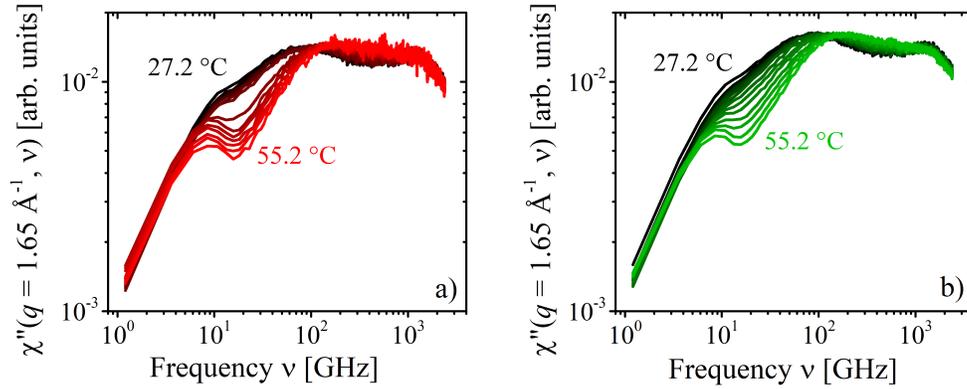
Figure 7.7: Imaginary part of the dynamic susceptibility $\chi''(q,\nu)$, determined according to equation 7.1, at 0.1 MPa (a) and 130 MPa (b) at different temperatures, as indicated in the graphs.

To account for these two additional processes in comparison with pure $H_2O$, the susceptibility spectra were modeled with the expression

$$\chi''(q,\nu) = \chi''_{el}(q,\nu) + \chi''_h(q,\nu) + \chi''_d(q,\nu) + \chi''_l(q,\nu) + \chi''_v(q,\nu) \tag{7.6}$$

with $\chi''_{el}(q,\nu)$ the elastic contribution, $\chi''_h(q,\nu)$ the relaxation process of hydration water, and $\chi''_d(q,\nu)$, $\chi''_l(q,\nu)$ and $\chi''_v(q,\nu)$ the contributions from pure water, as described above. $\chi''_{el}(q,\nu)$ is modeled by an elastic fraction with the shape of the measured resolution function $\chi''_{van}(q,\nu)$ multiplied by a $q$-dependent scaling factor:

$$\chi''_{el}(q,\nu) = C_{el}(q) \cdot \chi''_{van}(q,\nu) \tag{7.7}$$

The contribution from the relaxation of the hydration water is well described by a Debye function (equation 7.3), implying dynamic homogeneity of the hydration water. On the other hand, a Cole-Davidson function,

$$\chi''_h(q,\nu) = -\mathrm{Im}\left[ C_h(q) \frac{1}{(1 + 2\pi i \tau_h(q)\nu)^\beta} \right] \tag{7.8}$$

with $C_h(q)$ a $q$-dependent scaling factor, $\tau_h$ the relaxation time of hydration water and $\beta$ the stretching exponent, can be employed to account for a distribution of relaxation times. This dynamic heterogeneity appears as broadening of the peak at the high frequency side. Both a Debye function and a Cole-Davidson function describe the susceptibility of the hydration water, giving excellent fits over the entire frequency range. In preliminary fits, values of $\beta$ = 0.65 - 0.75 in the one-phase state of PNIPAM were found. However, the uncertainties are large. Previous studies revealed the dynamic heterogeneity of hydration water in PNIPAM

solutions [243] and in other solutions of macromolecules [244]. Furthermore, the relative fraction of hydration water in the one-phase state at 0.1 MPa (as discussed below) is determined to be ~0.45 using the Cole-Davidson function with $\beta = 0.7$, whereas it is ~0.35 using the Debye function to model the relaxation process of hydration water. In previous studies, the number of hydration water molecules bound to each PNIPAM monomer was determined to be ~11 [243, 245, 246, 247, 248], which would for the 25 wt% PNIPAM solution used here imply that approximately half of the water population is hydration water. As the use of the Cole-Davidson function results in realistic fractions of hydration water and can account for dynamic heterogeneities, it is used in this analysis with $\beta$ fixed at 0.7.

During the fits, the values of $\tau_d(q)$ and $\tau_l(q)$ were kept fixed using interpolated values from the measurement of pure water. Furthermore, the fraction of hydration water as well as the peak frequency $\nu_0$ and peak width $\Gamma$ of the DHO term were assumed to be independent of $q$. To model the curves at all $q$ values, the mean values determined from fits of the measurements at $q = 1.45$, 1.55 and 1.65 Å$^{-1}$ were used.

Fits of equation 7.6 are exemplarily shown for the measurement at 27.2 °C and 51.7 °C at 0.1 MPa in Figure 7.8, providing more details about the contributions from the individual components. At 27.2 °C (Figure 7.8a), the spectrum is dominated by the contribution from hydration water. The measurement at 51.7 °C (Figure 7.8b) confirms that the majority of hydration water ($h$) is released only deep in the two-phase state. The contribution from elastic scattering ($el$), however, strongly increases in strength compared to the measurement at 27.2 °C. Presumably, water molecules are trapped inside the polymer-rich domains formed in the two-phase state, which are therefore strongly restricted in their motion and contribute to the elastic component. Furthermore, motion of the chains in the one-phase state may have contributed to a certain extent to the peak assigned to relaxation processes in hydration water. In the two-phase state, the reduced mobility of the chains leads to an increased strength of the elastic fraction. However, previously described relaxation modes of PNIPAM are much slower than the measured frequency range, and are therefore expected to play a weaker role [249]. With heating across $T_{cp}$, the contribution at low frequencies decreases sharply in strength, whereas an increase is observed at intermediate frequencies. Thus, hydration water that is released from the chains joins the bulk water phase.
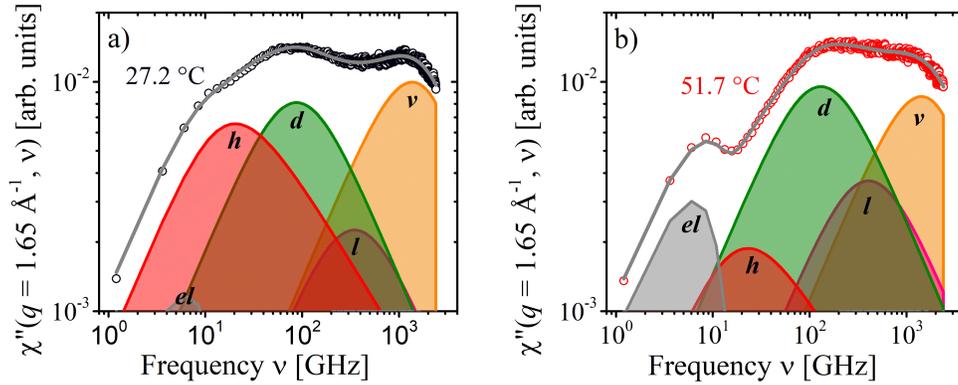
Figure 7.8: Example fits of $\chi''(q,\nu)$, at 0.1 MPa at 27.2 °C (a) and 51.7 °C (b). Data (open circles), fits of equation 7.6 (grey lines) and their individual contributions: Elastic fraction $el$ (grey), relaxation process of hydration water $h$ (red), diffusion process of bulk water $d$ (olive), local process of bulk water $l$ (pink) and the vibrational process $v$ (orange).

## 7.4.2   Distribution of water in the PNIPAM solution

From the amplitudes $C_j(q)$, with the index $j$ standing for $h$, $d$ or $l$, the relative fractions of the different water species can be determined. Since the values of $C_j(q)$ are proportional to the respective scattering intensities, the relative fractions of the different water species $f_j$ can be determined as

$$f_j = \frac{C_j(q)}{C_h(q) + C_d(q) + C_l(q)} \tag{7.9}$$

At this, it is assumed that both bulk water and hydration water contribute to the vibrational process, which is therefore not included in the determination of the relative fractions. Furthermore, the elastic fraction is not taken into account, since its strength cannot be compared with that of the dynamic processes. As evident from the fits, shown in Figure 7.8, the elastic line strength increases at high temperatures. Thus, the amount of water molecules considered for the determination of $f_j$ may not be constant over the entire temperature range, and the resulting values should be taken with caution.

Figure 7.9a shows the relative populations of hydration water $f_h$, the diffusion process of bulk water $f_d$, and the local process of bulk water $f_l$ in dependence on temperature at 0.1 and 130 MPa. In the one-phase state at atmospheric pressure, $f_h$ equals ~0.4. At ~35 °C, $f_h$ decreases abruptly, which coincides with $T_{cp}$. Thus, the chains dehydrate strongly, which was previously observed and explained by the cooperative association of water molecules to the chains in the one-phase state [105]. However, after this abrupt decrease, a significant fraction of hydration water remains, which decreases gradually with increasing temperature,

extending to ∼10 K above $T_{cp}$. A small fraction of ∼0.15 remains at the highest measured temperature of 55.2 °C. Previously, it was observed with infrared absorption spectroscopy [116] and molecular dynamics simulations [250] that PNIPAM chains do not dehydrate completely during phase separation at atmospheric pressure. The majority of the hydrophilic groups remain hydrogen bonded with water rather than forming intra- or interchain hydrogen bonds. Therefore, the dehydration is mainly due to the release of water from hydrophobic groups.
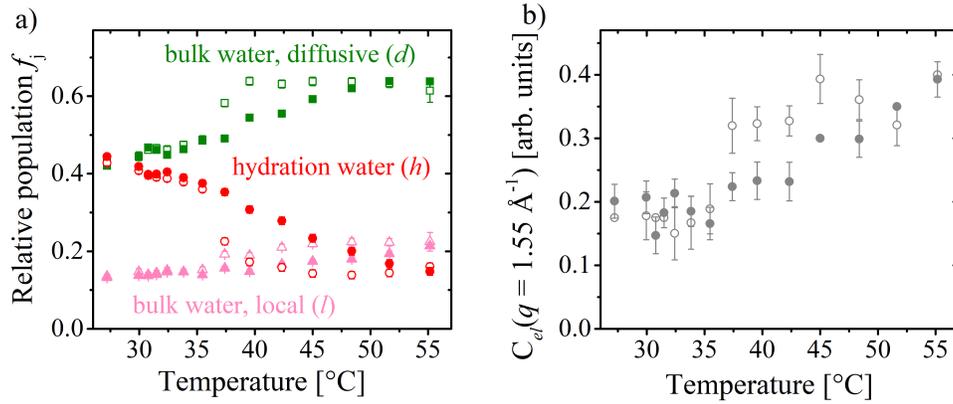


Figure 7.9: (a) Relative populations of the different water species $f_j$ in dependence on temperature at 0.1 MPa (open symbols) and 130 MPa (closed symbols), determined according to equation 7.9. Red circles: hydration water $h$, green squares: diffusion process of bulk water $d$, pink triangles: local process of bulk water $l$. (b) Elastic line strength $C_{el}(q)$ in dependence on temperature at $q = 1.55$ Å$^{-1}$ at 0.1 MPa (open grey circles) and 130 MPa (closed grey circles).

At high pressure, the relative population of hydration water is similar to the one at atmospheric pressure in the one-phase state. However, no sharp transition is observed at $T_{cp}$; rather, the relative population of hydration water decreases gradually over the entire temperature range. In the one-phase state, the decrease is weak. At $T_{cp}$ at ∼35 °C, it decreases more strongly but flattens again at ∼50 °C. At 55.2 °C, the relative population of hydration water is ∼0.15, similar to the value at atmospheric pressure. From this point of view, the transition from the one-phase state to the two-phase state is fundamentally different at both pressures. Although polymer-rich domains already form within 0.1 K above $T_{cp}$ in both pressure regimes (Chapter 6), the dehydration of the chains occurs in a much broader temperature range at high pressure than at atmospheric pressure.

Contrary to the relative fraction of hydration water, the relative fraction of bulk water increases with temperature. At 0.1 MPa, $f_d$ increases sharply at $T_{cp}$, whereas the increase is gradual at 130 MPa. Thus, at both pressure, the hydration water that is released from

the chains joins the bulk water phase. Also $f_l$ increases with temperature at both pressures, however, the changes are significantly smaller in this case.

The elastic line strength $C_{el}(q)$, shown in Figure 7.9b for the measurements at $q = 1.55$ Å$^{-1}$, increases with temperature at 0.1 MPa. At atmospheric pressure, it stays constant in the one-phase state and increases sharply at $T_{cp}$. Thus, the amount of hydrogen atoms involved in dynamic processes that are too slow to be resolved increases at $T_{cp}$. As stated earlier, this may have two reasons. Firstly, water may be trapped inside the polymer-rich domains, therefore being strongly restricted in its movement. Secondly, hydrogen atoms on the chains that are mobile in the one-phase state, lose their mobility in the two-phase state, thereby increasing the elastic line strength. Also at 130 MPa, $C_{el}(q)$ increases, but the change is gradual.

## 7.5   Dynamic properties of hydration water

The $q$ dependence of the relaxation time reveals the physical nature of the relaxation process of hydration water. As shown in Figure 7.10a for the measurements at 0.1 MPa and 27.2 °C, a clear increase in frequency of the contribution from hydration water (at frequencies between ~10 and ~100) with increasing $q$ is observed at 27.2 °C. As for pure water, the relaxation time of hydration water $\tau_h$ therefore increases if larger length scales are probed. In addition, the intensity of both contributions at low frequencies decreases with $q$. At 0.1 MPa and 51.7 °C (Figure 7.10b), the relative fraction of hydration water is very small, and the $q$ dependence of $\tau_h$ can only be determined with large uncertainties.

Figure 7.11a shows the $q$ dependence of $\tau_h$ at 27.2 °C at both 0.1 and 130 MPa, i.e., in the one-phase state. At both pressure, the $q$ dependence of $\tau_h$ deviates from the $q^{-2}$ law in the investigated $q$ range, which would be expected for a purely diffusive process. For both pressures, a weaker dependence than $q^{-2}$ is observed in the entire measured $q$ range, which shows that the motion of these water molecules follows a different relaxation process. Furthermore, a change of the slope is observed with varying $q$. At low $q$ values, the slope is close to $q^{-2}$, but flattens with increasing $q$. Several types of anomalous diffusion can be considered. Subdiffusive behavior, where the molecules are restricted in space, may lead to different $q$ dependencies. In case the diffusion is hindered by an impenetrable surface but the molecule is not confined, which is the case for protein solutions, stronger dependences than $q^{-2}$ are expected [221, 251]. For diffusion in confined geometries, e.g. inside a sphere, the
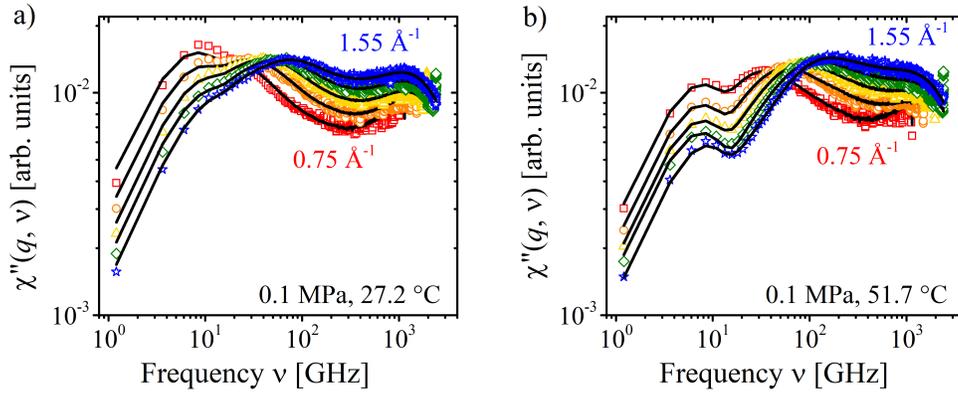
Figure 7.10: Imaginary part of the dynamic susceptibility $\chi''(q,\nu)$ at 0.1 MPa at 27.2 °C (a) and 51.7 °C (b) at 1.55 Å$^{-1}$ (blue stars), 1.35 Å$^{-1}$ (olive diamonds), 1.15 Å$^{-1}$ (yellow triangles), 0.95 Å$^{-1}$ (orange circles) and 0.75 Å$^{-1}$ (red squares). Black lines: fits of equation 7.6 to the data.

slope is shallower than $q^{-2}$, but increases in steepness towards higher $q$ values [252]. Such behavior is also expected for superdiffusive behavior [251, 253]. However, this would imply the presence of an anisotropic force acting on the molecules, which is in this case unlikely.
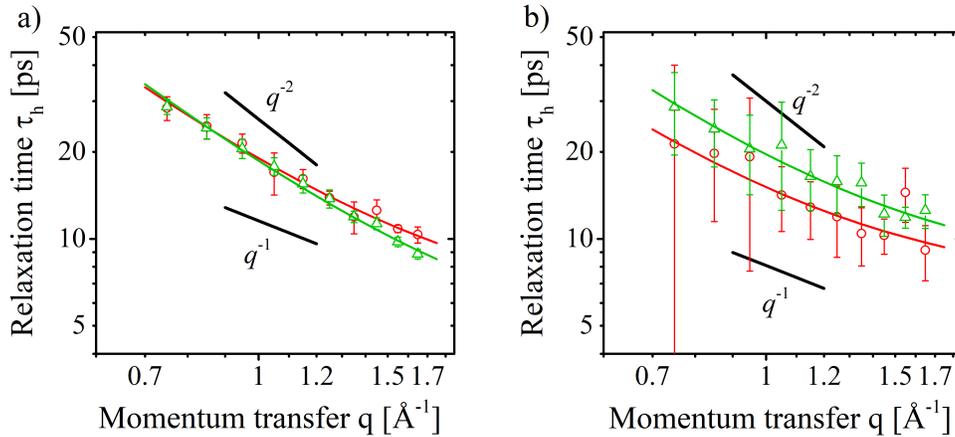


Figure 7.11: Relaxation time of hydration water $\tau_h$ in dependence on $q$ at 27.2 °C (a) and 51.7 °C (b), at 0.1 MPa (red circles) and 130 MPa (green triangles). The solid lines are fits to the data using equation 7.5.

Analogous to the diffusion process of pure water, the isotropic jump model (equation 7.5) can be used to describe the dynamic behavior of the hydration water, which yields a residence time $\tau_{0,h}$ as well as an apparent jump length $l_h$. The fits, also shown in Figure 7.11, are excellent over the entire measured $q$ range. In the two-phase state, shown in Figure 7.11b for 51.7 °C at both 0.1 and 130 MPa, the observed slope is shallower than in the one-phase state. Also in this case, the $q$ dependence of $\tau_h$ can be modeled by the isotropic jump model. Since the $q^{-2}$ dependence is expected at smaller $q$ values than can be resolved, statements

on the diffusive part of the dynamics of hydration water in the two-phase state are based on extrapolation. Furthermore, the uncertainties of $\tau_{0,h}$ are large, due to the small relative population of hydration water in the two-phase state.

Figure 7.12a shows the residence time $\tau_{0,h}$, obtained from fits of the $q$ dependence of $\tau_h$ with the isotropic jump model (equation 7.5). At atmospheric pressure below $T_{cp}$, a constant value of $\sim 5 \times 10^{-12}$ s is observed, which is a factor of $\sim 10$ larger than $\tau_{0,d}$ under the same conditions (Figure 7.5). The residence time of water molecules depends strongly on the number of vacant positions around it, influenced by the local environment of the hydration water: Less available positions decrease the probability of a jump, thereby increasing the residence time. The local environment of the hydration water is determined by the polarity of the adjacent polymeric groups. Around hydrophobic groups, the bond strength of water molecules is similar to that of bulk water molecules. However, the number of accessible positions is reduced by the presence of the hydrophobic group, thus leading to an increased residence time that does not exceed a factor of 2 in dilute solutions [254, 255]. For hydrophilic groups, the strength of the hydrogen bond between water and the hydrophilic groups hinders in addition to the reduced number of available positions, as was the case for hydrophobic groups, the motion of hydration water even more. The dissociation of the water molecule and the hydrophilic group requires overcoming an activation energy, which therefore restricts the diffusion of the water molecule with retardation factors up to 4 [256]. The difference in residence time of a factor of $\sim 10$ between bulk water and hydration water in the one-phase state thus shows that, on average, multiple polymeric groups are involved in the binding of hydration water molecules.
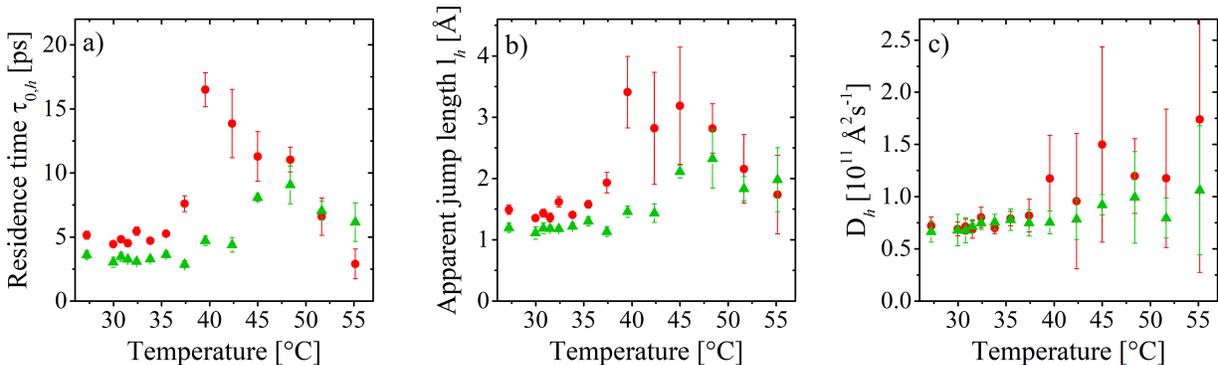


Figure 7.12: Residence time $\tau_{0,h}$ (a), apparent jump length $l_h$ (b) and the diffusion coefficient $D_h$ (c) of the relaxation process of hydration water, obtained from fits of the isotropic jump model (equation 7.5) to $\tau_h(q)$. 0.1 MPa: red circles, 130 MPa: green triangles.

At 130 MPa below $T_{cp}$, $\tau_{0,h}$ is significantly lower, $\sim 3 \times 10^{-12}$ s. Since the relative fraction of hydration water is very similar at both pressures in the one-phase state, the hydration water molecules must be distributed differently on the chains. The shorter residence time in the one-phase state at high pressure therefore reflects a weaker hindrance of hydration water in comparison with atmospheric pressure. As the effect of pressure on the individual hydrogen bond strength is insignificant in the investigated pressure range [257, 258], it follows that, at high pressure, hydrophobic groups are more hydrated at the expense of hydrophilic groups. This is in accordance with previous work using molecular simulations that suggested that the dissociation of close hydrophobic contacts is favored at high pressure [259, 260], which may be due to the increased compressibility of hydration water around hydrophobic groups [20, 93, 94] leading to an enhanced hydration. At high pressure, the hydration of hydrophobic groups thus enables a reduction of the volume of the system.

Above $T_{cp}$ at atmospheric pressure (above $\sim 35$ °C), $\tau_{0,h}$ increases sharply, which takes place simultaneously with both the decrease of $f_h$ (Figure 7.9a) and the increase in $C_{el}(q)$ (Figure 7.9b). This increase may be due to two different mechanisms: First, weakly bound hydration water (around hydrophobic groups) is released from the chains at $T_{cp}$, and strongly bound hydration water (around hydrophilic groups) remains, or second, both strongly and weakly bound hydration water are released in significant amount from the chains at $T_{cp}$ and the remaining population gets increasingly restricted in its motion. The latter also follows from the increase of the elastic line strength at $T_{cp}$ and therefore presumably dominates. A combination of both contributions may, however, be present. This result is in accordance with the well-known picture of the phase separation process of PNIPAM at atmospheric pressure. At $T_{cp}$, the hydrophobic collapse causes a strong dehydration of the hydrophobic groups on the chains and their subsequent aggregation [116, 131]. During this process, water molecules get trapped inside the aggregates [118, 217], which results in longer residence times. Furthermore, it was observed previously that the hydrophilic amide groups stay mostly hydrated above $T_{cp}$ [116, 118, 119].

Also at 130 MPa, $\tau_{0,h}$ increases directly above $T_{cp}$. However, the increase is more gradual (extending to $\sim 10$ K above $T_{cp}$) and less pronounced than at atmospheric pressure. Since the relative population of hydration water decreases gradually in the two phase state, a different set of water molecules is considered in the two-phase state than in the one-phase state. Also in this case, the increase in $\tau_{0,h}$ is most likely caused by an increased hindrance of the remaining hydration water in the two-phase state, as is also evident from the increase

in the elastic line strength (Figure 7.9b). The increase in hindrance is, however, smaller than at atmospheric pressure. Thus, it is likely that the process of hydrophobic collapse extends to ∼10 K above $T_{cp}$. During this process, the hydration water around hydrophobic groups is released from the chains and joins the bulk water phase, as is evident from the decreasing fraction of hydration water (Figure 7.9a). The hydration water around hydrophilic groups remains, thus, the overall population of hydration water is more strongly hindered at high temperatures.

At higher temperatures at 0.1 MPa, a decrease in $\tau_{0,h}$ is observed. In the same temperature range, the relative population of hydration water and the elastic line strength remain, however, constant. The loosening of the hydration water can therefore be attributed to further rearrangement of hydration water with increasing temperature, which may be due to structural changes in the system. Rearrangements of chains in the polymer-rich phases may allow strongly hindered water to relax, possibly by forming small voids containing mainly water. At 130 MPa, $\tau_{0,h}$ remains constant deep in the two-phase state. Since the phase transition is observed to be more gradual in this case, the system had more time to reach a kinetically stable state upon phase separation and structural rearrangements presumably play a much weaker role.

The apparent jump length $l_h$ follows similar trends as $\tau_{0,h}$ for both pressures, as shown in Figure 7.12b. The apparent jump length is a measure for the spatial extension of the hindrance to the motion of water molecules, since it represents the distance between neighboring potential minima [233]. Therefore, $l_h$ can be expected to behave similar to $\tau_{0,h}$, which is indeed observed. Quantitatively, the values of $l_h$ in the one-phase state are ∼1.5 Å at 0.1 MPa and ∼1.2 Å at 130 MPa, which are significantly larger than the values of $l_d$ under the same conditions (Figure 7.5b). It can be concluded that the packing of hydration water is less dense than in bulk water.

The diffusion coefficient of hydration water $D_h$ is shown in Figure 7.12c. At both pressures in the one-phase state, $D_h$ increases from ∼7 to ∼8×$10^{10}$Å$^2$s$^{-1}$, which may be due to the enhanced thermal energy with increasing temperature. In the two-phase state at atmospheric pressure, $D_h$ increases more strongly than in the one-phase state, whereas at 130 MPa, the increase remains similar. However, the uncertainties are large at both pressures, which is due to the low relative population of hydration water in the two-phase state. As discussed above, possible structural rearrangements in the polymer-rich phases deep in the two-phase

state at 0.1 MPa may allow for a less hindered diffusion of the hydration water molecules.

## 7.6 Chain dynamics

Beside the dynamics of water, also the dynamics of the PNIPAM chains can be studied with QENS. Although more suitable experimental methods exist for the study of chain dynamics in solution, such as neutron spin-echo spectroscopy, it is also accessible from the elastic line strength. Mainly neutrons scattered by the hydrogen atoms at the PNIPAM chains contribute to the elastic signal. However, it may also include very strongly bound water, as discussed above. In Figure 7.13a, the dependence of the elastic line strength on $q^2$ is shown at 27.2 and 51.7 °C at both 0.1 and 130 MPa. In all presented cases, it follows a straight line in the lin-log representation, which allows a description using the Debye-Waller factor, given by [261]

$$C_{el}(q) \propto \exp\left[ - \langle u_{\text{eff}}^2 \rangle \frac{q^2}{3} \right] \tag{7.10}$$

with $\langle u_{\text{eff}}^2 \rangle$ the effective mean-square displacement of the relaxation processes. At 0.1 MPa, $\langle u_{\text{eff}}^2 \rangle$, shown in Figure 7.13b, decreases sharply at $T_{cp}$ from ~1.3 Å$^2$ in the one-phase state to ~0.7 Å$^2$ in the two-phase state, which is due to the sudden collapse of the chains at $T_{cp}$. In dense systems, as in the two-phase state, translational motion of a particle is only possible if neighboring particles also move, which is strongly hindered. Vibrational motion, however, requires only a small change in volume and results in a small value of $\langle u_{\text{eff}}^2 \rangle$. Furthermore, the observed displacement may involve rotational motion of (predominantly) the methyl groups of PNIPAM [262], also observed in dry as well as hydrated protein samples [263, 264]. In the one-phase state, translational motion is less hindered, and local changes in chain conformation also contribute to the elastic line strength, resulting in a large value of $\langle u_{\text{eff}}^2 \rangle$.

At 130 MPa, a gradual decrease of $\langle u_{\text{eff}}^2 \rangle$ from ~1.0 Å$^2$ to ~0.6 Å$^2$ is observed around $T_{cp}$. As followed from the behavior of hydration water, the conformation of the chains changes gradually from a swollen and mobile state, to a collapsed and immobile state, which is confirmed by the gradual decrease of $\langle u_{\text{eff}}^2 \rangle$. Therefore, just above $T_{cp}$, the chains are more mobile at 130 MPa than at 0.1 MPa. In comparison with the measurement at 0.1 MPa, the value of $\langle u_{\text{eff}}^2 \rangle$ in the one-phase state is significantly lower at 130 MPa than at 0.1 MPa. Thus, the motion of the chains is more restricted at high pressure, which may be due to the changed hydration state at high pressure. It can be argued that the enhanced hydrophobic
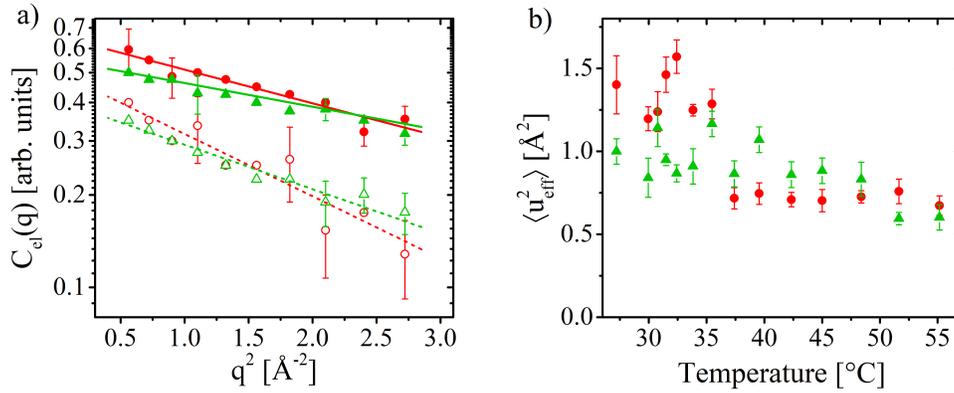
Figure 7.13:  (a) Elastic line strength $C_{el}(q)$ in dependence on $q^2$ at 0.1 MPa (red symbols) and 130 MPa (green symbols) at 27.2 °C (open symbols) and 51.7 °C (closed symbols). Lines are fits of equation 7.10 to $C_{el}(q)$ at 0.1 MPa (red lines) and 130 MPa (green lines) at 27.2 °C (dashed lines) and 51.7 °C (solid lines). (b) Effective mean-square displacement of the chain dynamics $\langle u_{\text{eff}}^2 \rangle$ in dependence on temperature at 0.1 MPa (red circles) and 130 MPa (green triangles).

hydration of the side groups causes a certain degree of steric hindrance to conformational changes of the polymer, thereby restricting translational motion. On the other hand, the reduced hydration of hydrophilic groups may increase the number of N-H$\cdots$O=C bonds between adjacent monomers, stiffening the chains.

## 7.7   Conclusion

In this chapter, the water dynamics of pure $H_2O$ and of a 25 wt% PNIPAM solution in $H_2O$ was investigated at both low and high pressures using quasi-elastic neutron scattering in dependence on temperature. Converting the obtained dynamic structure factors to the imaginary part of the dynamic susceptibility, it was possible to obtain the entire spectrum of the molecular dynamic processes of water in the aqueous PNIPAM solution, and to identify all individual contributions.

In pure $H_2O$, three contributions were identified: a diffusion process at low frequencies, an effective local process at intermediate frequencies and a vibrational process at high frequencies. It was shown that, whereas increasing temperature leads to larger values of the diffusion coefficient of water molecules, a pressure of 130 MPa does not influence the dynamic properties of liquid water. In addition to the three processes observed in pure water, two processes were observed in the 25 wt% PNIPAM solution in $H_2O$, both at lower frequencies than the diffusional process of pure water. At very low frequencies, below the resolution limit of the experiment, elastic scattering from very slowly moving moieties was observed,

which comprises mainly scattering from the chains. At higher frequencies, a contribution related to the motion of hydration water was observed.

The relative fraction of hydration water in the one-phase state is ∼0.45 for both pressures. The relaxation time of hydration water in dependence on momentum transfer was modeled using the isotropic jump model. From the residence time between discrete jumps of hydration water molecules, it follows that the polymer-water bonds are stronger at 0.1 MPa than at 130 MPa, indicating that, at high pressure, the hydrophobic groups are more hydrated than at atmospheric pressure, at the expense of hydrophilic groups. With increasing temperature through $T_{cp}$, a strong decrease of the relative fraction of hydration water towards ∼0.15 is observed, which is abrupt at 0.1 MPa and gradual at 130 MPa. Simultaneously, the residence time of water molecules increases at both pressures. It was argued that both strongly and weakly bound hydration water are released from the chains at $T_{cp}$. The small amount of remaining hydration water is strongly hindered in its motion, which shows that mainly the hydrophilic groups remain hydrated. At the highest measured temperature of 55.2 °C, both the residence time of hydration and its relative fraction is again the same at both pressures. Thus, although the hydration properties of the chains are very similar deep in the one-phase state and deep in the two-phase state and two-phase state at both pressures, the phase separation mechanism is fundamentally different at both pressures.

Furthermore, the mean-square displacement of the chains, related to their mobility is determined from the elastic line strength, and is mainly due to translational, vibrational and rotational displacement of the chains. At $T_{cp}$ at atmospheric pressure, it decreases strongly, which points to the collapse of the chains. At high pressure, however, the decrease of the mean-square displacement is more gradual and less pronounced. In the one-phase state, it is smaller at 130 MPa than at 0.1 MPa, suggesting that the chains are stiffer at high pressure. It was argued that this stiffening may be due to steric hindrance of conformational changes because of the enhanced hydration of the hydrophobic groups. At temperatures just above $T_{cp}$, the chains are more mobile at 130 MPa than at 0.1 MPa due to the weaker dehydration at high pressure. This provides an additional argument for the strong influence of the visco-elastic effect on the formation of mesoglobules at atmospheric pressure, as discussed in Chapter 6.

# Chapter 8. Pathway of mesoglobule formation

In this chapter, the mechanisms involved in the formation of mesoglobules are investigated. At this, kinetic SANS experiments following rapid pressure jumps are performed at both low and high pressures. The results presented in this chapter were published previously in B.-J. Niebuur et al., *ACS Macro Lett.*, 7:1155-1160, 2018 [132] and B.-J. Niebuur et al., *Macromolecules*, 52:6416-6427, 2019 [265].

## 8.1  Introduction

The drastic differences between mesoglobules formed at atmospheric pressure and at high pressure, described extensively in Chapter 6, raise curiosity about the growth processes involved in the formation of the mesoglobules. From the increased size as well as the stronger hydration of the mesoglobules at high pressure compared to atmospheric pressure, it can be expected that in both situations, different growth processes dominate.

Small-angle neutron scattering (SANS) is the method of choice for kinetic structural studies of soft matter systems, as it covers all relevant length scales (1-100 nm) and offers a time resolution of tens of milliseconds. In an earlier study, the kinetics of phase separation of PNIPAM homopolymer solutions was investigated with SANS using a temperature jump to induce phase separation [121]. However, the early stages of phase separation were not accessible due to the long temperature equilibration time of the large sample volume required for SANS (few 100 s). Alternatively, pressure jumps can be applied. In contrast to temperature jumps, the equilibration time is much shorter (<0.1 s), and the jumps can be applied bi-directional [266, 267, 268, 269]. Despite these advantages, only few kinetic studies were carried out using SANS in combination with fast pressure jumps [146, 270].

In this study, the elliptical shape of the coexistence line of aqueous PNIPAM solutions in the temperature-pressure frame, discussed in Chapter 5, is utilized. At temperatures between 33.7 °C and 35.9 °C, the two-phase state can be reached at both low and high pressures by a decrease or increase in pressure, respectively. In this way, the influence of chain hydration on the phase separation process is addressed. In addition to the choice of the pressure regime, also the depth of the jump can be varied. As discussed in Chapter 5, varying the target pressure of the jump, i.e., the pressure distance from the coexistence line, changes the tendency of the system to phase separate.

## 8.2   Experimental details

**Materials.**   Poly($N$-isopropylacrylamide) (PNIPAM) with a molar mass $M_n = 36\ 000$ g mol$^{-1}$ and a dispersity of 1.26 (end groups carboxylic acid and a hydrogen atom, respectively) was purchased from Sigma-Aldrich. It was dissolved at a concentration of 3 wt% in D$_2$O, which is above the overlap concentration. D$_2$O was used to ensure a maximum contrast between water-rich and polymer-rich phases during the SANS measurements.

**Small-angle neutron scattering.**   Small-angle neutron scattering (SANS) measurements were performed at the instrument D11 at the Institute Laue-Langevin, Grenoble, France. A neutron beam with a wavelength $\lambda = 0.6$ nm and spread $\Delta\lambda/\lambda = 0.09$ was used. Measurements were performed at a sample-detector distance (SDD) of 1.5, 8.0 and 34.0 m, covering a $q$ range of $1.7\times10^{-2}$ - 3.3 nm$^{-1}$.

The sample was mounted in a temperature-controlled copper-beryllium pressure cell, capable of withstanding pressures of 350 MPa. The sample was placed between sapphire windows with a sample thickness of 2 mm, independent of pressure. The pressure system used for the pressure jumps is similar to previously reported systems [267, 268], and is schematically shown in Figure 8.1. The external pressure system (section (a) in Figure 8.1) was connected with the pressure cell (section (b) in Figure 8.1) by a pneumatic valve. To avoid mixing of the sample with the pressure transmitting medium, a movable piston (separator) was placed between the pressure cell and the pneumtic valve. Before the jump, the pneumatic valve was open and the pressure was set to the desired initial value. Afterwards, the pneumatic valve was closed and the pressure in the external pressure system was decreased or increased. The system was equilibrated for 5 min and a static SANS measurement with a measuring time of 1 min was carried out. The pressure jump was performed by a rapid

opening of the pneumatic valve, leading to equilibration of the pressure in sections (a) and (b). A transistor-transistor logic (TTL) pulse, induced by the opening of the valve, triggered the start of the data acquisition, and was found to result in good reproducibility. The frame duration was increased after each frame by a factor of 1.1, starting with 0.05 s. After each pressure jump, 85 frames were recorded, which implies a total measuring time of 1649 s. The measurement at SDD = 34.0 m was repeated at least 5 times for each jump to obtain sufficient statistics. Selected measurements shortly after the pressure jumps were binned to improve statistics to allow reliable fits. The data reduction was performed as described in Section 4.2.2, with a measurement of $H_2O$ to determine the detector sensitivity.
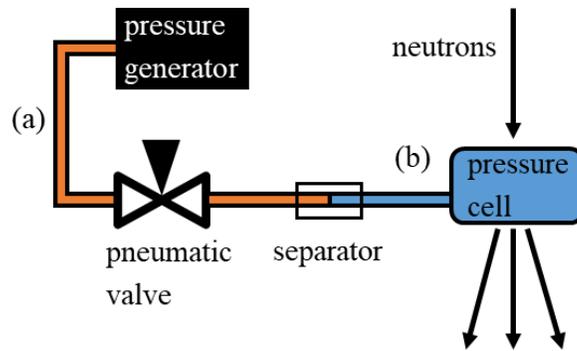


Figure 8.1: Sketch of the pressure system used to perform pressure jumps. The external system, section (a), is connected to the separator and the pressure cell, section (b), with a pneumatic valve. The separator is used to avoid mixing of the sample (blue) with the pressure transmitting medium (orange). See the text for more details about the protocol of the experiments.

In Figure 8.2, an overview of the performed pressure jumps is presented. In the low-pressure (LP) regime, four jumps, starting at $p = 31$ MPa and $T = 35.1$ °C, are performed with pressure changes of $\Delta p = $ -11 MPa, -15 MPa, -21 MPa and -31 MPa. In the high-pressure (HP) regime, three jumps with a starting point at $p = 87$ MPa and $T = 35.1$ °C and pressure changes of $\Delta p = $ 14 MPa, 25 MPa and 45 MPa are performed.

## 8.3 Mesoglobule formation in the low-pressure regime

In Figure 8.3, the SANS curves after the jumps from the one-phase state to the two-phase state in the LP regime are presented. The pre-jump scattering curves feature a shoulder above ∼0.06 nm$^{-1}$, indicating the presence of concentration fluctuations in the semi-dilute polymer solution [77, 121]. The appearance of the scattering curves depend strongly on the depth of the jump. After the shallowest jump ($\Delta p = $ -11 MPa), the scattering curves do not
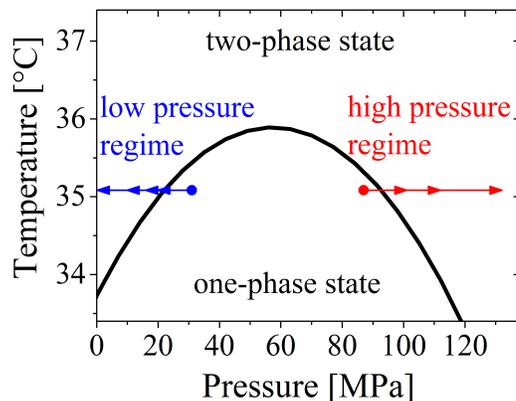
Figure 8.2:  Phase diagram of the 3 wt% PNIPAM solution in $D_2O$ in the temperature-pressure frame [132]. The start and target pressure of the performed pressure jumps are marked with blue arrows in the LP regime and with red arrows in the HP regime.

differ significantly from the pre-jump curve during the first $\sim$10 s. After that, an additional shoulder in the low-$q$ region appears, indicating the formation of large particles, identified as mesoglobules. The position of this shoulder does not change notably and only increases in intensity very slowly, i.e., phase separation occurs only slowly.

In contrast, the scattering curves for $\Delta p$ = -15, -21 and -31 MPa display rapid changes, and several growth processes are observed. Directly after the jump (marked as regime I), the shoulder present at 0.06 $nm^{-1}$ increases slightly in intensity for all three jumps. During this stage, small clusters of PNIPAM chains are formed, as discussed below in more detail. At a time depending on the depth of the jump, a second shoulder in the low-$q$ range appears (below 0.04 $nm^{-1}$), which shifts to lower $q$ values and increases in intensity, indicating the presence of growing mesoglobules. The behavior of the second shoulder depends strongly on $\Delta p$: For shallow jumps, i.e., $\Delta p$ = -15 MPa, the second shoulder appears later than after deep jumps, i.e., $\Delta p$ = -31 MPa. Moreover, for shallow jumps, the intensity increase at low $q$ values is weaker than for large $\Delta p$. Thus, the kinetics of mesoglobule growth is faster after deep jumps than after shallow ones. Two different growth processes of the mesoglobules can be distinguished: At intermediate times, the shoulder at low $q$ values shifts rapidly to lower $q$ values, and its intensity increases strongly (marked as regime II). At later times, the shift to lower $q$ values and the increase in intensity continue, but are less pronounced, meaning a slower growth of the mesoglobules (marked as regime III). The deeper the jump, the earlier the slow growth process sets in.

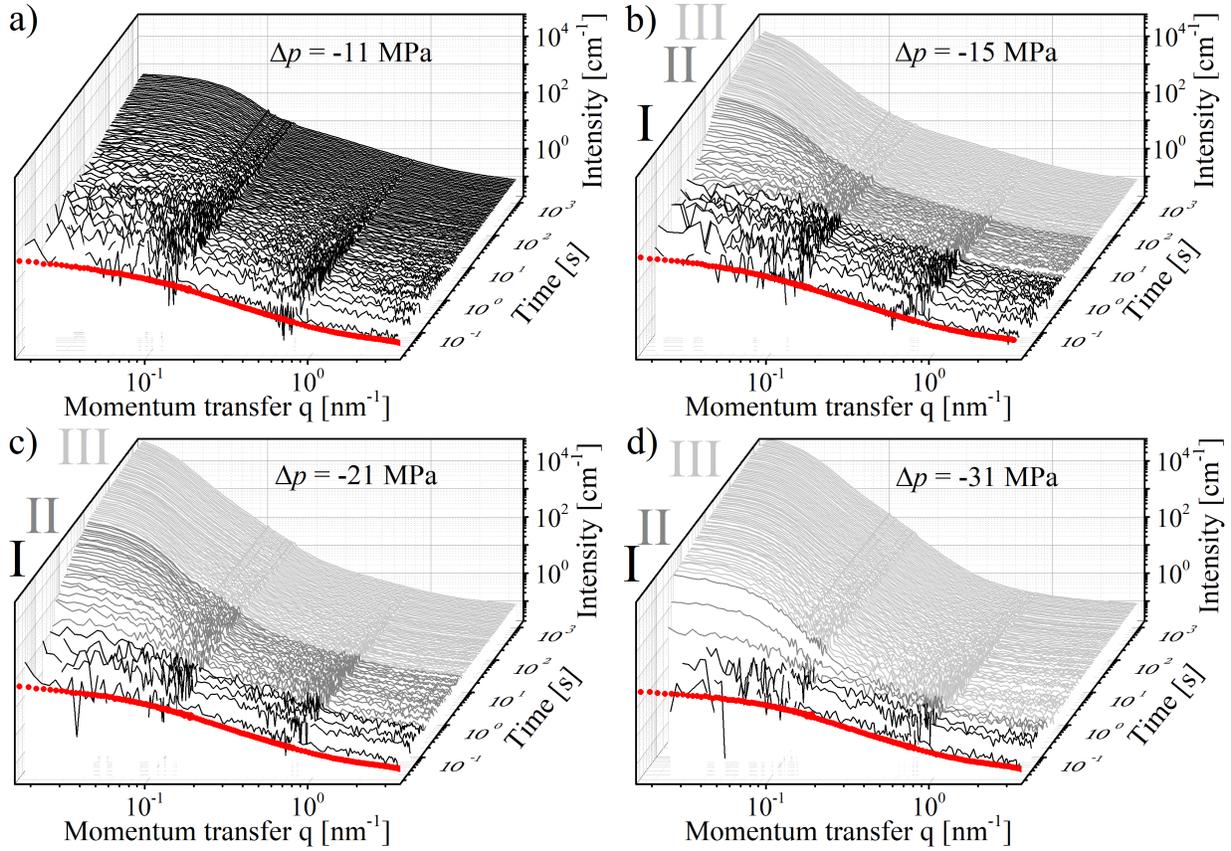The changes in the scattering curves at high $q$ values are less pronounced. The shoulder

Figure 8.3: SANS curves of the 3 wt% PNIPAM solution in $D_2O$ in the LP regime after jumps from the one-phase state to the two-phase state starting at $T = 35.1$ °C and $p = 31$ MPa with pressure changes of $\Delta p = $ -11 MPa (a), -15 MPa (b), -21 MPa (c) and -31 MPa (d). Red symbols: pre-jump measurements. The growth regimes I (black curves), II (grey curves) and III (light grey curves) are indicated on the left.

observed in the pre-jump measurement persists in all cases, but decreases in intensity. Thus, also at small length scales, concentration fluctuations are present in the two-phase state. The decrease in intensity of the shoulder is stronger after large than after small jump amplitudes, showing that the inner structure of the mesoglobules is more homogeneous after jumps with large $\Delta p$.

In Figure 8.4, representative scattering curves along with their fits for the jumps with $\Delta p$ = -15, -21 and -31 MPa in each regime of growth are presented. In all cases, the scattering curves were fitted using the function

$$I(q) = I_{GP}(q) + I_{OZ}(q) + I_{bkg} \tag{8.1}$$

Here, $I_{GP}(q)$ denotes the Guinier-Porod form factor (equation 4.26), which gives the Guinier intensity $I_G$, the radius of gyration $R_g$ of the mesoglobules and their Porod exponent $m$.

$I_{OZ}(q)$ is the Ornstein-Zernike structure factor (equation 4.31), which gives the Ornstein-Zernike intensity $I_{OZ}$ and the correlation length of concentration fluctuations $\xi$, and $I_{bkg}$ is an incoherent background. The forward scattering in the pre-jump measurements is very weak, $I_{GP}(q)$ was therefore set to zero. In regime I for $\Delta p$ = -15 MPa, -21 MPa and -31 MPa, the chains collapse and form small fractal-like clusters. Therefore, the scattering curves can be modeled by the Ornstein-Zernike structure factor only, and $I_{GP}(q)$ was set to zero as well. In regimes II and III, the contribution from mesoglobules was modeled with the Guinier-Porod form factor. The contribution at high $q$ values, resulting mainly from inhomogeneities in the inner structure of the mesoglobules, can be modeled by the Ornstein-Zernike structure factor, too. For $\Delta p$ = -31 MPa, this contribution is very weak in regime II and the beginning of regime III. Due to the absence of a shoulder, as can be observed in Figure 8.4c, it was not possible to determine $I_{OZ}$ and $\xi$ during this time. $I_{OZ}$ was therefore kept fixed at 5 cm$^{-1}$ to allow a reliable determination of the other fitting parameters. Also directly after $\Delta p$ = -11 MPa, the Ornstein-Zernike structure factor sufficed to model the scattering curves. After $\sim$10 s, the Guinier-Porod form factor was added to describe the contribution to the scattered intensity from mesoglobules at low $q$ values. Since this contribution is weak in intensity, the value of $m$ was kept fixed at 4 to avoid unstable fits, thereby assuming smooth surfaces of the mesoglobules. In all cases, excellent fits are obtained.
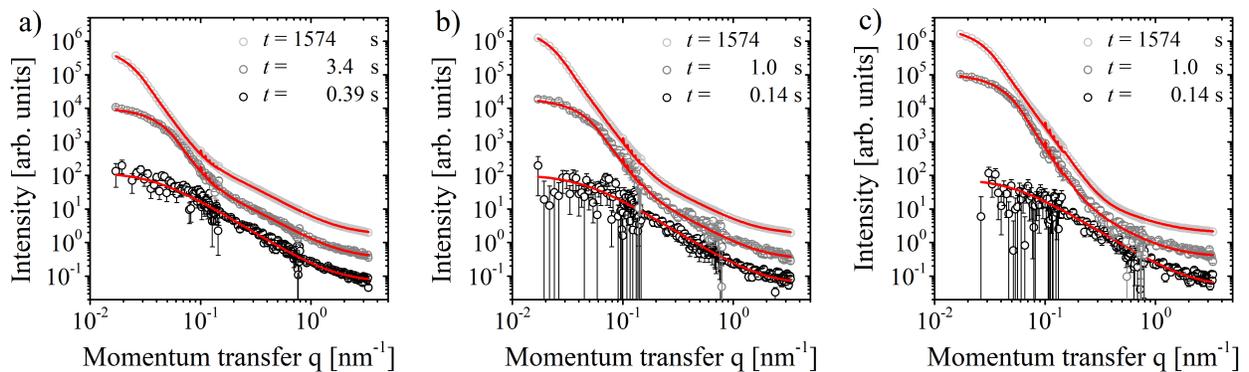


Figure 8.4: Representative fits of the SANS data in the LP regime at $\Delta p$ = -15 MPa (a), -21 MPa (b) and -31 MPa (c). For each jump scattering curves are shown in regime I (black curves), regime II (grey curves) and regime III (light grey curves) at times as indicated in the graphs. Red lines: fits of equation 8.1. For clarity, the curves are shifted by factors of 5.

The time dependence of the characteristic parameters from fitting are presented in Figure 8.5. At first, the jumps with $\Delta p$ = -15 MPa, -21 MPa and -31 MPa are discussed in detail, followed by the discussion of the jump with $\Delta p$ = -11 MPa.

Directly after the jumps with $\Delta p$ = -15, -21 and -31 MPa (regime I), a weak increase in $I_{OZ}$ from the pre-jump value of $\sim$35 cm$^{-1}$ is observed (Figure 8.5b-d), indicating that scattering from concentration fluctuations on a local scale becomes stronger. Simultaneously, $\xi$ (Figure 8.5f-h), becomes larger. As described in Section 2.1, the mechanism of phase separation depends on the depth of the jump into the two-phase state. For shallow jumps, the metastable phase is reached, and phase separation is expected to occur via nucleation and growth, whereas for deep jumps into the unstable state, phase separation follows spinodal decomposition (Section 2.1.2). In case of spinodal decomposition, the scattering intensity of concentration fluctuations increases exponentially but their sizes stay constant [46, 271]. In this case, however, phase separation may be influenced by the dynamic asymmetry in the system. As the solution is in the semi-dilute concentration regime, the chains may form a network-like structure after the jump due to entanglements [113], maintained temporally by an elastic force balance [49, 53]. During the disentanglement of the chains, loose clusters of chains are formed. This process, which is similar to a nucleation and growth process [53], may be observed here as an increase in $\xi$ during regime I.
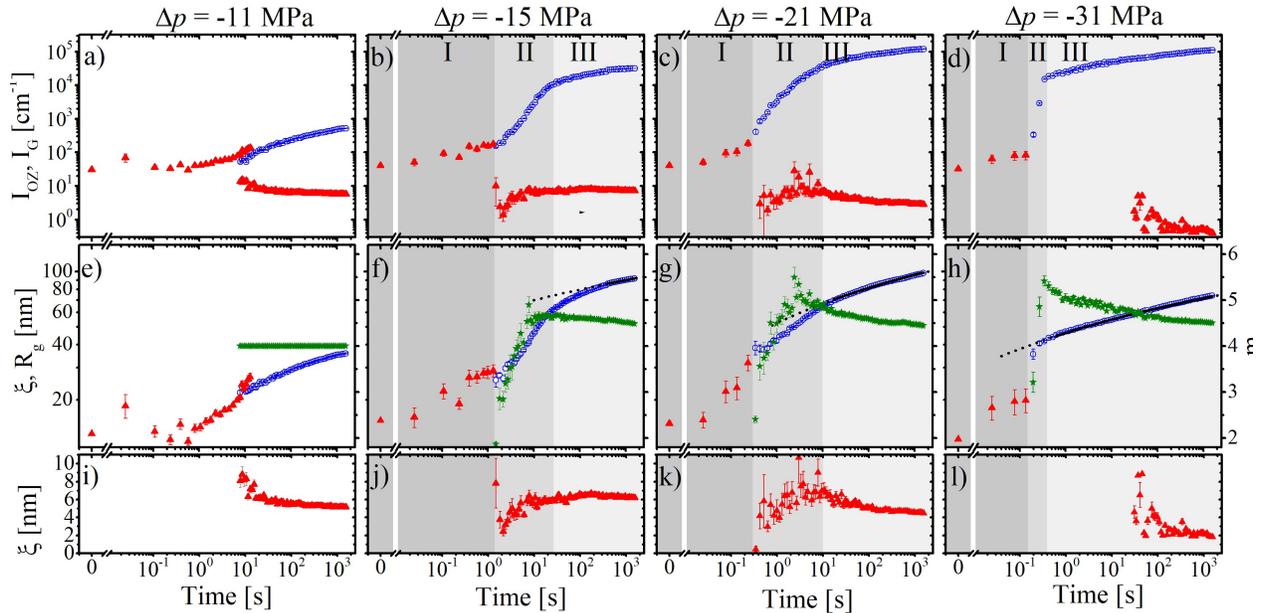


Figure 8.5: Time dependence of the parameters from fitting the SANS data in the LP regime for the pressure jumps, as indicated above the graphs. (a) - (d): Ornstein-Zernike intensity $I_{OZ}$ (red triangles) and Guinier intensity $I_G$ (blue circles). (e) - (h): Correlation length of concentration fluctuations $\xi$ directly after the jumps (red triangles, left axis), radius of gyration $R_g$ of the mesoglobules (blue circles, left axis), and Porod exponent $m$ (green stars, right axis). (i) - (l): $\xi$ at later times (red triangles). The solid black lines in (f) - (h) are fits of equation 2.6, the dotted black lines are their extrapolations. The time regimes are indicated at the top of (b), (c) and (d).

In regime II (after 1.4 s, 0.3 s and 0.15 s for $\Delta p$ = -15, -21 and -31 MPa, respectively), the clusters transformed to particles with well-defined surfaces, identified as mesoglobules (Chapter 6). Mesoglobules form earlier after deep jumps than after shallow ones, which may be related to the solvent quality after the jump: After deeper jumps, the tendency to phase separate is stronger due to the worse solvent quality (Chapter 5), leading to faster formation of mesoglobules. The time dependence of the scattering intensity from the mesoglobules $I_G$ follows the increasing trend of $I_{OZ}$ in regime I. However, its slope increases after these jumps, which indicates that phase separation becomes faster. The behavior of $R_g$ shows that this is mainly due to the fast growth of the mesoglobules: For $\Delta p$ = -15 and -31 MPa, $R_g$ follows the trend of $\xi$ with a steeper slope. Foror $\Delta p$ = -21 MPa, however, $R_g$ follows a similar slope as $\xi$. In regime II, the mesoglobules have presumably still a loose structure due to the ongoing phase separation. The high mobility of the chains therefore allows coalescence and therefore a fast mesoglobule growth. In the beginning of regime II for $\Delta p$ = -15 and -21 MPa, the growth follows a rate of $R_g \propto t^{1/3}$, which is expected for coalescence that is limited by the diffusion of the mesoglobules [70]. For $\Delta p$ = 31 MPa, this process is not observed. The strong thermodynamic driving force for phase separation may lead to a faster dehydration of the chains. The duration of the regime of fast growth is therefore shortened.

The Porod exponent $m$ provides insights into the surfaces of the mesoglobules, and therefore into their interaction with each other. It increases rapidly from 2 to values above 4 during regime II. A value of $m$ below 4, i.e., in the beginning of regime II, indicates a rough surface of the mesoglobules [215]. This confirms that the mesoglobules still have a loose structure during their fast growth. The rapid increase of $m$ to above 4 may be due to two different processes. The surfaces become smooth, which changes $m$ towards 4 [215], and a composition gradient at the surface arises, raising the apparent value of $m$ to above 4 [169, 170]. The smoothening of the surfaces may be due to the diffusion of water out of the surface-near layers of the mesoglobules, resulting in closely packed chains at their surfaces. As a result, the water captured inside the mesoglobules during their formation is trapped, leading to a composition gradient at the surface. The entrapment of water inside the mesoglobules is also evident from the significant scattering of concentration fluctuations at smaller length scales. At the end of regime II, $I_{OZ}$ reaches a value of ~10 cm$^{-1}$ for both $\Delta p$ = -15 MPa and -21 MPa (at the beginning of regime II, the Ornstein-Zernike structure factor and the Guinier-Porod form factor strongly overlap, the values of $I_{OZ}$ are therefore not reliable during these times). It indicates that the inner structure of the mesoglobules is inhomogeneous and thus contain water. The same follows from the value of $\xi$ in this regime. It reaches a value of ~8 nm

for both jumps, which is a reasonable size for concentration fluctuations in dense polymeric systems. Presumably, the mesoglobules formed after the jump with pressure change $\Delta p =$ -31 MPa evolve similarly. The values of $\xi$ and $I_{OZ}$ can, however, not be determined.

At later times in regime III (after $\sim$27 s, $\sim$10 s and $\sim$0.4 s for $\Delta p =$ -15 MPa, -21 MPa and -31 MPa, respectively), the increase in $R_g$ slows down, and deviations from the $\sim t^{1/3}$ growth are observed. Furthermore, $I_G$ increases much slower than in regime II. The slower growth is caused by the changing structure of the mesoglobules: Starting from a loose, fractal structure, a compact aggregate with a dense shell is formed, which is expected to reduce the probability of coalescence. $m$ decreases slowly towards a value of 4, which is the expected value for particles with a smooth surface without the presence of a concentration gradient. This change may be attributed to slow permeation of water through the dense PNIPAM shell, making the mesoglobules more homogeneous. This also follows from the behavior of $\xi$ during this stage. For both $\Delta p =$ -21 MPa and -31 MPa, $\xi$ decreases in regime III, indicating that the mesoglobules become more homogeneous and therefore loose water. For $\Delta p =$ -15 MPa, $\xi$ stays constant in regime III.

The very slow growth of the mesoglobules in regime III suggest the presence of an energy barrier, hindering the merging of mesoglobules. To quantify this energy barrier, the logarithmic growth model (equation 2.6) is applied to model the evolution of $R_g$ during this stage, as discussed in Section 2.2. It gives the reduced energy barrier for coalescence $\epsilon$ and the average time between collisions $\tau_{log}$ of mesoglobules of radius $R_0$. To extract these values, a reasonable value of $R_0$ must be known. As shown earlier, the early stages of phase separation is a process in which several mechanisms that influence the growth of the mesoglobules overlap. Therefore, an unambiguous determination of $R_0$ is not possible. Here, $R_0$ is chosen as $R_g$ at the beginning of regime II. At these times, the clusters of chains can firstly be described as well-defined particles, having $R_g$ values of 27, 40 and 30 nm for $\Delta p =$ -15, -21 and -31 MPa, respectively. Fits of equation 2.6 to $R_g$ are also given in Figure 8.5. Using the mentioned values for $R_0$, reduced energy barriers of $\epsilon = 6.2$ $k_BT$, 6.3 $k_BT$ and 8.0 $k_BT$ are obtained. Thus, the energy barriers are significantly larger than the thermal energy, meaning that aggregation is strongly hindered and a kinetically stable state is reached. The obtained collision times are $\tau_{log} = 2.2 \times 10^{-6}$ s, $\tau_{log} = 5.2 \times 10^{-4}$ s and $\tau_{log} = 8.5 \times 10^{-6}$ s for the jumps with $\Delta p =$ -15 MPa, -21 MPa and -31 MPa, respectively. These may be compared with the encounter and coalescence time $\tau_D$ from the Smoluchowski model for coalescence,

which reads

$$\tau_D = \frac{3\eta}{8C_0 k_B T} \qquad (8.2)$$

with $\eta$ the viscosity of the solvent and $C_0$ the concentration of mesoglobules in the solution. Using a volume fraction of the mesoglobules of $\phi = 0.03$, which is roughly the polymer concentration in the solution, and $R_0 = 50$ nm, a mesoglobule concentration of $C_0 \approx 200$ $\mu$m$^{-3}$ is determined. Using $\eta = 10^{-3}$ Pa·s and $T = 305$ K, a value of $\tau_D \approx 5 \times 10^{-4}$ s is obtained. This value is comparable to $\tau_{log}$ obtained for $\Delta p =$ -21 MPa. For $\Delta p =$ -15 and -31 MPa, however, the logarithmic growth model underestimates the collision times and the obtained values for $\epsilon$ should therefore be taken with caution.

In a comparable study in which aggregation was induced by rapidly mixing of the solution with a co-solvent, Kyriakos et al. [71] found energy barriers of $\sim$3 k$_B T$ for aggregating PS-$b$-PNIPAM micelles in mixtures of water and methanol, which is smaller than the 6 - 8 k$_B T$ observed here. It can be argued that the inter-penetration of PNIPAM chain ends into two micelles results in smaller conformational changes than PNIPAM chains in two merging globules, leading to the observed smaller energy barrier for PS-$b$-PNIPAM micelles. However, also the difference in used solvent may play a role. Furthermore, the system in regime III is similar to the 'moving droplet' phase observed previously [49, 52, 53], where the observed growth that follows a power law with small exponents ($\beta \sim 0.1$). This is consistent with the logarithmic growth observed here, since both models follow a similar trend in restricted time ranges. It was shown that also this regime is strongly influenced by the dynamic asymmetry in the system, leading to an entanglement force that prevents coalescence (Section 2.1.3). Rough calculations by Chuang et al. [51] showed that an energy of the order of tens of k$_B T$ is needed to overcome this entanglement force hindering the coalescence of two mesoglobules, i.e., even more than is observed in the present experiments. As solvent entrainment was not taken into account in their model, it can be concluded that the finite degree of hydration of PNIPAM in the two-phase state has a destabilizing effect on the mesoglobules.

The behavior of the system after the smallest jump ($\Delta p =$ -11 MPa) is fundamentally different from that after the deepest three jumps. Directly after the jump, no changes in the system compared to the pre-jump measurement are observed: As seen in Figure 8.5a and e, $I_{OZ}$ and $\xi$ stay constant during the first $\sim$1 s. After this incubation period, a weak increase in both $I_{OZ}$ and $\xi$ is observed, which shows that clusters are formed. Scattering from mesoglobules was only observed after $\sim$10 s. It is, however, weak. Both $I_G$ and $R_g$ continue the trend of $I_{OZ}$ and $\xi$, respectively. Until the end of the measurement ($t = 1649$

s), both quantities slowly increase.

After the jump with $\Delta p$ = -11 MPa, the thermodynamic driving force for phase separation is weak, and the growth after this jump is slow in comparison with the three deepest jumps. Furthermore, the three regimes of the growth of the mesoglobules, as described above, cannot be identified for the jump with $\Delta p$ = -11 MPa. The incubation period directly after the jump suggests that stable clusters are not formed immediately. As this is a common feature in nucleating systems [272, 273], it can be expected that, also after deeper jumps, an incubation time is present. For these jumps it is, however, too short to be resolved in the present experiments. After clusters have formed for $\Delta p$ = -11 MPa, a stage of diffusion-limited coalescence, as was the case in regime II for the three deepest jumps, is not observed. Instead, the size of the mesoglobules increases slowly during the entire measurement because the energy gain due to the coalescence of clusters is only small, i.e., the probability of merging upon collision is low. Because of the limited thermodynamic driving force for phase separation, it is believed that the chains do not significantly dehydrate. Therefore, the slow growth towards the end of the measurement is not due to the visco-elastic effect, as for the three deepest jumps, but due to the weak tendency to phase-separate. Thus, the scattering at later times at high $q$ values may originate from the inner structure of the clusters as well as from single chains in the solution, and the resulting values of $I_{OZ}$ and $\xi$ cannot be related to the water content inside the clusters in this case.

Overall, the size and structure of the mesoglobules depend strongly on the depth of the jump. The final size of the mesoglobules does not scale with $\Delta p$: After 1649 s, the size of the mesoglobules is ∼38 nm, ∼92 nm, ∼98 nm and ∼74 nm for the jumps with $\Delta p$ = -11, -15, -21 and -31 MPa, respectively. This non-linear behavior is a result of the different growth processes and their pressure-dependent time scales. As follows from the decreasing trend of the final value of $\xi$ at the end of the measurements with increasing jump depth, the mesoglobules have a more homogeneous inner structure after deep jumps, i.e., their water content is lower. These results show that the properties of the mesoglobules can be tuned by varying the jump depth in the LP regime.

## 8.4    Mesoglobule formation in the high-pressure regime

Figure 8.6 displays the SANS curves after the jumps from the one-phase state to the two-phase state in the HP regime. As in the LP regime, the pre-jump scattering curves feature a shoulder above 0.06 nm$^{-1}$, with, however, a lower intensity. The concentration fluctuations are therefore less pronounced at 87 MPa than at 31 MPa, which may be related to the different chain conformation at high pressure [274] or to different distances to the respective cloud point [77].

Immediately after all three jumps, the intensity in the low-$q$ region (below $\sim$0.1 Å$^{-1}$) increases strongly, indicating that mesoglobules are formed immediately. Already during this formation stage (regime I), the sizes of the mesoglobules are too large to be resolved: Only a steep slope resulting from scattering from the surfaces of the mesoglobules is visible. During the remaining time (regime II), the intensity at low $q$ values decreases. Presumably, this contribution shifts to lower $q$ values, observed as a decrease in intensity in the low $q$ region, indicating that the mesoglobules continue growing during the entire time of the measurement. At high $q$ values (above $\sim$0.2 Å$^{-1}$), no significant changes are observed, concentration fluctuations at small length scales therefore remain. Due to the weakened dehydration close to the coexistence line at high pressure (Chapter 7), the chains do not collapse completely, but remain in a swollen conformation.

Quantitative information from the scattering curves was in all cases obtained from model fitting with the expression

$$I(q) = I_P(q) + I_{OZ}(q) + I_{bkg} \tag{8.3}$$

Here, $I_P(q)$ is the Porod approximation (equation 4.25), accounting for the surface structure of the mesoglobules, and gives the Porod amplitude $K_P$ and Porod exponent $m$. $I_{OZ}(q)$ is the Ornstein-Zernike structure factor (equation 4.31), and gives the correlation length of concentration fluctuations $\xi$, and $I_{bkg}$ is an incoherent background. Only for the pre-jump measurements, the forward scattering is very weak and $I_P(q)$ was set to zero. In Figure 8.7, representative scattering curves with their fits are shown for all three jumps at various times after the jump. In all cases, the model reproduced the data excellently.

In Figure 8.8, the time dependence of the characteristic parameters from fitting is presented. In regime I, an increasing value of $m$ is observed and reaches a value of 4 after 0.31 s, 0.17 s and 0.17 s for $\Delta p = 14$, 25 and 45 MPa. It follows that the time needed to form
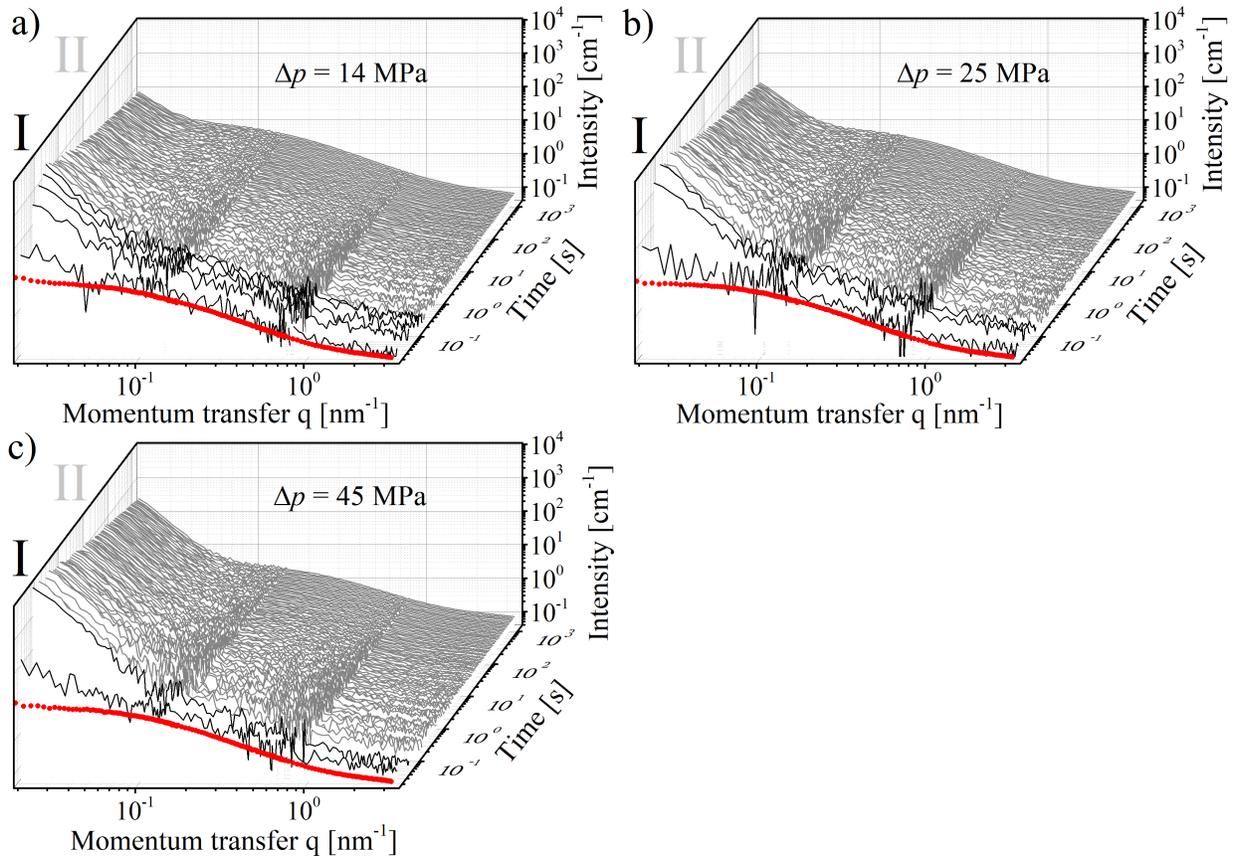
Figure 8.6: SANS curves of the 3 wt% PNIPAM solution in $D_2O$ in the HP regime after jumps from the one-phase state to the two-phase state starting at $T = 35.1\ °C$ and $p = 87$ MPa with pressure changes of $\Delta p = 14$ MPa (a), 25 MPa (b), 45 MPa (c). Red symbols: pre-jump measurements. The growth regimes I (black curves) and II (grey curves) are indicated on the left.
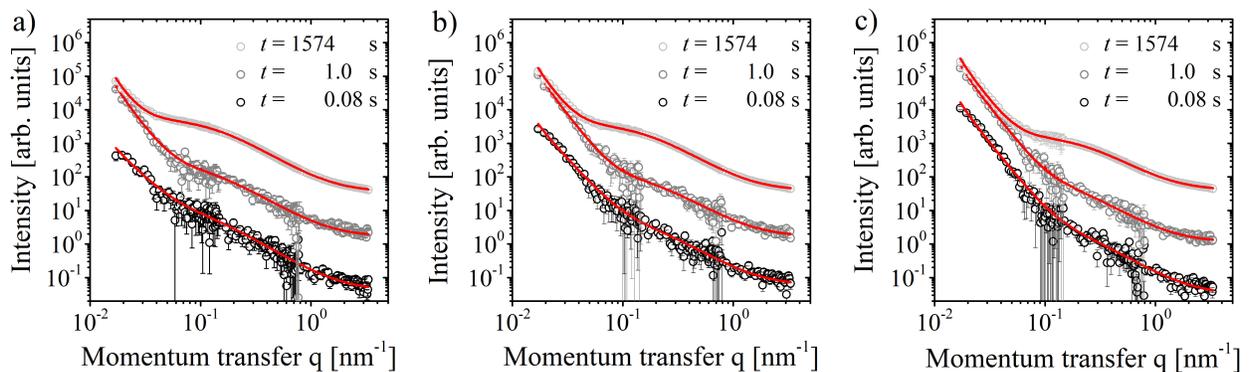


Figure 8.7: Representative fits of the SANS data in the HP regime at $\Delta p = 14$ MPa (a), 25 MPa (b) and 45 MPa (c). For each jump scattering curves are shown in regime I (black curves) and regime II (grey curves and light grey curces) at times as indicated in the graphs. Red lines: fits of equation 8.3. For clarity, the curves are shifted by factors of 25.

mesoglobules with well-defined surfaces is significantly shorter in the HP regime than in the

LP regime. At high pressure, dynamic asymmetry in the system does not seem to affect the

initial stages of phase separation: Contrary to the measurements in the LP regime, an initial slow cluster formation phase is not observed. Due to the enhanced hydration of the chains in the two-phase state at high pressure in comparison with low pressure, a network-like structure due to entanglements directly after the jump that may hinder phase separation is not formed. Instead, many chains cluster together immediately.
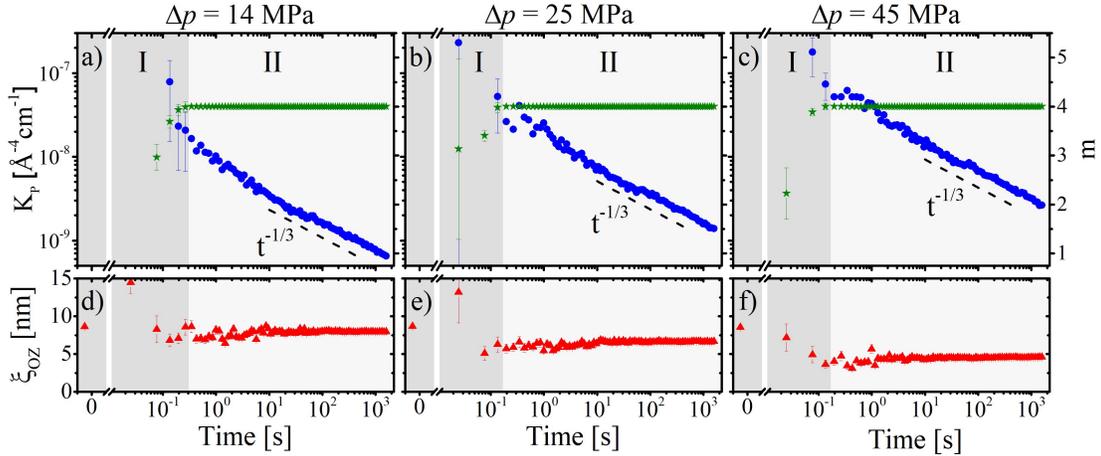


Figure 8.8: Time dependence of the parameters from fitting the SANS data in the HP regime for the pressure jumps, as indicated above the graphs. (a) - (c): Porod amplitude $K_P$ (blue circles, left axis), and Porod exponent $m$ (green stars, right axis). (d) - (f): Correlation length of concentration fluctuations $\xi$. The time regimes are indicated at the top of (a), (b) and (c).

The values of $\xi$ in regime I depends on $\Delta p$. After the jump with $\Delta p = 14$ MPa, $\xi$ maintains the value from the pre-jump measurement of $\sim 8.6$ nm (the higher value of the first data point at 0.025 s may be due to the low quality of the first scattering curve). After the jump with $\Delta p = 25$ and 45 MPa, however, $\xi$ decreases weakly to $\sim 6.2$ and $\sim 3.6$ nm, respectively. These differences reflect the degree of dehydration after the jumps. From previous studies on PNIPAM solutions under high pressure conditions (described in Section 3.2) and the results presented in Chapter 6 and 7, it followed that the chains dehydrate only weakly in the two-phase state at high pressure. The value of $\xi$ is therefore still related to the chain conformation. Since the chains do not span the entire volume of the system, as is the case in the one-phase state, a larger value of $\xi$ indicates a higher chain density in the mesoglobules and a stronger dehydration. Thus, the stronger decrease of $\xi$ after deep jumps reflects the pressure-distance to the cloud point: The thermodynamic driving force for phase separation is stronger deep in the two-phase state.

At the beginning of regime II (after 0.31 s, 0.17 s and 0.17 s for $\Delta p = 14$, 25 and 45

MPa), $\xi$ increases again slightly for all jumps and stays unchanged after $\sim$10 s. Therefore, slight rearrangements inside the mesoglobules occur during the first $\sim$10 s, which may result from the complex kinetics during the formation stage. In regime II, $m$ was fixed at a value of 4 during the fits, thereby assuming smooth surfaces of the mesoglobule. Figure 8.7 displays that the fits were still excellent. In preliminary fits, a floating value of $m$ resulted in values of 3.7-3.9, which points to a certain surface-roughness of the mesoglobules. However, fixing $m$ at a value of 4 allows to relate $K_P$ to the composition of the mesoglobules and their size, as [215]

$$K_P = 2\pi(\Delta\rho)^2 S_v \tag{8.4}$$

Here, $\Delta\rho$ is the difference in scattering length density between the water-rich and polymer-rich domains and $S_v$ is the specific surface of the mesoglobules.

The constant value of $\xi$ after $\sim$10 s shows that, after this time, the composition of the mesoglobules does not change anymore, and $\Delta\rho$ remains constant. The decrease in $K_P$ is solely due to a decrease in $S_v$. For all jumps, $K_P$ decreases with a $t^{-1/3}$ dependence after $\sim$10 s. As the specific surface is proportional to the inverse radius of the mesoglobules, i.e., $S_v \sim R^{-1}$, the growth of the mesoglobules follows a $R \propto t^{1/3}$ dependence, which is expected for diffusion-limited coalescence [70]. This growth continues until the end of the measurements, which shows that no energy barrier that hinders coalescence builds up at later times, as was the case in the LP regime. Due to the hydrated state of the chains in the two-phase state, no dense shell that hinders the coalescence is formed. Although the surfaces are smooth on larger length scales, as follows from the value of $m$, they may be rough on small length scales, allowing the formation of entanglements and therefore the coalescence of mesoglobules. Thus, the visco-elastic effect, hindering the coalescence of mesoglobules in the LP regime, does not play a role in the phase separation of aqueous PNIPAM solutions at high pressures.

## 8.5 Conclusions

In this chapter, the kinetics of mesoglobule formation in a 3 wt% PNIPAM solution in $D_2O$ was investigated at both low and high pressures, combining time-resolved small-angle neutron scattering and pressure jumps to rapidly induce phase separation. The elliptical shape of the phase diagram in the temperature-pressure frame allowed to reach the two-phase state at both low and high pressures by a change in pressure only. As pressure jumps can

be performed much faster than temperature jumps, the formation of mesoglobules could be followed with a time resolution of 50 ms.

The mechanisms involved in mesoglobule formation are illustrated in Figure 8.9. At low pressure, the measurements resolved the presence of three regimes of growth. Directly after the jumps, i.e., in regime I, a slow formation of clusters consisting of collapsed chains is observed that subsequently grow rapidly by diffusion-limited coalescence in regime II. At later times (regime III), the growth is hindered due to the visco-elastic effect that leads to the kinetic stability of the mesoglobules. Varying the jump depth influences the thermodynamic driving force for phase separation, which changes the duration of the different growth processes and therefore the final size and structure of the mesoglobules. At high pressure, only two regimes of growth are observed. Directly after the jump in regime I, large clusters of chains are formed immediately. After their formation (regime II), the clusters grow by diffusion-limited coalescence until the end of the run. The visco-elastic effect does not affect the kinetics of mesoglobule formation at high pressures, since the chains remain hydrated in the two-phase state. The third regime of slow growth is therefore not observed at high pressures, resulting in very large mesoglobules.
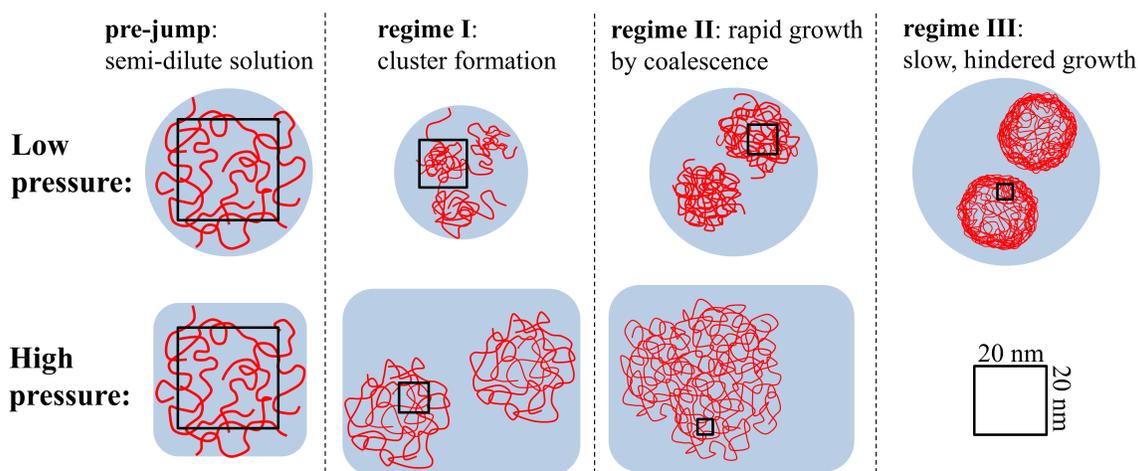


Figure 8.9: Schematic representation of the different regimes of mesoglobule formation and growth following a pressure jump at both low and high pressures. Similar length scales in each regime are indicated by the black square.

To conclude, the possibility was demonstrated to tune the size and structure of the mesoglobules using variations in chain hydration, mainly influenced by the different pressure regimes, and in jump depth, which allows variation in the duration of the different growth processes.

# Chapter 9.   Pathway of mesoglobule disintegration

Following the investigation of the mesoglobule formation in Chapter 8, the mesoglobule disintegration at both low and high pressure is in the focus of this chapter. At this, kinetic SANS experiments following rapid pressure jumps from the two-phase state to the one-phase state are performed.

## 9.1   Introduction

Understanding nanoparticle dissolution may be important in various fields, for example to study the dissolution of protein complexes in the food or medical sciences [275], or the disintegration of drug-carriers after drug-administration [276]. Despite its importance, only few studies addressed the kinetics of dissolution of polymeric systems. Earlier work focused on the dissolution of bulk phases of glassy polymers [277] or polymer grains [278, 279]. In contrast to particles composed of small molecules or atoms, the dissolution of polymers may be a complex process. In these cases, the dissolution is hindered by two processes: the diffusion of solvent into the particles and the disentanglement of the chains [277].

In this chapter, the dissolution of mesoglobules composed of PNIPAM homopolymers is investigated. As shown in Chapter 6, these differ from polymer grains in two important aspects. Firstly, their sizes range from tens of nanometers to several micrometers, i.e., in the relevant range for the above mentioned applications. Secondly, mesoglobules composed of PNIPAM homopolymers already contain a significant amount of water. Therefore, this study may provide fundamentally new insights in the dissolution properties of nanoparticles composed of macromolecules.

By combining small-angle neutron scattering with rapid pressure jumps, it is possible to

follow the process of mesoglobule dissolution at all relevant length scales with a time resolution of 50 ms. Pressure jumps are performed from the two-phase state, where mesoglobules are present in the system, to the one-phase state, where a semi-dilute polymer solution is formed. Analogous to the measurements performed to investigate the formation of mesoglobules (Chapter 8), their dissolution is investigated at low and high pressure to vary the water content of the mesoglobules, and at different jump depths to influence the thermodynamic driving force in the solution to mix.

## 9.2    Experimental details

**Materials.**    Poly($N$-isopropylacrylamide) (PNIPAM) with a molar mass $M_n = 36\ 000$ g mol$^{-1}$ and a dispersity of 1.26 (end groups carboxylic acid and a hydrogen atom, respectively) was purchased from Sigma-Aldrich. It was dissolved at a concentration of 3 wt% in D$_2$O, which is above the overlap concentration. D$_2$O was used to ensure a maximum contrast between water-rich and polymer-rich phases during the SANS measurements.

**Small-angle neutron scattering.**    The SANS experiments were carried out in the same way as described in Chapter 8, see Section 8.2 for more details. However, jumps are performed from the two-phase state to the one-phase state to investigate the disintegration of mesoglobules. The performed pressure jumps are shown in Figure 9.1. In the low-pressure (LP) regime, four jumps are performed with pressure changes of $\Delta p = 8$ MPa, 13 MPa, 19 MPa and 31 MPa, starting at $p = 17$ MPa and $T = 35.1$ °C. In the high-pressure (HP) regime, three jumps with pressure changes of $\Delta p = $ -17 MPa, -25 MPa and -45 MPa with a starting point at $p = 105$ MPa and $T = 35.1$ °C are performed.

## 9.3    Mesoglobule disintegration in the low-pressure regime

Figure 9.2 displays the scattering curves after the jumps from the two-phase state to the one-phase state in the LP regime, revealing the disintegration process of mesoglobules. The pre-jump scattering curves feature a shoulder at low $q$ values, which indicates that mesoglobules with sizes of $\sim$70-80 nm are present. In the high-$q$ region, a weak shoulder is present, which originates from the inhomogeneities inside the mesoglobules. As discussed in Chapter 8, the mesoglobules in the LP regime have a dense PNIPAM shell, that prevents their coalescence. In addition, the shell traps water inside the mesoglobules, leading to the ob-
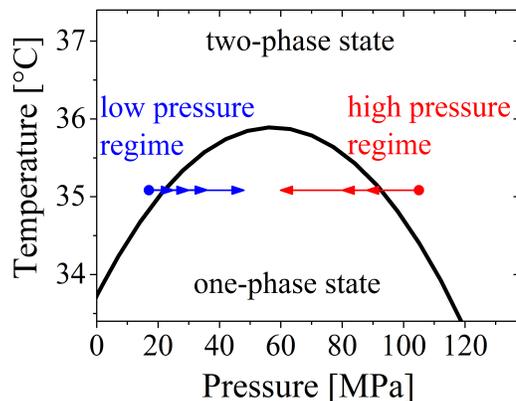
Figure 9.1: Phase diagram of the 3 wt% PNIPAM solution in $D_2O$ in the temperature-pressure frame [132]. The start and target pressure of the performed pressure jumps are marked with blue arrows in the LP regime and with red arrows in the HP regime.

served inhomogeneities at small length scales.

After each jump, the solvent quality is increased sharply, resulting in a good solubility of PNIPAM. The most obvious feature after all four jumps is the decreasing intensity at small $q$ values until a plateau is reached at later times, which shows that the mesoglobules disappear completely within the duration of the measurement for all jumps. In the high-$q$ region, however, the intensity increases. Chains forming the mesoglobules are dissolved and form structures on small length scales, which are concentration fluctuations in the semi-dilute solution towards the end of the measurement. Only small differences can be distinguished between the jumps: With increasing jump depth, the mesoglobules dissolve more rapidly. The solvent quality is controlled by the depth of the jump. After a shallow jump, the one-phase state is reached but the system remains close to the cloud point. After a deep jump, a state deep in the one-phase state is reached, meaning that the solvent quality is in this case significantly better, and the solubility of the chains is higher. From this argument, it can be expected that mesoglobules disintegrate faster after deep jumps.

Figure 9.3 presents representative scattering curves obtained after the jumps with $\Delta p = 8$, 19 and 31 MPa at various times after the jumps. In this representation, differences in the mechanism of mesoglobule disintegration between the jumps can be observed. After a shallow jump (Figure 9.3a), the shoulder originating from scattering from mesoglobules remains, but becomes weaker in intensity, whereas after a deep jump (Figure 9.3c), the shoulder shifts to lower $q$ values, i.e., the mesoglobules expand.
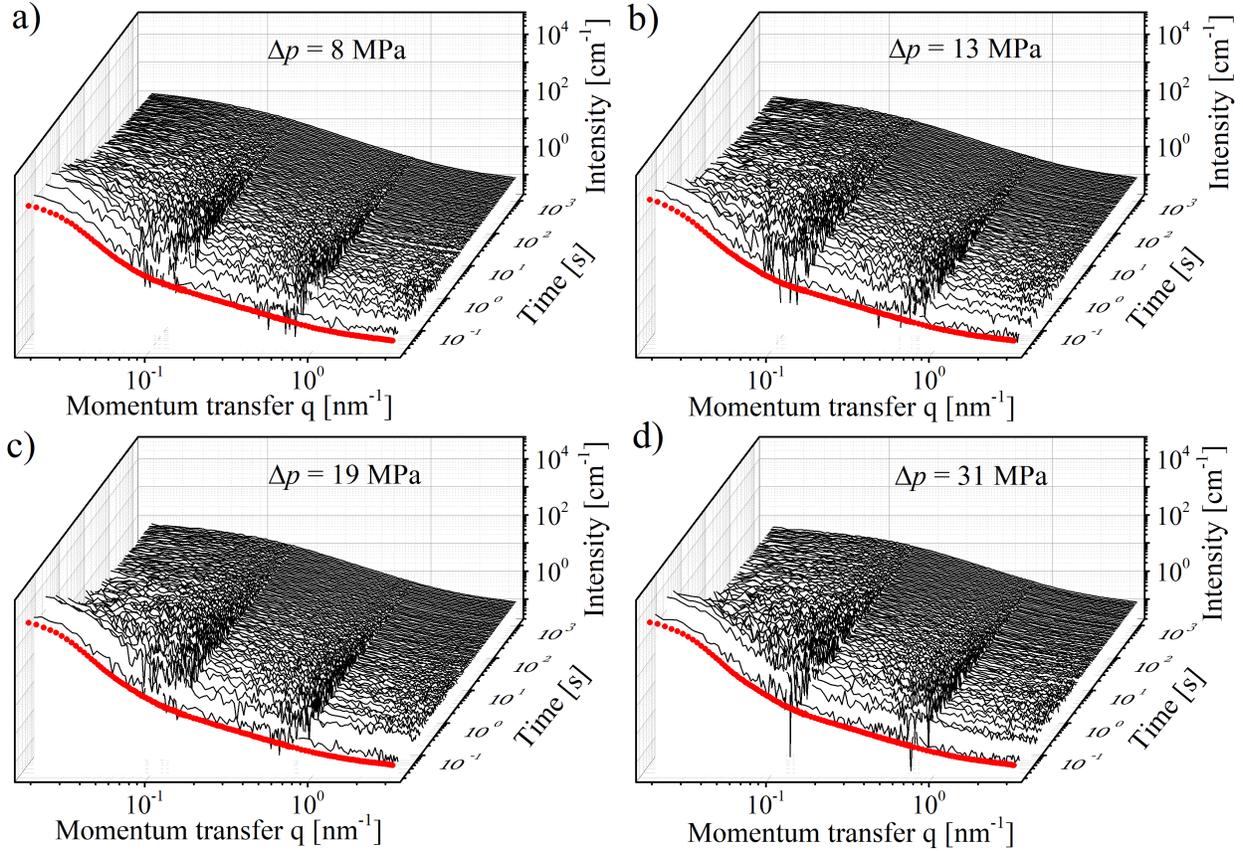
Figure 9.2: SANS curves of the 3 wt% PNIPAM solution in $D_2O$ in the LP regime after jumps from the two-phase state to the one-phase state starting at $T = 35.1$ °C and $p = 17$ MPa with pressure changes of $\Delta p = 8$ MPa (a), 13 MPa (b), 19 MPa (c) and 31 MPa (d). Red symbols: pre-jump measurements.

Model fitting is applied to obtain more details on the mesoglobule disintegration after the different jumps. All scattering curves were modeled using the expression

$$I(q) = I_{agg}(q) + I_{OZ}(q) + I_{bkg} \tag{9.1}$$

where $I_{agg}(q)$ is a contribution describing the scattering from mesoglobules, $I_{OZ}(q)$ is the Ornstein-Zernike structure factor (equation 4.31), and $I_{bkg}$ is an incoherent background. In Figure 9.3, respresentative scattering curves with their fits are shown for three jumps at various times after the jump. Directly after the jumps, the sizes of the mesoglobules can still be resolved, and the Guinier-Porod form factor (equation 4.26) is used for $I_{agg}(q)$. It provides the radius of gyration $R_g$ of the mesoglobules, the Guinier amplitude $I_G$ and the Porod exponent $m$, indicative of the surface structure of the mesoglobules. During these times, the Ornstein-Zernike structure factor accounts for scattering from inhomogeneities inside the mesoglobules as well as from chains in the solution, and gives the correlation length of concentration fluctuations $\xi$ and the Ornstein-Zernike amplitude $I_{OZ}$, which is a

measure of the scattering strength. At later times (after 4.0 s, 0.31 s, 0.39 s and 0.48 s for $\Delta p = 8$ MPa, 13 MPa, 19 MPa and 31 MPa, respectively), scattering from mesoglobules cannot be distinguished anymore, and the system is characterized by a single length scale, the correlation length of concentration fluctuations, modeled with the Ornstein-Zernike structure factor. The remaining weak forward scattering resulting from large-scale inhomogeneities was modeled using the Porod approximation (equation 4.25), which provides a value for $m$. Excellent agreement between the data and the fits is obtained in all cases.
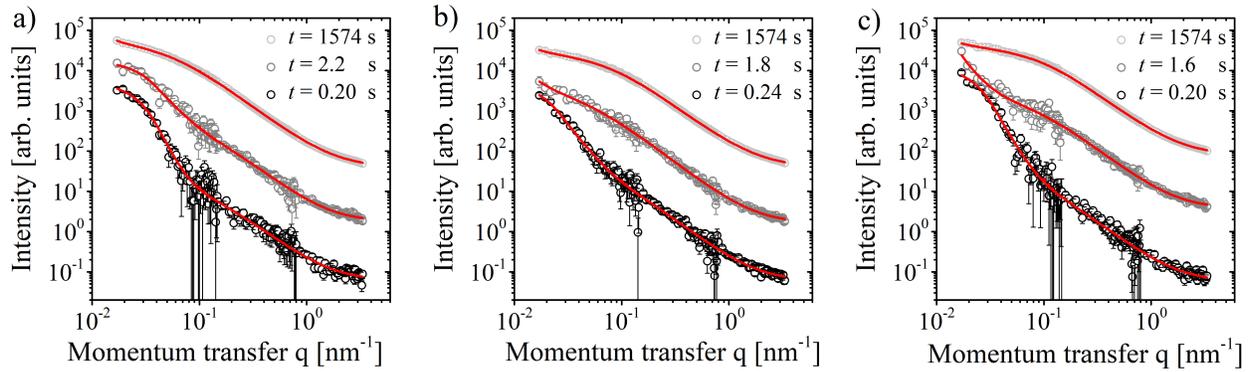


Figure 9.3: Representative fits of the SANS data in the LP regime at $\Delta p = 8$ MPa (a), 19 MPa (b) and 31 MPa (c). For each jump scattering curves are shown in directly after the jump (black curves), at intermediate times (grey curves) and at the end of the run (light grey curves) at times as indicated in the graphs. Red lines: fits of equation 9.1. For clarity, the curves are shifted by factors of 25.

Figure 9.4 displays the parameters obtained from fitting the scattering curves after jumps with pressure changes $\Delta p = 8$, 13, 19 and 31 MPa. After the shallowest jump with pressure change $\Delta p = 8$ MPa (Figure 9.4a and e), $I_G$ and $R_g$ start to decrease at $\sim$0.3 s after the jump, which shows that the mesoglobules decrease in size, accompanied by a decrease in contrast between the polymer-rich and solvent-rich domains. Two contributions to the shrinkage of the mesoglobules can be considered from this observation. Firstly, chains at the shell of the mesoglobules are in contact with the solvent. Therefore, these chains can be dissolved and are released from the mesoglobules, causing their shrinkage with time. Secondly, the trapped water inside the mesoglobules may play an important role. Due to the opening of the shell of the mesoglobules, the trapped water can diffuse out, leading to further shrinkage of the mesoglobules and an increased homogeneity. This type of phase separation would, however, be counter-intuitive, since further de-mixing of water and PNIPAM would be energetically unfavorable. The decreasing size of the mesoglobules is accompanied by a decrease in $m$ from $\sim$4.6 to values well below 4. This shows that the mesoglobules become rough with time, probably caused by the dissolution of chains from the dense shell of the mesoglobules. Simultaneously, $I_{OZ}$ remains constant for $\sim$2 s and decreases afterwards, which suggests that

the mesoglobules become more homogeneous at later times. This may, however, also be an artifact from fitting, since the Guinier-Porod form factor and the Ornstein-Zernike structure factor increasingly overlap (Figure 9.3a). Presumably, the trapped water dissolves the chains inside the mesoglobules, forming a concentrated PNIPAM solution. As this leads to an increased homogeneity of the mesoglobules, a decrease in $I_{OZ}$ may be expected. However, the increasing amount of dissolved chains in the solvent-rich phase contributes with time to the scattered intensity, leading to the constant trend of $I_{OZ}$ during the first $\sim$2 s.
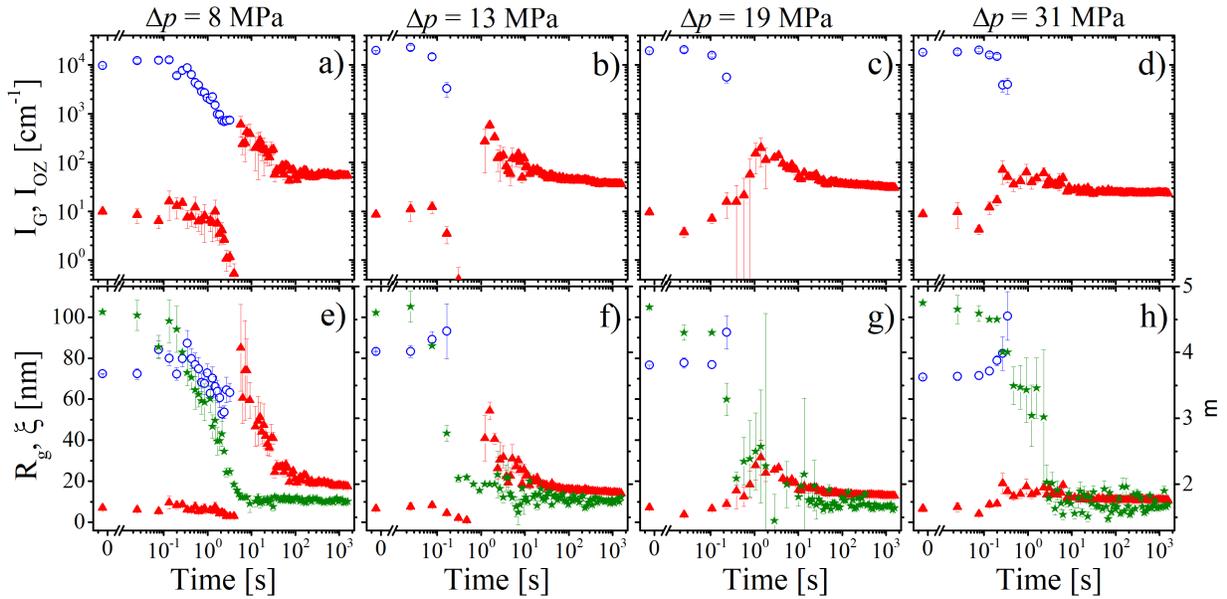


Figure 9.4: Time dependence of the parameters from fitting the SANS data in the LP regime for the pressure jumps as indicated above the graphs. (a) - (d): Guinier amplitude $I_G$ (blue circles) and Ornstein-Zernike intensity $I_{OZ}$ (red triangles). (e) - (h): Radius of gyration of the mesoglobules $R_g$ (blue circles, left axis), correlation length of concentration fluctuations $\xi$ (red triangles, left axis), and Porod exponent $m$ (green stars, right axis).

After $\sim$5 s, the Ornstein-Zernike structure factor in combination with the Porod approximation was sufficient to fully describe the scattering curves. At this time, the mesoglobules transformed from well-defined particles to rough concentrated phases inside a dilute polymer solution. Except for a discontinuity at $\sim$5 s after the jump, which may be due to the differences in both fitting expressions, $\xi$ follows the decreasing trend of $R_g$ of the mesoglobules, until it reaches a steady value. This shows the ongoing disintegration by dissolution of chains at the surface of the concentrated phases. As disintegration continues, the polymer solution around the concentrated phases changes from dilute to semi-dilute. Initially, scattering from isolated chains is dominated by the scattering from the concentrated phases, as both con-

tributions overlap. With time, when more chains are dissolved completely, the fraction of scattering from the solution becomes more important, and the value of $\xi$ obtained from the fits approaches the correlation length of concentration fluctuations in the now semi-dilute solution.

The parameters obtained from fitting the scattering curves after the deepest jump with $\Delta p = 31$ MPa are shown in Figure 9.4d and h. Contrary to the behavior of the mesoglobules after the smallest jump, swelling of the mesoglobules is observed at $\sim$0.08 s after the jump until $R_g$ cannot be resolved anymore due to the limited $q$ range. This shows that the mechanism of mesoglobule disintegration must be fundamentally different from the mechanism described above for the shallowest jump. Also $I_{OZ}$ and $\xi$ behave differently: After $\sim$0.08 s, both quantities increase and describe the structure of the system until a semi-dilute solution is reached. From these observations, the mechanism of mesoglobule disintegration can be deduced. Similar to the shallowest jump, the trapped water inside the mesoglobule dissolves chains around it immediately. The swelling of the mesoglobules may be due to the diffusion of water into the mesoglobules, which is influenced by the visco-elastic effect. Due to the low mobility of the dehydrated chains and the entanglements between them, the diffusion of water into the mesoglobules is hindered. After the shallowest jump, the tendency to mix is only weak, and therefore, the water molecules are not able to penetrate the mesoglobules. After the deepest jump, however, the tendency to mix is strong, and the diffusion of water into the mesoglobules occurs. This is consistent with the observed decrease of $m$, which, similarly to the shallowest jump, starts to decrease immediately after the jump, showing that the aggregates rough with time. In addition, the dilution of the concentrated phases inside the mesoglobules leads to an increase of $\xi$, as observed. This process of swelling presumable continues until the mesoglobules span over the entire solution, resulting in a homogeneous semi-dilute solution.

The description of mesoglobule disintegration after the jumps with moderate pressure changes is more complicated, as it contains contributions from both mechanisms described so far. Figure 9.4c and g present the parameters obtained from fitting the scattering curves after the jump with $\Delta p = 19$ MPa. The time dependencies of the determined lengths and corresponding intensity contributions to the total scattering are similar to those obtained for the jump with $\Delta p = 31$ MPa. At $\sim$0.1 s after the jump, an increase in $R_g$ accompanied by a strong decrease in $m$ are observed, which shows that the dense shell of the mesoglobules opens. This allows water to enter the mesoglobules, resulting in their swelling.

Simultaneously, both $\xi$ and $I_{OZ}$ increase. Thus, also in this case, chains in the interior of the mesoglobules are dissolved and diluted immediately with the water entering the mesoglobules, leading to decreased homogeneity of the mesoglobules. At later times, a maximum in $\xi$ as well as in $I_{OZ}$ is observed, which are more pronounced than the respective maxima observed after the jump with $\Delta p = 31$ MPa. The Ornstein-Zernike structure factor describes scattering from both concentration fluctuations in the (semi-) dilute solution and the interior of the mesoglobules, it is therefore impossible to separate both contributions. At early times after the pressure jump, the scattered intensity from concentration fluctuations inside the mesoglobules dominates. After the mesoglobules have disintegrated completely, the concentration fluctuations in the now semi-dilute solution are observed. After the jump with $\Delta p = 19$ MPa, the disintegration of the mesoglobules is slower than after the jump with pressure change $\Delta p = 31$ MPa. Therefore, inhomogeneities in the mesoglobules may exist longer, leading to the observed increase of $\xi$.

The behavior of the system after the jump with $\Delta p = 13$ MPa, shown in Figure 9.4b and f, shows similarities with the behavior after both $\Delta p = 8$ MPa and $\Delta p = 31$ MPa. Directly after the jump, an increase in the size of the mesoglobules, similar to that after the jump with pressure change $\Delta p = 31$ MPa, shows that water diffuses into the mesoglobules, resulting in their swelling. However, this is not reflected in the evolution of $\xi$, which shows a decreasing trend, as for $\Delta p = 8$ MPa. Thus, the mesoglobules become more homogeneous, meaning that the chains in the interior of the mesoglobules are dissolved shortly after the jump, but stays dense. At later times, the size of the mesoglobules cannot be resolved anymore, and the Porod approximation was used to account for scattering from the mesoglobules. Between $\sim0.5$ and $\sim1$ s after the jump, only the Porod approximation was sufficient to describe the system in the measured $q$ range, i.e., no inhomogeneities at smaller length scales were observed. After that, a shoulder at low $q$ values appeared, indicating the presence of structures on large length scales. $\xi$, resulting from fits with the Ornstein-Zernike structure factor, decreases until the end of the run. This behavior is incompatible with the mechanism of mesoglobule disintegration after large jumps, where the ongoing expansion of the mesoglobules resulted in an increasing $\xi$. A speculative explanation for this behavior is that the mesoglobules disintegrate into fragments before being dissolved completely.

For all jump, the time where the final value of $\xi$ is reached reflects the time needed to dissolve the mesoglobules completely, which is $\sim500$, $\sim300$, $\sim100$ and $\sim10$ s for $\Delta p = 8$, 13, 19 and 31 MPa, respectively. It follows that, after deep jumps, the dissolution of mesoglob-

ules is faster than after shallow jumps, which scales with the quality of the solvent after the jumps (Chapter 5). At the end of the runs, $\xi$ reaches a value of $\sim$17, $\sim$14, $\sim$13 and $\sim$11 nm for $\Delta p = 8$, 13, 19 and 31 MPa. Thus, for target pressures deep in the one-phase state, the chains adopt an extended conformation due to the strong polymer-water interaction, resulting in small values of $\xi$.
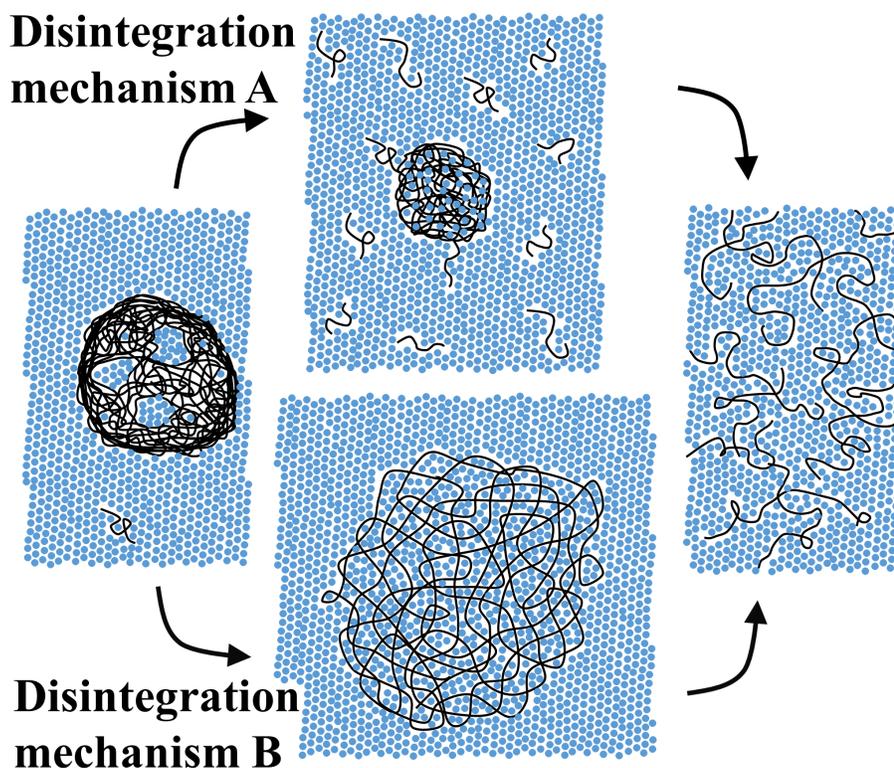


Figure 9.5: Schematic representation of the pathway of mesoglobule disintegration in the LP regime after shallow jumps (disintegration mechanism A) and after deep jumps (disintegration mechanism B).

In summary, two mechanisms of mesoglobule disintegration are observed in the LP regime, schematically represented in Figure 9.5. For shallow jumps, disintegration mechanism A in Figure 9.5 dominates: Water trapped inside the mesoglobules dissolves the chains inside, leading to increased homogeneity. Furthermore, the chains at the surface of the mesoglobules are dissolved, changing the solution around the mesoglobules from dilute to semi-dilute, until the mesoglobules disintegrated completely. For deep jumps, the disintegration is dominated by mechanism B in Figure 9.5: Also in this case, trapped water inside the mesoglobule dissolve chains around it immediately. The mesoglobules swell because the high solvent quality allows the water to diffuse directly into them, thereby diluting the polymer-rich phases. This swelling process continues until the mesoglobules span over the entire solution, result-

ing in a homogeneous semi-dilute solution. Presumably, both mechanisms affect mesoglobule disintegration after jumps with intermediate $\Delta p$.

## 9.4    Mesoglobule disintegration in the high-pressure regime

Figure 9.6 displays the scattering curves after the jumps from the two-phase state to the one-phase state in the HP regime, revealing the deformation process of mesoglobules at high pressures. The pre-jump scattering curves consist of weak forward scattering and a pronounced shoulder above $\sim 0.1$ nm$^{-1}$. As discussed in Chapter 8, these contributions are due to the scattering from very large mesoglobules that contain a large amount of water. After all pressure jumps, the solvent quality changes rapidly from bad to good. Already after 0.1 s, the forward scattering weakened significantly after all jumps, meaning that the mesoglobules have disappeared. However, the data are rather noisy during this time. Thus, the disintegration of the mesoglobules is significantly faster in the HP regime than in the LP regime, where it took, depending on $\Delta p$, between 0.3 and 5 s to the point at which particles with well-defined surfaces disappeared completely. In all cases, a shoulder at $\sim 0.1$ nm$^{-1}$ remains, indicating the presence of concentration fluctuations in the semi-dilute solutions.
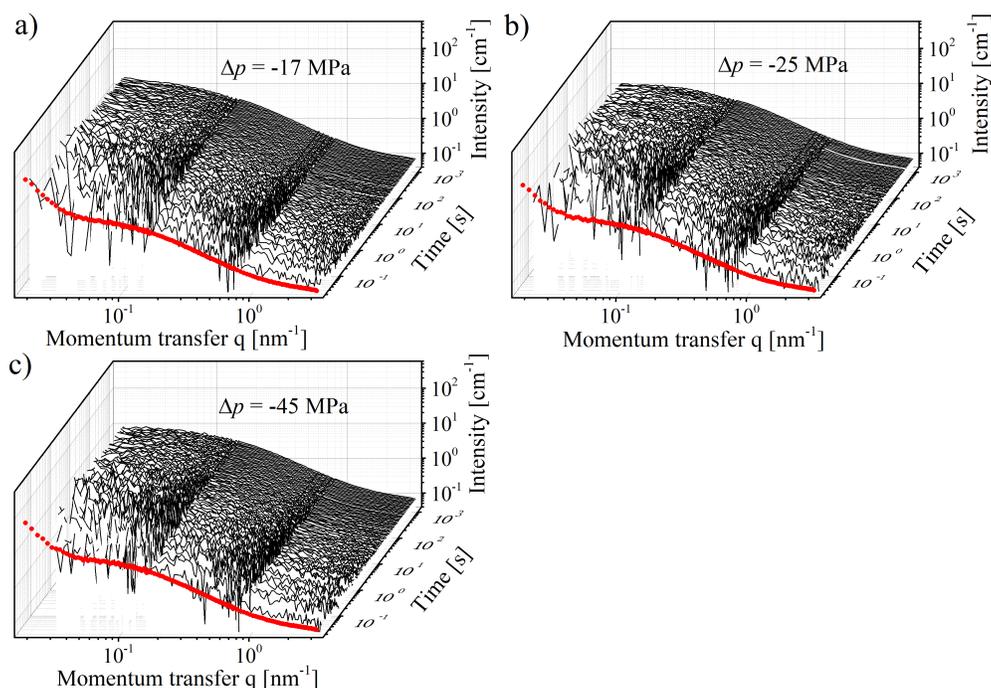


Figure 9.6:   SANS curves of the 3 wt% PNIPAM solution in D$_2$O in the HP regime after jumps from the two-phase state to the one-phase state starting at $T = 35.1$ °C and $p = 105$ MPa with pressure changes of $\Delta p = $ -17 MPa (a), -25 MPa (b), -45 MPa (c). Red symbols: pre-jump measurements.

Representative scattering curves obtained at various times after all jumps are presented in Figure 9.7. The graphs reveal that the dissolution is faster after deep jumps than after shallow ones: At $\sim$2 s, significant forward scattering is still present for $\Delta p$ = -17 MPa, whereas it is very weak for $\Delta p$ = -25 and -45 MPa. Due to a mismatch in the slope of the scattering curve in the overlap region between the SANS measurements performed at SDDs of 34 m and 8 m (at $\sim$0.2 nm$^{-1}$), only the measurements at SDD = 8 and 1.5 m, i.e., between 0.09 and 3.3 nm$^{-1}$, are evaluated. Therefore, the scattering curves in the HP regime were modeled by

$$I(q) = I_{OZ}(q) + I_{bkg} \qquad (9.2)$$

Here, $I_{OZ}(q)$ is the Ornstein-Zernike structure factor (equation 4.31) and $I_{bkg}$ an incoherent background. Figure 9.8 displays $I_{OZ}$ and $\xi$, resulting from the fits, after the pressure jumps with $\Delta p$ = -14, -25 and -45 MPa. After all jumps, $I_{OZ}$ decreases slightly, from $\sim$8 cm$^{-1}$ to $\sim$7, $\sim$6 and $\sim$4 cm$^{-1}$ for $\Delta p$ = -14, -25 and -45 MPa, respectively. After this minimum, $I_{OZ}$ increases again until it reaches its final value of $\sim$8, $\sim$7.5 and $\sim$7 cm$^{-1}$ for $\Delta p$ = -14, -25 and -45 MPa, respectively, at the end of the measurement. The time at which the final value of $I_{OZ}$ is reached reflects the time that is needed for the complete dissolution of the mesoglobules. For $\Delta p$ = -17, -25 and -45 MPa, it is $\sim$100, $\sim$30 and $\sim$4 s, respectively. Thus, the strong tendency to mix after deep jumps results in a fast dissolution process. Similar behavior is observed for $\xi$: Directly after the jump, $\xi$ decreases after all jumps. At later times, $\xi$ increases and reaches a value of $\sim$8.0, $\sim$7.5 and $\sim$6.9 cm$^{-1}$ for $\Delta p$ = -14, -25 and -45 MPa, respectively, at the end of the measurement. As in the LP regime, the strong polymer-water interaction at target pressures deep in the one-phase state results in extended chain conformations, and therefore a smaller value of $\xi$.

These results provide insights into the disintegration mechanism of the mesoglobules at high pressure. As described in Chapter 6, in the two-phase state at high pressure the mesoglobules are large and contain a significant amount of water. The initial decrease of $\xi$ directly after the jump may be a result of rearrangements inside the mesoglobules: Inhomogeneities inside the mesoglobules disappear due to the increased solubility of the chains. As the less dense regions with large concentration fluctuations scatter more strongly than denser regions, this increased homogeneity of the interior of the mesoglobules therefore leads to a decrease in $\xi$. Due to the absence of a dense shell around the mesoglobules at high pressure, water can diffusive into the mesoglobules, leading to their swelling. The density of PNIPAM in the mesoglobules therefore reduces, which leads to an increase in $\xi$ at later times. The disintegration mechanism after all jumps in the HP regime is therefore similar to that
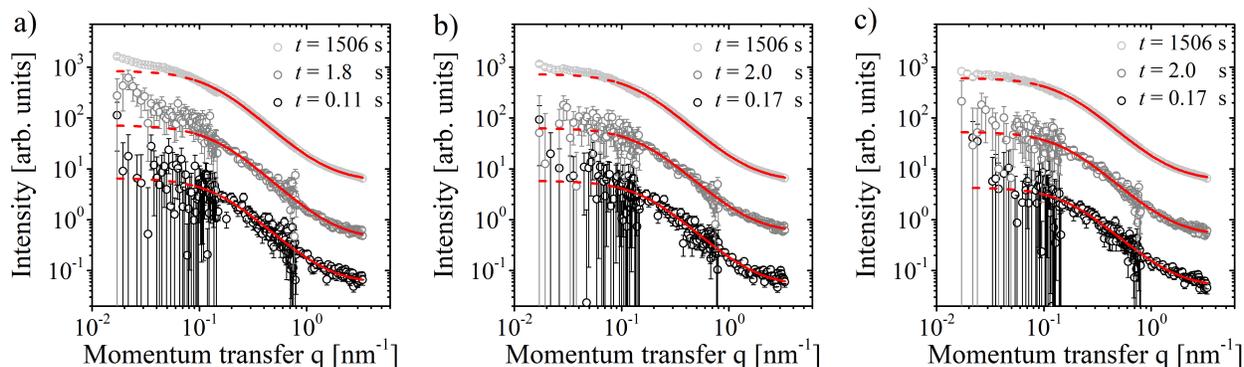
Figure 9.7:   Representative fits of the SANS data in the LP regime at $\Delta p$ = -17 MPa (a), -25 MPa (b) and -45 MPa (c). For each jump scattering curves are shown in directly after the jump (black curves), at intermediate times (grey curves) and at the end of the run (light grey curves) at times as indicated in the graphs. Red solid lines: fits of equation 9.2. Red dashed lines: extrapolations of the fits to lower $q$ values. For clarity, the curves are shifted by factors of 10.

after large $\Delta p$ in the LP regime (disintegration mechanism B in Figure 9.5): Presumably, the mesoglobules swell due to the diffusion of water into the mesoglobules, which dilutes their interior until the mesoglobules span the entire system, thus forming a semi-dilute solution.

## 9.5    Conclusions

For the first time, the kinetics of the dissolution of mesoglobules composed of homopolymers is investigated. At this, pressure jumps from the two-phase state to the one-phase state of an aqueous PNIPAM solution at both low and high pressure were performed in combination with small-angle neutron scattering, varying the depth of the jump to control the solvent quality.

At low pressure, the two-phase state is composed of mesoglobules that consist of a dense PNIPAM shell that traps a significant amount of water inside them. Their dissolution may follow two different mechanisms, depending on the depth of the jump. After shallow jumps, i.e., to a pressure close to the cloud point, the thermodynamic driving force for mixing is weak. Although water present inside the mesoglobules dissolves the surrounding chains, the system remains dense, which hinders water from outside the mesoglobules to diffuse in. As a result, chains at the surfaces are dissolved one by one, which leads to a shrinkage of the mesoglobules and eventually their complete dissolution. After deep jumps, the thermodynamic driving force for mixing is strong. In this case, the mesoglobules expand due to the diffusion of water into them. This process continues until the mesoglobules span the entire
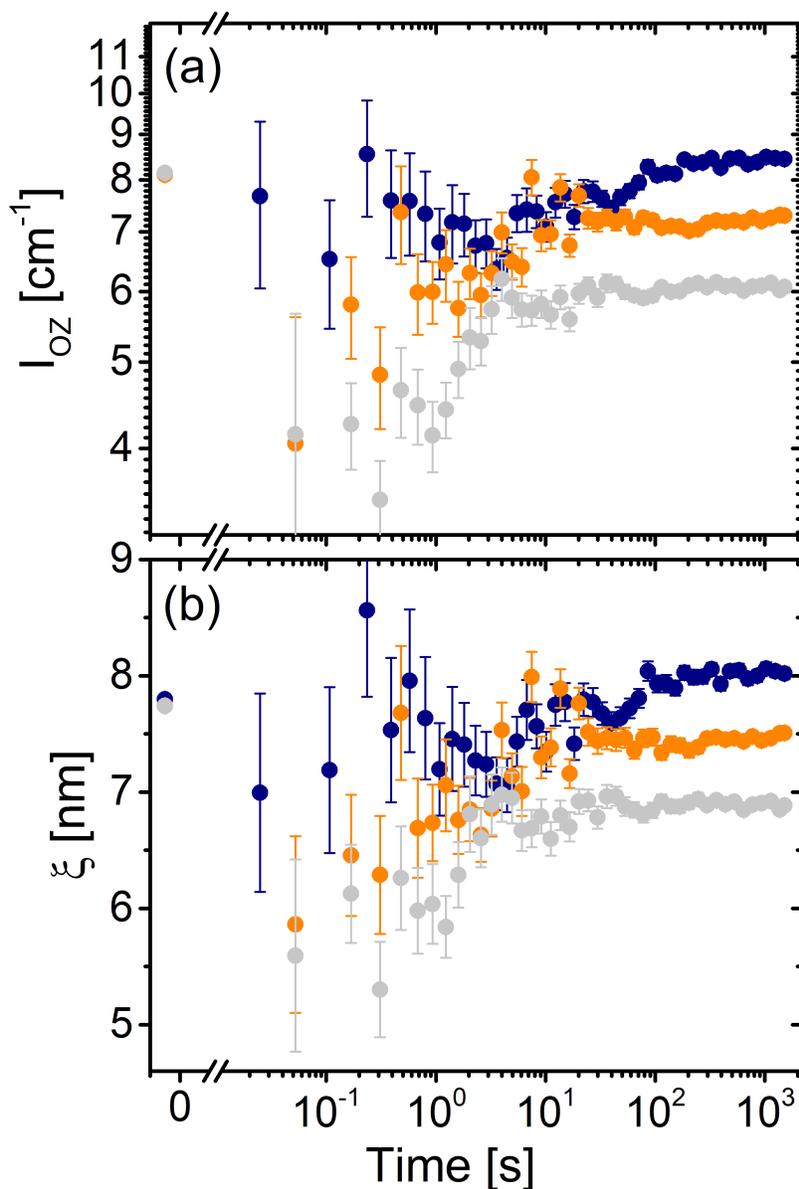
Figure 9.8: (a) $I_{OZ}$ and (b) $\xi$ in dependence on time after the pressure jumps in the HP regime with pressure changes $\Delta p$ = -14 MPa (navy blue symbols), $\Delta p$ = -25 MPa (orange symbols) and $\Delta p$ = -45 MPa (light grey symbols).

system, resulting in a semi-dilute polymer solution.

At high pressure, the mesoglobules present before the jump are large and water-rich. As a result, their dissolution is significantly faster than at low pressures. Furthermore, the results suggest that, also in this case, the mesoglobules expand after the jumps. The loose structure of the mesoglobules does not hinder their enrichment with water, thus, they swell until the mesoglobules span the entire system, also resulting in a semi-dilute polymer solution.

In conclusion, similar to the mechanisms involved in the formation of mesoglobules, the mechanism of mesoglobule disintegration is determined by the balance between visco-elastic effects and the thermodynamic driving force for mixing.

# Chapter 10. Equilibrium-state structure characterization of aqueous PNIPAM solutions containing methanol

In this chapter, the structural properties of a PNIPAM solution in a mixture of water and methanol are determined under equilibrium conditions in dependence on temperature and pressure using small-angle neutron scattering as well as very small angle neutron scattering. The results may provide new insights in the co-nonsolvency effect under high pressure conditions.

## 10.1  Introduction

The work presented in this chapter focuses on the influence of methanol on the structural properties of semi-dilute aqueous PNIPAM solutions, both in the one-phase state and in the two-phase state. In the one-phase state, the chain conformation is strongly influenced by polymer-solvent interactions. In purely aqueous semi-dilute PIPAM solutions, the correlation length of concentration fluctuations, related to the chain conformation (Section 2.1.4), increases with temperature in the one-phase state until it diverges at the critical temperature, following critical behavior [121]. The resulting critical exponents were shown to be smaller than the ones predicted by mean-field theory. As described in Section 3.3, the solubility of PNIPAM is strongly reduced in mixtures of water and methanol in comparison with PNIPAM in pure water or pure methanol, which therefore strongly influences the chain conformation [280]. This effect, the so-called co-nonsolvency effect, is destroyed at high pressure. Whereas at atmospheric pressure, the cloud point temperature is reduced in comparison with that of PNIPAM in pure water, it is strongly increased at high pressures. Earlier theoretical work,

molecular dynamics simulations and Fourier transform infrared spectroscopy measurements suggested that this is due to the preferential binding of water to the chains at high pressure [36, 37], described extensively in Section 3.4. At atmospheric pressure, the competitive binding between water and methanol to the chains results in a decreased solvation, and therefore a reduced solubility of the chains. Due to the preferential binding of the chains with water at high pressure, competition between water and methanol on the chains is strongly reduced, and the co-nonsolvency effect is lost. In addition, the solvent phase is enriched with methanol, which becomes therefore more hydrophobic, resulting in an enhanced solubility of the chains.

In the Chapters 6 and 8, the structural properties of purely aqueous PNIPAM solutions were investigated. It was found that, at atmospheric pressure, dense mesoglobules are formed in the two-phase state that are stabilized by the visco-elastic effect. At high pressure, however, the mesoglobules are water-rich and the visco-elastic effect is strongly weakened. As a result, the mesoglobules are large, and grow by coalescence. Previous SANS experiments also proved the existence of kinetically stable mesoglobule in the two-phase state of aqueous PNIPAM solutions including small fractions of methanol [71]. However, the effect of methanol on the size of the mesoglobules could not be determined. Structural studies on the co-nonsolvency effect are therefore lacking, especially studies under high pressure conditions. In this work, small-angle neutron scattering (SANS) and very small angle neutron scattering (VSANS) are applied to obtain information on the structure at local length scales and large length scales, respectively. In the one-phase state, the chain conformation is probed using SANS, which depends strongly on the interaction between PNIPAM and the solvent molecules. Its changes with varying temperature and pressure may therefore provide new insights in the co-nonsolvency effect under high pressure. The influence of methanol on the formation of mesoglobules is probed by VSANS. By comparing these results with the ones from VSANS on purely aqueous PNIPAM solutions (Chapter 6), the effects of the specific interactions due to the presence of methanol can be identified.

## 10.2   Experimental details

**Materials.**   Poly($N$-isopropylacrylamide) (PNIPAM) with a molar mass $M_n = 36\ 000$ g mol$^{-1}$ and a dispersity of 1.26 (end groups carboxylic acid and a hydrogen atom, respectively) was purchased from Sigma-Aldrich. For the turbidimetry and VSANS measurements, it was dissolved at a concentration of 3 wt% in 80:20 v/v $D_2O$/$CD_3OD$, which is above the

overlap concentration. Fully deuterated solvents were used to ensure a maximum contrast between solvent-rich and polymer-rich phases during the VSANS measurements. For the SANS measurements, PNIPAM was dissolved at a concentration of 3 wt% in 6:74:20 v/v/v $H_2O/D_2O/CD_3OD$, i.e., in 80 vol% water and 20 vol% methanol. The combination of protonated and deuterated water was used to match the scattering length density of water with that of deuterated methanol in order to avoid scattering from solvent clusters, predicted in the literature [149, 151, 281].

**Turbidimetry.** Turbidimetry measurements were performed using a 10 mW HeNe laser ($\lambda = 632.8$ nm) in combination with a photodiode detector. A custom-made copper-beryllium pressure cell with sapphire windows, capable of withstanding pressures up to 400 MPa, was placed in between the laser and the detector. A Viton O-ring separated the sample from the pressure medium (water) with a sample thickness of 1 mm. A pressure generator from SITEC (Maur, Switzerland) was connected to the pressure cell. The temperature in the pressure cell was controlled by a Julabo F12 circulating bath thermostat, and a Pt100 resistance thermometer, attached to the pressure cell, was used to precisely determine its temperature.

The measured transmitted intensity was normalized to the transmitted intensity of the empty pressure cell. During transitions from the one-phase to the two-phase state, the cloud point was defined as the temperature and pressure at which the transmitted intensity starts to decrease. The clearing point during scans from the two-phase to the one-phase state was defined as the temperature and pressure at which the maximum intensity is again reached. Temperature scans were performed with a gradual temperature increase or decrease with a rate of 0.06 K min$^{-1}$, pressure scans were performed in steps of 2.5 MPa in the vicinity of the cloud/clearing point.

**Small-angle neutron scattering.** Small-angle neutron scattering (SANS) measurements were performed at the instrument D11 at the Institute Laue-Langevin, Grenoble, France. A neutron beam with a wavelength $\lambda = 0.6$ nm and spread $\Delta\lambda/\lambda = 0.09$ was used. Measurements were performed at a sample-detector distance (SDD) of 3.0, 10.0 and 39.0 m, resulting in a covered $q$ range of $1.5\times10^{-2}$ - 2.2 nm$^{-1}$. The sample with a thickness of 2 mm was mounted in a temperature-controlled copper beryllium pressure cell, capable of withstanding pressures up to 350 MPa. Temperature scans were performed at pressure of 0.1, 75, 150, 200

and 265 MPa at wide temperature ranges around the respective cloud points. After each change in temperature or pressure, the sample was equilibrated for at least 30 min, followed by measurements with exposure times of 3 min, 12 min and 15 min at the SSD of 3.0, 10.0 and 39.0 m, respectively. The data reduction was performed as described in Section 4.2.2, with a measurement of $H_2O$ to determine the detector sensitivity.

**Very small angle neutron scattering.** Very small angle neutron scattering (VSANS) measurement were performed at the instrument KWS-3 at the Heinz Maier-Leibnitz Zentrum, Garching, Germany [165]. Using a neutron wavelength $\lambda = 1.28$ nm with a spread $\Delta\lambda/\lambda = 0.18$ and an SDD of 9.4 m, a $q$ range of $2.1\times10^{-3}$ - $2.3\times10^{-2}$ $nm^{-1}$ is covered. The sample was mounted in a temperature-controlled custom-made pressure cell withstanding pressures up to 500 MPa, based on the one described in ref. [206]. The sample was placed between sapphire windows and had a thickness of 2 mm, independent of pressure. Temperature scans were performed at pressure of 0.1 and 265 MPa at wide temperature ranges around the respective cloud points. After each change in temperature or pressure, the sample was equilibrated for 5 min, followed by at least 4 measurements of 5 min. The data reduction was performed as described in Section 4.2.2, with a measurement of plexiglass to determine the detector sensitivity.

## 10.3  Phase behavior of PNIPAM in a water/methanol mixture

In Figure 10.1, the phase diagram in the temperature-pressure frame of the 3 wt% PNIPAM solution in 80:20 v/v $D_2O/CD_3OD$, determined from turbidimetry, is presented together with the phase diagram of the 3 wt% PNIPAM solution in $D_2O$. As is the case for PNIPAM solutions in a water/ethanol [35] and water/DMSO mixture [34], the coexistence line of the one-phase and two-phase state has a convex-upward shape. In comparison with the phase diagram of the 3 wt% PNIPAM solution in $D_2O$, it lies at lower temperatures up to a pressure of $\sim$90 MPa. At higher pressures, however, the cloud points exceed that of the purely aqueous solution: The maximum of the coexistence line is shifted to both a higher temperature ($\sim$40 °C) and a higher pressure ($\sim$230 MPa), thus showing that the solubility of PNIPAM is strongly increased at high pressure relative to the purely aqueous PNIPAM solution.

Contrary to the 3 wt% PNIPAM solutions in pure $D_2O$, the measured cloud points of the
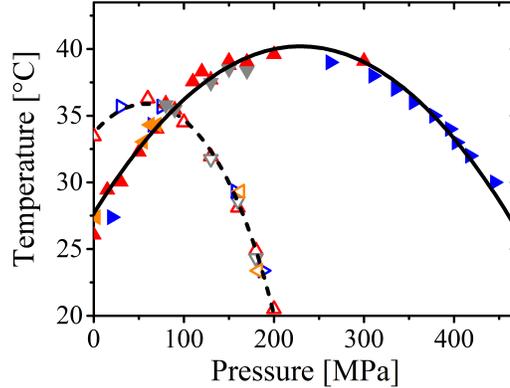
Figure 10.1: Cloud points of the 3 wt% PNIPAM solution in 80:20 v/v $D_2O/CD_3OD$ (filled symbols) and of the 3 wt% PNIPAM solution in $D_2O$ (open symbols). The symbols represent the direction of the scan: heating: red ▲, cooling: grey ▼, increasing pressure: blue ▶, decreasing pressure: orange ◀. The lines are fits of equation 2.11.

Table 10.1: Results from fitting the cloud point data from Figure 10.1 with the Hawley theory (equation 2.11).

|  | $p_0$ [MPa] | $T_0$ [K] | $\frac{V_0 \Delta \beta}{\Delta G_0}$ [MPa$^{-2}$] | $\frac{V_0 \Delta C_p}{\Delta G_0}$ [K$^{-1}$] |
|---|---|---|---|---|
| 3 wt% PNIPAM in $D_2O$ | $59.5 \pm 5.9$ | $263.3 \pm 1.9$ | $(5.89 \pm 0.36) \times 10^{-5}$ | $(2.50 \pm 0.23) \times 10^{-1}$ |
| 3 wt% PNIPAM in 80:20 v/v $D_2O/CD_3OD$ | 230.5 | n/a | n/a | n/a |

3 wt% PNIPAM solution in 80:20 v/v $D_2O/CD_3OD$ cannot be modeled satisfactorily with the Hawley theory (equation 2.11), since only a small part of the total ellipse is available. From a fit (Figure 10.1), it follows that the data follows an elliptical trend, but $p_0$, the pressure at the maximum of the ellipse, is the only parameter that can be determined independently. It equals $230.5 \pm 0.1$ MPa, which is significantly higher than for the 3 wt% PNIPAM solution in pure $D_2O$ (table 10.1). As discussed in section 3.4, this shows that the co-nonsolvency effect in a 3 wt% PNIPAM solution in 80:20 v/v $D_2O/CD_3OD$ is destroyed at high pressures. Whereas the $T_{cp}$ is lower than the one of the PNIPAM solution in pure water, i.e., the solubility is reduced, it is significantly higher at high pressures. To further investigate this effect, insights in the local-scale structures in dependence on pressure from SANS experiments are discussed in the following section.

## 10.4 Local-scale structures from SANS

Figure 10.2 displays the scattering curves of the 3 wt% PNIPAM solution in 6:74:20 v/v/v $H_2O/D_2O/CD_3OD$ in dependence on temperature at all measured pressures. At atmospheric

pressure below the cloud point temperature $T_{cp}$ (Figure 10.2a), a shoulder at $q \sim 0.2$ nm$^{-1}$ is observed, which shows the presence of concentration fluctuations at small length scales. With increasing temperature below $T_{cp}$, a weak increase in intensity is observed. Thus, the concentration fluctuations become more pronounced near $T_{cp}$. Above $T_{cp}$, the scattering curve is dominated by a strong contribution at low $q$ values that indicates the presence of large-scale structures. Still, a weak contribution to the total scattering at high $q$ values is discernible, pointing to the presence of concentration fluctuations at small length scales.
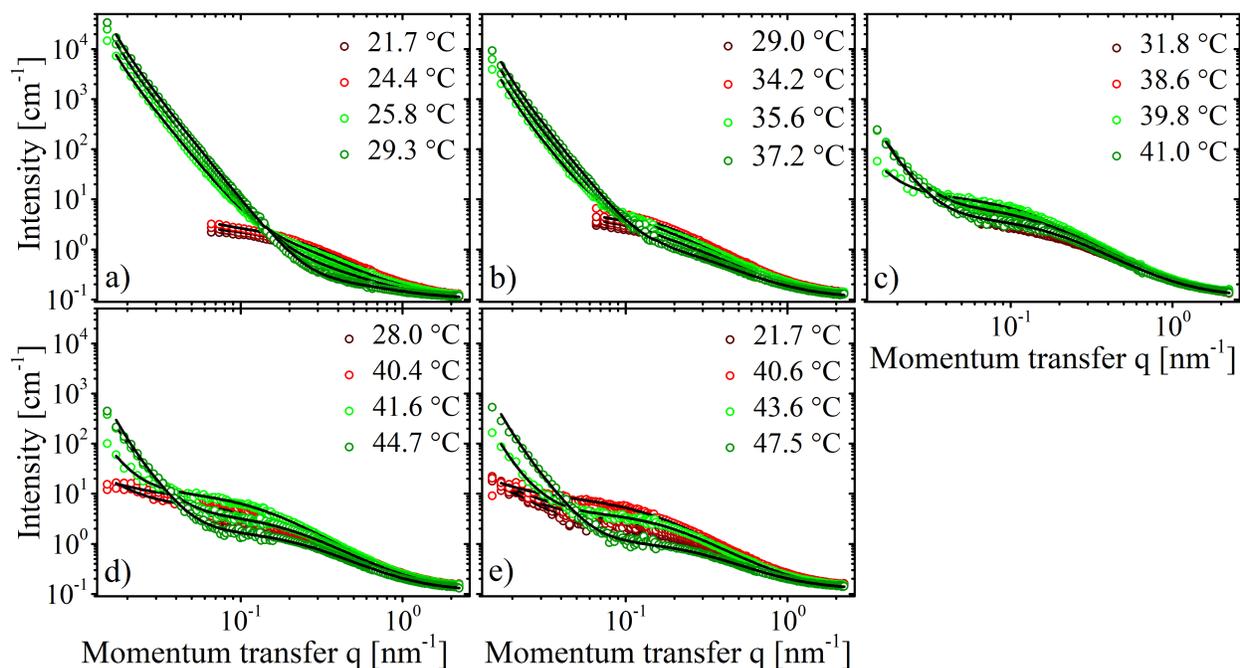


Figure 10.2:  SANS data of the 3 wt% PNIPAM solution in 6:74:20 v/v/v $H_2O/D_2O/CD_3OD$ from heating scans at 0.1 (a), 75 (b), 150 (c), 200 (d) and 265 MPa (e) below $T_{cp}(p)$ (red curves) and above $T_{cp}(p)$ (green curves). Black lines are fits of equation 10.1.

Also at higher pressures (Figure 10.2b-e), the scattering in the one-phase state (below $T_{cp}$) is dominated by concentration fluctuations at small length scales, which becomes more pronounced close to $T_{cp}$. However, a significant contribution of scattering from large scale structures is already observed in the one-phase state, and is most pronounced at 265 MPa (Figure 10.2e). The intensity of forward scattering increases strongly above $T_{cp}$, albeit to a lesser extent than at atmospheric pressure. In the two-phase state, the scattered intensity decreases at high $q$ values, but remains prominent. Thus, concentration fluctuations at small length scales remain present in the two-phase state, which shows that the solvation only decreases weakly.

Quantitative information from the scattering curves was in all cases obtained from fits using the expression

$$I(q) = I_P(q) + I_{OZ}(q) + I_{bkg} \tag{10.1}$$

Here, $I_P(q)$ is the Porod approximation (equation 4.25), accounting for the surface structure of the mesoglobules, and gives the Porod exponent $m$. $I_{OZ}(q)$ is the Ornstein-Zernike structure factor (equation 4.31), which describes concentration fluctuations on small length scales, and gives the Ornstein-Zernike intensity $I_{OZ}$ and the correlation length of concentration fluctuations $\xi$. $I_{bkg}$ is an incoherent background. In Figure 10.3 the Porod exponent $m$, is shown in dependence on the temperature distance from the pressure-dependent cloud point, as determined by turbidimetry. At atmospheric pressure the value increases sharply from $\sim$1.2 below $T_{cp}$ to values of $\sim$4 above. This clearly indicates that, at $T_{cp}$, the system changes from a one-phase state with only very weak composition fluctuations at large length scales to a phase separated structure with smooth interfaces between both phases. In this case, the polymer-rich domains can be identified as mesoglobules, similar to the ones formed in purely aqueous PNIPAM solutions (Chapter 6). At higher pressures, a transition from small to large values of $m$ at $T_{cp}$ is observed as well. The value of $m$ in the one-phase state depends on pressure. Deep in the one-phase state, $m$ increases with pressure from $\sim$1.2 to $\sim$2.5. Thus, the structures at large length scales become more pronounced at high pressure. Furthermore, the strong increase in $m$ at $T_{cp}$ is more gradual than at atmospheric pressure, which shows that the phase transition spans over a large temperature range.
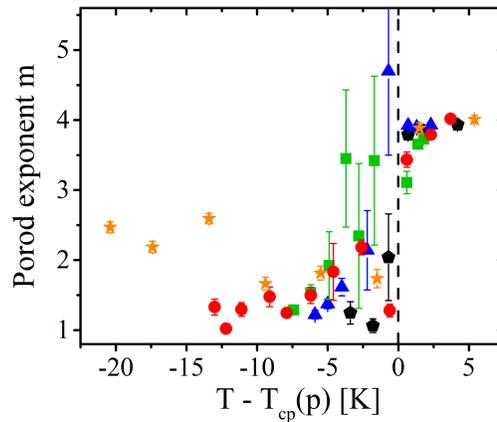


Figure 10.3: Porod exponent $m$ at 0.1 MPa (black pentagons), 75 MPa (blue triangles), 150 MPa (green squares), 200 MPa (red circles) and 265 MPa (orange stars) in dependence on the temperature distance to the respective cloud point temperatures.

$\xi$ gives information on the structure on small length scales, shown in Figure 10.4 in depen-

dence on the temperature distance to the pressure-dependent critical temperature $T_c$, which is close to $T_{cp}$, as discussed below. At all pressures, $\xi$ increases in the one-phase state until it diverges at $T_c$. With increasing temperature in the one-phase state, the solvent quality decreases. As described in section 2.1.4, the value of $\xi$ depends on the conformation of the chains. With increasing temperature the chains shrink, which decreases the total number of overlap points between the chains in the system, leading to an increase in $\xi$. At high pressures, the value of $\xi$ is larger than at low pressures at the same temperature distance to the respective critical temperature. It follows that pressure influences the chain conformation, which may be due to changes in the solvation. Above $T_c$, $\xi$ decreases at all pressures. In this case, the concentration fluctuations inside the mesoglobules mainly contribute to the total scattering at high $q$ values. With increasing temperature, the mesoglobules become more homogeneous, which may be due to non-equilibrium effects due to slow rearrangements in the system. Also in this case, the value of $\xi$ is larger at high pressures, which may be due to the enhanced solvation, even in the two-phase state.
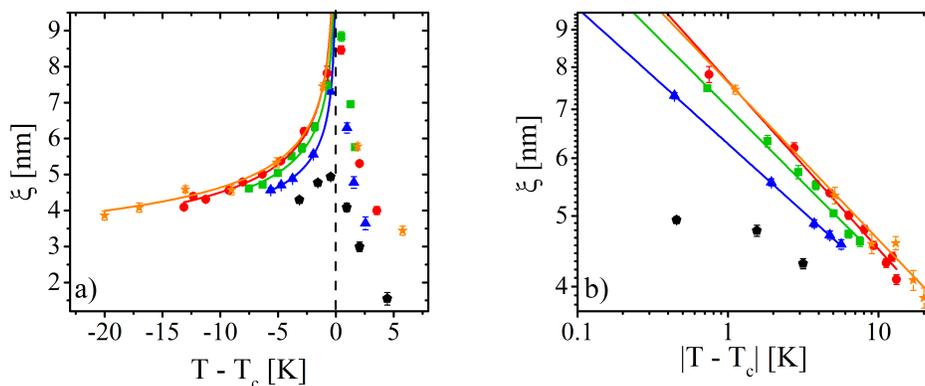


Figure 10.4: (a) Correlation length of concentration fluctuations $\xi$ at 0.1 MPa (black pentagons), 75 MPa (blue triangles), 150 MPa (green squares), 200 MPa (red circles) and 265 MPa (orange stars) in dependence on the temperature distance to the respective critical temperatures. The lines are fits of equation 10.2. (b) One-phase state data of (a) in dependence on the absolute value of the temperature distance to the respective critical temperatures.

Also $I_{OZ}$, the scattering intensity of concentration fluctuations at $q = 0$, increases with temperature below $T_c$ and decreases above for all pressures, as shown in Figure 10.5a. As the scattering strength increases with $\xi$, $I_{OZ}$ and $\xi$ follow the same trends [41]. Therefore, the temperature and pressure dependence of $I_{OZ}$ behave similar to $\xi$.
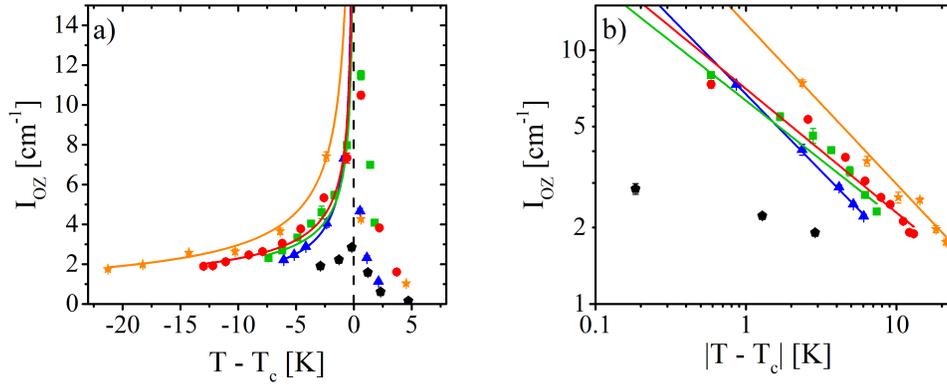
Figure 10.5: (a) Ornstein-Zernike amplitude $I_{OZ}$ at 0.1 MPa (black pentagons), 75 MPa (blue triangles), 150 MPa (green squares), 200 MPa (red circles) and 265 MPa (orange stars) in dependence on the temperature distance to the respective critical temperatures. The lines are fits of equation 10.3. (b) One-phase state data of (a) in dependence on the absolute value of the temperature distance to the respective critical temperatures.

## 10.4.1 Critical behavior

The increase of $\xi$ and $I_{OZ}$ in the one-phase state and their divergence around the phase separation temperature suggest that both quantities follow critical behavior at all pressures, as described in Section 2.1.4. Although it was argued that the phase separation of aqueous PNIPAM solution is a first-order process [100, 101], the divergence of the correlation length at $T_c$ suggests that the transition is a higher-order one [55] and power laws describing physical quantities such as the one given in equation 2.3 may be applied to determine the critical exponents and thereby the universality class it belongs to. The temperature dependence of the correlation length can be described by [55]

$$\xi \propto |T_c - T|^{-\nu_\xi} \tag{10.2}$$

with $T_c$ the critical temperature and $\nu_\xi$ the critical exponent of concentration fluctuations. Similarly, $I_{OZ}$ is expected to follow a power law, given by [55]

$$I_{OZ} \propto |T_c - T|^{-\gamma_I} \tag{10.3}$$

where $\gamma_I$ is the critical exponent of the susceptibility. In Figures 10.4b and 10.5b, the data are shown in a log-log representation. As can be seen, at all pressures except 0.1 MPa, straight lines are obtained, which allows the use of equations 10.2 and 10.3 to determine $\nu_\xi$ and $\gamma_I$ in dependence on pressure. At 0.1 MPa, the deviation from a straight line are presumbly caused by the poor quality of the data as well as the small number of data points

in the one-phase state. Therefore, the critical exponents cannot be determined for 0.1 MPa.

The fits to the data are shown in Figures 10.4 and 10.5, respectively, in both representations, where the values of $T_c$ are adapted from the fits. In all cases, excellent fits are obtained. At all analyzed pressures, the value of $\nu_\xi$ equals $\sim$0.2, i.e., independent of pressure. This is in agreement with previous studies on PNIPAM in purely aqueous solutions at atmospheric pressure [121] and high pressures [77], where also values well below 0.5 were found. The obtained values of $\nu_\xi$ do not match with previously described universality classes. For polymer solutions, it is expected that, close to $T_c$, the system can be described by the 3D Ising model [122]. Further away, a cross-over temperature determined by the Ginzburg criterion exists, which marks the transition to mean-field universality class [282]. The obtained value of $\nu_\xi$ is much lower than the ones predicted by both mean-field theory ($\nu_\xi = 0.5$) and the 3D Ising model ($\nu_\xi = 0.63$) [55]. $\gamma_I$ adopts values between $\sim$0.4 and $\sim$0.6, without a clear pressure dependence. Also in this case, the values are much lower than those predicted by mean-field theory ($\gamma_I = 1$) and the 3D Ising model ($\gamma_I = 1.24$). In this respect, PNIPAM behaves differently from solutions of other types of polymers. Studies on polystyrene in cyclohexane [62, 283, 284] and methylcyclohexane [285] in a broader temperature range confirmed the validity of the 3D Ising model close to the critical temperature and the mean-field theory further away. Therefore, not all types of polymer solutions belong to the same universality class.
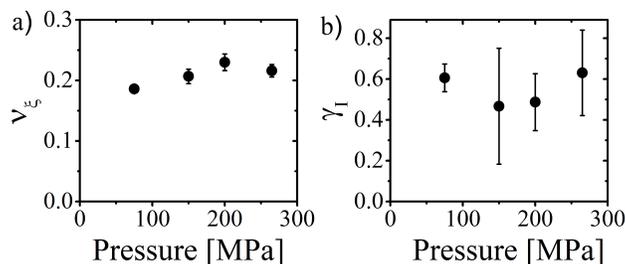


Figure 10.6:  Critical exponent of the correlation length $\nu_\xi$ and (b) the critical exponent of the susceptibility $\gamma_I$ in dependence on pressure.

Several reasons for the discrepancy between the determined values of the critical exponents and the theoretical values may exist. Firstly, it was shown previously using dynamic light scattering measurements on purely aqueous PNIPAM solutions that temporal correlation on long time-scales exist [137]. This may imply the presence of long-range order, which also follows from the weak forward upturn in the scattering curves at low $q$ values (Figure 10.2). As this is not accounted for in the mean-field or 3D Ising universality classes, PNIPAM solutions must be assigned to a different one. Secondly, as mentioned above, the

phase separation in PNIPAM solutions may be a first order phase transition [100, 101]. It was argued before that a purely first-order phase transition leads to an apparent value of $\gamma_I$ of 0 [286]. As the obtained values of $\gamma_I$ in this case are below that expected by all existing universality classes [55], the phase transition may comprise elements of both a first-order and a higher-order transition.

## 10.4.2 Determination of interaction parameters

To evaluate the data in terms of thermodynamics, the Flory-Huggins interaction parameter $\chi$ is determined from the values of $\xi$. In this way, the interaction strength between the chains and the solvent can be quantified. The chain conformation, quantified by the correlation length of concentration fluctuations, depends on the interaction strength between chains and solvent. Thus, it is possible to relate $\xi$ to $\chi$. Following the Panyukov-Rabin theory for the scattering patterns from gels [287, 288], the scattering from polymer solutions is determined, considering only thermal fluctuations, i.e., static correlations due to chemical crosslinks are discarded [289, 290]. From a mean-field approach, taking into account excluded volume effects, an Ornstein-Zernike type structure factor was obtained (equation 4.31) with the correlation length of concentration fluctuations given by [289, 290]

$$\xi = a[12\phi(1 - 2\chi + \phi)]^{-1/2} \tag{10.4}$$

with $\chi$ the polymer-solvent interaction parameter, $a$ the monomer length and $\phi$ the polymer volume fraction. In this case, PNIPAM is dissolved in a mixture of water and methanol. In principle, the interaction strengths between the three different components should be distinguished from each other, i.e., three different values of $\chi$ should be determined [280]. For a reliable analysis, the solvent mixture is considered as a single solvent in the present case, and the determined interaction parameter between polymer and the solvent molecules $\chi_{eff}$ is thus an effective one.

In Figure 10.7a, $\chi_{eff}$ of the 3 wt% in 6:74:20 v/v/v $H_2O/D_2O/CD_3OD$, calculated using a value of $a$ of 0.812 nm [120, 289] and a PNIPAM volume fraction $\phi$ of 0.03, at all measured pressures is presented in dependence on temperature. In all cases, an increasing trend towards 0.5 at $T_c$ is observed, which shows that the quality of the solvent decreases with temperature until poor solvent conditions are reached at $T_c$. In the one-phase state, $\chi_{eff}$ adopts higher values at high pressure than at low pressure, i.e., the slope of $\chi_{eff}$ is shallower
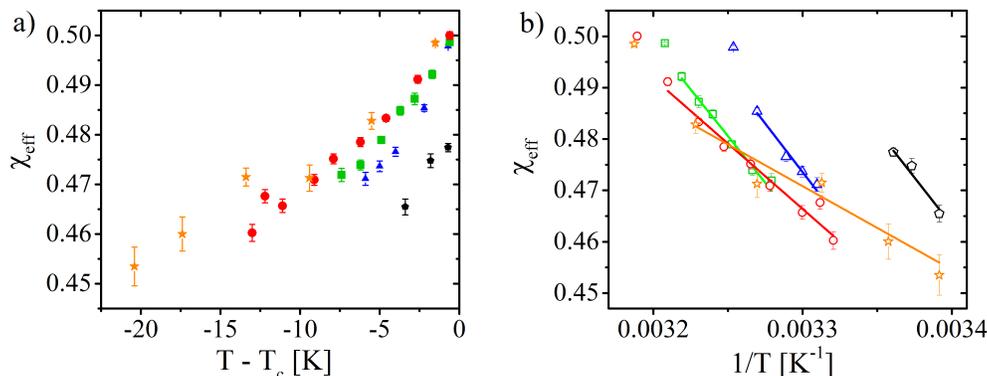
at high pressure.



Figure 10.7: (a) Effective polymer-solvent interaction parameter $\chi_{eff}$ at 0.1 MPa (black pentagons), 75 MPa (blue triangles), 150 MPa (green squares), 200 MPa (red circles) and 265 MPa (orange stars) in dependence on the temperature distance to the respective critical temperatures. (b) Data of (a) in dependence on $1/T$. The lines are fits of equation 10.5.

In the classical Flory-Huggins theory, the energy of mixing is determined from the (enthalpic) interaction between the solute and the solvent, and of the configurational entropy of the polymer (equation 3.1). Entropic effects related to the solvent, e.g. the hydrophobic effect, can be accounted for using an additional entropic term. Alternatively, it can be included in the Flory-Huggins interaction parameter. It was shown emperically that $\chi_{eff}$ follows the relation [291]

$$\chi_{eff} = A + \frac{B}{T} \tag{10.5}$$

with $A$ a local entropic contribution and $B$ an enthalpic contribution. In the Flory-Huggins theory, $B$ is related to interaction energies in the system as [42]

$$B \propto \epsilon_{ps} - \frac{1}{2}(\epsilon_{pp} + \epsilon_{ss}) \tag{10.6}$$

with $\epsilon_{ps}$ the polymer-solvent interaction energy, $\epsilon_{pp}$ the polymer-polymer interaction energy, and $\epsilon_{ss}$ the solvent-solvent interaction energy. Thus, for negative values of $B$, mixing is enthalpically favored.

In Figure 10.7b, $\chi_{eff}$ is presented in dependence on $1/T$. In all cases, a linear trend is observed except very close to the phase separation temperature, i.e., at low values of $1/T$, and can therefore be fitted using equation 10.5, also shown in Figure 10.7b. In all cases, excellent fits are obtained. $A$ and $B$, resulting from the fits, are shown in Figure 10.8 in

dependence on pressure. At atmospheric pressure, the values of $A$ and $B$ are $1.73 \pm 0.27$ and $-372 \pm 78$ K, respectively, which is similar to previously reported values for PNIPAM microgels in pure $H_2O$ (2.15 and -513 K, respectively) [140]. Up to 150 MPa, both quantities stay approximately constant. At higher pressures, however, $A$ decreases towards $\sim 1$ at 265 MPa, whereas $B$ increases to approximately -160 K. A positive value of $A$ implies that local entropic effects favor demixing of the system [291], the decreasing value of $A$ at high pressure therefore shows that the tendency to demix becomes weaker, i.e., the local entropic effects favoring demixing become weaker. In this case, $B$ adopts negative values, which shows that mixing is favored on enthalpic ground [291]. The increasing value of $B$ towards 0 thus implies that the tendency to mix due to enthalpic interactions becomes weaker at high pressure.
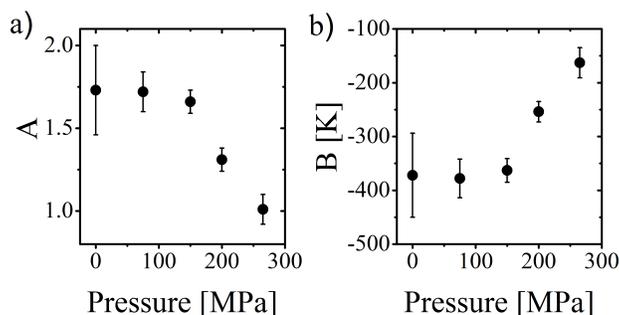


Figure 10.8: Entropic part $A$ and the enthalpic part $B$ of the polymer-solvent interaction parameter according to equation 10.5.

The contribution from local entropic effects to $\chi_{eff}$, quantified by the value of $A$, may originate from the arrangement of water molecules around hydrophobic groups of PNIPAM, i.e., the hydrophobic effect. At atmospheric pressure, the ordered layer of water around hydrophobic groups results in an entropic penalty to the free energy of mixing, which favors de-mixing. The decrease in $A$ indicates that the hydrophobic effect is weakened at high pressure. Two effects may play a role. Firstly, as described in Section 2.3, the bulk water phase becomes more ordered at high pressure, which may also be the case in the presence of methanol. The entropic penalty resulting from the ordered layer of water around hydrophobic groups is therefore reduced, weakening the hydrophobic effect. Secondly, it was suggested previously [37, 38, 39] that methanol is released from the PNIPAM chains at high pressure, described in Section 3.4. As a result, the solvent phase is enriched with methanol and becomes therefore more hydrophobic, thereby further weakening the hydrophobic effect.

The weaker tendency to mix on enthalpic grounds with increasing pressure, as follows from the increase in $B$, suggests that the enthalpic polymer-solvent interactions become weaker at high pressure. This observation can, however, not be explained by the replacement

of methanol with water on the chains. Since the interaction between water and PNIPAM is mediated by hydrogen bonds, enthalpic interaction between water and PNIPAM is much stronger than between methanol and PNIPAM, where the number of hydrogen bonds is strongly reduced [292]. Pica et al. [38] argued that the smaller difference in the solvent-excluded volume between the one-phase state and two-phase state due to a contracted chain conformation at high pressure stabilizes the one-phase state. The resulting decrease in overall chain solvation may therefore lead to weaker enthalpic polymer-solvent interactions, apparent from the increase in $B$. In addition, the predicted contraction of the chain conformation may explain the larger values of $\xi$ in the one-phase state at high pressures (Figure 10.4), as the distance between overlap points, and therefore $\xi$, is larger for contracted chains.

## 10.5    Large-scale structures from VSANS

VSANS allows the investigation of structural properties in the two-phase state, since it probes length scales in the range from ∼100 nm to several $\mu$m. Temperature scans are performed from the one-phase state to the two-phase state at 0.1 and 265 MPa, shown in Figure 10.9. In accordance with the results from VSANS measurements on purely aqueous PNIPAM solutions, presented in Chapter 6, very weak scattering is observed in the one-phase state. In the two-phase state, a single shoulder is present, which marks the presence of structure on large length scales, identified as mesoglobules. At 0.1 MPa, the decay in scattered intensity starts at ∼3×10$^{-3}$ nm$^{-1}$, whereas at 265 MPa, the start of the decay lies at lower $q$ values than can be resolved during the measurements. Thus, also when methanol is present in the solutions, the mesoglobules are much larger at 265 MPa than at 0.1 MPa.

To extract quantitative information from the data, model fitting is applied. As for the purely aqueous PNIPAM solutions (Chapter 6), the scattering curves in the two-phase state are fitted using the expression

$$I(q) = I_{Beaucage}(q) + I_{bkg} \tag{10.7}$$

where $I_{Beaucage}(q)$ is the Beaucage model, given by equation 4.29, and gives the radius of gyration $R_g$ of the mesoglobules as well as their Porod exponent $m$. $I_{bkg}$ is an incoherent background, which was fixed at a value of 300 cm$^{-1}$ for all curves. As can be seen in Figure 10.9, the fits are excellent in all cases. The radius of gyration of the mesoglobules $R_g$, following from fitting the scattering curves, is presented in dependence on temperature at
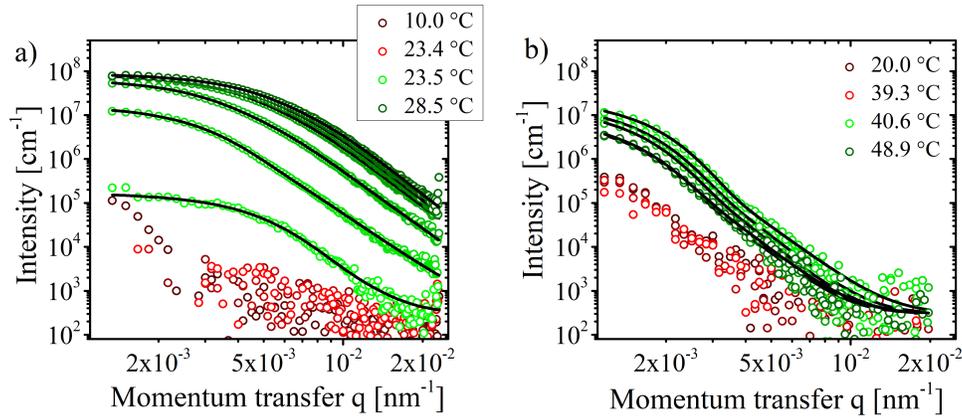
Figure 10.9: SANS data of the 3 wt% PNIPAM solution in 80:20 v/v $D_2O/CD_3OD$ from heating scans at 0.1 (a) and 265 MPa (b) below $T_{cp}(p)$ (red curves) and above $T_{cp}(p)$ (green curves). Black lines are fits of equation 10.7.

both pressures in Figure 10.10a. At 0.1 MPa, $R_g$ decreases steadily from ∼0.8 μm directly after crossing $T_{cp}$, to ∼0.8 μm at a temperature of 4 K above $T_{cp}$, where a constant value is reached. Shortly after crossing $T_{cp}$, stable mesoglobules are formed. As was the case in the purely aqueous PNIPAM solution at atmospheric pressure (Chapter 6), their merging is strongly hindered by the visco-elastic effect. It follows that phase separation continues in the two-phase state: Solvent is released from the mesoglobules during the first 4 K above $T_{cp}$, thereby decreasing their size. The Porod exponent $m$ is shown in Figure 10.10b. It increases from ∼4 to above 4.5 in the first 4 K above $T_{cp}$. This shows that the mesoglobule are initially smooth, and develop a concentration gradient at their surfaces with temperature. This confirms the hypothesis that mesoglobules shrink due to the diffusion of solvent out of the mesoglobules. At the surface, the diffusion of solvent towards the bulk water phase results in a denser structure and becomes inpenetrable for the solvent molecules. Solvent inside the mesoglobules is therefore trapped, leading to a concentration gradient at the surface. It is, however, not possible to distinguish between water and methanol in this case.

At 265 MPa, $R_g$ follows a different trend. Directly after their formation, the mesoglobules shrink from ∼1.4 μm to ∼1.2 μm at $T_{cp} + 1.5$ K. Directly after this decrease in $R_g$, it increases to ∼1.5 μm at $T_{cp} + 4$ K. Therefore, a second mechanism that influences $R_g$ must be present at high pressure. As this was not observed in purely aqueous PNIPAM solutions at high pressure (Chapter 6), it can be attributed to the influence of methanol on the system. $m$ scatters around 4.4 in the entire measured temperature range in the two-phase state. Contrary to the mesoglobules formed at 0.1 MPa, a composition gradient forms directly after their formation at 265 MPa.
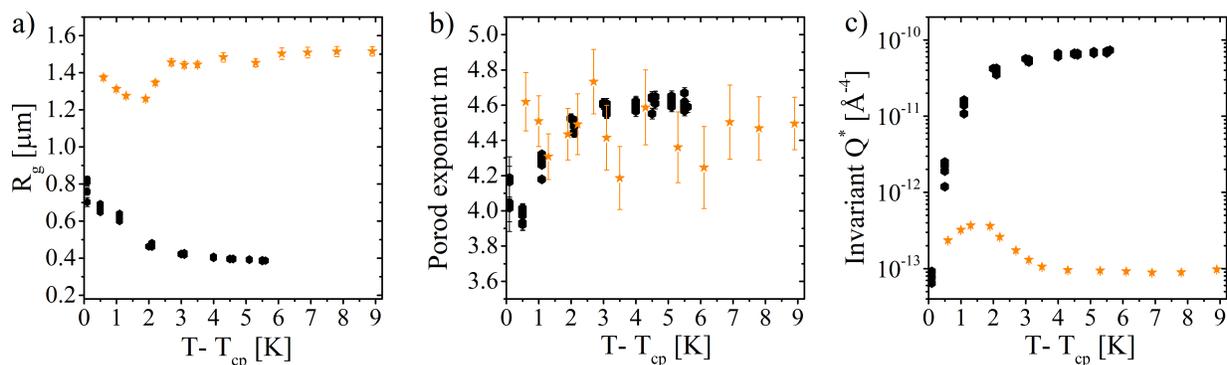
Figure 10.10: (a) Radius of gyration of the mesoglobule $R_g$, (b) Porod exponent $m$, and (c) invariant scattering $Q^*$ in dependence on the temperature distance from the respective cloud points at 0.1 MPa (black pentagons) and 265 MPa (orange stars).

More information follows from the invariant scattering $Q^*$, which is determined from integrating the scattering curves over $q$ according to equation 6.2. Since the $q$ range of the performed experiment is limited, the scattering intensity at $q$ values outside the measured range is extrapolated with the Beaucage model using the obtained fit parameters to be able to integrate over the entire $q$ range. At atmospheric pressure, shown in Figure 10.10c, $Q^*$ increases strongly during the first 4 K above $T_{cp}$, starting at $\sim 10^{-13}$ Å$^{-4}$, until it converges at a value of $\sim 10^{-10}$ Å$^{-4}$ at high temperatures. $Q^*$ is related to the volume fraction of the polymer rich phase as well as the difference in scattering length density between the two phases, as follows from equation 6.3. As $R_g$ decreases significantly, the increase of $Q^*$ by more than a factor of 100 must be mainly due to stronger contrast between the two phases, i.e., the phase separation continues in the entire measured temperature range. This may be due to two processes: Single chains that were left in the solvent phase attach to mesoglobules, or solvent molecules leave the mesoglobules. It is unlikely that the former results in an increase in $Q^*$ of a factor of $\sim 100$, it must therefore be caused mainly by solvent that is released from the mesoglobules that become therefore denser.

At 265 MPa, a shallow increase in $Q^*$ from $\sim 2 \times 10^{-13}$ to $\sim 4 \times 10^{-13}$ Å$^{-4}$ at $T_{cp} + 1.5$ K is followed by a decrease until a constant value of $\sim 10^{-13}$ Å$^{-4}$ is reached at $T_{cp} + 4$ K. Overall, $Q^*$ is much lower at 265 MPa than at 0.1 MPa, which shows that the mesoglobules are solvent-rich at 265 MPa, as was the case in the PNIPAM solution in pure water (Chapter 6). The maximum in $Q^*$ may be caused by the preferential binding of water at the chains in the one-phase state, as was predicted by several theories about the co-nonsolvency effect at high pressure, described in Section 3.4. Possibly, the formation of mesoglobules from PNIPAM

chains in the presence of water and methanol at high pressure follows the mechanism that is illustrated in Figure 10.11: Due to the preferential binding of water to PNIPAM in the one-phase state, the mesoglobules are water-rich directly after their formation. The mechanism resulting in the decrease in $R_g$ and the simultaneous increase in $Q^*$ may be the diffusion of water out of the mesoglobules due to the ongoing phase separation in the two-phase state. In addition, the preferential binding of water to the chains may be lost in the two-phase state due to the strong changes in polymer-solvent interaction. Therefore, the entropy in the system is increased by the diffusion of methanol from the methanol-rich solvent phase to the water-rich mesoglobules, leading to the growth of the mesoglobules.
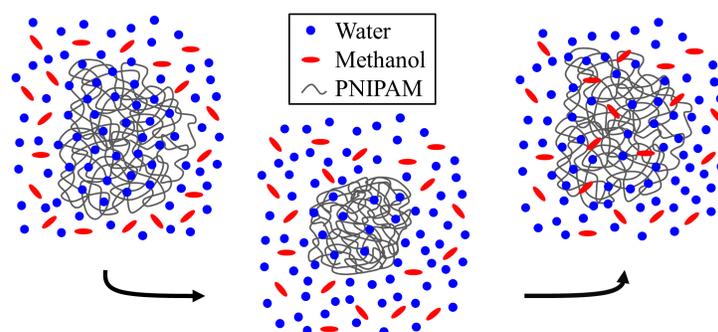


Figure 10.11: Schematic overview of the formation of mesoglobules at 265 MPa, as follows from VSANS.

## 10.6   Conclusion

In this chapter, the structure of a 3 wt% PNIPAM solution in 80:20 v/v water/methanol was investigated using small-angle neutron scattering (SANS) and very small angle neutron scattering (VSANS). Initial characterization of its phase behavior by means of turbidimetry revealed that, in agreement with previous studies, the co-nonsolvency effect is destroyed at high pressure. Whereas the cloud point is located at lower temperatures in comparison with purely aqueous PNIPAM solution, it is strongly increased at high pressures.

From SANS measurements, it was shown that large aggregates are formed at the cloud point temperature at all measured pressures. In the one-phase state, i.e., below the cloud point temperature, the correlation length of concentration fluctuations $\xi$ was probed, which is a measure for the chain conformation. At all pressures, it increases with temperature until it diverges at the critical temperature. Generally, it is larger at high pressure, which shows that the conformation is contracted in comparison with atmospheric pressure. The

increase in $\xi$ as well as the corresponding scattered intensity can be described by power laws at all pressures, which allows the derivation of the critical exponents describing the phase transition. For both quantities at all pressures, the resulting components are significantly smaller than those predicted by the mean-field or 3D Ising universality class, which may be due to large-scale structures present in the one-phase state and the order of the transition.

Furthermore, the relation of the correlation length of concentration fluctuations with the chain conformation allows the determination of the effective Flory-Huggins interaction parameter $\chi_{eff}$ between the PNIPAM and the solvent molecules in dependence on temperature and pressure. By isolating the entropic and enthalpic contributions to $\chi_{eff}$, it was deduced that the hydrophobic effect is strongly weakened at high pressure, which suggests that the solvent is enriched with methanol due to the replacement of methanol on the chains with water molecules, as was predicted by several theories on the co-nonsolvency effect at high pressure. In addition, the enthalpic polymer-solvent interactions are weakened at high pressure.

From VSANS, the influence of methanol on the formation of mesoglobules was determined. In agreement with the results from purely aqueous PNIPAM solutions, mesoglobules are significantly larger at high pressure than at low pressure, which is related to the enhanced chain solvation at high pressure. There are, however, differences in the evolution of the mesoglobules with increasing temperature in the two-phase state. At atmospheric pressure, solvent molecules are released from the mesoglobules with increasing temperature. The mesoglobules therefore shrink and become denser, i.e., the phase separation continues inside the two-phase state. At high pressure, however, two mechanisms are present that affect the size of the mesoglobules. Due to the preferential binding of water with PNIPAM in the one-phase state, the formed mesoglobules in the two-phase state are initially water-rich and decrease in size due to the ongoing phase separation. In addition, methanol presumably diffuses into the mesoglobules to balance to local methanol concentration, leading to an increase in the mesoglobule size.

# Chapter 11. Water interactions in aqueous PNIPAM solutions containing methanol

In this chapter, the molecular interactions of water in mixtures of PNIPAM and methanol are investigated using quasi-elastic neutron scattering (QENS) and Raman spectroscopy in dependence on temperature and pressure. The obtained results are discussed in view of the existing theories on the breakdown of the co-nonsolvency effect at high pressure.

## 11.1  Introduction

In anology to the QENS study of a purely aqueous 25 wt% PNIPAM solution, presented in Chapter 7, this chapter focuses on PNIPAM dissolved in a mixture of water and methanol to investigate the co-nonsolvency effect. In addition to polymer-water interactions, the system is complicated by additional interactions between methanol and water, and between methanol and PNIPAM.

At atmospheric pressure, the solubility of PNIPAM in mixtures of water and methanol is strongly reduced in comparison with PNIPAM dissolved in the pure solvents. This effect, termed the co-nonsolvency effect in the literature, was shown to be destroyed at high pressure, i.e., the solubility of PNIPAM in mixtures of water and an organic solvent is increased with respect to PNIPAM solutions in pure water [34, 35]. As described in Section 3.4, several theories describing the breakdown of the co-nonsolvency effect at high pressure are proposed, and can be classified into theories based on solvent-solvent and polymer-solvent interactions. The theory based on solvent-solvent interactions proposed that complexes formed by water and methanol act as a poor solvent for the chains at atmospheric pressure, i.e., solvent-solvent interactions are more preferable than polymer-solvent interactions [150, 151]. At high pres-

sure, it was suggested that these complexes are destroyed, thereby allowing methanol to interact with PNIPAM, leading to an increased solubility [35]. Theories based on polymer-solvent interactions consider the pressure-dependent preferential adsorption of either solvent type to the chains, as described extensively in Section 3.3 and 3.4. It was suggested that, at atmospheric pressure, methanol is preferentially bound to the chains [152, 154, 156]. The competitive binding between water and methanol leads to a reduced total solvation of the chains and therefore a reduced solubility, following mechanisms that differ between the described theories. At high pressure, however, it was suggested that water preferentially binds to the chains [37, 38, 39]. The competition between water and methanol is therefore lost, increasing the total solvation of the chains. The excess methanol in the solvent phase increases its hydrophobicity, further enhancing the solubility of the chains.

In this study, QENS is applied to investigate the solvent dynamics in mixtures of PNIPAM, water and methanol at both low and high pressure. Previously, Kyriakos et al. investigated the co-nonsolvency effect of PNIPAM in mixtures of water and methanol using QENS at atmospheric pressure [293]. The investigation on the dynamics of water revealed that two water species are present: water interacting with PNIPAM and water interacting with methanol in the solvent phase. The dynamic properties do not change significantly at the phase separation temperature. However, the relative fraction of water interacting with PNIPAM decreases upon phase separation. The investigation on the dynamics of methanol also revealed two different species, with diffusion coefficients close to the ones found for water in the entire measured temperature range. It was concluded that the association behavior of water and methanol to PNIPAM is very similar at atmospheric pressure.

In the present study, the dynamics of water is in focus. Although the investigation of the dynamics of methanol would allow a more direct investigation on the co-nonsolvency effect, the exchange of deuterium and hydrogen in a 80:20 v/v $D_2O/CH_3OH$ mixture results in a significant amount of protonated water, thereby complicating an unambiguous description of the results [293]. Therefore, to investigate the polymer-solvent interactions, the dynamics of water is measured in a 25 wt% PNIPAM solution in 80:20 v/v $H_2O/CD_3OD$ in a wide temperature range around the cloud point at both 0.1 and 200 MPa. Insights into the solvent-solvent interactions are obtained by measuring pure 80:20 and a 70:30 v/v $H_2O/CD_3OD$ solvent mixtures under the same conditions. In addition, Raman spectroscopy is applied to investigate the hydration of the hydrophobic groups of PNIPAM specifically, in order to differentiate between the hydration of hydrophilic and hydrophobic groups of PNIPAM.

## 11.2    Experimental details

**Materials.**    Poly($N$-isopropylacrylamide) (PNIPAM) with a molar mass $M_n = 36\,000$ g mol$^{-1}$ and a dispersity of 1.26 (end groups carboxylic acid and a hydrogen atom, respectively) was purchased from Sigma-Aldrich. For the QENS measurements, it was dissolved at a concentration of 25 wt% in 80:20 v/v $H_2O$/$CD_3OD$. The combination of $H_2O$ and $CD_3OD$ was used to maximize the incoherent scattering from water and to minimize that of methanol to probe the motion of single water molecules. It was shown previously that H/D exchange in these kinds of systems is negligible [293, 294], i.e., (partly) protonated methanol may only be present in an insignificant amount. The cloud points of this sample at 0.1 and 200 MPa are $23.5 \pm 0.1$ and $40.0 \pm 0.1$ °C, respectively, measured with turbidimetry (see Appendix 13.2 for more details). From the composition of the sample and the scattering cross sections of the present elements [183], it follows that 69 % of the measured neutrons were incoherently scattered by water molecules (see Appendix 13.3).

For Raman spectroscopy measurements, PNIPAM was dissolved at a concentration of 25 wt% in 80:20 v/v $D_2O$/$CD_3OD$. Furthermore, a 25 wt% PNIPAM solution in pure $D_2O$ is measured as a reference. Fully deuterated solvents were chosen to avoid overlap of the contributions from the stretching vibrations of the C$\cdots$H groups of PNIPAM and those of water and the hydrophobic groups of methanol.

**Quasi-elastic neutron scattering.**    Quasi-elastic neutron scattering (QENS) measurements were performed at the instrument TOFTOF at the FRM II, Garching, Germany. An incident neutron beam with a wavelength $\lambda = 6$ Å$^{-1}$ was used with a chopper rotation speed of 16 000 rpm, resulting in an energy resolution of $\sim$0.03 meV.

The sample was mounted in a flat aluminum (EN AW-7075) pressure cell with a thickness of 5 mm [218]. Inside the cell, the sample is located in 10 parallel channels with a diameter of 1.6 mm, which can withstand a maximum pressure of 200 MPa. A membrane, placed between the pressure cell and the pressure generator, prevents mixing of the sample and the pressure transmitting medium ($D_2O$). The temperature of the pressure cell was controlled using a circulating bath thermostat, which heats the pressure cell at one side. The temperature of the pressure cell was measured using a Pt100 resistance thermometer attached close to the sample position. As the geometry of the pressure cell did not allow a proper insulation, the temperature was calibrated afterwards to determine the temperature at the

position of the sample. The pressure cell was positioned at an angle of 135° with respect to the incident neutron beam, resulting in an accessible $q$ range of 0.1-1.7 Å$^{-1}$. The sample was measured during heating scans around the respective cloud points at 0.1 and 200 MPa with an integration time of 120 min at each temperature, following an equilibration time of 30 min after each temperature change. In addition, pure 80:20 v/v $H_2O/CD_3OD$ and 70:30 v/v $H_2O/CD_3OD$ were measured at both pressures at selected temperatures.

The data reduction is performed as described in Section 4.3.2. The self-shielding factor due to the pressure cell geometry is estimated using the measurement of pure 80:20 v/v $H_2O/CD_3OD$. Since elastic scattering is not expected in pure water, the entire elastic signal that is measured originates from scattering of neutrons at the pressure cell, which allows for an estimation of the self-shielding factor.

**Raman spectroscopy.** For the Raman spectroscopy measurements, a LabRam Hr 800 system from JY Horiba (Kyoto, Japan) in combination with a frequency-doubled Nd:YAG laser with a wavelength of 532 nm was used, resulting in a spectral resolution of 2 cm$^{-1}$. The laser beam was focused on the sample with a spot size of ~1.5 $\mu$m with a power of less than 3 mW.

The sample was mounted in a fused silica micro capillary with a squared cross section with inner and outer side lengths of 75 and 350 $\mu$m, respectively. One side of the micro capillary was connected to a pressure generator from High Pressure Equipment Company (Erie, Pennsylvania, U.S.A.). The other side of the capillary was sealed by melting the fused silica, and was capable of withstanding pressures up to 300 MPa. The sample and the pressure medium (ethanol) were not separated. However, the length of the micro capillary (~30 cm) avoided mixing of both liquids at the probed spot for at least the duration of the experiment. The micro capillary was placed between two copper blocks to ensure good thermal contact. The temperature of the setup was controlled using a circulating bath thermostat. A Pt100 resistance thermometer attached close to the micro capillary at the probed spot was used to determine the temperature. The temperature was calibrated afterwards to determine its value at the position of the sample.

Raman spectra were acquired at 0.1 and 200 MPa for the 25 wt% in 80:20 v/v $D_2O/CD_3OD$, and at 0.1 and 130 MPa for the 25 wt% in $D_2O$ during heating scans around the respective cloud points. The integration time was 5 min, following an equilibration time of 10 min after

each change of temperature or pressure. A dark current measurement was subtracted from the data.

## 11.3   Water dynamics in water/methanol mixtures

To determine the influence of methanol on the dynamics of bulk water, water/methanol mixtures in the absence of PNIPAM were measured at a 80:20 and a 70:30 v/v water/methanol ratio. Similar to the QENS measurements of pure water, presented in Chapter 7, the dynamic structure factors were converted to the imaginary part of the dynamic susceptibility $\chi''(q,\nu)$, as described extensively in Section 7.3.1. Figure 11.1 presents the susceptibility spectra of the 80:20 v/v $H_2O/CD_3OD$ mixture at different temperatures at 0.1 MPa (Figure 11.1a) and 200 MPa (Figure 11.1b) at $q = 1.65$ Å$^{-1}$. As for pure water, the susceptibility spectra consist of two distinct peaks. At low frequencies, i.e., slow dynamics, the diffusion of water molecules is observed. With increasing temperature at both pressures, this contribution shifts to higher frequencies, indicating a faster diffusion of the water molecules. At high frequencies, fast local dynamic processes are observed that do not show a clear temperature dependence.
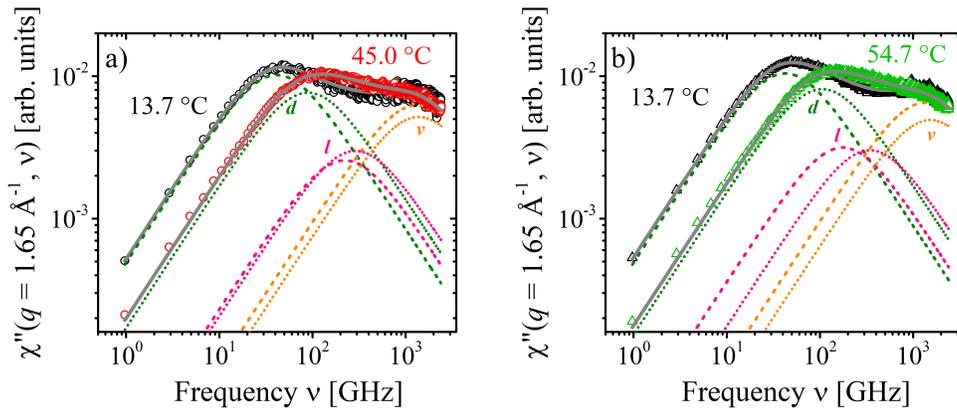


Figure 11.1: Imaginary part of the dynamic susceptibility $\chi''(q,\nu)$, of 80:20 v/v $H_2O/CD_3OD$, determined according to equation 7.1, at 0.1 MPa (a) and 200 MPa (b). The temperatures are given in the graphs. Also shown are fits of equation 7.2 (grey lines) and their individual contributions: diffusion process $d$ (olive lines), local process $l$ (pink lines) and the vibrational process $v$ (orange lines) at low temperature (dashed lines) and high temperature (dotted lines).

## 11.3.1   Data analysis

Model fitting revealed the presence of a third relaxation process, apparent from a shallow peak at intermediate frequencies. Following the fitting procedure of the susceptibility spectra from pure water (equation 7.2), the susceptibility spectra were fitted by

$$\chi''(q,\nu) = \chi''_d(q,\nu) + \chi''_l(q,\nu) + \chi''_v(q,\nu) \tag{11.1}$$

where the three contributions are attributed to the diffusion process of water ($d$), modeled with a Debye function (equation 7.3), an effective local process ($l$), also modeled with a Debye function, and a vibrational process ($v$), modeled with a damped harmonic oscillator (DHO) function (equation 7.4). Fits of equation 11.1 are exemplarily shown in Figure 11.1. In all cases, the fits are excellent, i.e., no separate contributions from dynamic processes of methanol are observed.

In Figure 11.2, $\chi''(q,\nu)$ is presented at various $q$ values at 13.7 (Figure 11.2a) and 45.0 °C (Figure 11.2b) at atmospheric pressure along with their fits. At both temperatures, the relaxation peak assigned to the diffusion process shifts to higher frequencies with increasing $q$. It follows that this process indeed involves translational motion, since the relaxation time increases if larger length scales are probed. At high frequencies, only weak changes in frequency are observed. Thus, in the effective local and the vibrational process, translational motion is of minor importance.
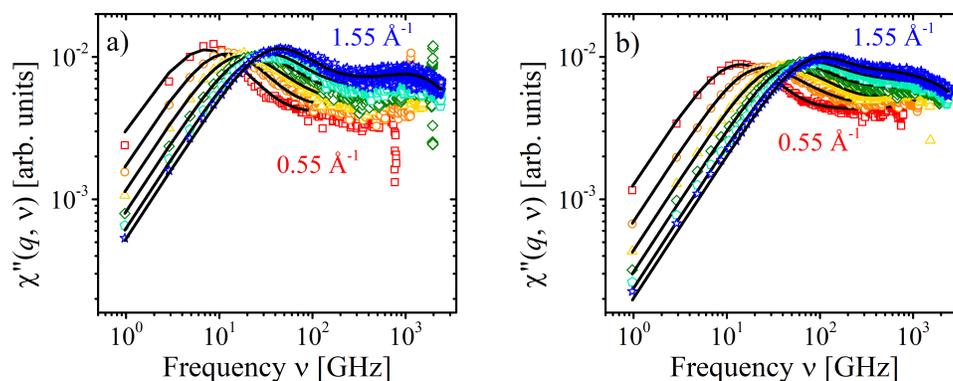


Figure 11.2:  Imaginary part of the dynamic susceptibility, $\chi''(q,\nu)$, of 80:20 v/v $H_2O$/$CD_3OD$ at 0.1 MPa at 13.7 °C (a) and 45.0 °C (b) at 1.55 Å$^{-1}$ (blue stars), 1.35 Å$^{-1}$ (light green pentagons), 1.15 Å$^{-1}$ (olive diamonds), 0.95 Å$^{-1}$ (yellow triangles), 0.75 Å$^{-1}$ (orange circles) and 0.55 Å$^{-1}$ (red squares). Black lines: fits of equation 7.2 to the data.

## 11.3.2 Results

The relaxation time of the diffusion process of the water molecules $\tau_d$, resulting from fitting the susceptibility spectra, is shown in Figure 11.3 in dependence on $q$ at different temperatures at atmospheric pressure (Figure 11.3a) and 200 MPa (Figure 11.3b). At low $q$ values, the slope of $\tau_d$ approaches $q^{-2}$ in all cases, which shows that this process indeed involves long-range diffusion of the water molecules. At high $q$ values, however, a weaker dependence is observed, pointing to the presence of a localized process at small length scales. As for pure water, described in Section 7.3.2, such behavior is described by the isotropic jump model, which assumes diffusion due to discrete jumps of apparent length $l_d$ between residence times $\tau_{0,d}$, during which the water molecules perform a local motion. The predicted dependence of the relaxation time on $q$ follows the relation

$$\tau_d = \tau_{0,d}\left[1 + \frac{6}{q^2 l_d^2}\right] \tag{11.2}$$

with the diffusion coefficient of the water molecules $D_d$, given by $D_d = l_d^2/(6\tau_{0,d})$. The fits of equation 11.2 are also given in Figure 11.3. In all cases, excellent agreement with the data is obtained.
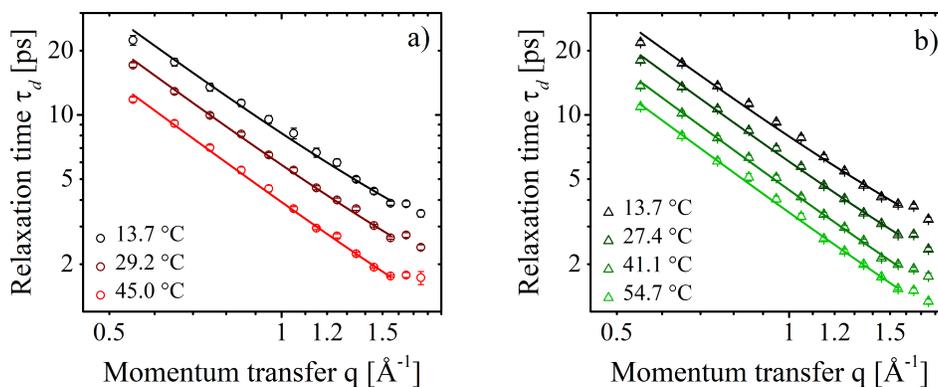


Figure 11.3: Relaxation times $\tau_d$ of 80:20 v/v $H_2O$/$CD_3OD$ in dependence on $q$ at 0.1 MPa (a) and 200 MPa (b). The temperatures are given in the graphs. Solid lines: fits of equation 7.5 to the data.

$D_d$, determined from the fits, is shown in Figure 11.4 at low and high pressures in dependence on temperature for pure $H_2O$ (adapted from Chapter 7), 80:20 v/v $H_2O$/$CD_3OD$ and 70:30 v/v $H_2O$/$CD_3OD$. In all cases, an increasing trend is observed with increasing temperature. Thus, the diffusion of the water molecules is faster due to the enhanced thermal energy at high temperature. Furthermore, it is observed that $D_d$ decreases with methanol content,

i.e., the presence of methanol in the system slows down the diffusion of water molecules, both at atmospheric and at high pressure. The reduction in the mobility of water molecules is due to the formation of clusters consisting of methanol and water molecules, as observed previously at atmospheric pressure [149, 151, 281, 293]. These clusters diffuse significantly slower than individual water molecules, leading to a lower value of $D_d$.
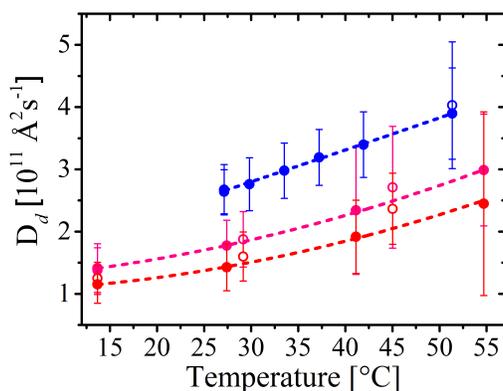


Figure 11.4: Diffusion coefficients $D_d$ in dependence on temperature of pure $H_2O$ (blue symbols) 80:20 v/v $H_2O/CD_3OD$ (pink symbols) and 70:30 v/v $H_2O/CD_3OD$ (red symbols). Open symbols: 0.1 MPa, closed symbols: 130 MPa for pure $H_2O$ and 200 MPa for both 80:20 and 70:30 v/v $H_2O/CD_3OD$. Solid lines: Guides to the eye to follow the trend of $D_d$ of the respective solvents at high pressure.

Previously reported theories on the co-nonsolvency effect at atmospheric pressure were based on solvent-solvent interactions. As described in Section 3.3, clusters of water and methanol molecules may be responsible for the co-nonsolvency effect at atmospheric pressure. According to this theory, the clusters form a new species that acts as a poor solvent for the chains, leading to a reduced solubility [150, 151]. It was suggested that, at high pressure, the clusters disintegrate (Section 3.4). This allows individual methanol molecules to interact with the chains, resulting in an increase in the cloud point temperature [35]. The change of $D_d$ at high pressure with respect to the value at atmospheric pressure depends on the methanol content. It is observed that, in pure water, a pressure of 130 MPa does not influence $D_d$ significantly. For 80:20 v/v $H_2O/CD_3OD$ and 70:30 v/v $H_2O/CD_3OD$, however, $D_d$ is lower at 200 MPa than the one at the same temperature at atmospheric pressure. Thus, water molecules diffuse slower at high pressure in case methanol is present, i.e., cluster formation is enhanced. This finding therefore contradicts the above mentioned theory for the co-nonsolvency effect at high pressure based on solvents-solvent interactions.

# 11.4 Bulk water dynamics in PNIPAM/water/methanol mixtures

To determine the role of polymer-solvent interactions on the co-nonsolvency effect at high pressure, the dynamics of $H_2O$ molecules is investigated in a PNIPAM solution in 80:20 v/v $H_2O/CD_3OD$. Figure 11.5 displays the susceptibility spectra at different temperatures at 0.1 MPa (Figure 11.5a) and at 200 MPa (Figure 11.5b). In the one-phase state at both pressures, a strong contribution at low frequencies ($\sim$10 GHz) is present that was not observed in the susceptibility spectra of the pure solvents. It is mainly due to the relaxation of water molecules having a strong interaction with the chains. Furthermore, the intensity at higher frequencies is lower compared to the one of the pure solvents, i.e., only a small amount of bulk water molecules is present in the one-phase state at both pressures. In the entire temperature range at both pressure, the intensity at low frequencies decreases, whereas it increases at higher frequencies. Upon heating, water is released from the chains, and joins the bulk solvent phase. At temperatures above $T_{cp}$ at atmospheric pressure (23.5 $\pm$ 0.1 °C), the decrease in intensity is more pronounced than in the one-phase state, i.e., the dehydration is stronger. At high pressure, however, the decrease in intensity is gradual over the entire temperature range, without an abrupt transition at $T_{cp}$ (40.0 $\pm$ 0.1 °C). Deep in the two-phase state at both pressures, a contribution at frequencies below 10 GHz remains, which shows that very slowly moving moieties with dynamics that cannot be resolved with the resolution of the experiment remain present in the system. As discussed in Chapter 7, this contribution can be attributed to scattering of neutrons at the chains as well as at very strongly bound water molecules.

## 11.4.1 Data analysis

Analogous to the susceptibility spectra of the purely aqueous PNIPAM solution (Chapter 7), the spectra of the 25 wt% PNIPAM solution in 80:20 v/v $H_2O/CD_3OD$ were modeled using the expression

$$\chi''(q,\nu) = \chi''_{el}(q,\nu) + \chi''_{h}(q,\nu) + \chi''_{d}(q,\nu) + \chi''_{l}(q,\nu) + \chi''_{v}(q,\nu) \qquad (11.3)$$

where, besides the three contributions from the bulk solvent phase, as described above, $\chi''_{el}(q,\nu)$ represents the contribution from elastically scattered neutrons ($el$) and $\chi''_{h}(q,\nu)$
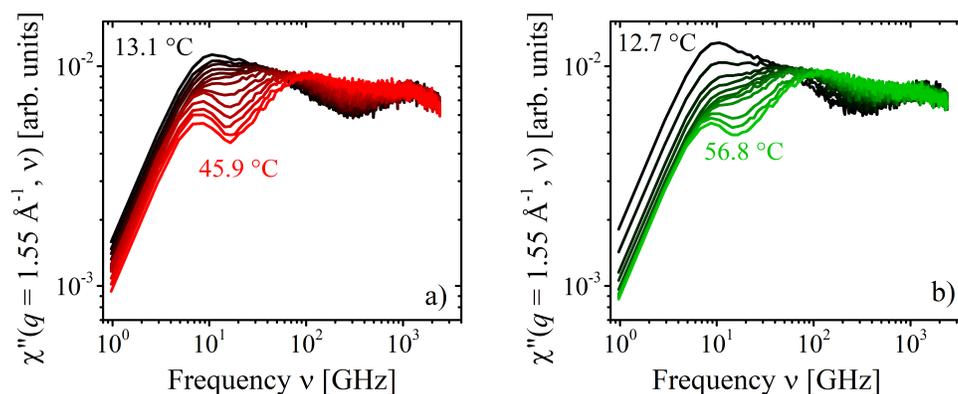
Figure 11.5:  Imaginary part of the dynamic susceptibility $\chi''(q,\nu)$, determined according to equation 7.1, at 0.1 MPa (a) and 200 MPa (b) at different temperatures, as indicated in the graphs.

the relaxation of hydration water ($h$). $\chi''_{el}(q,\nu)$ is modeled using the measured resolution function (equation 7.7). To account for the dynamic heterogeneity of hydration water, its contribution is modeled using the Cole-Davidson function (equation 7.8). Also in this case, the stretching exponent $\beta$ was kept fixed at 0.7 for all spectra. As the methanol content may vary in the bulk solvent phase, $\tau_d(q)$ cannot be kept fixed during fitting. This additional degree of freedom with respect to the fits of the measurements of the purely aqueous PNIPAM solutions resulted in unstable fits of the spectra at low momentum transfers. Therefore, only the spectra at 1.45, 1.55 and 1.65 $\text{Å}^{-1}$ were analyzed. Also $\tau_l(q)$ may be influenced by the methanol content of the solvent phase. However, due to the low absolute intensity of the effective local process, $\tau_l(q)$ was kept fixed at the value obtained for the 80:20 v/v $H_2O/CD_3OD$ solvent mixture in the absence of the polymer to allow a reliable determination of the other fitting parameters. The presented results are averaged values resulting from the measurements at 1.45, 1.55 and 1.65 $\text{Å}^{-1}$.

Fits of equation 11.3 are exemplarily shown for the measurement at 15.7 °C and 41.1 °C at 0.1 MPa (Figure 11.6), and at 33.2 °C and 56.8 °C at 200 MPa (Figure 11.7), i.e., both in the one-phase state and in the two-phase state at both measured pressures. In the one-phase state at both pressures, the spectra are dominated by the contribution from hydration water. At atmospheric pressure, its contribution is significantly stronger than at 200 MPa. In the two-phase state at both pressures, its contribution is strongly decreased in intensity, but remains present. At both pressures, the intensity of the elastic process is strongly increased in the two-phase state. Thus, the amount of hydrogen atoms that participate in a dynamic process that is too slow to be resolved increases. As discussed in Chapter 7, this may be due to two factors. Firstly, water molecules may be trapped inside the polymer-rich
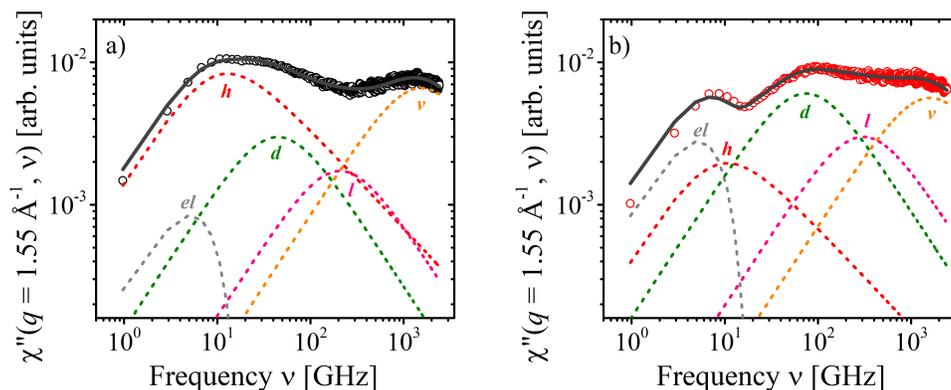
Figure 11.6: Example fits of $\chi''(q,\nu)$ of the 25 wt% PNIPAM solution in 80:20 v/v $H_2O/CD_3OD$, at 0.1 MPa at 15.7 °C (a) and 41.4 °C (b). Data (open circles), fits of equation 11.3 (dark grey lines) and their individual contributions: Elastic fraction $el$ (grey), relaxation process of hydration water $h$ (red), diffusion process of bulk water $d$ (olive), local process of bulk water $l$ (pink) and the vibrational process $v$ (orange).

domains, which strongly hinders their motion. Secondly, it may be due to hydrogen atoms on the PNIPAM chains. Whereas in the one-phase state, the side groups of PNIPAM may be involved in a relatively fast dynamic process, their motion is strongly restricted in the two-phase state, which increases the elastic line strength. However, the latter presumably plays a minor role due to the low frequencies of dynamic processes of the chains [249]. The intensity of the diffusion process of bulk water and of the effective local process also increases in the two-phase state. It follows that the hydration water in the one-phase state is released from the chains at $T_{cp}$ and joins the bulk solvent phase. At both pressures, the intensity of the vibrational process is not significantly affected by the increase in temperature.
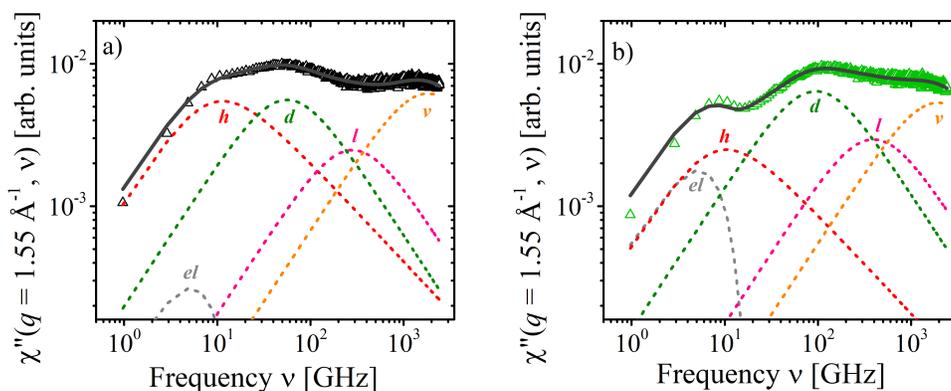


Figure 11.7: Example fits of $\chi''(q,\nu)$ of the 25 wt% PNIPAM solution in 80:20 v/v $H_2O/CD_3OD$, at 200 MPa at 33.2 °C (a) and 56.8 °C (b). Data (open triangles), fits of equation 11.3 (dark grey lines) and their individual contributions: Elastic fraction $el$ (grey), relaxation process of hydration water $h$ (red), diffusion process of bulk water $d$ (olive), local process of bulk water $l$ (pink) and the vibrational process $v$ (orange).

## 11.4.2    Results

In this section, the focus is on the relaxation time of the diffusion of water molecules in the bulk solvent phase, $\tau_d$, to determine its composition. In Figure 11.8, $\tau_d$ is presented in dependence on temperature at 0.1 MPa (Figure 11.8a) and 200 MPa (Figure 11.8b), along with the relaxation times measured in the pure 80:20 v/v $H_2O/CD_3OD$ and 70:30 v/v $H_2O/CD_3OD$ solvent mixtures. As discussed in Section 11.3, water molecules diffuse slower in the presence of methanol, which increases the relaxation time. From these values, the composition of the bulk solvent phase in the presence of PNIPAM can be estimated.
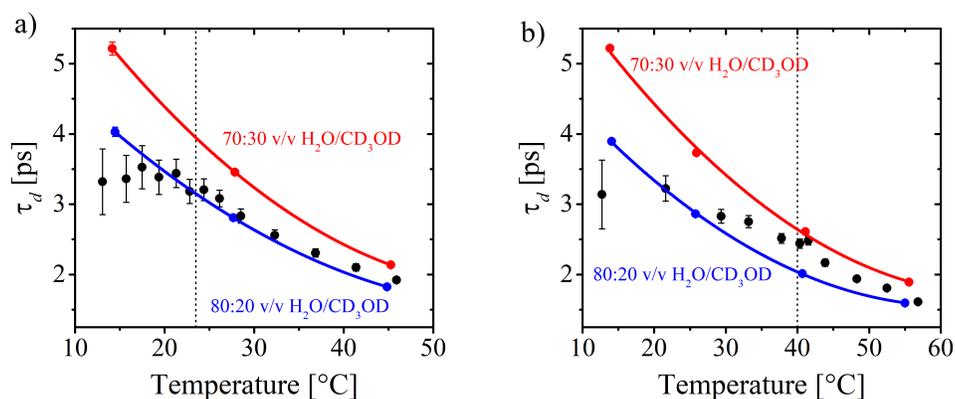


Figure 11.8:   Relaxation time of the diffusive mode of $H_2O$ molecules in the bulk solvent phase $\tau_d$ in the 25 wt% PNIPAM solution in 80:20 v/v $H_2O/CD_3OD$ (black dots), 80:20 v/v $H_2O/CD_3OD$ (blue dots) and 70:30 v/v $H_2O/CD_3OD$ (red dots), in dependence on temperature at 0.1 MPa (a) and 200 MPa (b). The red and blue lines are guides to the eye.

At 0.1 MPa at low temperatures (below ∼20 °C), $\tau_d$ of the PNIPAM solution in 80:20 v/v $H_2O/CD_3O$ is lower than the one of the pure 80:20 v/v $H_2O/CD_3OD$ solvent mixture, which points to an excess of water in the bulk solvent phase, i.e., methanol is preferentially adsorbed at the PNIPAM chains. This supports the theories on the co-nonsolvency effect at atmospheric pressure that predict the preferential adsorption of the organic solvent at the chains in the one-phase state [152, 154, 156], as described in Section 3.3. However, the weak intensity at low temperatures hinders a reliable determination of the relaxation time, resulting in large uncertainties for these data points. Around $T_{cp}$, $\tau_d$ of the PNIPAM solution follows the trend of the pure 80:20 v/v $H_2O/CD_3O$ mixture, thus, preferential adsorption does not occur in this temperature range. Deep in the two-phase state (above 30 °C), $\tau_d$ of the PNIPAM solution is higher than the one of the pure 80:20 v/v $H_2O/CD_3OD$ solvent mixture, which indicates the enrichment of methanol in the bulk solvent phase. Possibly, methanol molecules are expelled more strongly from the polymer-rich domains than water

molecules, leading to the enrichment of the bulk solvent phase with methanol at high temperatures.

At 200 MPa, different behavior is observed. At low temperatures, $\tau_d$ of the PNIPAM solution is close to the one of the pure 80:20 v/v $H_2O$/$CD_3OD$ mixture. With increasing temperature, the difference between both quantities increases until $\tau_d$ of the PNIPAM solution reaches a value close to the one of the 70:30 v/v $H_2O$/$CD_3OD$ mixture at $T_{cp}$. Thus, the bulk solvent phase is enriched with methanol, i.e., the chains are preferentially decorated by water. This observation supports the theories on the co-nonsolvency effect at high pressure based on polymer-solvent interactions [37, 38, 39]. However, the different mechanisms leading to the increased solubility after the replacement of methanol by water of the chains, proposed in the different theories, cannot be distinguished. The preferential adsorption of water on the chains is only present close to $T_{cp}$. At very low temperatures, relaxation times similar to the ones of the pure 80:20 v/v $H_2O$/$CD_3OD$ are found, i.e., preferential adsorption is not present. In the two-phase state, $\tau_d$ decreases more strongly and reaches a value close to the one of the pure 80:20 v/v $H_2O$/$CD_3OD$ mixture at high temperatures. As for the purely aqueous PNIPAM solution, described in Chapter 7, the transition may span over a broad temperature range at high pressure. At $T_{cp}$, the solvent molecules are gradually released from the chains. Deep in the two-phase state at high temperature, preferential adsorption is not present anymore. In both the polymer- and solvent-rich phases, water and methanol are present in an 80:20 ratio.

These results allow for an estimation of the absolute composition in the different phases. As shown below, at 200 MPa around $T_{cp}$, 40 % of all water molecules in the system are hydration water molecules, i.e., 60 % are in the bulk solvent phase. The 70:30 water/methanol ratio in the bulk solvent phase therefore implies that 38 % of all water molecules and 2 % of all methanol molecules are bound to the chains, which corresponds to a 95:5 water/methanol ratio. It follows that, at 200 MPa, the presence of methanol on the chains is reduced by a factor of 4 with respect to the nominal ratio, which is observed at atmospheric pressure.

## 11.5 Hydration water dynamics in PNIPAM/water/methanol mixtures

Beside the dynamics of water molecules in the bulk solvent phase, the properties of the hydration water provide additional insights into the polymer-solvent interactions. In this

section, the relative fraction of hydration water $f_h$ as well as its relaxation time $\tau_h$ are evaluated.

## 11.5.1   Relative fraction of hydration water

$f_h$ can be determined from the amplitudes of the individual contributions to the suscepti-bility spectra $C_j(q)$, where the index $j$ stands for $h$, $d$ and $l$. As is evident from the spectra (Figure 11.5), the vibrational process does not change in intensity with increasing temper-ature, it can thus be assumed that both hydration water and bulk water contribute to this process. $f_h$ can therefore be determined by

$$f_h = \frac{C_h(q)}{C_h(q) + C_d(q) + C_l(q)} \tag{11.4}$$

with $C_h(q)$, $C_d(q)$ and $C_l(q)$ the scattering amplitudes of the relaxation of hydration water, the diffusion process of water, and the effective local process, respectively. As is the case in the purely aqueous PNIPAM solutions (Chapter 7), the elastic line strength increases at high temperatures. Thus, the amount of water molecules considered for the determination of $f_h$ may not be constant over the entire temperature range, and the resulting values should be taken with caution.

In Figure 11.9a, $f_h$, averaged from the values at $q = 1.45$, $1.55$ and $1.65$ Å$^{-1}$, is presented in dependence on the temperature distance to the cloud point at both 0.1 and 200 MPa. In the one-phase state at 0.1 MPa, $f_h$ decreases with temperature from $\sim$0.8 at $T_{cp} - 10$ K to $\sim$0.5 at $T_{cp}$, which agrees with the decreasing intensity of the susceptibility at low frequencies with increasing temperature (Figure 11.5). Also at 200 MPa, $f_h$ decreases in the one-phase state. The changes are, however, weaker, and a value of $\sim$0.4 is reached at $T_{cp}$. The significantly larger fraction of hydration water at 0.1 MPa in comparison with 200 MPa suggests that the solvent quality is better at 0.1 MPa. This finding agrees with the determined Flory-Huggins interaction parameter in dependence on temperature and pres-sure, presented in Chapter 10. In the concentrated solution investigated in this chapter, the expanded chain conformation at 0.1 MPa therefore influences the dynamics of a larger fraction of water molecules than at 200 MPa. In addition, the enhanced fraction of hydration water at 0.1 MPa may be due to the interaction with methanol. The preferential adsorption of methanol on the chains may lead to a more prominent hydration shell around them.

In the two-phase state at 0.1 MPa, $f_h$ decreases initially more strongly than in the
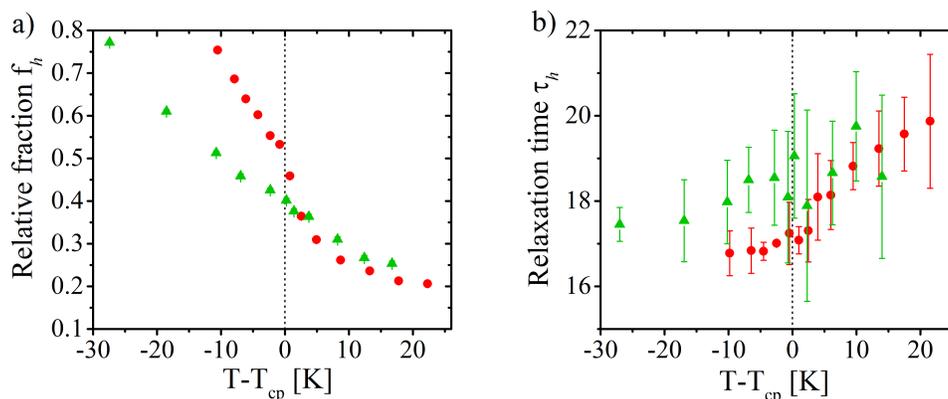
Figure 11.9: Relative fraction of hydration water $f_h$ (a) and the relaxation time of the hydration water $\tau_h$ measured at 1.55 Å$^{-1}$ (b) in the 25 wt% PNIPAM solution in 80:20 v/v H$_2$O/CD$_3$OD at 0.1 MPa (red dots) and at 200 MPa (green triangles) in dependence on the temperature distance from the cloud point temperature.

one-phase state, but reaches a constant value of $\sim$0.2 at high temperatures. At 200 MPa, the decrease of $f_h$ in the two-phase state is shallower than at 0.1 MPa, and it continues the decreasing trend observed in the one-phase state. However, also at 200 MPa, it seems to converge towards a constant value larger than 0. These observations are in agreement with results presented in previous chapters. The relatively sharp transition at 0.1 MPa in comparison with 200 MPa reflects the narrower temperature range in which phase separation takes place, as observed in purely aqueous PNIPAM solutions (Chapter 7). The finite value of $f_h$ deep in the two-phase state confirms that water is trapped inside the polymer-rich phases, as determined using VSANS (Chapter 10).

## 11.5.2 Relaxation time of hydration water

The relaxation time of hydration water $\tau_h$, averaged from the values at $q = 1.45$, 1.55 and 1.65 Å$^{-1}$, is presented in Figure 11.9b. At both pressures, an increasing trend is observed in the entire measured temperature range. Around $T_{cp}$ at 0.1 MPa, however, the slope of $\tau_h$ strongly increases, whereas at 200 MPa, the increase is gradual in the entire measured temperature range. As discussed in Chapter 7, a large relaxation time may point to strong hydrophilic hydration, since the strong hydrogen bonds in this case restrict the motion of the water molecules more strongly than around hydrophobic groups, where hydrogen bonds between water and the polymers are very weak [247]. Thus, the increase in $\tau_h$ at both pressures points to an increasing hydrophilic hydration in comparison with hydrophobic hydration, which is due to the hydrophobic effect. At 200 MPa, this effect is significantly weaker than at 0.1 MPa, thus leading to the weaker and more gradual increase at $T_{cp}$. Ad-

ditionally, as observed in purely aqueous PNIPAM solutions (Chapter 7), water molecules that are trapped inside the polymer-rich phase may contribute to the large relaxation time in the two-phase state.

In the one-phase state, $\tau_h$ is larger at 200 MPa than at 0.1 MPa, which shows that the motion of hydration water is more restricted at 200 MPa. Two effects that influence the relaxation time of hydration water in the one-phase state may play a role. Firstly, as for the purely aqueous PNIPAM solutions, pressure enhances hydrophobic hydration, which leads to a decrease of $\tau_h$. Secondly, the preferential adsorption of water at the hydrophilic groups of PNIPAM at 200 MPa leads to larger values of $\tau_h$ than at 0.1 MPa, where the hydrophilic groups may be solvated with methanol. The higher value of $\tau_h$ at 200 MPa therefore shows that the latter must play a dominant role in this case.

## 11.6    Hydrophobic hydration in PNIPAM/water/methanol mixtures

Raman spectroscopy is applied to investigate the hydrophobic hydration on the PNIPAM chains in dependence on temperature at different pressures. The spectra of the 25 wt% PNIPAM solution in 80:20 v/v $D_2O/CD_3OD$ at different temperatures at 0.1 and 200 MPa are shown in Figure 11.10. As for the 3 wt% PNIPAM solution in $D_2O$ (Chapter 6), four peaks in the CH stretching region are observed, assigned to symmetric $CH_3$ stretching in the side groups ($\nu_s(CH_3)$), CH stretching ($\nu(CH)$), antisymmetric $CH_2$ stretching at the backbone ($\nu_{as}(CH_2)$), and antisymmetric $CH_3$ stretching in the side groups ($\nu_{as}(CH_3)$) at around 2884, 2923, 2947 and 2990 cm$^{-1}$, respectively [116, 207, 208]. As deuterated methanol is used, the vibrational modes of its hydrophobic group do not contribute to the measured intensity in this frequency range. At both pressures, only weak changes in the peak position are observed with increasing temperature. At 0.1 MPa, the peak positions of the $\nu_s(CH_3)$ and $\nu_{as}(CH_3)$ mode at $\sim$2884 and $\sim$2990 cm$^{-1}$, respectively, are constant in the one-phase state. At $T_{cp}$ at $\sim$25.2 °C, as determined by in-situ optical microscopy, both peak frequencies shift abruptly to lower values, and then remain again constant. At 200 MPa, the frequencies of both vibrational modes also shift to lower values, but the change occurs initially in a gradual manner. Deep in the two-phase state, however, both vibrational modes shift abruptly to even lower frequencies. Thus, a second transition may be present in this case.
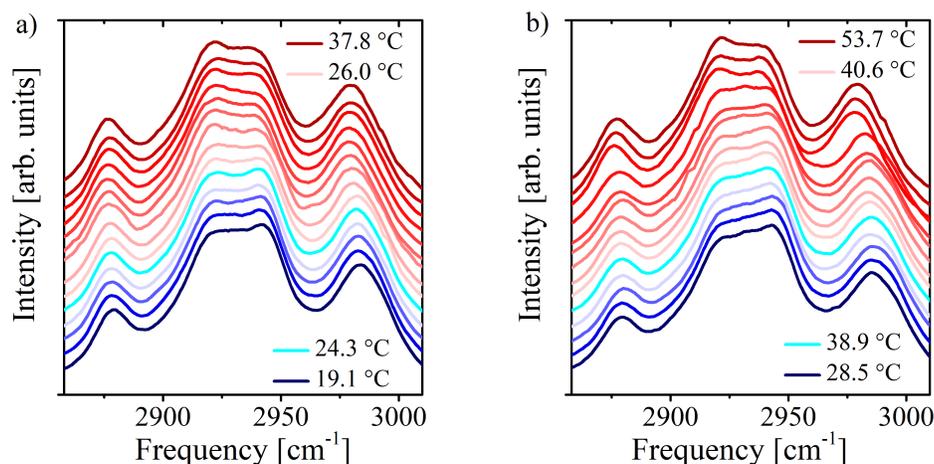
**Figure 11.10:** Raman spectra of the 25 wt% PNIPAM solution in 80:20 v/v $D_2O/CD_3OD$ in the CH stretching region in dependence on temperature at 0.1 MPa (a) and 200 MPa (b). Spectra taken in the one-phase state are given in blue, spectra taken in the two-phase state in red. The measured start- and end-temperatures of both states are given in each graph. For clarity, the curves are shifted in intensity and smoothed using the Savitzky-Golay algorithm.

Due to the high polymer concentration, the signal-to-noise ratio is better than for the measurements on the 3 wt% PNIPAM solution in $D_2O$, presented in Chapter 6. It was therefore possible to distinguish between different broadening mechanisms of the peaks. For a precise determination of the peak frequencies, the spectra were fitted with a combination of four Voigtian functions (equation 4.52) and a constant background. In Figure 11.11, representative fits are shown for the 25 wt% PNIPAM solution in 80:20 v/v $D_2O/CD_3OD$ at 0.1 MPa at 19.1 and 34.6 °C, i.e., in the one-phase and in the two-phase state, respectively. In all cases, excellent fits are obtained.

In Figure 11.12, the peak frequencies of the $\nu_{as}(CH_2)$ and the $\nu_{as}(CH_3)$ vibration mode are presented in dependence on the temperature distance to the pressure-dependent cloud point at 0.1 MPa and 200 MPa for the 25 wt% PNIPAM solution in 80:20 v/v $D_2O/CD_3OD$, and at 0.1 MPa and 130 MPa for the 25 wt% PNIPAM solution in $D_2O$ as a reference. Since the slope of the coexistence line in the temperature pressure frame is very steep at 200 MPa for the purely aqueous PNIPAM solution (Figure 3.3), a lower pressure is chosen to allow a steady crossing of the cloud point. The behavior of the stretching frequency of the $\nu_{as}(CH_3)$ mode in the 25 wt% PNIPAM solution in $D_2O$ is as expected from the measurement on 3 wt% PNIPAM in $D_2O$ (Chapter 6). At 0.1 MPa, the frequency of the $\nu_{as}(CH_3)$ mode decreases abruptly at $T_{cp}$ and remains constant above. At 130 MPa, the decrease in frequency is gradual, which shows that the phase transition spans over a broad temperature range.
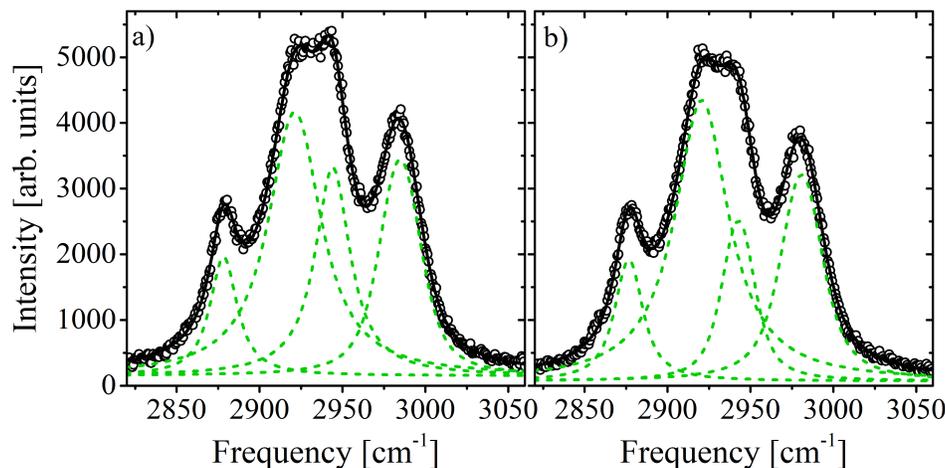
Figure 11.11: Deconvolution of Raman spectra of the 25 wt% PNIPAM solution in 80:20 v/v $D_2O/CD_3OD$ at 0.1 MPa and 19.1 °C (a) and 34.6 °C (b). Open circles: reduced data, black lines: cumulative fits, and green dashed lines: individual contributions (for details, see text).

The absolute frequency is, however, slightly lowered in comparison with the 3 wt% PNIPAM in $D_2O$. As was discussed in Section 6.4, this indicates that the monomers are slightly less hydrated, which may be due to the low number of available water molecules per monomer in the 25 wt% solution, i.e., the polymer is not able to make all the contacts with water that would be possible in a more dilute solution. Furthermore, changes in the $\nu_{as}(CH_2)$ mode are less pronounced. At both pressures, it decreases weakly at $T_{cp}$. Contrary to the measurement with the 3 wt% PNIPAM solution in $D_2O$, the frequency in the one-phase state is significantly higher at high pressure. It can be concluded that the backbone is more hydrated at high pressure than at atmospheric pressure, which may also be caused by the low number of available water molecules in the 25 wt% PNIPAM solution.

In the 25 wt% PNIPAM solution in 80:20 v/v $D_2O/CD_3OD$, both vibration modes behave similarly. In the one-phase state, the determined frequencies fluctuate around a constant value. At the $T_{cp}$ at atmospheric pressure, both frequencies decrease abruptly and remain constant above, whereas at 200 MPa, the decrease is less pronounced but continues in the entire measured temperature range. Solvation of hydrophobic groups with an organic solvent does not lead to an increase in stretching frequency [295]. Thus, also in the 25 wt% PNIPAM solution in 80:20 v/v $D_2O/CD_3OD$, the decreasing stretching frequency is due to the release of water molecules from the hydrophobic groups at the phase separation temperature, which occurs abruptly at 0.1 MPa and gradually at 200 MPa. However, at both atmospheric and high pressure in the entire measured temperature range, the absolute values of the peak
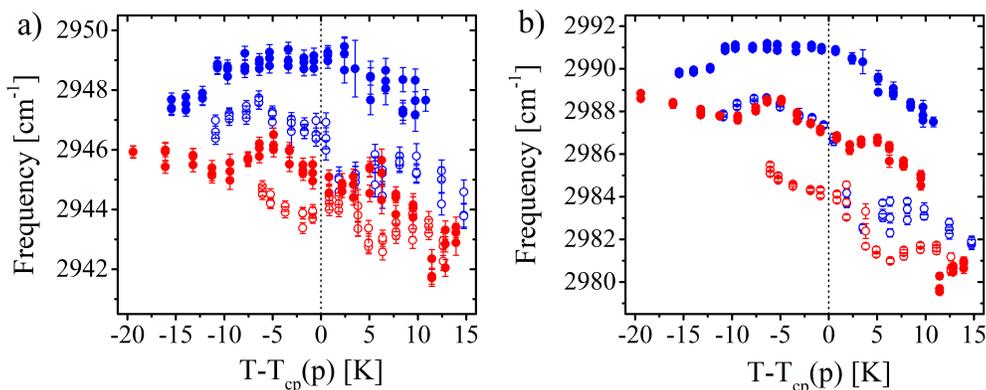
Figure 11.12: Peak frequencies $\nu_{as}(CH_2)$ (a) and $\nu_{as}(CH_3)$ (b) of the 25 wt% PNIPAM solution in 80:20 v/v $D_2O/CD_3OD$ at 0.1 MPa (open red circles) and 200 MPa (closed red circles), and of the 25 wt% PNIPAM solution in $D_2O$ at 0.1 MPa (open blue circles) and 130 MPa (closed blue circles), in dependence on the temperature distance from the cloud point.

frequencies are lower than that for the purely aqueous PNIPAM solution. Thus, the overall hydration of PNIPAM in the 25 wt% solution in 80:20 v/v $D_2O/CD_3OD$ is weaker than the hydration of the chains in pure $D_2O$. It may be that water is partially replaced by methanol on the hydrophobic groups of the chains, leading to a lower frequency. The relative differences in frequencies of both samples do not become significantly smaller at high pressure. It can be concluded that the replacement of methanol by water at high pressure, as follows from QENS, does not notably occur at the hydrophobic groups of PNIPAM, but, instead, mainly occurs at the hydrophilic Amide groups.

Previous Raman spectroscopy measurements of PNIPAM solutions in water/DMSO mixtures at atmospheric pressure, where the co-nonsolvency effect also takes place, revealed that the presence of DMSO does not affect the solvation of the C=O group. However, water on the C-H and N-H groups is partially replaced upon the addition of DMSO to the system [295]. Furthermore, it was shown that, in PNIPAM microgels in mixtures of water and methanol, the methanol molecules that were H-bonded with C=O groups at atmospheric pressure are replaced with water molecules at high pressure [36]. These studies confirm that mainly the preferential adsorption of either water or methanol at the hydrophilic Amide groups are affected by pressure, rather than at the hydrophobic CH groups.

The strong decrease in the peak frequency of the $\nu_{as}(CH_3)$ mode in the 25 wt% PNIPAM solution in 80:20 v/v $D_2O/CD_3OD$ at 200 MPa and $T_{cp} + 10$ K (Figure 11.12) suggests the presence of a second phase transition. This may, however, be caused by the interaction with

the inner surfaces of the glass capillary, as it was not observed in the QENS experiments. The inner diameter of the capillary ($\sim$100 $\mu$m) is in the same order of magnitude of the size of the polymer-rich domains at high pressure, resulting in additional variations in the composition, which may also influence the stretching frequency of the $\nu_{as}$(CH$_3$) mode.

## 11.7   Conclusion

In this chapter, the dynamics of water in mixtures with methanol and PNIPAM is investigated using quasi-elastic neutron scattering (QENS) at various temperatures and pressures, and discussed in view of existing theories on the breakdown of the co-nonsolvency effect at high pressure.

The evaluation of QENS experiments on pure 70:30 and 80:20 v/v H$_2$O/CD$_3$OD solvent mixtures as well as pure H$_2$O revealed that methanol molecules form complexes with water, which reduces the diffusion coefficient of water. At high pressure, it was found that the complex formation is enhanced, thus leading to a further reduction of the diffusion coefficient of the water molecules. This finding disproves the theory for the co-nonsolvency effect at high pressure based on solvent-solvent interactions, which predicts that the clusters of water and methanol, suggested to be responsible for the co-nonsolvency effect at atmospheric pressure, are destroyed at high pressure.

QENS measurements on a 25 wt% PNIPAM solution in 80:20 v/v H$_2$O/CD$_3$OD allowed the investigation of the preferential adsorption of solvent molecules on the chains. In the presence of the polymer, it was observed that, at 200 MPa, the relaxation time of the diffusion of water molecules in the bulk solvent phase is similar to that of the pure 70:30 v/v H$_2$O/CD$_3$OD solvent mixtures close to $T_{cp}$, whereas at atmospheric pressure, it follows the trend of the pure 80:20 v/v H$_2$O/CD$_3$OD solvent mixtures. This shows that, at high pressure, the solvent phase is enriched with methanol at high pressure, meaning that water is preferentially adsorbed at the chains, as predicted by theories on the breakdown of the co-nonsolvency.

At 200 MPa, the relaxation time of the hydration water in the one-phase state, i.e., water that is bound to the polymer, is larger than at 0.1 MPa, which points to an enhanced hydrophilic hydration with respect to hydrophobic hydration at high pressure. It was con-

cluded that the exchange of methanol with water takes place mainly at the hydrophilic Amide groups of PNIPAM, rather than at the hydrophobic isopropyl groups or at the backbone of the chains. This conclusion is supported by complementary Raman spectroscopy measurements, probing the interaction between the solvent molecules and the hydrophobic groups of PNIPAM. The hydration of the hydrophobic groups of PNIPAM in the presence of methanol was found to be weaker than in a purely aqueous PNIPAM solutions in the one-phase state at both pressure. The relative difference between the stretching frequencies between the purely aqueous PNIPAM solution and the PNIPAM solution in the solvent mixture does not depend on pressure, which indicates that the replacement of methanol by water, as followed from the QENS experiments, does not take place at the hydrophobic groups.

# Chapter 12. Dissertation summary and outlook

In the present thesis, the pressure-dependent phase behavior of aqueous PNIPAM solutions is investigated, with a focus on structural properties and PNIPAM-solvent interactions. The presented work therefore complements the existing theoretical and experimental studies on aqueous PNIPAM solutions under high pressure that mainly focused on molecular interactions.

In the first part (Chapters 5 to 9), the phase transition purely aqueous PNIPAM solutions is investigated in dependence on temperature and pressure. Various experimental methods are employed to study the different aspects of the phase transition.

In Chapter 5, the phase behavior of purely aqueous PNIPAM solutions is determined. In agreement with previously published studies on aqueous PNIPAM solutions, an elliptical shape of the coexistence line of the one-phase and two-phase state in the temperature-pressure frame is obtained. The cloud point increases from $\sim$33.7 °C at atmospheric pressure until a maximum is reached at 35.1 °C and 55 MPa, and it decreases again at higher pressures. Thus, at temperatures between 33.7 and 35.1 °C, two phase transitions in different pressure regimes are encountered. Furthermore, the solubility of PNIPAM in the different locations in the pressure-temperature phase diagram is quantified in terms of the Gibbs free energy of mixing, determined using a second-order Taylor expansion around atmospheric pressure. Although these calculations predict cloud points in the high-pressure regime, the cloud point pressure is strongly overestimated. Thus, pressure strongly influences molecular interactions, resulting in finite third-order derivatives of the free energy.

The implications of the pressure-dependent molecular interactions on the equilibrium-state structure are investigated in Chapter 6. Raman spectroscopy allowed the character-

ization of the hydrophobic hydration. At atmospheric pressure, the hydrophobic groups strongly dehydrate upon heating through the phase transition temperature, however, the dehydration is significantly weaker and more gradual at pressures of 80 and 114 MPa. The hydrophobic effect, responsible for the phase separation at atmospheric pressure, therefore plays a weaker role at high pressure. Structural characterization using very small angle neutron scattering revealed that, at both atmospheric pressure and high pressure, stable mesoglobules are formed upon heating from the one-phase state to the two-phase state. Their size and structure depend strongly on pressure as well as on the temperature distance from the cloud point temperature. At atmospheric pressure, the mesoglobules are small ($\sim$0.3 $\mu$m) and are surrounded by a dense PNIPAM shell.This points to the visco-elastic effect as the mechanism behind the mesoglobule stability: The low chain hydration of the strongly dehydrated chains in the shell prevent the coalescence of mesoglobules. At high pressure, the mesoglobules are significantly larger ($\sim$1.3 $\mu$m), water-rich and do not have a dense shell; the visco-elastic effect is therefore weakened.

The role of water during the temperature-induced phase transition at both low and high pressure is in focus of Chapter 7. Using quasi-elastic neutron scattering, it was possible to obtain the entire relaxation spectrum of water molecules, and to identify all individual contributions. The fraction of hydration water, i.e., water molecules that are restricted in their motion due to interaction with PNIPAM, decreases at the phase transition temperature from $\sim$0.45 to $\sim$0.15 at both 0.1 and 130 MPa. At 0.1 MPa, it deceases abruptly, whereas at 130 MPa, the decrease is gradual and spans over a temperature range of $\sim$15 K. The motion of hydration water molecules follows jump diffusion, i.e., they perform a local motion during a certain residence time between discrete translational jumps. The duration of the residence time was attributed to the interaction strength between PNIPAM and the water molecules. In the one-phase state, the lower residence time at high pressure was assigned to the enhanced hydrophobic hydration. Upon phase separation, the residence time at both pressures increases strongly. It was concluded that mainly the hydrophilic groups stay hydrated in the two-phase state, whereas hydrophobic groups dehydrate. In addition, the mobility of the chains just above the cloud point temperature is significantly higher at high pressure than at atmospheric pressure, due to the weaker dehydration of the chains. This provides an additional argument for the importance of the visco-elastic effect during the formation of mesoglobules.

In Chapter 8, the investigation on the pathway of the mesoglobule formation is presented.

Using a combination of time-resolved small-angle neutron scattering and fast pressure jumps to induce phase separation, the structural processes involved in the formation of mesoglobules were followed with a time resolution of 0.05 s with an accessible range of length scales from $\sim$1 to $\sim$100 nm. By exploiting the elliptical shape of the coexistence line in the temperature-pressure frame, the two-phase state was reached at low as well as at high pressures by a change in pressure only. At low pressures, three kinetic processes with different growth rates were observed, with their time scales strongly depending on the depth of the jumps. Directly after the jump, a slow cluster formation stage is observed, followed by fast cluster growth growth due to coalescence that is diffusion-limited. The dehydration of the chains at later times strongly hinders further coalescence, resulting in kinetically stable mesoglobules with sizes of tens of nm. Thus, by varying the depth of the jump in the low-pressure region, the final size and structure of the mesoglobules can be tuned. At high pressure, the formation of mesoglobules comprises only two kinetic processes. During the first $\sim$0.3 s, clusters of chains with sizes larger than 100 nm are formed that subsequently grow by diffusion-limited coalescence. A kinetically stable state is not reached within the duration of the experiment. Thus, the visco-elastic effect, responsible for the stability of the mesoglobules at low pressures, does not play a role at high pressures, which is due to the rather weak dehydration of the chains in the two-phase state.

Furthermore, the kinetics of the dissolution of mesoglobules were investigated, discussed in Chapter 9. Also in this case, small-angle neutron scattering was combined with fast pressure jumps, in this case to induce mixing of the system. At low pressures, the mechanism of dissolution strongly depends on the pressure distance of the target pressure from the cloud point. For target pressures close to the cloud point, the thermodynamic driving force for mixing is weak, preventing water to enter the mesoglobules. Their disintegration occurs via the dissolution of single chains at the surface of the mesoglobules, until they have vanished completely. For target pressures far from the cloud point, the thermodynamic driving force for mixing is strong, and water is able to enter the mesoglobules. The mesoglobules contain an increasing amount of water with time, leading to their growth until the entire volume of the system is spanned, resulting in a semi-dilute polymer solution. At high pressures, the mesoglobules in the two-phase state have an open structure. Upon a jump of any depth to the one-phase state, water is able to enter the mesoglobules, leading to their growth until they span the entire system.

The results from the different experimental methods applied to the system, presented in

Chapters 5 to 7, may be compared with each other. The dehydration of PNIPAM chains upon heating through the cloud point at atmospheric pressure, determined with Raman spectroscopy, with the invariant scattering determined from very small angle neutron scattering curves, and with quasi-elastic neutron scattering, revealed that the dissociation of water molecules from the chains extends over a temperature range of a few Kelvin. At high pressure, however, all three experimental methods revealed that the dehydration occurs over a much broader temperature range, of at least 10 K above the cloud point temperature.

The differences in sensitivity of the used experimental methods to the way the water molecules are associated with the chains allows a more detailed description of the hydration behavior. It is possible to distinguish between hydrophilic hydration, hydrophobic hydration, and water that may be associated with the chains in second hydration layers or water molecules that are trapped into the polymer-rich phases in the two-phase state. Comparing the results from the invariant scattering determined from the VSANS measurements and the fraction of hydration water determined with QENS, it emerges that the water content of the mesoglobules is ~10 times larger at high pressure than at atmospheric pressure, whereas the fraction of hydration water, i.e., water that has a strong interaction with the chains, differs not more than by a factor of 2. It follows that the mesoglobules at high pressure contain a significant amount of water that does not notably interacts with the chains. With QENS, the decreased mobility of the hydration water in the two-phase state points to an increased hydrophilic hydration relative to hydrophobic hydration. This finding, in combination with the found dehydration of the hydrophobic groups from Raman spectroscopy, provides a clear indication that the hydrophilic groups stay hydrated in the two-phase state, both at low and high pressures. Consequently, the formation of hydrogen bonds between the Amide groups of adjacent monomers on the chains is insignificant.

The size of the mesoglobule depends on the protocol used for inducing phase separation. After heating at atmospheric pressure, significantly larger mesoglobules are formed than after a pressure jump in the low-pressure regime, which is due to the significantly slower dehydration of the chains. After a pressure jump, however, the dehydration of the chains occurs much faster, since a state deep inside the two-phase state is reached almost instantly. It may, however, be expected that a similar pathway of mesoglobule formation is present in both cases. In addition, the size of the mesoglobules decreases with distance from the cloud point, along both the pressure and temperature axis: Upon heating at atmospheric pressure, the size of the aggregates decreases with temperature starting from $T_{cp} + 0.5$ K, whereas

the size of the mesoglobules long time after the pressure jump decreases with the pressure distance from the cloud point pressure. Deeper in the two-phase state, the thermodynamic driving force for phase separation is stronger, as followed from the Gibbs free energy. Therefore, the phase separation is stronger, leading to denser and smaller mesoglobules.

Also in the high-pressure regime, significant differences between temperature- and pressure-induced phase separation is observed. Whereas upon heating, the size of the mesoglobules remains constant after their formation, the mesoglobules formed after pressure-induced phase separation are not stable and grow continuously. The mechanism of phase separation may therefore differ between both cases. Raman spectroscopy showed that the hydrophobic groups also dehydrate upon heating through the cloud point at high pressure, albeit to a lesser extent than at low pressure. The hydrophobic effect may still play a role during temperature-induced phase separation at high pressure, but not during pressure-induced phase separation at high pressure. A deeper study of the hydration behavior of the hydrophobic groups may resolve this issue, e.g. with Raman spectroscopy during pressure scans.

In the second part (Chapters 10 and 11), the effect of pressure on the co-nonsolvency effect is investigated. Using the newly gained knowledge about purely aqueous PNIPAM solutions, the same experimental methods are applied to study the influence of the interactions with methanol in the system.

The equilibrium-state structure of a semi-dilute PNIPAM solution in a water/methanol mixture is investigated in Chapter 10. In the one-phase state, the correlation length of concentration fluctuations, indicative of the chain conformation, is determined using small-angle neutron scattering. At all pressures, it increases with temperatures until it diverges close to the cloud point temperature. At high pressure, it is generally larger than at low pressure, indicating that the chains are more contracted at high pressure. From the Flory-Huggins interaction parameter, determined from the correlation length of concentration fluctuations, it was deduced that the hydrophobic effect is strongly weakened at high pressure. This may be due to the enrichment of the solvent with methanol, indicating that methanol is replaced by water on the chains. Furthermore, enthalpic polymer-solvent interactions were shown to be weakened at high pressure. Upon heating from the one-phase state to the two-phase state, stable mesoglobules are formed that are significantly larger at high pressure than at atmospheric pressure, as follows from very small angle neutron scattering. With increasing temperature at atmospheric pressure, solvent molecules are released from the mesoglobules,

as for the purely aqueous PNIPAM solution. At high pressure, however, water-rich mesoglobules are formed at the cloud point temperature due to the preferential adsorption of water at the chains in the one-phase state. The ongoing phase separation leads to the shrinkage of the mesoglobules with increasing temperature. Simultaneously, the lost preferential adsorption of water at the chains in the two-phase state allows methanol molecules to diffuse into the mesoglobules from the solvent phase, thereby increasing their size.

In Chapter 11, the insights from quasi-elastic neutron scattering experiments on the molecular interactions in the system were discussed. The investigation of pure water/methanol mixtures indicated the presence of clusters consisting of methanol and water molecules at atmospheric pressure. At high pressure, cluster formation is enhanced, which disproves the theory suggesting that the breakdown of the co-nonsolvency effect at high pressure is due to the disruption of the clusters formed by methanol and water molecules [35], suggested to be responsible for the co-nonsolvency effect at atmospheric pressure [150, 151]. The polymer-solvent interactions were investigated in a concentrated PNIPAM solution in water/methanol. In contrast to atmospheric pressure conditions, the solvent in the one-phase state at high pressure is enriched with methanol at high pressure, pointing to the preferential adsorption of water on the chains, as was predicted by several theories of the co-nonsolvency effect at high pressure [37, 38, 39]. However, it was not possible to differentiate between the different mechanisms leading to the enhanced solubility of PNIPAM due to the preferential adsorption of water on the chains, proposed in these theories. The investigation on the hydration water with quasi-elastic neutron scattering and Raman spectroscopy revealed that the replacement of methanol by water on the chains mainly occurs at the hydrophilic Amide groups of PNIPAM, rather than at the hydrophobic isopropyl groups or at the backbone of the chains.

The provided data on the co-nonsolvency effect at high pressure in Chapter 10 and 11 consistently point to the preferential adsorption of water on the chains at high pressure, which leads to the enhanced solubility of PNIPAM at high pressures.

In conclusion, a comprehensive description of the physical processes involved in the phase transition of aqueous PNIPAM solutions at various pressures, and their implications on the structural properties is given. The results may help to understand phase transitions in more complex systems, such as solutions of polymers consisting of multiple blocks or biological macromolecules.

# Chapter 13. Appendix

## 13.1 Mesoglobule structure during pressure scans

### 13.1.1 Experimental details

**Materials.** Poly($N$-isopropylacrylamide) (PNIPAM) with a molar mass $M_n = 36\,000$ g mol$^{-1}$ and a dispersity of 1.26 (end groups carboxylic acid and a hydrogen atom, respectively) was purchased from Sigma-Aldrich. It was dissolved at a concentration of 3 wt% in D$_2$O, which is above the overlap concentration. D$_2$O was used to ensure a maximum contrast between water-rich and polymer-rich phases in VSANS measurements.

**Very small angle neutron scattering.** Very small angle neutron scattering (VSANS) measurement were performed at the instrument KWS-3 at the Heinz Maier-Leibnitz Zentrum, Garching, Germany [165]. Using a neutron wavelength $\lambda = 1.28$ nm with a spread $\Delta\lambda/\lambda = 0.18$ and a sample-detector distance of 9.4 m, a $q$ range of $2.1{\times}10^{-3}$ - $2.3{\times}10^{-2}$ nm$^{-1}$ is covered. The sample was mounted in a temperature-controlled custom-made pressure cell based on the one described in ref. [206], which is capable of withstanding pressures up to 500 MPa. The sample was placed between sapphire windows and had a thickness of 2 mm, independent of pressure. The measurements were performed during pressure scans from 10 to 110 MPa in steps of 10 MPa at 38, 39 and 40 °C, i.e., in the two-phase state. After each change in temperature or pressure, the sample was equilibrated for 5 min, followed by at least 3 measurements of 5 min. The data reduction was performed as described in Section 4.2.2, with a measurement of plexiglass to determine the detector sensitivity.

### 13.1.2 Results

Figure 13.1a shows the scattering curves in dependence on pressure obtained during a pressure scan to higher pressures at 38 °C started after heating from the one-phase state at 10 MPa. At low pressures, a shoulder at $\sim10^{-3}$ Å$^{-1}$ indicates the presence of mesoglobules

of several hundreds of nanometers in size. Up to 40 MPa, the intensity of the shoulder at $\sim 10^{-3}$ Å$^{-1}$ decreases. Above 30 MPa, a shoulder suddenly appears at $\sim 1.5 \times 10^{-4}$ Å$^{-1}$ and increases in intensity, while the intensity of the shoulder at $\sim 10^{-3}$ Å$^{-1}$ strongly decreases. Thus, a sharp transition from a solution consisting of mainly small mesoglobules to one with mainly large clusters takes place. During the pressure scan back to lower pressures, shown in Figure 13.1d, the opposite behavior is observed. At 30 MPa, a shoulder at intermediate $q$ values appears, which shows the presence of structures with sizes similar to the ones of the mesoglobules observed during the pressure scan to higher pressures before reaching 30 MPa. However, the strong contribution at low $q$ values remains. Presumably, the large structures at high pressures are clusters of those mesoglobules that are present at low pressures. Rearrangements of chains take place inside the large clusters, but the structure of the individual mesoglobules is not lost completely and is again uncovered after releasing the pressure to below the transition value. Probably, they persist inside the large clusters, but it cannot be excluded that these mesoglobules coexist with the large clusters in the solution.

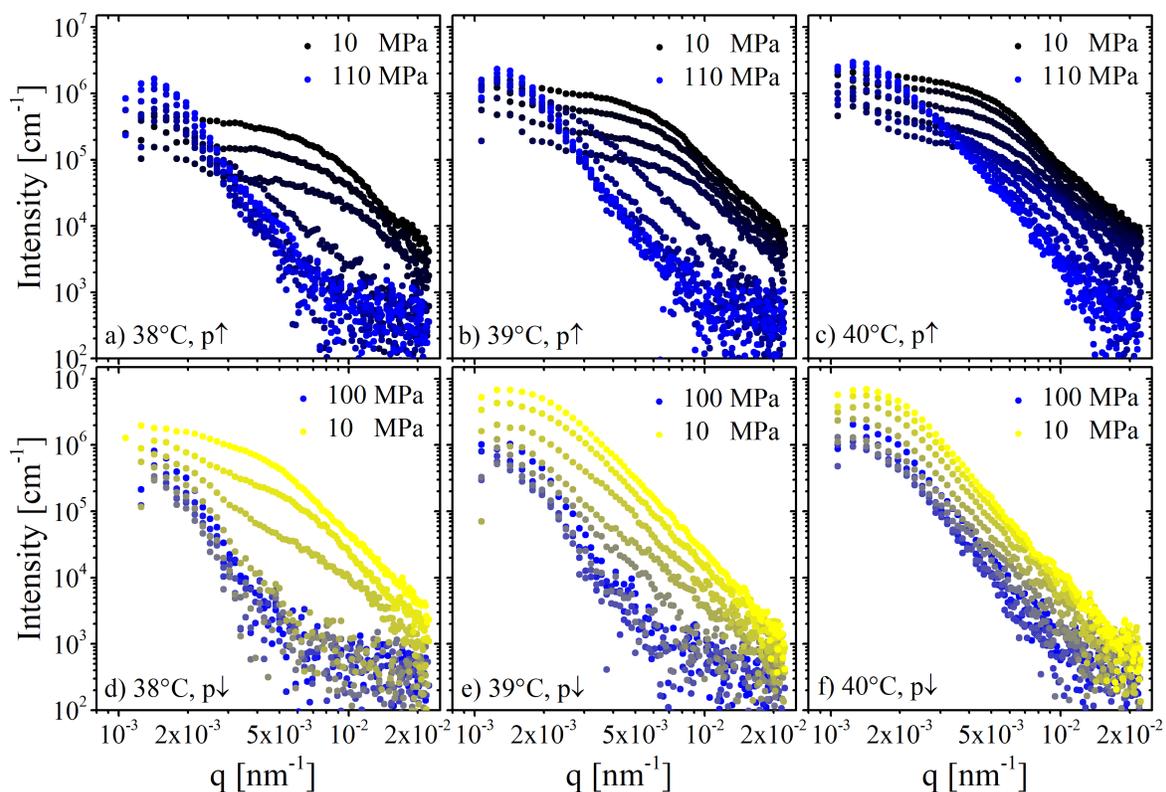Similar behavior is observed at 39 and 40 °C. The shoulder present at low pressures around



Figure 13.1:  VSANS cattering curves of the 3 wt% PNIPAM solution in D$_2$O obtained during a pressure scan from 10 to 110 MPa (a-c), and back to 10 MPa (d-f) at 38 °C (a,d), 39 °C (b,e) and at 40 °C (c,f).

$10^{-3}$ Å$^{-1}$ decreases in intensity with increasing pressure. At 50 MPa for 39 °C and 70 MPa for 40 °C, a shoulder at low $q$ values appears, showing that also at 39 and 40 °C, a sharp transition between both size regimes is present. The transition pressures increases, however, with increasing temperature. Contrary to the pressure scan back to lower pressures at 38 °C, the shoulder at intermediate $q$ values is not observed at low pressures at 39 and 40 °C (Figure 13.1e and f, respectively). At these temperatures, rearrangements of chains inside the large structures at high pressures are stronger, and the mesoglobules merge completely when clusters are formed. The intensity of the shoulder at low $q$ values increases during the entire pressure scan to lower pressures at both temperatures. It follows that the structures dehydrate, thereby increasing the contrast between the polymer-rich and water-rich phases.
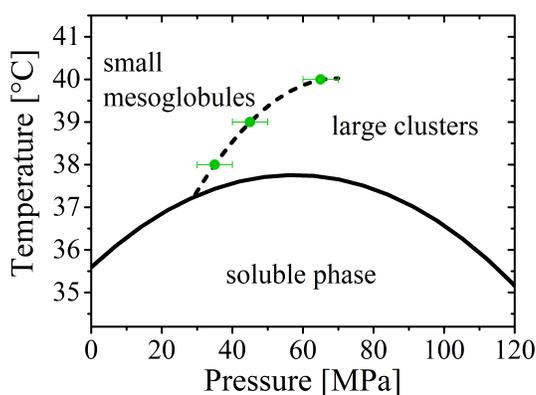


Figure 13.2: Phase diagram in the pressure-temperature frame. Solid line: coexistence line as determined by turbidimetry (Chapter 5), green circles: transition pressures between phases containing small mesoglobules and large clusters at the three measured temperatures. The dashed line is a guide to the eye.

With these observations from the scattering curves obtained during pressure scans, an additional branch in the temperature-pressure phase diagram of aqueous PNIPAM solutions is identified and shown in Figure 13.2. It separates a solution of small mesoglobules from a solution of large clusters. This behavior closely resembles that of percolation [41] where particles cluster together to interconnected domains upon crossing a certain threshold, as observed earlier in polymeric systems [296, 297]. In this case, the percolation threshold is crossed by increasing pressure due to changes in the inter-particle potential. However, the system is not completely reversible; the large clusters remain after the pressure scan to lower pressures. The mesoglobules can therefore not be described as hard particles, but they interconnect irreversibly when clusters are formed. Both the attractive interaction between mesoglobules and their interconnection when they cluster may be caused by the increased hydration of the chains at high pressure. The stability of the mesoglobules was earlier shown

to be a result of a dense shell, leading to an entanglement force preventing aggregation. With increasing pressure, the dense shell hydrates, which allows the merging of mesoglobules.

# 13.2 Cloud point determination of 25 wt% PNIPAM solutions

## 13.2.1 Experimental details

**Materials.** Poly($N$-isopropylacrylamide) (PNIPAM) with a molar mass $M_n = 36\ 000$ g mol$^{-1}$ and a dispersity of 1.26 (end groups carboxylic acid and a hydrogen atom, respectively) was purchased from Sigma-Aldrich. It was dissolved at a concentration of 25 wt% in $H_2O$ and in 80:20 v/v $H_2O$/$CD_3OD$, and stirred for at least 48 h to ensure complete dissolution.

**Turbidimetry.** Turbidimetry measurements were performed using a 10 mW HeNe laser ($\lambda$ = 632.8 nm) in combination with a photodiode detector. A custom-made copper-beryllium pressure cell with sapphire windows, capable of withstanding pressures up to 400 MPa, was placed in between the laser and the detector. A Viton O-ring separated the sample from the pressure medium (water) with a sample thickness of 1 mm. A pressure generator from SITEC (Maur, Switzerland) was connected to the pressure cell. The temperature in the pressure cell was controlled by a Julabo F12 circulating bath thermostat, and a Pt100 resistance thermometer, attached to the pressure cell, was used to precisely determine its temperature.

Both samples were measured during heating scans at pressures of 0.1, 130 and 200 MPa with a heating rate of 0.06 K min$^{-1}$. The measured transmitted intensity was normalized to the maximum intensity that was reached during the measurement. The cloud point was defined as the temperature and pressure at which the transmitted intensity starts to decrease.

## 13.2.2 Results

In Figure 13.3, the transmission curves of the 25 wt% PNIPAM solution in $H_2O$ and in 80:20 v/v $H_2O$/$CD_3OD$ in dependence on temperature at different pressures are shown. For 25 wt% PNIPAM in $H_2O$, the cloud points are 31.4 ± 0.1, 34.1 ± 0.1 and 28.5 ± 0.1 °C for 0.1, 130 and 200 MPa, respectively. For 25 wt% PNIPAM in 80:20 v/v $H_2O$/$CD_3OD$, they are 23.5 ± 0.1, 38.5 ± 0.1 and 40.0 ± 0.1 °C for 0.1, 130 and 200 MPa, respectively.
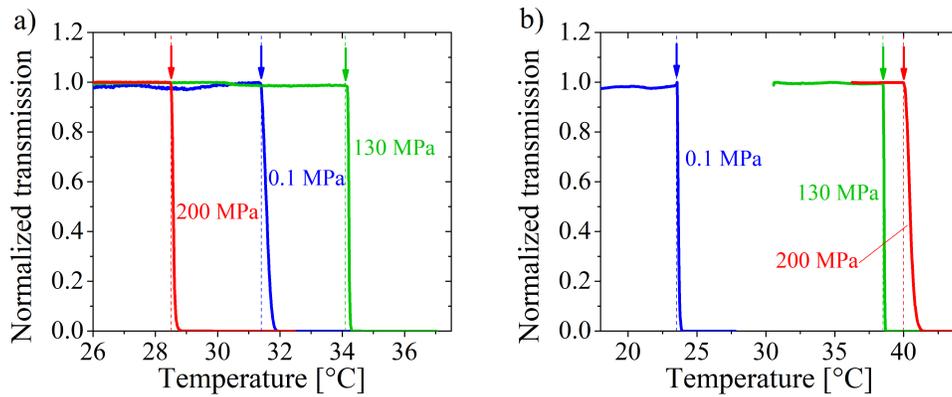
Figure 13.3: Transmission curves in dependence on temperature of the 25 wt% PNIPAM solution in $H_2O$ (a) and in 80:20 v/v $H_2O/CD_3OD$ (b) at 0.1 MPa (blue curves), 130 MPa (green curves) and 200 MPa (red curves). The cloud points are marked with the arrows.

## 13.3  Neutron scattering cross sections

In Table 13.1, the coherent and incoherent scattering cross sections of NIPAM ($C_6H_{11}NO$), water ($H_2O$) and fully deuterated methanol ($CD_3OD$) are presented. From the weight fractions and densities of the individual components, it is determined that in the 25 wt% PNIPAM solution in $H_2O$, measured using QENS (Chapter 7), it follows that 74 % of the measured neutrons were incoherently scattered by water molecules. The remaining neutrons are mainly incoherently scattered by NIPAM, whereas a negligible fraction is scattered coherently. For the 25 wt% PNIPAM solution in 80:20 v/v $H_2O/CD_3OD$, also measured using QENS (Chapter 11), 69 % of the measured neutrons were incoherently scattered by water molecules. Also in this case, the remaining neutrons are mainly incoherently scattered by NIPAM. A negligible fraction is scattered incoherently by $CD_3OD$ or is scattered coherently.

Table 13.1: Incoherent and coherent neutron scattering cross sections for NIPAM ($C_6H_{11}NO$), water ($H_2O$) and fully deuterated methanol ($CD_3OD$), as determined from scattering cross sections in ref. [183].

|  | $\sigma_{inc}$ [b] | $\sigma_{coh}$ [b] |
|---|---|---|
| $C_6H_{11}NO$ | 883.54 | 67.89 |
| $H_2O$ | 160.54 | 7.74 |
| $CD_3OD$ | 8.21 | 32.16 |

# Bibliography

[1] S. Alberti. Phase Separation in Biology. *Curr. Biol.*, 27:1097–1102, 2017.

[2] P. G. Vekilov. Phase Transitions of Folded Proteins. *Soft Matter*, 6:5254–5257, 2010.

[3] M. Wuttig and N. Yamada. Phase-Change Materials for Rewriteable Data Storage. *Nat. Mater*, 6:824–832, 2007.

[4] I. W. Hamley. *Introduction to Soft Matter*. Wiley, 2007.

[5] J. van der Gucht. Grand Challenges in Soft Matter Physics. *Front. Phys.*, 6:87, 2018.

[6] P. L. Privalov and C. Crane-Robinson. Role of Water in the Formation of Macromolecular Structures. *Eur. Biophys. J.*, 46:203–224, 2017.

[7] A. Horwich. Protein Aggregation in Disease: A Role for Folding Intermediates Forming Specific Multimeric Interactions. *J. Clin. Invest.*, 110:1221–1232, 2002.

[8] C. A. Ross and M. A. Poirier. Protein Aggregation and Neurodegenerative Disease. *Nat. Med.*, 10:10–17, 2004.

[9] A. Aguzzi and T. O'Connor. Protein Aggregation Diseases: Pathogenicity and Therapeutic Perspectives. *Nat. Rev. Drug Discov.*, 9:237–248, 2010.

[10] M. A. Ward and T. K. Georgiou. Thermoresponsive Polymers for Biomedical Applications. *Polymers*, 3:1215–1242, 2011.

[11] Y.-J. Kim and Y. T. Matsunaga. Thermo-Responsive Polymers and their Application as Smart Biomaterials. *J. Mater. Chem. B*, 5:4307–4321, 2017.

[12] M. E. Harmon, M. Tang, and C. W. Frank. A Microfluidic Actuator Based on Thermoresponsive Hydrogels. *Polymer*, 44:4547–4556, 2003.

[13] M. Wei, Y. Gao, X. Li, and M. J. Serpe. Stimuli-Responsive Polymers and their Applications. *Polym. Chem*, 8:127–143, 2017.

[14] M. Rubinstein and R. H. Colby. *Polymer Physics*. Oxford University Press, 2003.

[15] G. Strobl. *The Physics of Polymers*. Springer-Verlag, 1996.

[16] T. Pellegrino, S. Kudera, T. Liedl, A. Muñoz Javier, L. Manna, and W. J. Parak. On the Development of Colloidal Nanoparticles towards Multifunctional Structures and their Possible Use for Biological Applications. *Small*, 1:48–63, 2005.

[17] F. Gröhn. Soft Matter Nanoparticles with Various Shapes and Functionalities can form through Electrostatic Self-Assembly. *Soft Matter*, 6:4296–4302, 2010.

[18] W. J. Stark, P. R. Stoessel, W. Wohlleben, and A. Hafner. Industrial Applications of Nanoparticles. *Chem. Soc. Rev.*, 44:5793–5805, 2015.

[19] B. B. Boonyaratanakornkit, C. B. Park, and D. S. Clark. Pressure Effects on Intra- and Intermolecular Interactions within Proteins. *Biochim. Biophys. Acta*, 1595:235–249, 2002.

[20] V. M. Dadarlat and C. B. Post. Decomposition of Protein Experimental Compressibility into Intrinsic and Hydration Shell Contributions. *Biophys. J.*, 91:4544–4554, 2006.

[21] P. C. Michels, D. Hei, and D. S. Clark. Pressure Effects on Enzyme Activity and Stability at High Temperature. *Adv. Protein Chem.*, 48:341–376, 1996.

[22] R. Jaenicke. Enzymes under Extremes of Physical Conditions. *Ann. Rev. Biophys. Bioeng.*, 10:1–67, 1981.

[23] C. Berger, R. Phillips, A. Centeno, A. Zurutuza, and A. Vijayaraghavan. Capacitive Pressure Sensing with Suspended Graphene-Polymer Heterostructure Membranes. *Nanoscale*, 9:17439–17449, 2017.

[24] P. Escudero, J. Yeste, C. Pascual-Izarra, R. Villa, and M. Alvarez. Color Tunable Pressure Sensors Based on Polymer Nanostructured Membranes for Optofluidic Applications. *Sci. Rep.*, 9:3259, 2019.

[25] A. Halperin, M. Kröger, and F. M. Winnik. Poly($N$-isopropylacrylamide) Phase Diagrams: Fifty Years of Research. *Angew. Chem., Int. Ed.*, 54:15342–15367, 2015.

[26] A. V. Gorelov, A. Du Chesne, and K. A. Dawson. Phase Separation in Dilute Solutions of Poly($N$-isopropylacrylamide). *Physica A*, 240:443–452, 1997.

[27] K. Chan, R. Pelton, and J. Zhang. On the Formation of Colloidally Dispersed Phase-Separated Poly($N$-isopropylacrylamide). *Langmuir*, 15:4018–4020, 1999.

[28] V. Aseyev, S. Hietala, A. Laukkanen, M. Nuopponen, O. Confortini, F. E. Du Prez, and H. Tenhu. Mesoglobules of Thermoresponsive Polymers in Dilute Aqueous Solutions Above the LCST. *Polymer*, 46:7118–7131, 2005.

[29] P. Kujawa, V. Aseyev, H. Tenhu, and F. M. Winnik. Temperature-Sensitive Properties of Poly($N$-isopropylacrylamide) Mesoglobules Formed in Dilute Aqueous Solutions Heated above Their Demixing Point. *Macromolecules*, 39:7686–7693, 2006.

[30] E. A. Maresov and A. N. Semenov. Mesoglobule Morphologies of Amphiphilic Polymers. *Macromolecules*, 41:9439–9457, 2008.

[31] C. Balu, M. Delsanti, P. Guenoun, F. Monti, and M. Cloitre. Colloidal Phase Separation of Concentrated PNIPAm Solutions. *Langmuir*, 23:2404–2407, 2007.

[32] F. Meersman, J. Wang, Y. Wu, and K. Heremans. Pressure Effect on the Hydration Properties of Poly($N$-isopropylacrylamide) in Aqueous Solution Studied by FTIR Spectroscopy. *Macromolecules*, 38:8923–8928, 2005.

[33] R. O. R. Costa and R. F. S. Freitas. Phase Behavior of Poly($N$-isopropylacrylamide) in Binary Aqueous Solutions. *Polymer*, 43:5879–5885, 2002.

[34] N. Osaka and M. Shibayama. Pressure Effects on Cononsolvency Behavior of Poly($N$-isopropylacrylamide) in Water/DMSO Mixed Solvents. *Macromolecules*, 45:2171–2174, 2012.

[35] B. Ebeling, S. Eggers, N. Hendrich, A. Nitschke, and P. Vana. Flipping the Pressure- and Temperature-Dependent Cloud-Point Behavior in the Cononsolvency System of Poly($N$-isopropylacrylamide) in Water and Ethanol. *Macromolecules*, 47:1462–1469, 2014.

[36] C. H. Hofmann, S. Grobelny, M. Erlkamp, R. Winter, and W. Richtering. Influence of High-Pressure on Cononsolvency of Poly($N$-isopropylacrylamide) Nanogels in Water/Methanol Mixtures. *Polymer*, 55:2000–2007, 2014.

[37] T. E. de Oliveira, P. A. Netz, D. Mukherji, and K. Kremer. Why Does High Pressure Destroy Co-Non-Solvency of PNIPAm in Aqueous Methanol? *Soft Matter*, 11:8599–8604, 2015.

[38] A. Pica and G. Graziano. Hydrostatic Pressure Effect on PNIPAM Cononsolvency in Water-Methanol Solutions. *Biophys. Chem.*, 231:34–38, 2017.

[39] Y. A. Budkov and A. L. Kolesnikov. Statistical Description of Co-Nonsolvency Suppression at High Pressures. *Soft Matter*, 13:8362–8367, 2017.

[40] G. Yuan, X. Wang, C. C. Han, and C. Wu. Reexamination of Slow Dynamics in Semidilute Solutions: From Correlated Fluctuation to Collective Diffusion. *Macromolecules*, 39:3642–3647, 2006.

[41] P.-G. de Gennes. *Scaling Concepts in Polymer Physics*. Cornell University Press, 1979.

[42] I. Teraoka. *Polymer Solutions: An Introduction to Physical Properties.* John Wiley and Sons, Inc., 2002.

[43] J. W. Cahn. On Spinodal Decomposition. *Acta Metall.*, 9:795–801, 1961.

[44] N. Kuwahara and K. Kubota. Spinodal Decomposition in a Polymer Solution. *Phys. Rev. A*, 45:7385–7394, 1992.

[45] J. W. Cahn. The Later Stages of Spinodal Decomposition and the Beginnings of Particle Coarsening. *Acta Metall.*, 14:1685–1692, 1966.

[46] K. Liu and E. Kiran. Pressure-Induced Phase Separation in Polymer Solutions: Kinetics of Phase Separation and Crossover from Nucleation and Growth to Spinodal Decomposition in Solutions of Polyethylene in *n*-Pentane. *Macromolecules*, 34:3060–3068, 2001.

[47] S. Krishnamurthy and R. Bansil. Nucleation and Growth in a Polymer Solution. *Phys. Rev. Lett.*, 50:2010–2013, 1983.

[48] C. Sagui and M. Grant. Theory of Nucleation and Growth During Phase Separation. *Phys. Rev. E*, 59:4175–4187, 1999.

[49] H. Tanaka. Viscoelastic Phase Separation. *J. Phys.: Condens. Matter*, 12:207–264, 2000.

[50] M. Y. Lin, H. M. Lindsay, D. A. Weitz, R. C. Ball, R. Klein, and P. Meakin. Universal Reaction-Limited Colloid Aggregation. *Phys. Rev. A*, 41:2005–2020, 1990.

[51] J. Chuang, A. Y. Grosberg, and T. Tanaka. Topological Repulsion between Polymer Globules. *J. Chem. Phys.*, 112:6434–6442, 2000.

[52] H. Tanaka. Appearance of a Moving Droplet Phase and Unusual Networklike or Spongelike Patterns in a Phase-Separating Polymer Solution With a Double-Well-Shaped Phase Diagram. *Macromolecules*, 25:6377–6380, 1992.

[53] H. Tanaka. Unusual Phase Separation in a Polymer Solution Caused by Asymmetric Molecular Dynamics. *Phys. Rev. Lett.*, 71:3158–3161, 1993.

[54] R. Hołyst and T. A. Vilgis. The Structure and Phase Transition in Polymer Blends, Diblock Copolymers and Liquid Crystalline Polymers: the Landau-Ginzburg Approach. *Macromol. Theory Simul.*, 5:573–643, 1996.

[55] J. M. Yeomans. *Statistical Mechanics of Phase Transitions.* Oxford Science Publications, 1992.

[56] J. Schmitz, L. Belkoura, and D. Woermann. Concentration Fluctuations in the Vicinity of the Liquid/Liquid Coexistence Curve of a Binary Mixture with a Lower Critical Point. *Ber. Bunsenges. Phys. Chem.*, 99:848–852, 1995.

[57] F. Giavazzi, A. Fornasieri, A. Vailati, and R. Cerbino. Equilibrium and Non-Equilibrium Concentration Fluctuations in a Critical Binary Mixture. *Eur. Phys. J. E*, 39:103, 2016.

[58] G. Meier, B. Momper, and E. W. Fischer. Critical Behavior in a Binary Polymer Blend as Studied by Static and Dynamic Light Scattering. *J. Chem. Phys.*, 97:5884–5897, 1992.

[59] H. Sato, N. Kuwahara, and K. Kubota. Critical Behavior in a Polymer Blend. *Phys. Rev. E*, 53:3854–3863, 1996.

[60] K. To and H. J. Choi. Polymer Conformation near the Critical Point of a Binary Mixture. *Phys. Rev. Lett.*, 80:536–539, 1998.

[61] P. Štěpánek, T. L. Morkved, K. Krishnan, T. P. Lodge, and F. S. Bates. Critical Phenomena in Binary and Ternary Polymer Blends. *Physica A*, 314:411–418, 2002.

[62] R. Kita, K. Kubota, and T. Dobashi. Critical Behavior of a Polydisperse Polymer Solution as Revealed by Turbidity. *Phys. Rev. E*, 56:3213–3218, 1997.

[63] Y. B. Melnichenko, M. A. Anisimov, A. A. Povodyrev, G. D. Wignall, J. V. Sengers, and W. A. Van Hook. Sharp Crossover of the Susceptibility in Polymer Solutions near the Critical Demixing Point. *Phys. Rev. Lett.*, 79:5266–5269, 1997.

[64] J. Szydlowski, L. P. Rebelo, H. Wilczura, M. Dadmun, Y. Melnichenko, G. D. Wignall, and W. A. Van Hook. Comparison of SANS and DLS Hydrodynamic Correlation Lengths for a Polystyrene/Methyl-Cyclohexane Solution in the Vicinity of Temperature-or Pressure-Induced Critical Demixing. *Physica B*, 214-243:1035–1037, 1998.

[65] A. Furukawa. Dynamic Critical Phenomena of Polymer Solutions. *J. Phys. Soc. Jpn.*, 72:1436–1445, 2003.

[66] B.-J. Niebuur, J. Puchmayr, C. Herold, L. P. Kreuzer, V. Hildebrand, P. Müller-Buschbaum, A. Laschewsky, and C. M. Papadakis. Polysulfobetaines in Aqueous Solution and in Thin Film Geometry. *Materials*, 11:850, 2018.

[67] D. A. Weitz, J. S. Huang, M. Y. Lin, and J. Sung. Limits of the Fractal Dimension for Irreversible Kinetic Aggregation of Gold Colloids. *Phys. Rev. Lett.*, 54:1416–1419, 1985.

[68] M. Y. Lin, H. M. Lindsay, D. A. Weitz, R. C. Ball, R. Klein, and P. Meaking. Universality in Colloid Aggregation. *Nature*, 339:360–362, 1989.

[69] Marián Sedlák. A Novel Approach to Controlled Self-Assembly of pH-Responsive Thermosensitive Homopolymer Polyelectrolytes into Stable Nanoparticles. *Adv. Colloid Interface Sci.*, 232:57–69, 2016.

[70] R. Stepanyan, J. G. J. L. Lebouille, J. J. M. Slot, R. Tuinier, and M. A. Cohen-Stuart. Controlled Nanoparticle Formation by Diffusion Limited Coalescence. *Phys. Rev. Lett*, 109:138301, 2012.

[71] K. Kyriakos, M. Philipp, J. Adelsberger, S. Jaksch, A. V. Berezkin, D. M. Lugo, W. Richtering, I. Grillo, A. Miasnikova, A. Laschewsky, P. Müller-Buschbaum, and C. M. Papadakis. Cononsolvency of Water/Methanol Mixtures for PNIPAM and PS-*b*-PNIPAM: Pathway of Aggregate Formation Investigated Using Time-Resolved SANS. *Macromolecules*, 47:6867–6879, 2014.

[72] L. Smeller. Pressure-Temperature Phase Diagrams of Biomolecules. *Biochim. Biophys. Acta*, 1595:11–29, 2002.

[73] F. Meersman, L. Smeller, and K. Heremans. Protein Stability and Dynamics in the Pressure-Temperature Plane. *Biochim. Biophys. Acta*, 1764:346–354, 2006.

[74] S. A. Hawley. Reversible Pressure-Temperature Denaturation of Chymotrypsinogen. *Biochemistry*, 10:2436–2442, 1971.

[75] R. L. Cook, H. E. King, and D. G. Peiffer. Pressure-Induced Crossover from Good to Poor Solvent Behavior for Polyethylene Oxide in Water. *Phys. Rev. Lett.*, 69:3072–3075, 1992.

[76] K. Otake, R. Karaki, T. Ebina, C. Yokoyama, and S. Takahashi. Pressure Effects on the Aggregation of Poly(*N*-isopropylacrylamide) and Poly(*N*-isopropylacrylamide-co-acrylic acid) in Aqueous Solutions. *Macromolecules*, 26:2194–2197, 1993.

[77] M. Shibayama, K. Isono, S. Okabe, T. Karino, and M. Nagao. Sans Study on Pressure-Induced Phase Separation of Poly(*N*-isopropylacrylamide) Aqueous Solutions and Gels. *Macromolecules*, 37:2909–2918, 2004.

[78] E. Loozen, K. Heremans, and H. Berghmans. The Influence of Pressure on the Lower Critical Solution Temperature Miscibility Behavior of Aqueous Solutions of Poly(vinyl methyl ether) and the Relation to the Compositional Curvature of the Volume of Mixing. *J. Phys. Chem. B*, 110:7793–7802, 2006.

[79] S. Saeki, N. Kuwahara, K. Hamano, Y. Kenmochi, and T. Yamaguchi. Pressure Dependence of Upper Critical Solution Temperatures in Polymer Solutions. *Macromolecules*, 19:2353–2356, 1986.

[80] S. Janssen, D. Schwahn, K. Mortensen, and T. Springer. Pressure Dependence of the Flory-Huggins Interaction Parameter in Polymer Blends: A SANS Study and a Comparison to the Flory-Orwoll-Vrij Equation of State. *Macromolecules*, 26:5587–5591, 1993.

[81] D. Schwahn, H. Frielinghaus, K. Mortensen, and K. Almdal. Temperature and Pressure Dependence of the Order Parameter Fluctuations, Conformational Compressibility, and the Phase Diagram of the PEP-PDMS Diblock Copolymer. *Phys. Rev. Lett.*, 77:3153–3156, 1996.

[82] B. Steinhoff, M. Rüllmann, M. Wenzel, M. Junker, I. Alig, R. Oser, B. Stühn, G. Meier, O. Diat, P. Bösecke, and H. B. Stanley. Pressure Dependence of the Order-to-Disorder Transition in Polystyrene/Polyisoprene and Polystyrene/Poly(methylphenylsiloxane) Diblock Copolymers. *Macromolecules*, 31:36–40, 1998.

[83] P. Atkins and J. de Paula. *Physical Chemistry, 8th Edition*. Oxford University Press, 2006.

[84] G. Panick, G. J. A. Vidugiris, R. Malessa, G. Rapp, R. Winter, and C. Royer. Exploring the Temperature-Pressure Phase Diagram of Staphylococcal Nuclease. *Biochemistry*, 38:4157–4164, 1999.

[85] J. Zhang, X. Peng, A. Jonas, and J. Jonas. NMR Study of the Cold, Heat, and Pressure Unfolding of Ribonuclease A. *Biochemistry*, 34:8361–8641, 1995.

[86] N. Takeda, M. Kato, and Y. Taniguchi. Pressure- and Thermally-Induced Reversible Changes in the Secondary Structure of Ribonuclease A Studied by FT-IR Spectroscopy. *Biochemistry*, 34:5980–5987, 1995.

[87] G. Panick, R. Malessa, and R. Winter. Differences between the Pressure- and Temperature-Induced Denaturation and Aggregation of β-Lactoglobulin A, B, and AB Monitored by FT-IR Spectroscopy and Small-Angle X-ray Scattering. *Biochemistry*, 38:6412–6519, 1999.

[88] T. V. Chalikian. Volumetric Properties of Proteins. *Annu. Rev. Biophys. Biomol. Struc.*, 32:207–235, 2003.

[89] A. Yamaguchi, T. H. Yamada, and K. Akasaka. Thermodynamics of Unfolding of Ribonuclease A under High Pressure. A Study by Proton NMR. *J. Mol. Biol.*, 250:689–694, 1995.

[90] A. Zipp and W. Kauzmann. Pressure Denaturation of Metmyoglobin. *Biochemistry*, 12:4217–4228, 1973.

[91] L. Smeller. *High Pressure Bioscience*, chapter Protein Denaturation on $p$-$T$ Axes — Thermodynamics and Analysis. Springer Science+Business Media, 2015.

[92] J. Raúl Grigera and A. N. McCarthy. The Behavior of the Hydrophobic Effect under Pressure and Protein Denaturation. *Biophys J.*, 98:1626–1631, 2010.

[93] N. Smolin and R. Winter. A Molecular Dynamics Simulation of SNase and its Hydration Shell at High Temperature and High Pressure. *Biochim. Biophys. Acta*, 1764:522–534, 2006.

[94] S. Sarupria and S. Garde. Quantifying Water Density Fluctuations and Compressibility of Hydration Shells of Hydrophobic Solutes and Proteins. *Phys. Rev. Lett*, 103:037803, 2009.

[95] H. G. Schild. Poly(*N*-isopropylacrylamide): Experiment, Theory and Application. *Prog. Polym. Sci.*, 17:163–249, 1992.

[96] Y. Guan and Y. Zhang. PNIPAM Microgels for Biomedical Applications: From Dispersed Particles to 3D Assemblies. *Soft Matter*, 7:6375–6384, 2011.

[97] A. Gandhi, A. Paul, S. O. Sen, and K. K. Sen. Studies on Thermoresponsive Polymers: Phase Behaviour, Drug Delivery and Biomedical Applications. *Asian J. Pharm. Sci.*, 10:99–107, 2015.

[98] A. Richter, G. Paschew, S. Klatt, J. Lienig, K.-F. Arndt, and H.-J. Adler. Review on Hydrogel-Based pH Sensors and Microsensors. *Sensors*, 8:561–581, 2008.

[99] J. Hu and S. Liu. Responsive Polymers for Detection and Sensing Applications: Current Status and Future Developments. *Macromolecules*, 43:8315–8330, 2010.

[100] G. Graziano. On the Temperature-Induced Coil to Globule Transition of Poly-*N*-isopropylacrylamide in Dilute Aqueous Solutions. *Int. J. Biol. Macromol.*, 27:89–97, 2000.

[101] Q. Zhang, C. Weber, U. S. Schubert, and R. Hoogenboom. Thermoresponsive Polymers with Lower Critical Solution Temperature: From Fundamental Aspects and Measuring Techniques to Recommended Turbidimetry Conditions. *Mater. Horiz.*, 4:109–116, 2017.

[102] C. Wu and S. Zhou. Laser Light Scattering Study of the Phase Transition of Poly(*N*-isopropylacrylamide) in Water. 1. Single Chain. *Macromolecules*, 28:8381–8387, 1995.

[103] X. Wang, X. Qiu, and C. Wu. Comparison of the Coil-to-Globule and the Globule-to-Coil Transition of a Single Poly(*N*-isopropylacrylamide) Homopolymer Chain in Water. *Macromolecules*, 31:2972–2976, 1998.

[104] S. Fujishige, K. Kubota, and I. Ando. Phase Transition of Aqueous Solutions of Poly(*N*-isopropylacrylamide) and Poly(*N*-isopropylmethacrylamide). *J. Phys. Chem*, 93:3311–3313, 1989.

[105] Y. Okada and F. Tanaka. Cooperative Hydration, Chain Collapse, and Flat LCST Behavior in Aqueous Poly(*N*-isopropylacrylamide) Solutions. *Macromolecules*, 38:4465–4471, 2005.

[106] F. Tanaka, T. Koga, I. Kaneda, and F. M. Winnik. Hydration, Phase Separation and Non-linear Rheology of Temperature-Sensitive Water-Soluble Polymers. *J. Phys.: Condens. Matter*, 23:284105, 2011.

[107] P. G. de Gennes. Kinetics of Collapse for a Flexible Coil. *J. Physique Lett.*, 46:639–642, 1985.

[108] A. Y. Grosberg, S. K. Nechaev, and E. I. Shakhnovich. The Role of Topological Constraints in the Kinetics of Collapse of Macromolecules. *J. Phys. France*, 49:2095–2100, 1988.

[109] K. A. Dawson, E. G. Timoshenko, and P. Kiernan. Theoretical and Experimental Approaches to Kinetics at the Collapse Transition of a Homopolymer. *Nuovo Cimento Soc. Ital. Fis. D*, 16:675–687, 1994.

[110] X. Ye, Y. Lu, L. Shen, Y. Ding, S. Liu, G. Zhang, and C. Wu. How Many Stages in the Coil-to-Globule Transition of Linear Homopolymer Chains in a Dilute Solution? *Macromolecules*, 40:4750–4752, 2007.

[111] C. Li, X. Ye, Y. Ding, and S. Liu. Kinetics of Coil-to-Globule Transition of Dansyl-Labeled Poly-($N$-isopropylacrylamide) Chains in Aqueous Solution. *Chin. J. Chem. Phys.*, 25:389–397, 2012.

[112] J. Xu, Z. Zhu, S. Luo, C. Wu, and S. Liu. First Observation of Two-Stage Collapsing Kinetics of a Single Synthetic Polymer Chain. *Phys. Rev. Lett.*, 96:027802, 2006.

[113] Y. Lu, X. Ye, J. Li, C. Li, and S. Liu. Kinetics of Laser-Heating-Induced Phase Transition of Poly($N$-isopropylacrylamide) Chains in Dilute and Semidilute Solutions. *J. Phys. Chem. B*, 115:12001–12006, 2011.

[114] T. Terada, T. Inaba, H. Kitano, Y. Maeda, and N. Tsukida. Raman Spectroscopic Study on Water in Aqueous Solutions of Temperature-Responsive Polymers: Poly($N$-isopropylacrylamide) and Poly[$N$-(3-ethoxypropyl)acrylamide]. *Macromol. Chem. Phys.*, 195:3261–3270, 1994.

[115] P. I. Haris and D. Chapman. Does Fourier-Transform Infrared Spectroscopy Provide Useful Information on Protein Structures? *Trends Biochem. Sci.*, 17:328–333, 1992.

[116] Y. Maeda, T. Higuchi, and I. Ikeda. Change in Hydration State during the Coil-Globule Transition of Aqueous Solutions of Poly($N$-isopropylacrylamide) as Evidenced by FTIR Spectroscopy. *Langmuir*, 16:7503–7509, 2000.

[117] S.-Y. Lin, K.-S. Chen, and R.-C. Liang. Thermal Micro ATR/FT-IR Spectroscopic System for Quantitative Study of the Molecular Structure of Poly($N$-isopropylacrylamide) in Water. *Polymer*, 40:2619–2624, 1999.

[118] O. Ramon, E. Kesselman, R. Berkovici, Y. Cohen, and Y. Paz. Attenuated Total Reflectance/Fourier Transform Infrared Studies on the Phase-Separation Process of Aqueous Solutions of Poly($N$-isopropylacrylamide). *J. Polym. Sci. B*, 39:1665–1677, 2001.

[119] Z. Ahmed, E. A. Gooding, K. V. Pimenov, L. Wang, and S. A. Asher. UV Resonance Raman Determination of Molecular Mechanism of Poly($N$-isopropylacrylamide) Volume Phase Transition. *J. Phys. Chem. B*, 113:4248–4256, 2009.

[120] M. Shibayama, T. Tanaka, and C. C. Han. Small Angle Neutron Scattering Study on Poly($N$-isopropyl acrylamide) Gels near their Volume-Phase Transition Temperature. *J. Chem. Phys.*, 97:6829–6841, 1992.

[121] A. Meier-Koll, V. Pipich, P. Busch, C. M. Papadakis, and P. Müller-Buschbaum. Phase Separation in Semidilute Aqueous Poly($N$-isopropylacrylamide) Solutions. *Langmuir*, 28:8791–8798, 2012.

[122] A. Sariban and K. Binder. Critical Properties of the Flory-Huggins Lattice Model of Polymer Mixtures. *J. Chem. Phys*, 86:5859–5873, 1987.

[123] J. Wang and C. Wu. Reexamination of the Origin of Slow Relaxation in Semidilute Polymer Solutions - Reptation Related or Not? *Macromolecules*, 49:3184–3191, 2016.

[124] C. Wu, W. Li, and X. X. Zhu. Viscoelastic Effect on the Formation of Mesoglobular Phase in Dilute Solutions. *Macromolecules*, 39:4989–4992, 2004.

[125] V. V. Vasilevskaya, P. G. Khalatur, and A. R. Khokhlov. Conformational Polymorphism of Amphiphilic Polymers in a Poor Solvent. *Macromolecules*, 36:10103–10111, 2003.

[126] A. Laukkanen, L. Valtola, F. M. Winnik, and H. Tenhu. Formation of Colloidally Stable Phase Separated Poly($N$-vinylcaprolactam) in Water: A Study by Dynamic Light Scattering, Microcalorimetry, and Pressure Pertubation Calorimetry. *Macromolecules*, 37:2268–2274, 2004.

[127] S. Kunugi, K. Takano, N. Tanaka, K. Suwa, and M. Akashi. Effects of Pressure on the Behavior of the Thermoresponsive Polymer Poly($N$-vinylisobutyramide) (PNVIBA). *Macromolecules*, 30:4499–4501, 1997.

[128] S. Kunugi, Y. Yamazaki, K. Takano, N. Tanaka, and M. Akashi. Effects of Ionic Additives and Ionic Comonomers on the Temperature and Pressure Responsive Behavior of Thermoresponsive Polymers in Aqueous Solutions. *Langmuir*, 15:4056–4061, 1999.

[129] N. Osaka, M. Shibayama, T. Kikuchi, and O. Yamamuro. Quasi-Elastic Neutron Scattering Study on Water and Polymer Dynamics in Thermo/Pressure Sensitive Polymer Solutions. *J. Phys. Chem. B*, 113:12870–12876, 2009.

[130] L. P. N. Rebelo, Z. P. Visak, H. C. de Sousa, J. Szydlowski, R. Gomes de Azevedo, A. M. Ramos, V. Najdanovic-Visak, M. Nunes da Ponte, and J. Klein. Double Critical Phenomena in (Water + Polyacrylamides) Solutions. *Macromolecules*, 35:1887–1895, 2002.

[131] B.-J. Niebuur, K.-L. Claude, S. Pinzek, C. Cariker, K. N. Raftopoulos, V. Pipich, M.-S. Appavou, A. Schulte, and C. M. Papadakis. Pressure-Dependence of Poly($N$-isopropylacrylamide) Mesoglobule Formation in Aqueous Solution. *ACS Macro Lett.*, 6:1180–1185, 2017.

[132] B.-J. Niebuur, L. Chiappisi, X. Zhang, F. Jung, A. Schulte, and C. M. Papadakis. Formation and Growth of Mesoglobules in Aqueous Poly($N$-isopropylacrylamide) Solutions Revealed with Kinetic Small-Angle Neutron Scattering and Fast Pressure Jumps. *ACS Macro Lett.*, 7:1155–1160, 2018.

[133] H. Ohta, I. Ando, S. Fujishige, and K. Kubota. Molecular Motion and $^1$H NMR Relaxation of Aqueous Poly($N$-isopropylacrylamide) Solution Under High Pressure. *J. Polym. Sci. B*, 29:963–968, 1991.

[134] K. Mochizuki, T. Sumi, and K. Koga. Driving Forces for the Pressure-Induced Aggregation of Poly($N$-isopropylacrylamide) in Water. *Phys. Chem. Chem. Phys.*, 18:4697–4703, 2016.

[135] M. Pühse, M. Keerl, C. Scherzinger, W. Richtering, and R. Winter. Influence of Pressure on the State of Poly($N$-isopropylacrylamide) and Poly($N$,$N$-diethylacrylamide) Derived Polymers in Aqueous Solution as Probed by FTIR-Spectroscopy. *Polymer*, 51:3653–3659, 2010.

[136] V. Y. Grinberg, A. A. Senin, N. V. Grinberg, T. V. Burova, A. S. Dubovik, S. A. Potekhin, and I. Y. Erukhimovich. High Pressure Effects under Phase Separation of Aqueous Solutions of Poly($N$-isopropylacrylamide): A HS-DSC Study. *Polymer*, 64:14–18, 2015.

[137] S. Kunugi, K. Kameyama, T. Tada, N. Tanaka, M. Shibayama, and M. Akashi. Differences in Pressure and Temperature Transitions of Proteins and Polymer Gels. *Braz. J. Med. Biol. Res.*, 38:1233–1238, 2005.

[138] E. Kato. Pressure-Induced Concentration Fluctuations in $N$-isopropylacrylamide Gels. *J. Chem. Phys.*, 101:468–472, 1994.

[139] X. Zhong, Y.-X. Wang, and S.-C. Wang. Pressure Dependence of the Volume Phase-Transition of Themperature-Sensitive Gels. *Chem. Eng. Sci.*, 51:3235–3239, 1996.

[140] C. Nakamoto, T. Kitada, and E. Kato. Pressure Dependence on the Flory-Huggins Interaction Parameter of Poly($N$-isopropylacrylamide) Gels. *Polym. Gels Networks*, 4:17–31, 1996.

[141] E. Kato. Volume-Phase Transition of $N$-isopropylacrylamide Gels Induced by Hydrostatic Pressure. *J. Chem. Phys.*, 106:3792–3797, 1997.

[142] I. Nasimova, T. Karino, S. Okabe, M. Nagao, and M. Shibayama. Effects of Ionization on the Temperature- and Pressure-Induced Phase Transitions of Poly($N$-isopropylacrylamide) Gels. *J. Chem. Phys.*, 121:9708–9715, 2004.

[143] E. Kato. Thermodynamic Study of a Pressure-Temperature Phase Diagram for Poly($N$-isopropylacrylamide) Gels. *J. Appl. Polym. Sci.*, 97:405–412, 2005.

[144] J. J. Liétor-Santos, B. Sierra-Martín, U. Gasser, and A. Fernández-Nieves. The Effect of Hydrostatic Pressure over the Swelling of Microgel Particles. *Soft Matter*, 7:6370–6374, 2011.

[145] S. Grobelny, C. H. Hofmann, M. Erlkamp, F. A. Plamper, W. Richtering, and R. Winter. Conformational Changes upon High Pressure Induced Hydration of Poly(*N*-isopropylacrylamide) Microgels. *Soft Matter*, 9:5862–5866, 2013.

[146] O. Wrede, Y. Reimann, S. Lülsdorf, D. Emmrich, K. Schneider, A. J. Schmid, D. Zauser, Y. Hannappel, A. Beyer, R. Schweins, A. Gölzhäuser, T. Hellweg, and T. Sottmann. Volume Phase Transition Kinetics of Smart *N-n*-propylacrylamide Microgels Studied by Time-Resolved Pressure Jump Small Angle Neutron Scattering. *Sci. Rep.*, 8:13781, 2018.

[147] H. G. Schild, M. Muthukumar, and D. A. Tirrell. Cononsolvency in Mixed Aqueous Solutions of Poly(*N*-isopropylacrylamide). *Macromolecules*, 24:948–952, 1991.

[148] I. Bischofberger, D. C. E. Calzolari, and V. Trappe. Co-Nonsolvency of PNIPAM at the Transition between Solvation Mechanisms. *Soft Matter*, 10:8288–8295, 2014.

[149] A. Wakisaka, H. Abdoul-Carime, Y. Yamamoto, and Y. Kiyozumi. Non-Ideality of Binary Mixtures. *J. Chem. Soc. Faraday Trans.*, 94:369–374, 1998.

[150] G. Zhang and C. Wu. Reentrant Coil-to-Globule-to-Coil Transition of a Single Linear Homopolymer Chain in a Water/Methanol Mixture. *Phys. Rev. Lett.*, 86:822–825, 2001.

[151] J. Hao, H. Cheng, P. Butler, L. Zhang, and C. C. Han. Origin of Cononsolvency, Based on the Structure of Tetrahydrofuran-Water Mixture. *J. Chem. Phys.*, 132:154902, 2010.

[152] F. Tanaka, T. Koga, H. Kojima, N. Xue, and F. M. Winnik. Preferential Adsorption and Co-nonsolvency of Thermoresponsive Polymers in Mixed Solvents of Water/Methanol. *Macromolecules*, 44:2978–2989, 2011.

[153] D. Mukherji and K. Kremer. Coil-Globule-Coil Transition of PNIPAm in Aqueous Methanol: Coupling All-Atom Simulations to Semi-Grand Canonical Coarse-Grained Reservoir. *Macromolecules*, 46:9158–9163, 2013.

[154] D. Mukherji, C. M. Marques, and K. Kremer. Polymer Collapse in Miscible Good Solvents is a Generic Phenomenon Driven by Preferential Adsorption. *Nat. Commun.*, 5:4882, 2014.

[155] D. Mukherji, C. M. Marques, T. Stuehn, and K. Kremer. Co-non-solvency: Mean-Field Polymer Theory does not Describe Polymer Collapse Transition in a Mixture of Two Competing Good Solvents. *J. Chem. Phys.*, 142:114903, 2015.

[156] F. Rodríguez-Ropero, T. Hajari, and N. F. A. van der Vegt. Mechanism of Polymer Collapse in Miscible Good Solvents. *J. Phys. Chem. B*, 119:15780–15788, 2015.

[157] A. Pica and G. Graziano. An Alternative Explanation of the Cononsolvency of Poly($N$-isopropylacrylamide) in Water-Methanol Solutions. *Phys. Chem. Chem. Phys.*, 18:25601–25608, 2016.

[158] R. Pynn. Neutron Scattering — A Primer. *Los Alamos Science*, 19:1–31, 1990.

[159] D. S. Sivia. *Elementary Scattering Theory*. Oxford University Press, 2011.

[160] Q. Berrod, K. Lagrené, J. Ollivier, and J.-M. Zanotti. Inelastic and Quasi-Elastic Neutron Scattering Application to Soft-Matter. *EPJ WEB Conf.*, 188:05001, 2018.

[161] H. Nyquist. Thermal Agitation of Electrical Charge in Conductors. *Phys. Rev.*, 32:110–113, 1928.

[162] H. B. Callen and T. A. Welton. Irreversibility and Generalized Noise. *Phys. Rev.*, 83:34–40, 1951.

[163] W. Brenig. *Statistical Theory of Heat*. Springer Verlag, 1989.

[164] Instrument D11, ILL. https://www.ill.eu/users/instruments/instruments-list/d11/. Accessed: 19-11-2018.

[165] V. Pipich and Z. Fu. KWS-3: Very Small Angle Scattering Diffractometer with Focusing Mirror. *Journal of Large-Scale Research Facilities*, 1:A31, 2015.

[166] I. Grillo. *Soft-Matter Characterization*, chapter Small-Angle Neutron Scattering and Application in Soft Condensed Matter. Springer, 2008.

[167] A. Guinier and G. Fournet. *Small Angle Scattering of X-Rays*. Wiley, 1955.

[168] G. Porod. Die Röntgenkleinwinkelstreuung von Dichtgepackten Kolloiden Systemen. *Kolloid K.*, 124:83–114, 1951.

[169] J. T. Koberstein, B. Morra, and R. S. Stein. The Determination of Diffuse-Boundary Thicknesses of Polymers by Small-Angle X-ray Scattering. *J. Appl. Cryst.*, 13:34–45, 1980.

[170] S. Ciccariello. On the Porod Law. *J. Appl. Cryst.*, 21:117–128, 1988.

[171] B. Hammouda. A New Guinier-Porod Model. *J. Appl. Cryst.*, 43:1474–1478, 2010.

[172] G. Beaucage. Approximations Leading to a Unified Exponential/Power-Law Approach to Small-Angle Scattering. *J. Appl. Cryst.*, 28:717–728, 1995.

[173] G. Beaucage. Small-Angle Scattering from Polymeric Mass Fractals of Arbitrary Mass-Fractal Dimension. *J. Appl. Cryst.*, 29:134–146, 1996.

[174] B. R. Saunders. On the Structure of Poly($N$-isopropylacrylamide) Microgel Particles. *Langmuir*, 20:3925–3932, 2004.

[175] H. Frielinghaus. *Scattering Methods for Condensed Matter Research: Towards Novel Applications at Future Sources*, chapter D1, Small Angle Scattering and Large Scale Structures. Forschungszentrum Jülich GmbH, 2012.

[176] W. Lohstroh and Z. Evenson. TOFTOF: Cold Neutron Time-of-Flight Spectrometer. *Journal of Large-Scale Research Facilities*, 1:A15, 2015.

[177] T. Unruh, J. Neuhaus, and W. Petry. The High-Resolution Time-of-Flight Spectrometer TOFTOF. *Nucl. Instrum. Methods Phys. Res., Sect. A*, 580:1414–1422, 2007.

[178] M. Bée. *Quasielastic Neutron Scattering*. Adam Hilger, 1988.

[179] H. R. Glyde and E. C. Svensson. *Methods of Experimental Physics, Vol. 23, Part B*, chapter Solid and Liquid Helium. Academic Press, 1987.

[180] B. Fåk and B. Dorner. Phonon Line Shapes and Excitation Energies. *Physica B*, 234-236:1107–1108, 1997.

[181] L. Silvi, E. Röhm, M. Fichtner, W. Petry, and W. Lohstroh. Hydrogen Dynamics in $\beta$-Mg(BH$_4$)$_2$ on the Picosecond Timescale. *Phys. Chem. Chem. Phys.*, 18:14323–14332, 2016.

[182] J. Wuttke. *Scattering Methods for Condensed Matter Research: Towards Novel Applications at Future Sources*, chapter D7, Quasielastic Scattering. Forschungszentrum Jülich GmbH, 2012.

[183] V. F. Sears. Neutron Scattering Lengths and Cross Sections. *Neutron News*, 3:29–37, 1992.

[184] F. G. Smith and J. H. Thomson. *Optics*. John Wiley and Sons, 1988.

[185] M. B. Fenn, P. Xanthopoulos, G. Pyrgiotakis, S. R. Grobmyer, P. M. Pardalos, and L. L. Hench. Raman Spectroscopy for Clinical Oncology. *Advances in Optical Technologies*, 2011:213783, 2011.

[186] M. A. Freeman. *Optics*. Butterworth-Heinemann, 1990.

[187] H. W. Siesler. *Polymer Science: A Comprehensive Reference. Volume 2: Polymer Characterization*, chapter Vibrational Spectroscopy. Elsevier, 2012.

[188] F. Siebert and P. Hildebrandt. *Vibrational Spectroscopy in Life Science*. Wiley, 2007.

[189] R. L. McCreery. *Raman Spectroscopy for Chemical Analysis*. John Wiley and Sons, 2000.

[190] A. Schulte and Y. Guo. *Handbook of Applied Solid State Spectroscopy*, chapter Applications of Laser Raman Spectroscopy. Springer US, 2006.

[191] W. Demtröder. *Laser Spectroscopy I*. Springer-Verlag Berlin Heidelberg, 2014.

[192] Marián Sedlák. High Precision Vibration-Type Densitometers Based on Pulsed Excitation Measurements. *Sensors*, 19:1627, 2019.

[193] S. Pinzek. Phasenverhalten responsiver Polymere unter hohem Druck. B.Sc. thesis, Technical University of Munich, 2015.

[194] R. Ravindra and R. Winter. On the Temperature-Pressure Free-Energy Landscape of Proteins. *Chem. Phys. Chem.*, 4:359–365, 2003.

[195] M. T. Zafarani-Moattar and H. Shekaari. Apparent Molar Volume and Isentropic Compressibility of Ionic Liquid 1-Butyl-3-Methylimidazolium Bromide in Water, Methanol, and Ethanol at $T =$ (298.15 to 318.15) K. *J. Chem. Thermodynamics*, 37:1029–1035, 2005.

[196] I. Bahadur and N. Deenadayalu. Apparent Molar Volume and Apparent Molar Isentropic Compressibilities for the Binary Systems (Methyltrioctylammoniumbis(trifluoromethylsulfonyl)imide + Ethyl Acetate or Ethanol) at Different Temperatures under Atmospheric Pressure. *Thermochimica Acta*, 566:77–83, 2013.

[197] R. de Lisi, S. Milioto, and R. E. Verrall. Partial Molar Volumes and Compressibilities of Alkyltrimethylammonium Bromides. *J. Solution Chem.*, 19:665–692, 1990.

[198] H. Seemann, R. Winter, and C. A. Royer. Expansivity and Isothermal Compressibility Changes Associated with Temperature and Pressure Unfolding of Staphylococcal Nuclease. *J. Mol. Biol.*, 307:1091–1102, 2001.

[199] W. D. Wilson. Speed of Sound in Heavy Water as a Function of Temperature and Pressure. *J. Acoust. Soc. Am.*, 33:314–316, 1961.

[200] R. N. Gupta, P. C. Jain, and V. S. Nanda. Speed of Sound Measurements in Mixtures of $H_2O$ and $D_2O$. *J. Chem. Thermodynamics*, 8:627–629, 1976.

[201] A. Milewska, J. Szydlowski, and L. P. N. Rebelo. Viscosity and Ultrasonic Studies of Poly($N$-isopropylacrylamide)-Water Solutions. *J. Polym. Sci. B*, 41:1219–1233, 2003.

[202] E. I. Tiktopulo, V. N. Uversky, V. B. Lushchik, S. I. Klenin, V. E. Bychkova, and O. B. Ptitsyn. "Domain" Coil-Globule Transition in Homopolymers. *Macromolecules*, 28:7519–7524, 1995.

[203] M. Salmerón Sánchez, L. Hanyková, M. Ilavský, and M. Monleón Pradas. Thermal Transition of Poly($N$-isopropylacrylamide) in Aqueous Solutions. *Polymer*, 45:4087–4094, 2004.

[204] Y. Yan, L. Huang, Q. Zhang, and H. Zhou. Concentration Effect on Aggregation and Dissolution Behavior of Poly($N$-isopropylacrylamide) in Water. *J. Appl. Polym. Sci.*, 132:41669, 2014.

[205] M. Tekmen and J. D. Müller. High-Pressure Cell for Fluorescence fluctuation Spectroscopy. *Rev. Sci. Instrum.*, 75:5143–5148, 2004.

[206] J. Kohlbrecher, A. Bollhalder, R. Vavrin, and G. Meier. A High Pressure Cell for Small Angle Neutron Scattering up to 500 MPa in Combination with Light Scattering to Investigate Liquid Samples. *Rev. Sci. Instrum.*, 78:125101, 2007.

[207] B. Sun, Y. Lin, and P. Wu. Structure Analysis of Poly($N$-isopropylacrylamide) Using Near-Infrared Spectroscopy and Generalized Two-Dimensional Correlation Infrared Spectroscopy. *Appl. Spectrosc.*, 61:765–771, 2007.

[208] B. Sun, Y. Lin, P. Wu, and H. W. Siesler. A FTIR and 2D-IR Spectroscopic Study on the Microdynamics Phase Separation Mechanism of the Poly($N$-isopropylacrylamide) Aqueous Solution. *Macromolecules*, 41:1512–1520, 2008.

[209] S. Scheiner and T. Kar. Red- versus Blue-Shifting Hydrogen Bonds: Are There Fundamental Distinctions? *J. Phys. Chem. A*, 106:1784–1789, 2002.

[210] C. D. Keefe, E. A. L. Gilles, and L. MacDonald. Improper Hydrogen-Bonding CH·Y Interactions in Binary Methanol Systems as Studied by FTIR and Raman Spectroscopy. *J. Phys. Chem. A*, 113:2544–2550, 2009.

[211] J. Joseph and E. D. Jemmis. Red-, Blue-, or No-Shift in Hydrogen Bonds: A Unified Explanation. *J. Am. Chem. Soc.*, 129:4620–2632, 2007.

[212] P. Hobza and Z. Havlas. Blue-Shifting Hydrogen Bonds. *Chem. Rev.*, 100:4253–4264, 2000.

[213] T. Kar and S. Scheiner. Comparison in Cooperativity in CH$\cdots$O and OH$\cdots$O Hydrogen Bonds. *J. Phys. Chem. A*, 108:9161–9168, 2004.

[214] M. H. Futscher, M. Philipp, P. Müller-Buschbaum, and A. Schulte. The Role of Backbone Hydration of Poly($N$-isopropyl acrylamide) Across the Volume Phase Transition Compared to its Monomer. *Sci. Rep.*, 7:17012, 2017.

[215] O. Spalla. *Neutrons, X-rays and Light: Scattering Methods Applied to Soft Condensed Matter*, chapter General Theorems in Small-Angle Scattering. North-Holland, 2002.

[216] B.-J. Niebuur, W. Lohstroh, M.-S. Appavou, A. Schulte, and C. M. Papadakis. Water Dynamics in a Concentrated Poly($N$-isopropylacrylamide) Solution at Variable Pressure. *Macromolecules*, 52:1942–1954, 2019.

[217] M. Philipp, K. Kyriakos, L. Silvi, W. Lohstroh, W. Petry, J. K. Krüger, C. M. Papadakis, and P. Müller-Buschbaum. From Molecular Dehydration to Excess Volumes of Phase-Separating PNIPAM Solutions. *J. Phys. Chem. B*, 118:4253–4260, 2014.

[218] M.-S. Appavou, S. Busch, W. Doster, A. Gaspar, and T. Unruh. The Influence of 2 kbar Pressure on the Global and Internal Dynamics of Human Hemoglobin Observed by Quasielastic Neutron Scattering. *Eur. Biophys. J.*, 40:705–714, 2011.

[219] A. Arbe, P. Malo de Molina, F. Alvarez, B. Frick, and J. Colmenero. Dielectric Susceptibilities of Liquid Water: Microscopic Insights from Coherent and Incoherent Neutron Scattering. *Phys. Rev. Lett.*, 117:185501, 2016.

[220] R. Bergman. General Susceptibility Functions for Relaxations in Disordered Systems. *J. Appl. Phys.*, 88:1356–1365, 2000.

[221] S. Perticaroli, G. Ehlers, C. B. Stanley, E. Mamontov, H. O'Neill, Q. Zhang, X. Cheng, D. A. A. Myles, J. Katsaras, and J. D. Nickels. Description of Hydration Water in Protein (Green Fluorescent Protein) Solution. *J. Am. Chem. Soc.*, 139:1098–1105, 2017.

[222] I. Ohmine. Liquid Water Dynamics: Collective Motions, Fluctuations, and Relaxation. *J. Phys. Chem.*, 99:6767–6776, 1995.

[223] G. E. Walrafen and Y. C. Chu. Linearity between Structural Correlation Length and Correlated-Proton Raman Intensity from Amorphous Ice and Supercooled Water up to Dense Supercritical Steam. *J. Phys. Chem.*, 99:11225–11229, 1995.

[224] Q. Wan, L. Spanu, G. A. Galli, and F. Gygi. Raman Spectra of Liquid Water from Ab Initio Molecular Dynamics: Vibrational Signatures of Charge Fluctuations in the Hydrogen Bond Network. *J. Chem. Theory. Comput.*, 9:4124–4130, 2013.

[225] D. Russo, A. Laloni, A. Filabozzi, and M. Heyden. Pressure Effects on Collective Density Fluctuations in Water and Protein Solutions. *Proc. Natl. Acad. Sci.*, 114:11410–11415, 2017.

[226] F. Sciortino, P. Gallo, P. Tartaglia, and S.-H. Chen. Supercooled Water and the Kinetic Glass Transition. *Phys. Rev. E*, 54:6331–6343, 1996.

[227] S.-H. Chen, P. Gallo, F. Sciortino, and P. Tartaglia. Molecular-Dynamics Study of Incoherent Quasielastic Neutron-Scattering Spectra of Supercooled Water. *Phys. Rev. E*, 56:4231–4243, 1997.

[228] S.-H. Chen, C. Liao, F. Sciortino, P. Gallo, and P. Tartaglia. Model for Single-Particle Dynamics in Supercooled Water. *Phys. Rev. E*, 59:6708–6714, 1999.

[229] W. Götze and L. Sjögren. Relaxation Processes in Supercooled Liquids. *Rep. Prog. Phys.*, 55:241–376, 1992.

[230] D. Laage and J. T. Hynes. A Molecular Jump Mechanism of Water Reorientation. *Science*, 311:832–835, 2006.

[231] D. Laage. Reinterpretation of the Liquid Water Quasi-Elastic Neutron Scattering Spectra Based on a Nondiffusive Jump Reorientation Mechanism. *J. Phys. Chem. B*, 113:2684–2687, 2009.

[232] J. Teixeira, M.-C. Bellissent-Funel, S. H. Chen, and A. J. Dianoux. Experimental Determination of the Nature of Diffusive Motions of Water Molecules at Low Temperatures. *Phys. Rev. A: At., Mol., Opt., Phys.*, 31:1913–1917, 1985.

[233] J. Qvist, H. Schober, and B. Halle. Structural Dynamics of Supercooled Water from Quasielastic Neutron Scattering and Molecular Simulations. *J. Chem. Phys.*, 134:144508, 2011.

[234] A. Cunsolo, A. Orecchini, C. Petrillo, and F. Sacchetti. Quasielastic Neutron Scattering Investigation of the Pressure Dependence of Molecular Motions in Liquid Water. *J. Chem. Phys.*, 124:084503, 2006.

[235] L. E. Bove, S. Klotz, T. Strässle, M. Koza, J. Teixeira, and A. M. Saitta. Translational and Rotational Diffusion in Water in the Gigapascal Range. *Phys. Rev. Lett.*, 111:185901, 2013.

[236] J. H. Wang. Self-Diffusion Coefficients of Water. *J. Phys. Chem.*, 69:4412–4412, 1965.

[237] K. Yoshida, N. Matubayasi, and M. Nakahara. Self-Diffusion Coefficients for Water and Organic Solvents at High Temperatures along the Coexistence Curve. *J. Chem. Phys.*, 129:214501, 2008.

[238] T. Kikuchi, K. Nakajima, S. Ohira-Kawamura, Y. Inamura, O. Yamamuro, M. Kofu, Y. Kawakita, K. Suzuya, M. Nakamura, and M. Arai. Mode-Distribution Analysis of Quasielastic Neutron Scattering and Application to Liquid Water. *Phys. Rev. E*, 87:062314, 2013.

[239] K. R. Harris and L. Woolf. Pressure and Temperature Dependence of the Self Diffusion Coefficient of Water and Oxygen-18 Water. *J. Chem. Soc., Faraday Trans. 1*, 76:377–385, 1980.

[240] R. Buchner, J. Barthel, and J. Stauber. The Dielectric Relaxation of Water between 0°C and 35°C. *Chem. Phys. Lett.*, 306:57–63, 1999.

[241] A. Y. Zasetsky. Dielectric Relaxation in Liquid Water: Two Fractions or Two Dynamics? *Phys. Rev. Lett.*, 107:117601, 2011.

[242] I. Popov, P. B. Ishai, A. Khamzin, and Y. Feldman. The Mechanism of the Dielectric Relaxation in Water. *Phys. Chem. Chem. Phys.*, 18:13941, 2016.

[243] M. Füllbrandt, E. Ermilova, A. Asadujjaman, R. Hölzel, F. F. Bier, R. von Klitzing, and A. Schönhals. Dynamics of Linear Poly($N$-isopropylacrylamide) in Water around the Phase Transition Investigated by Dielectric Relaxation Spectroscopy. *J. Phys. Chem. B*, 118:3750–3759, 2014.

[244] D. Laage, T. Elsaesser, and J. T. Hynes. Water Dynamics in the Hydration Shells of Biomolecules. *Chem. Rev.*, 117:10694–10725, 2017.

[245] M. Shibayama, M. Morimoto, and M. Nomura. Phase Separation Induced Mechanical Transition of Poly(*N*-isopropylacrylamide)/Water Isochore Gels. *Macromolecules*, 27:5060–5066, 1994.

[246] Y. Ono and T. Shikata. Hydration and Dynamic Behavior of Poly(*N*-isopropylacrylamide)s in Aqueous Solution: A Sharp Phase Transition at the Lower Critical Solution Temperature. *J. Am. Chem. Soc.*, 128:10030–10031, 2006.

[247] S. A. Deshmukh, S. K. R. S. Sankaranarayanan, K. Suthar, and D. C. Mancini. Role of Solvation Dynamics and Local Ordering of Water in Inducing Conformational Transitions in Poly(*N*-isopropylacrylamide) Oligomers through the LCST. *J. Phys. Chem. B*, 116:2651–2663, 2012.

[248] K. Shiraga, H. Naito, T. Suzuki, N. Kondo, and Y. Ogawa. Hydration and Hydrogen Bond Network of Water during the Coil-to-Globule Transition in Poly(*N*-isopropylacrylamide) Aqueous Solution at Cloud Point Temperature. *J. Phys. Chem. B*, 119:5576–5587, 2015.

[249] Y. Ono and T. Shikata. Contrary Hydration Behavior of N-isopropylacrylamide to its Polymer, P(NIPAm), with a Lower Critical Solution Temperature. *J. Phys. Chem. B*, 111:1511–1513, 2007.

[250] T. E. de Oliveira, D. Mukherji, K. Kremer, and P. A. Netz. Effects of Stereochemistry and Copolymerization on the LCST of PNIPAm. *J. Chem. Phys.*, 146:034904, 2017.

[251] P. Tan, Y. Liang, Q. Xu, E. Mamontov, J. Li, X. Xing, and L. Hong. Gradual Crossover from Subdiffusion to Normal Diffusion: A Many-Body Effect in Protein Surface Water. *Phys. Rev. Lett*, 120:248101, 2018.

[252] F. Volino and A. J. Dianoux. Neutron Incoherent Scattering Law for Diffusion in a Potential of Spherical Symmetry: General Formalism and Application to Diffusion Inside a Sphere. *Mol. Phys.*, 41:271–279, 1980.

[253] R. Metzler, J.-H. Jeon, A. G. Cherstvy, and E. Barkai. Anomalous Diffusion Models and their Properties: Non-Stationary, Non-Ergodicity, and Ageing at the Centenary of Single Particle Tracking. *Phys. Chem. Chem. Phys.*, 16:24128–24164, 2014.

[254] D. Laage, G. Stirnemann, and J. T. Hynes. Why Water Reorientation Slows Without Iceberg Formation around Hydrophobic Solutes. *J. Phys. Chem. B*, 113:2428–2435, 2009.

[255] D. Laage, G. Stirnemann, F. Sterpone, R. Rey, and J. T. Hynes. Reorientation and Allied Dynamics in Water and Aqueous Solutions. *Annu. Rev. Phys. Chem.*, 62:395–416, 2011.

[256] F. Sterpone, G. Stirnemann, J. T. Hynes, and D. Laage. Water Hydrogen-Bond Dynamics around Amino Acids: The Key Role of Hydrophilic Hydrogen-Bond Acceptor Groups. *J. Phys. Chem. B*, 114:2083–2089, 2010.

[257] H. Li, H. Yamada, and K. Akasaka. Effect of Pressure on Individual Hydrogen Bonds in Proteins. Basic Pancreatic Trypsin Inhibitor. *Biochemistry*, 37:1167–1173, 1998.

[258] R. C. Dougherty. Temperature and Pressure Dependence of Hydrogen Bond Strength: A Pertubation Molecular Orbital Approach. *J. Chem. Phys.*, 109:7372–7378, 1998.

[259] T. Ghosh, A. E. García, and S. Garde. Molecular Dynamics Simulations of Pressure Effects on Hydrophobic Interactions. *J. Am. Chem. Soc.*, 123:10997–11003, 2001.

[260] T. Ghosh, A. E. García, and S. Garde. Enthalpy and Entropy Contributions to the Pressure Dependence of Hydrophobic Interactions. *J. Chem. Phys.*, 116:2480–2486, 2002.

[261] W. Doster, S. Cusack, and W. Petry. Dynamic Instability of Liquidlike Motions in a Globular Protein Observed by Inelastic Neutron Scattering. *Phys. Rev. Lett.*, 65:1080–1083, 1990.

[262] C. Smuda, G. Gemmecker, and T. Unruh. Quasielastic and Inelastic Neutron Scattering Study of Methyl Group Rotation in Solid and Liquid Pentafluoroanisole and Pentafluorotoluene. *J. Chem. Phys.*, 128:194502, 2008.

[263] J. H. Roh, J. E. Curtis, S. Azzam, V. N. Novikov, I. Peral, Z. Chowdhuri, R. B. Gregory, and A. P. Sokolov. Influence of Hydration on the Dynamics of Lysozyme. *Biophys. J.*, 91:2573–2588, 2006.

[264] W. Doster and M. Settles. Protein-Water Displacement Distributions. *Biochim. Biophys. Acta, Proteins Proteomics*, 1749:173–186, 2005.

[265] B.-J. Niebuur, L. Chiappisi, F. Jung, X. Zhang, A. Schulte, and C. M. Papadakis. Kinetics of Mesoglobule Formation and Growth in Aqueous Poly(*n*-isopropylacrylamide) Solutions: Pressure Jumps at Low and at High Pressure. *Macromolecules*, 52:6416–6427, 2019.

[266] A. Mencke, A. Cheng, and M. A. Caffrey. A Simple Apparatus for Time-Resolved X-ray Diffraction Biostructure Studies using Static and Oscillating Pressures and Pressure Jumps. *Rev. Sci. Instrum.*, 64:383–389, 1993.

[267] M. Steinhart, M. Kriechbaum, K. Pressl, H. Amenitsch, P. Laggner, and S. Bernstorff. High-Pressure Instrument for Small- and Wide-Angle X-ray Scattering. II. Time-Resolved Experiments. *Rev. Sci. Instrum.*, 70:1540–1545, 1999.

[268] J. Woenckhaus, R. Köhling, R. Winter, P. Thiyagarajan, and S. Finet. High Pressure-Jump Apparatus for Kinetic Studies of Protein Folding Reaction Using the Small-Angle Synchrotron X-ray Scattering Technique. *Rev. Sci. Instrum.*, 71:3895–3899, 2000.

[269] N. J. Brooks, B. L. L. E. Gauthe, N. J. Terrill, S. E. Rogers, R. H. Templer, O. Ces, and J. M. Seddon. Automated High Pressure Cell for Pressure Jump X-ray Diffraction. *Rev. Sci. Instrum.*, 81:064103, 2010.

[270] A. Müller, Y. Pütz, R. Oberhoffer, N. Becker, R. Strey, A. Wiedenmann, and T. Sottmann. Kinetics of Pressure Induced Structural Changes in Super- or Near-Critical $CO_2$-Microemulsions. *Phys. Chem. Chem. Phys.*, 16:18092–18097, 2014.

[271] J. W. Cahn. Phase Separation by Spinodal Decomposition in Isotropic Systems. *J. Chem. Phys.*, 42:93–99, 1965.

[272] O. Söhnel and J. W. Mullin. Intepretation of Crystallization Induction Periods. *J. Colloid Interface Sci.*, 123:43–50, 1988.

[273] D. T. Wu. The Time Lag in Nucleation Theory. *J. Chem. Phys.*, 97:2644–2650, 1992.

[274] N. Höfer. Dynamics of Responsive Polymers under High Pressure. B.Sc. thesis, Technical University of Munich, 2017.

[275] A. Marabi, G. Mayor, A. Burbidge, R. Wallach, and I. S. Saguy. Assessing Dissolution Kinetics of Powders by a Single Particle Approach. *Chem. Eng. J.*, 139:118–127, 2008.

[276] M. Talelli, C. J. F. Rijcken, C. F. van Nostrum, G. Storm, and W. E. Hennink. Micelles Based on HPMA Copolymers. *Adv. Drug Deliv. Rev.*, 62:231–239, 2010.

[277] B. A. Miller-Chou and J. L. Koenig. A Review of Polymer Dissolution. *Prog. Polym. Sci.*, 28:1223–1270, 2003.

[278] A. Parker, F. Vigouroux, and W. F. Reed. Dissolution Kinetics of Polymer Powders. *AIChE J.*, 46:1290–1299, 2000.

[279] P. Valois, E. Verneuil, F. Lequeux, and L. Talini. Understanding the Role of Molar Mass and Stirring in Polymer Dissolution. *Soft Matter*, 12:8143–8154, 2016.

[280] M. J. A. Hore, B. Hammouda, Y. Li, and H. Cheng. Co-Nonsolvency of Poly(*N*-isopropylacrylamide) in Deuterated Water/Ethanol Mixtures. *Macromolecules*, 46:7894–7901, 2013.

[281] I. Bakó, L. Pusztai, and L. Temleitner. Decreasing Temperature Enhances the Formation of Sixfold Hydrogen Bonded Rings in Water-Rich Water-Methanol Mixtures. *Scientific Reports*, 7:1073, 2017.

[282] K. Mortensen. *Advanced Functional Molecules and Polymers*, chapter Structural Studies of Polymer Systems Using Small-Angle Neutron Scattering. OPA N.V., 2001.

[283] R. Kita, K. Kubota, and T. Dobashi. Static and Dynamic Light Scattering of a Critical Polydisperse Polymer Solution. *Phys. Rev. E*, 58:793–800, 1998.

[284] J. Jacob, M. A. Anisimov, J. V. Sengers, V. Dechabo, I. K. Yudin, and R. W. Gammon. Light Scattering and Crossover Critical Phenomena in Polymer Solutions. *Appl. Opt.*, 40:4160–4169, 2001.

[285] Y. B. Melnichenko, G. D. Wignall, and W. A. van Hook. Molecular Weight Scaling in Critical Polymer Solutions. *Europhys. Lett.*, 48:372–377, 1999.

[286] A. Meier-Koll. *Neutronenkleinwinkelstreuung und Brillouinspektroskopie an Thermoresponsiven Hydrogelen*. PhD thesis, Technical University of Munich, 2012.

[287] S. Panyukov and Y. Rabin. Statistical Physics of Polymer Gels. *Phys. Rep.*, 269:1–131, 1996.

[288] S. Panyukov and Y. Rabin. Polymer Gels: Frozen Inhomogeneities and Density Fluctuations. *Macromolecules*, 29:7960–7975, 1996.

[289] T. Norisuye, N. Masui, Y. Kida, D. Ikuta, E. Kokufuta, S. Ito, S. Panyukov, and M. Shibayama. Small Angle Neutron Scattering Studies on Structural Inhomogeneities in Polymer Gels: Irradiation Cross-Linked Gels vs Chemically Cross-Linked Gels. *Polymer*, 43:5289–5297, 2002.

[290] E. Krasovitksi, Y. Cohen, and H. Bianco-Peled. The Effect of Salts on the Conformation and Microstructure of Poly($N$-isopropylacrylamide) (PNIPA) in Aqueous Solution. *J. Polym. Sci. B*, 42:3713–3720, 2004.

[291] P. Knychała, K. Timachova, M. Banaszak, and N. P. Balsara. 50th Anniversary Perspective: Phase Behavior of Polymer Solutions and Blends. *Macromolecules*, 50:3051–3065, 2017.

[292] S. Hirotsu. Phase Transition of a Polymer Gel in Pure and Mixed Solvent Media. *J. Phys. Soc. Jpn.*, 56:233–242, 1987.

[293] K. Kyriakos, M. Philipp, L. Silvi, W. Lohstroh, W. Petry, P. Müller-Buschbaum, and C. M. Papadakis. Solvent Dynamics in Solutions of PNIPAM in Water/Methanol Mixtures — A Quasi-Elastic Neutron Scattering Study. *J. Phys. Chem. B*, 120:4679–4688, 2016.

[294] J. H. Rolston and K. L. Gale. Fractionation of Deuterium and Protium between Water and Methanol. *J. Phys. Chem.*, 88:4394–4397, 1984.

[295] H. Yamauchi and Y. Maeda. LCST and UCST Behavior of Poly($N$-isopropylacrylamide) in DMSO/Water Mixed Solvents Studied by IR and Micro-Raman Spectroscopy. *J. Phys. Chem. B*, 111:12964–12968, 2007.

[296] F. Mallamace, R. Beneduci, P. Gambadauro, D. Lombardo, and S. H. Chen. Glass and Percolation Transitions in Dense Attractive Micellar System. *Physica A*, 302:202–219, 2001.

[297] L. Lobry, N. Micali, F. Mallamace, C. Liao, and S.-H. Chen. Interaction and Percolation in the $L$64 Triblock Copolymer Micellar System. *Phys. Rev. E*, 60:7076–7087, 1999.

# Scientific contributions

**Publications related to this thesis.**

- B.-J. Niebuur, K.-L. Claude, S. Pinzek, C. Cariker, K. N. Raftopoulos, V. Pipich, M.-S. Appavou, A. Schulte, C. M. Papadakis. Pressure-Dependence of Poly($N$-isopropylacrylamide) Mesoglobule Formation in Aqueous Solution. *ACS Macro Lett.*, 6:1180-1185, 2017

- B.-J. Niebuur, L. Chiappisi, X. Zhang, F. Jung, A. Schulte, C. M. Papadakis. Formation and Growth of Mesoglobules in Aqueous Poly($N$-isopropylacrylamide) Solutions Revealed with Kinetic Small-Angle Neutron Scattering and Fast Pressure Jumps. *ACS Macro Lett.*, 7:1155-1160, 2018

- B.-J. Niebuur, W. Lohstroh, M.-S. Appavou, A. Schulte, C. M. Papadakis. Water Dynamics in a Concentrated Poly($N$-isopropylacrylamide) Solution at Variable Pressure. *Macromolecules*, 52:1942-1954, 2019

- B.-J. Niebuur, L. Chiappisi, F. Jung, X. Zhang, A. Schulte, C. M. Papadakis. Kinetics of Mesoglobule Formation and Growth in Aqueous Poly($N$-isopropylacrylamide) Solutions: Pressure Jumps at Low and at High Pressure. *Macromolecules*, 52:6416-6427, 2019

**Further publications.**

- N. S. Vishnevetskaya, V. Hildebrand, B.-J. Niebuur, I. Grillo, S. K. Filippov, A. Laschewsky, P. Müller-Buschbaum, C. M. Papadakis. Aggregation Behavior of Doubly Thermoresponsive Polysulfobetaine-*b*-Poly($N$-isopropylacrylamide) Diblock Copolymers. *Macromolecules*, 49:6655-6668, 2016

- M. A. Dyakonova, G. Gotzamanis, B.-J. Niebuur, N. S. Vishnevetskaya, K. N. Raftopoulos, Z. Di, S. K. Filippov, C. Tsitsilianis, C. M. Papadakis. pH Responsiveness of Hydrogels Formed by Telechelic Polyampholytes. *Soft Matter*, 13:3568-3579, 2017

- S. K. Filippov, N. S. Vishnevetskaya, B.-J. Niebuur, E. Koziolová, E. A. Lomkova, P. Chytil, T. Etrych, C. M. Papadakis. Influence of Molar Mass, Dispersity, and Type and Location of Hydrophobic Side Chain Moieties on the Critical Micellar Concentration and Stability of Amphiphilic HPMA-Based Polymer Drug Carriers. *Colloid Polym. Sci.*, 295:1313-1325, 2017

- N. S. Vishnevetskaya, V. Hildebrand, B.-J. Niebuur, I. Grillo, S. K. Filippov, A. Laschewsky, P. Müller-Buschbaum, C. M. Papadakis. Schizophrenic Micelles from Doubly Thermoresponsive Polysulfobetaine-*b*-Poly(*N*-isopropylmethacrylamide) Diblock Copolymers. *Macromolecules*, 50:3985-3999, 2017

- X. Zhang, B.-J. Niebuur, P. Chytil, T. Etrych, S. K. Filippov, A. Kikhney, D. C. F. Wieland, D. I. Svergun, C. M. Papadakis. Macromolecular *p*HPMA-Based Nanoparticles with Cholesterol for Solid Tumor Targeting: Behavior in HSA Protein Environment. *Biomacromolecules*, 19:470-480, 2018

- N. S. Vishnevetskaya, V. Hildebrand, M. A. Dyakonova, B.-J. Niebuur, K. Kyriakos, K. N. Raftopoulos, Z. Di, P. Müller-Buschbaum, A. Laschewsky, C. M. Papadakis. Dual Orthogonal Switching of the Schizophrenic Self-Assembly of Diblock Copolymers. *Macromolecules*, 51:2604-2614, 2018

- B.-J. Niebuur, J. Puchmayr, C. Herold, L. P. Kreuzer, V. Hildebrand, P. Müller-Buschbaum, A. Laschewsky, C. M. Papadakis. Polysulfobetaines in Aqueous Solution and in Thin Film Geometry. *Materials*, 11:850, 2018

**Conference talks.**

- B.-J. Niebuur, X. Zhang, N. S. Vishnevetskaya, P. Chytil, S. K. Filippov, C. M. Papadakis
  *Self-Assembled Micelles as Drug Carriers: Influence of Molar Mass and Chain Architecture*
  DPG Frühjahrstagung, Regensburg, 6-11 March 2016

- B.-J. Niebuur, C. M. Papadakis
  *PNIPAM Solutions at High Pressure*
  Greek-German Workshop 2016 Nano-structured soft materials: From polymer self-assembly to stimuli-responsive materials, Athens, 26-30 September 2016

- B.-J. Niebuur, K.-L. Claude, S. Pinzek, C. Cariker, K. N. Raftopoulos, V. Pipich, M.-S. Appavou, A. Schulte, C. M. Papadakis
  *Influence of Pressure on the Aggregation Behavior of Poly(N-isopropylacrylamide)*
  9th International symposium on molecular mobility and order in polymer systems, St. Petersburg, 19-23 June 2017

- B.-J. Niebuur, L. Chiappisi, X. Zhang, F. Jung, A. Schulte, C. M. Papadakis
  *Multi-Step Kinetics of Mesoglobule Formation in Aqueous PNIPAM Solutions During Pressure Jumps*
  DPG-Frühjahrstagung, Berlin, 11-16 March 2018

- B.-J. Niebuur, K.-L. Claude, S. Pinzek, C. Cariker, K. N. Raftopoulos, V. Pipich, M.-S. Appavou, A. Schulte, C. M. Papadakis
  *Pressure-Dependence of Poly(N-isopropylacrylamide) Mesoglobule Formation in Aqueous Solution*
  16th Conference of the International Association of Colloid and Interface Scientists, Rotterdam, the Netherlands, 21-25 May 2018

- L. Reb, D. Schwaiger, B.-J. Niebuur
  *Raman Spectroscopy*
  Polymer Physics Summer School Obertauern, Austria, 12-15 June 2018

- B.-J. Niebuur, L. Chiappisi, X. Zhang, F. Jung, A. Schulte, C. M. Papadakis
  *Formation and Growth of Mesoglobules in Aqueous Poly(N-isopropylacrylamide) Solutions Revealed with Fast Pressure Jumps*
  DPG-Frühjahrstagung, Regensburg, 31 March - 6 April 2018

**Conference poster presentations.**

- B.-J. Niebuur, K.-L. Claude, S. Pinzek, C. Cariker, K. N. Raftopoulos, V. Pipich, M.-S. Appavou, A. Schulte, C. M. Papadakis
  *Influence of Pressure on the Aggregation Behavior of Aqueous PNIPAM Solutions*
  DPG Frühjahrstagung, Dresden, 19-24 March 2017

- B.-J. Niebuur, K.-L. Claude, S. Pinzek, C. Cariker, K.N. Raftopoulos, V. Pipich, M.-S. Appavou, A. Schulte, C. M. Papadakis
  *Influence of Pressure on the Aggregation Behavior of Aqueous PNIPAM Solutions*
  Kolloid-Tagung "Multiresponsive systems", Garching, 9-11 October 2017

- B.-J. Niebuur, N. S. Vishnevetskaya, E. Koziolov, E. A. Lomkova, P. Chytil, T. Etrych, S. K. Filippov, C. M. Papadakis
  *Influence of Molecular Characteristics on the Critical Micelle Concentration of Amphiphilic HPMA-Based Polymer Drug Carriers*
  3rd Workshop "Fluorescence correlation spectroscopy in soft matter science, Garching, 11-12 October 2017

- B.-J. Niebuur, K.-L. Claude, R. Schweins, V. Pipich, M.-S. Appavou, A. Schulte, C. M. Papadakis
  *SANS Study on the Pressure-Dependence of the Co-Nonsolvency Effect in Aqueous PNIPAM Solutions*
  DPG-Frühjahrstagung, Berlin, 11-16 March 2018

- B.-J. Niebuur, L. Chiappisi, X. Zhang, F. Jung, A. Schulte, C. M. Papadakis
  *Kinetics of Mesoglobule Formation in Aqueous PNIPAM Solutions Revealed with SANS and Fast*

*Pressure Jumps*

4th German SNI Conference, Garching, 17-19 September 2018

- B.-J. Niebuur, W. Lohstroh, M.-S. Appavou, A. Schulte, C. M. Papadakis
  *Water Dynamics in a Concentrated Poly(N-isopropylacrylamide) Solution at High Pressure*
  DPG-Frühjahrstagung, Regensburg, 31 March - 6 April 2019

- B.-J. Niebuur, W. Lohstroh, M.-S. Appavou, A. Schulte, C. M. Papadakis
  *Water Dynamics in a Concentrated Poly(N-isopropylacrylamide) Solution at High Pressure*
  French-German opportunities of cooperation to face the European revolution in neutron science, Garching, 14 May - 16 May 2019

# Acknowledgments

In this chapter, I would like to express my gratitude to all the people that were involved in the progress and success of my Ph.D.'s research. Without their help, I could not have been able to start this project, performing measurements or to obtain results.

First of all, I want to thank Christine M. Papadakis for being my supervisor during my Ph.D. project. She took all aspects of this role very seriously, and spend for everything a lot of time and effort. I truly appreciate these efforts to let me grow scientifically as well as a personally. Her deep knowledge on polymer physics, open mind for new experiments and analysis methods, effective help with writing manuscripts, and clear guidance whenever I needed it resulted in efficient teamwork, leading to the numerous results that are presented in this thesis. In addition, she was always available for scientific discussions, also when our opinions differed from each other. Overall, I really enjoyed working in her group!

Alfons Schulte served as the best mentor a Ph.D. student could wish for. Due to his positive attitude, no problem in his vicinity remained unsolved. Whenever I needed advice, he never let me leave empty-handed. He contributed greatly to the work presented in this thesis in many aspects, for example, I could rely on his expertise in high pressure setups during beamtimes and with improvement of in-house setups, on his knowledge about the literature, and on linguistic help with writing manuscripts. Furthermore, he was an excellent host during my stays in Orlando.

During the first months, Konstantinos N. Raftopoulos helped me with many different aspects of the work. His efforts gave me a head start that helped me to work efficiently during the entire Ph.D. project. I really cannot thank you enough for everything! Also other present and former colleagues, in alphabetical order, Anatoly Berezkin, Kora-Lee Claude, Margarita A. Dyakonova, Katerina Giannakopoulou, Peter Haslauer, Shu-Hsien Huang, Florian Jung, Jia-Jhen Kang, Chia-Hsin Ko, Geethu P. Meledam, Kaltrina Shehu, Natalya S. Vishnevetskaya and Xiaohan Zhang, contributed greatly to the obtained results with their absolute commitment during beamtimes (also at night), to the progress of the work whenever I asked for help with any difficulty, with providing specific knowledge, and to the pleasure I had at the chair. I especially enjoyed the rides, runs, hikes, hamburgers and the Weißbier on many occasions.

I feel extremely lucky with the five bachelor students, André Deyerling, Nicole Höfer, Jonas Puch-